DEPARTURE FROM NUCLEATE BOILING AND PRESSURE DROP PREDICTION FOR TUBES CONTAINING MULTIPLE SHORT-LENGTH TWISTED-TAPE SWIRL PROMOTERS

By

Tyrell Wayne Arment

B.S. Mechanical Engineering 2010

United States Naval Academy

SUBMITTED TO THE DEPARTMENT OF NUCLEAR SCIENCE
AND ENGINEERING
IN PARTIAL FULFILLMENT OF THE REQUIREMENTS FOR THE DEGREE OF

MASTER OF SCIENCE IN NUCLEAR SCIENCE AND ENGINEERING
AT THE
MASSACHUSETTS INSTITUTE OF TECHNOLOGY

JUNE 2012

Signature of Author: ____________________
Tyrell W. Arment
Department of Nuclear Science and Engineering
18 May 2012

Certified by: ____________________
Professor Emeritus Neil E. Todreas
Department of Nuclear Science and Engineering
Thesis Supervisor

Certified by: ____________________
Professor Emeritus Michael J. Driscoll
Department of Nuclear Science and Engineering
Thesis Reader

Accepted by: ____________________
Mujid S. Kazimi
TEPCO Professor of Nuclear Engineering
Chair, Department Committee on Graduate Students

Departure from Nucleate Boiling and Pressure Drop Prediction for Tubes Containing Multiple Short-Length Twisted-Tape Swirl Promoters
by
Tyrell Wayne Arment
Submitted to the Department of Nuclear Science and Engineering on May 18, 2012 in partial fulfillment of the requirements for the degree of Master of Science in Nuclear Science and Engineering at the Massachusetts Institute of Technology

Abstract

Previous studies conducted at MIT showed that the power performance of an inverted pressurized water reactor (IPWR) conceptual design, i.e. the coolant and moderator are inverted such that the fuel is the continuous medium and the moderator flows through coolant channels, has potential to outperform a traditional pressurized water reactor (PWR). Similar to the traditional PWR, the IPWR design involves a tradeoff between core pressure drop and the minimum departure from nucleate boiling ratio (MDNBR). In order to increase the power density of the IPWR, Ferroni [23] examined the possibility of inserting multiple short-length twisted-tapes (MSLTTs) in the cooling channels. For a fixed coolant mass flow rate, the swirling flow produced by the MSLTTs allows the IPWR to have a higher operating heat flux while maintaining the design criteria of MDNBR as compared to either the traditional PWR or IPWR without swirl promoters. However, the addition of each twisted-tape increases the core pressure drop which limits the coolant flow rate due to pumping power limitations of existing reactor coolant pumps (RCPs).

In order to better characterize the critical heat flux (CHF) enhancement caused by the addition of MSLTTs, this study performed a critical analysis of existing CHF correlations and models. Initially a phenomenological model was sought to describe the mechanisms of CHF for tubes containing MSLTTs; however, the full-length twisted-tape (FLTT) model that was selected for modification was found to have terms that could not be reconciled for the transition from fully developed swirl to decaying swirl. The existing CHF correlations for swirling flow were also found to be unsatisfactory. Therefore, the insights gained through working with the phenomenological model were used to develop a new empirical correlation to describe the departure from nucleate boiling (DNB) using existing swirling flow DNB data as well as an existing swirl decay model.

In order to allow for more flexibility in the placement of the MSLTTs, an existing FLTT pressure drop correlation was modified to account for the form pressure drop at the entrance to each twisted-tape insert as well as the friction pressure drop in the decaying swirl region downstream from the exit of each MSLTT. A sensitivity analysis of the new pressure drop correlation was also performed to determine if the complete methodology could be simplified.

Design insights were presented that help to narrow the design space for the IPWR. These steps should be followed in order to find the maximum power density possible by the IPWR design.

Finally, the existing swirl flow CHF data and correlations are presented in the appendices of this thesis.

Thesis Supervisor:	Neil E. Todreas
Title:	Professor Emeritus of Nuclear Science and Engineering
Thesis Reader:	Michael J. Driscoll
Title:	Professor Emeritus of Nuclear Engineering

Acknowledgements

I would like to thank Prof. Todreas for the countless hours he spent helping me with this project. While he has worked me very hard, I appreciate the fact that he did so to see my intellect develop. I hope that I can have as much passion about my career as he does for his.

I would also like to thank Prof. Bergles for his insight and advice in making this thesis as technically accurate and thorough as possible. I appreciate the many trips he took from the Cape to meet and discuss the finer points of this study.

Prof. Driscoll also deserves acknowledgement for stepping in at the last minute to review my thesis. I am grateful for his quick action in helping me complete my thesis requirements on time.

I am grateful for the input from Dr. Ferroni. He was very gracious in helping with this study even though he had much more important things to tend to at Westinghouse.

I am also thankful to Audrey, my wife, for the amount of patience and understanding she has shown me during my time at MIT. She is a blessing to have by my side.

The friends that I have come to know while at MIT have also been an integral part of my education. They are some of the brightest individuals I have ever known and will go on to do wonderful things with their lives. Particularly, I would like to thank Alex Mieloszyk for being a great friend that I could depend on for good advice, both technical and social.

Finally, I would like to thank my family for always believing in me and pushing me to excel in everything I do. Their love and support has pushed me to be the hardworking person I am today.

Contents

List of Figures

List of Tables

Nomenclature

α_{avg}	Average void fraction
α_{eff}	Effective void fraction
β	Angle corresponding to the thin portion of the tube wall in NUC heat flux tests
$\dot{m}$	Mass flow rate
ϵ	Figure of merit indicating the relative gain for a SLTT over an empty tube of the same length
$\epsilon_{\Delta P}$	Figure of merit indicating the increased pressure drop caused by a SLTT
γ	Ratio of swirling flow CHF to the empty tube CHF, i.e. TTCHFR
γ	Void fraction calculated using the Homogeneous Equilibrium Model
$\mu(R)$	Average error
μ_{SL}	Standard liquid viscosity
Ω	Non-uniform boiling heat flux correction term
ω	Angular velocity
ω_{cr}	Angular velocity corresponding to y_{cr}
$\overline{v'^2}^{1/2}$	Root mean square of the radial fluctuating velocity
Φ	Non-uniform heat flux correction term
ϕ_{lo}^2	Two-phase multiplier
ψ	Fraction of turbulent velocity fluctuations that penetrate the bubbly layer
ρ_g	Saturated liquid density
ρ_l	Liquid phase density
ρ_m	Average fluid density

ρ_m^+	Dynamic density
ρ_{SL}	Standard liquid density
σ	Surface tension
$\sigma\,(R)$	Standard deviation of error
σ_{SL}	Standard liquid surface tension
$\sigma_v^{'}$	Standard deviation of radial velocity fluctuations
τ_w	Wall shear stress
ξ	Tube inner perimeter
ξ_i	Bubbly layer-bulk flow interface perimeter
f	Friction factor
t_{web}	Fuel web thickness for the IPWR fuel matrix
a	Velocity correct term
BOC	Bottom of Core
BOL	Beginning of Life, i.e. when the reactor has just been refueled
CHF	Critical Heat Flux
D	Tube Inside Diameter
d_b	Bubble diameter
D_e	Equivalent diameter
d_H	Hinze equilibrium bubble diameter
D_S	Standard diameter, 2.54 cm
DNB	Departure from Nucleate Boiling
dP	Change in pressure, a positive value indicates a decrease in pressure
DSM	Direct Substitution Method
dz	Differential axial zone of the tube
E-IPWR	IPWR with no twisted-tape inserts

EBM	Energy Balance Method
EOL	End of Life, i.e. just before the reactor is shut down for refueling
FLTT	Full-Length Twisted-Tape
Fr	Froude number
G	Mass Flux
g_{acc}	Combination of centrifugal and gravitational acceleration
G_c	Critical mass flux used to define the lower bound of the Usman-Weisman FLTT DNB model
g_c	Gravitational constant, 9.81 m/s^2
G_{sw}	Swirl mass flux
h_{1d}	Bulk enthalpy at bubble departure
h_1	Bulk flow enthalpy
h_2	Bubbly layer enthalpy
h_{fg}	Heat of vaporization
h_f	Saturated liquid enthalpy
H_l	Single-phase liquid heat transfer coefficient
H-IPWR	IPWR with a twisted-tape with y=2.5 inserted in the upper half of the core
$i_{b,1\phi}$	Single-phase turbulent intensity factor
i_b	Turbulent intensity factor
IPWR	Inverted Pressurized Water Reactor
j_l	Superficial liquid velocity
j_v	Superficial vapor velocity
K	Form loss coefficient
L_{eff}	Effective boiling length for NUC heated tubes
l_e	Prandtl mixing length
L_h	Heated Length

L_{mig}	Migration length, i.e. distance between a bubble departs and when it is transported to the center of the flow in a swirling flow
LUT	Look-up Table
MDNBR	Minimum Departure from Nucleate Boiling Ratio
MSLTTs	Multiple Short-Length Twisted-Tapes
N_{nodes}	Number of discrete computational nodes used for thermal-hydraulic analysis
N_{turns}	Number of 360^o rotations of the twisted-tape
NUC	Non-Uniform Circumferential
P	Pressure
Pr	Prandtl number
PWR	Pressurized Water Reactor
q_{AVG}	Average heat flux
q_{ONB}	Onset of Nucleate Boiling heat flux, i.e. the heat flux above which bubbles form on the tube wall
r_o	Tube inner radius
R-113	Refrigerant type 113
RCP	Reactor Coolant Pump
Re	Reynolds number
Ro	Rossby number
s	Bubbly layer thickness
S-IPWR	IPWR with a twisted-tapes with y=1.5 spaced throughout the upper half of the core
SLTT	Short-Length Twisted-Tape
T_{in}	Average fluid temperature at the inlet of the heated section of the tube
T_{ONB}	Onset of Nucleate Boiling temperature, i.e. the temperature above which bubbles form on the tube wall
T_{sat}	Saturation temperature
T_w	Wall temperature

TOC	Top of Core
TPC	Two-Phase Correction factor for turbulent intensity
TTCHFR	Twisted-Tape Critical Heat Flux Ratio
U_τ	Shear velocity
U_T	Terminal velocity of a bubble
$UTh_{0.5}Zr_{2.25}H_{5.625}$	Fuel utilized by the IPWR
v_{11}	Boiling velocity
V_{ax}	Axial fluid velocity
W-3	DNB correlation developed by Tong
x_2	Bubbly layer quality
x_{cr}	Equilibrium Quality at CHF Location
$x_{eff,1}$	Effective bulk quality for a swirling flow
x_{eq}	Equilibrium quality
y	Twist Ratio, i.e. Length to complete 180° turn/Tube Diameter
y_{crit}	Upper bound of twist ratio that can be used with the Jensen or Ferroni correlation
y_{cr}	Twist ratio above which bubbles no longer are centrifuged to the center of the flow
y_c	Distance from the tube wall where the bubbly layer and bulk flow interact
y_{eff}	Effective twist ratio
y_o	Twist ratio of a SLTT used as the initial twist ratio for swirl intensity calculations in a swirl decay region
z	Axial location
z_D	Location of bubble departure
z_{ONB}	Location of the Onset of Nucleate Boiling

Chapter 1

Introduction

This chapter introduces the research performed on departure from nucleate boiling and pressure drop in tubes containing multiple short-length twisted-tape swirl promoters in the following order:

- Motivation and Objectives of the Study: Section 1.1
- Background: Section 1.2
- Methodology of Investigation: Section 1.3

1.1 Motivation and Objectives

Previous work by Malen et al. [62], which was later explored in-depth by Ferroni [23] outlined the potential of an innovative pressurized water reactor (PWR) design to increase the power density relative to existing PWRs. In a traditional PWR, the fuel matrix consists of fuel rods surrounded by a continuous medium of coolant. The design of this new reactor involved inverting this geometry such that the fuel takes the place of the continuous medium and the coolant passes through the fuel in cooling channels. This reactor concept was aptly named the Inverted Pressurized Water Reactor (IPWR). A comparison of the unit cell geometry for the two fuel matrices is shown in Figure 1-1, where the IPWR design is on the left and the PWR design is on the right.

The tubular construction of the cooling channels of the IPWR lend themselves to the application of twisted-tape swirl promoters. These swirl promoters will increase the margin to boiling crisis, allowing for a higher operating heat flux. However, they also increase the core pressure drop, limiting the mass flow rate that can be produced by the reactor coolant pumps (RCPs). Therefore, in order to maximize the power output of the IPWR while satisfying the pumping capacity constraint, multiple short-length twisted-tapes (MSLTTs), i.e. short-length twisted-tapes spaced at user-defined intervals throughout the tube, were implemented in the design.

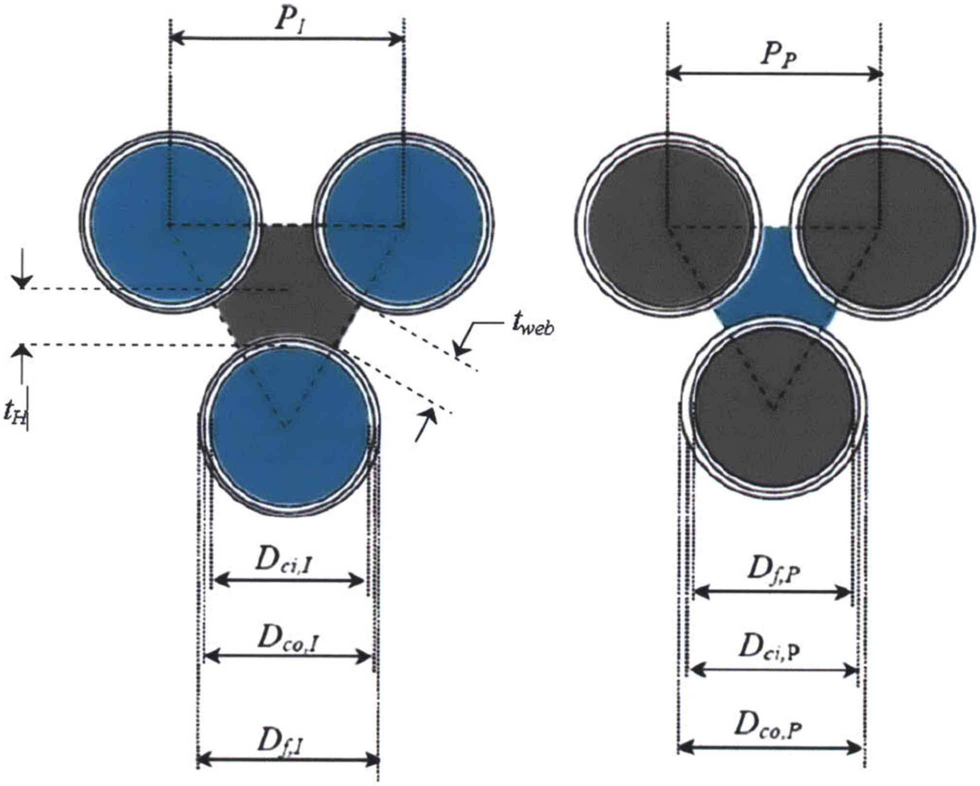

Figure 1-1: IPWR (left) vs. Triangular Lattice PWR (right) Fuel Matrix Geometry: Taken from Ferroni [23]

Blue = Coolant ; Grey = Fuel

The present work aims at developing enhanced analysis methodologies, with respect to those used by Ferroni [23], for investigating the performance of MSLTT-provided devices in general, and the IPWR in particular. The work performed by Ferroni had in fact three main limitations:

1. Limited choices for the twisted tape spacing: this parameter, defined as the distance from the downstream end of one twisted-tape to the upstream end of the subsequent one, was assigned three possible values only, i.e. 30, 40 and 50 diameters. In spite of being representative of the spacing range over which IPWR design optimization should likely focus, the limitation to discrete values clearly prevents identification of the optimal IPWR design, allowing only for an estimate.
2. Limited applicability range of the pressure drop correlation: as a consequence of the choice discussed on point 1) above, Ferroni et al. [24] developed an experimental pressure drop correlation only applicable to twisted-tape spacings ranging between 30 and 50 diameters.
3. Partially suited CHF correlation: the CHF correlation chosen by Ferroni for analyzing IPWR performance, i.e. a modified version of the Jensen correlation [44], was developed from saturated boiling data only, whereas subcooled boiling CHF is expected to characterize the IPWR operating conditions.

Moreover, the empty-tube CHF correlation on which that correlation is based, i.e. the Katto correlation [48], is formulated differently depending on the thermal-hydraulic regime under consideration. Because of this, and because of the axial variation of this regime expected for the IPWR channels, discontinuities in CHF predictions have been observed.

Therefore, in an attempt to better characterize the use of MSLTTs in heat-transfer applications in general, and in the design of the IPWR in particular, the following objectives were outlined for this study:

1. Develop an empirical DNB correlation that is based on physical phenomena and is applicable to the operating conditions in the IPWR in order to accurately predict DNB for tubes containing MSLTTs spaced at user defined intervals.
2. Develop a methodology for calculating friction pressure drop for heated tubes containing MSLTTs at user defined intervals.
3. Outline the design methodology for optimizing the power output of an IPWR equipped with MSLTTs.

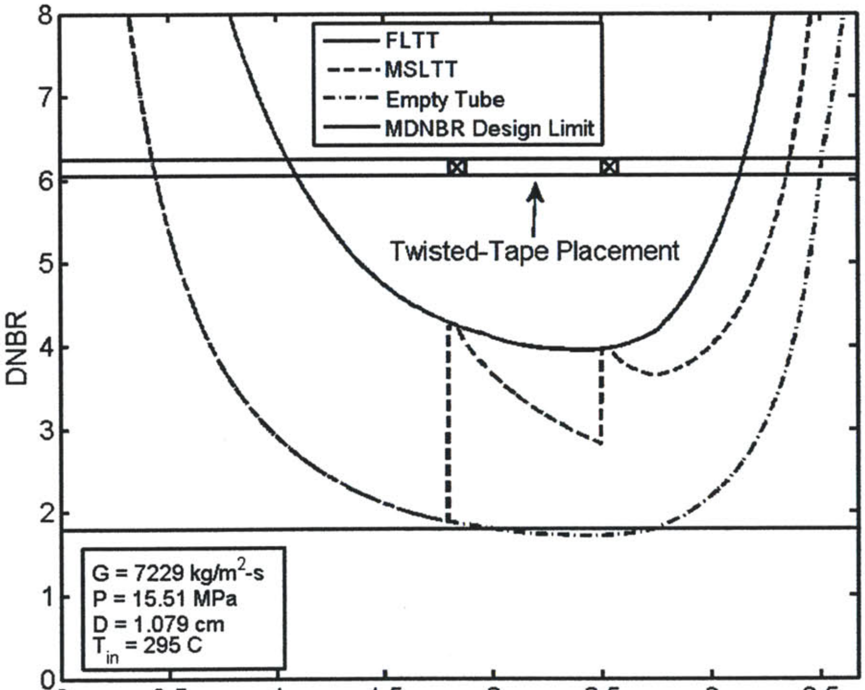

Figure 1-2: DNBR vs. Axial Height

The goals of this work can be better understood by anticipating the effect that SLTTs have on two of the main design constraints, i.e. minimum departure from nucleate boiling ratio (MDNBR) and pressure drop.

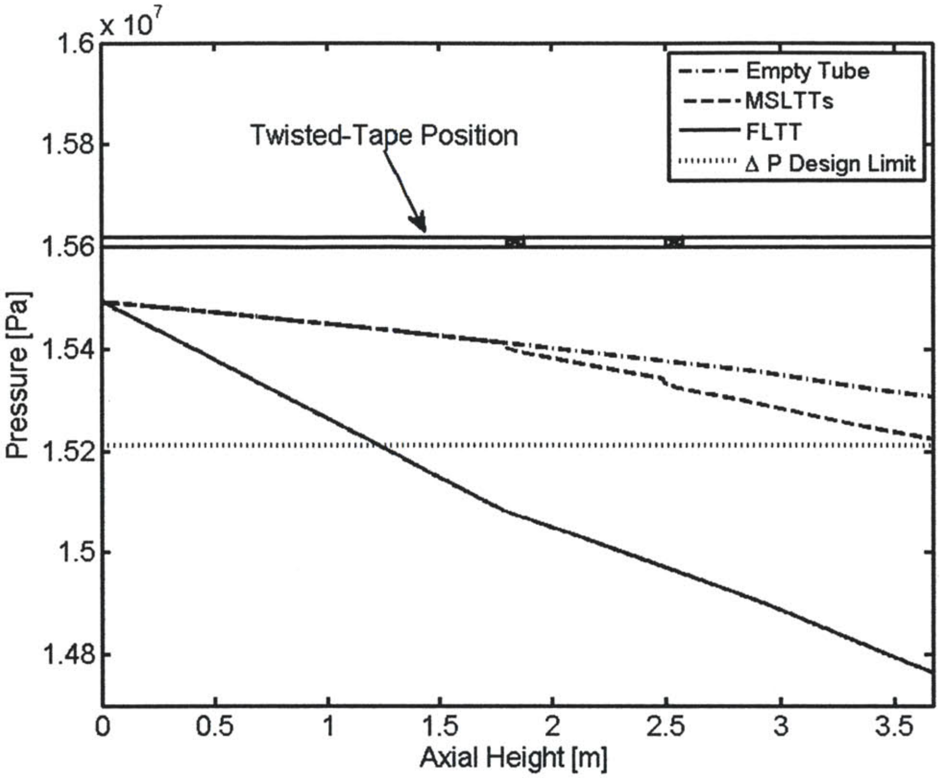

Figure 1-3: Pressure vs. Axial Height

One of the main design criteria is that the MDNBR does not fall below 1.79, i.e. the minimum ratio of the critical heat flux to the operating heat flux. An example of a DNBR analysis is shown in Figure 1-2 where two twisted-tapes, each with a twist ratio of 2.5 going through 1.5 360° rotations, were placed 1.8 and 2.5 meters from the bottom of the core. The other operating conditions are shown on the figure. The pressure vs. axial height curves for these same cases are shown in Figure 1-3. In both of these figures, the curves for the empty tube and the tubes with the full-length twisted-tape (FLTT) are well characterized through existing empirical correlations. The goal of this study is to characterize the curves for the MSLTTs such that they are bounded with the empty tube and FLTT analytic results. This goal will be accomplished by developing new critical heat flux and pressure drop correlations, and then a methodology on how to implement these correlations in the design of the IPWR in a way that meets the constraints of both the MDNBR and pressure drop limit as shown by the horizontal lines in Figures 1-2 and 1-3 will be proposed.

1.2 Background

This section will provide a brief background on the phenomena of interest to this study in the following order:

- Boiling Crisis Phenomenon: Section 1.2.1
- Thermal-Hydraulic Models vs. Correlations: Section 1.2.2
- Existing CHF Studies: Section 1.2.3
- Existing Pressure Drop Studies: Section 1.2.4
- Existing Heat Transfer Studies: Section 1.2.5
- IPWR Design History: Section 1.2.6

1.2.1 Boiling Crisis Phenomenon

The point where heat transfer rapidly degrades during convective heat transfer is known as the boiling crisis. This point is often referred to as the critical heat flux (CHF), or critical condition. In subcooled or low quality flows, a thin vapor blanket forms on the heating surface, the phenomenon is known as departure from nucleate boiling (DNB). DNB typically occurs in the bubbly flow regime, and is considered to be a local phenomenon, meaning that the onset of DNB only depends on the local conditions. In heat flux controlled systems, e.g. nuclear reactors, DNB causes the cladding to fail due to rapid temperature spikes.

In conditions of high void fraction, also known as annular flow, the boiling crisis typically takes the form of liquid film Dryout. This phenomena occurs when the thin liquid film on the tube wall disappears due to evaporation and entrainment. This process is highly dependent on the channel power history, and is typically expressed as a critical quality. In a high void fraction light water reactor, such as a boiling water reactor, Dryout is a transient process where the liquid film front is not stationary and the temperature of the cladding is typically not high enough to melt. Therefore, the cladding will fail due to cyclic thermal stresses caused by the transient nature of the phase front.

The typical void fraction distributions for DNB and Dryout are shown in Figure 1-4. This study will be primarily focused on the phenomena of DNB since this phenomena is applicable to the design of the IPWR.

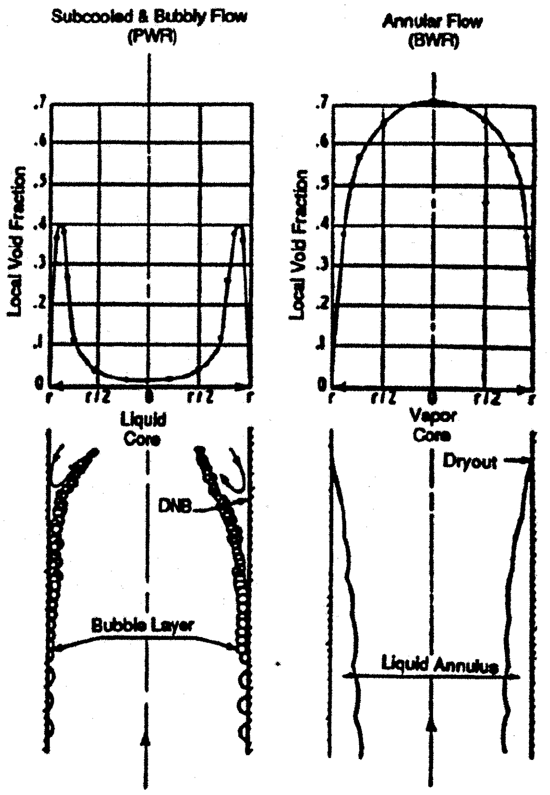

Figure 1-4: Radial Void Fraction Profile for DNB and Dryout: Taken from Todreas et al. [82]

1.2.2 Models vs. Correlations

When predicting a phenomena such as CHF, there are generally two approaches taken by researchers and designers. The first approach is to gather data over a specified range of interest and develop an analytic expression using the variables of the experiment to describe the data. This range is typically predesignated by the design constraints of the problem. An example of this is the development of the W-3 CHF correlation [84]. Once developed, a correlation is a powerful design tool for the operating range within the bounds of the data that were used to developed it.

A second approach to predicting the phenomenon is to develop a model. A model consists of a collection of correlations or sub-models that describe the underlying mechanisms that cause the phenomenon to occur. Models are generally complex; however, it can be argued that if the mechanism of a phenomenon, such as CHF, can be identified, then a model can be used to accurately predict the phenomenon over a wide range of operating conditions, some of which may be outside the range of existing experimental data. An example of this approach is the Pei-Weisman model for axial flow DNB [74]. In CHF studies, an added benefit of using a model is that, if properly developed, it can describe the behavior of a variety of fluids. This is beneficial since fluids other than water that have similar boiling properties at lower pressure and temperatures, i.e. R-113,

Table 1.1: Existing DNB and Dryout Correlations for Swirl Flow

Author	Ref.	P (MPa)	G $(\frac{kg}{m^2 s})$	x_{cr}*	L_h (cm)	D (mm)	y
Gambill et al.	[27]	0.101 - 3.758	4476 - 47555	(-0.383) - 0.113	3.454-44.12	3.45-10.21	2.08 - 12.03
Drizius et al.	[21]	0.393 - 1.335	4500 - 24800	(-0.157) - (-0.046)	3.7-14.1	1.6	1.25 - 10.25
Whalley	[97]	6.90	2712	not published	366.0	12.62	4.04
Jensen	[44]	0.101 - 13.8	120 - 5840	0.01 - 0.99	28.0-487.7	7.0-20.0	2.5 - 34.5
Nariai et al.	[71]	0.101 - 1.47	5300 - 7400	(-0.256) - (-0.054)	10.0	6	2.61 - ∞
Weisman et al.	[95]	0.777 - 20.75	$0.3G_c$ - 40000	$x_1 > -0.3$; $\langle\alpha\rangle < 0.64$	3.5-365.0	1.15-37.5	2.3 - 12
Tong et al.	[87]	0.392 - 1.398	5049 - 18290	(-0.306) - (-0.129)	0.664-15.7	2.44-6.54	1.9 - 7.1
Krug et al.	[57]	0.100 - 20.1	200 - 39000	(-0.45) - 0.95 (x_{in})	0.95-480 L/D		1 - 34.5
Modified Jensen	[23]	0.101 - 13.8	120 - 5840	0.01 - 0.99	28.0-487.7	7.0-20.0	y < y_{crit} **
Hata et al.	[34]	0.775 - 0.889	4016 - 13950	(-0.28) - (-0.11)	5.95	6.0	2.39 - 4.45

*x_{cr} is the equilibrium quality at the point of boiling crisis

**y_{crit} is an upper bound on twist-ratio needed to avoid non-physical trends of the correlation

can be used for CHF experiments, thereby reducing experimental costs. The results of such experiments can be used to adjust the model. Then the model can translate the results via fluid properties to similar conditions with water.

It is important to note that in this study, the use of the words "correlation" and "model" will be used to describe the two different techniques described in the previous paragraphs.

1.2.3 Existing CHF Studies

A number of existing DNB and Dryout correlations for FLTTs were examined to check if any of them could be modified to predict DNB in tubes containing MSLTTs. Due to a variety of reasons that will be discussed at length in Chapter 3, no satisfactory correlation was found that could be used for the design of the IPWR. Therefore the development of a new correlation was necessary. The operating ranges of the existing correlations are shown in Table 1.1. A full description of each of these correlations can be found in Appendix C.

1.2.4 Existing Pressure Drop Studies

Several correlations for FLTT and MSLTT friction pressure drop do exist, as shown in Table 1.2; however, these correlations were found to be lacking due to their limited range of applicability. Therefore, it was decided to select a FLTT correlation, i.e. Kanizawa et al. [47], and to modify it before application to the IPWR design. The description of how this correlation was modified to account for MSLTTs will be discussed in Chapter 5.

Table 1.2: Existing FLTT and MSLTT Friction Factor Correlations

Author	Ref.	FLTT/MSLTT	Single- or Two-Phase Flow
Agrawal et al.	[2]	FLTT	Two-Phase
Akhavan-Behabadi et al.	[3]	FLTT	Two-Phase
Jensen et al.	[46]	FLTT	Two-Phase
Kanizawa et al.	[47]	FLTT	Both
Manglik et al.	[63]	FLTT	Single-Phase
Ferroni et al.	[24]	MSLTT	Single-Phase
Saha et al.	[76]	MSLTT	Single-Phase

1.2.5 Existing Heat Transfer Studies

The goals of this study did not include the development of a new heat transfer coefficient calculation methodology for MSLTTs. Existing correlations were instead used. Heat transfer coefficients are important to the calculation of pressure drop because they provide the tube wall temperature, which in turn is used for a viscosity correction factor as detailed in Chapter 5. Furthermore, the heat transfer coefficients are important for two other design limiting factors, i.e. maximum cladding temperature and maximum fuel temperature. A complete listing of the heat transfer coefficients used in this study is shown in Table 1.3.

Table 1.3: Heat Transfer Coefficients Used in This Study

Boiling Condition	**Author(s)**	**Ref.**
	Axial Flow	
Single-phase	Gnielinski	[29]
Subcooled Boiling	Collier and Thome (modified Chen)	[15]
Saturated Boiling	Chen	[14, 82]
	Swirl Flow Inside a TT	
Single-phase	Manglik and Bergles	[63]
Subcooled Boiling	None Available, used Collier and Thome	[15]
Saturated Boiling	Jensen and Bensler	[45]
	Swirl Flow in Decaying Swirl	
Single-phase	Modified Jensen and Bensler	[23, 45]
Subcooled Boiling	None Available, used Collier and Thome	[15]
Saturated Boiling	Modified Jensen and Bensler	[23, 45]

1.2.6 IPWR Design History

The design work performed by Ferroni on the IPWR accounted for the design constraints listed in Table 1.4. The optimization of the IPWR consisted of balancing the limits of principle criteria, i.e. core pressure drop, maximum fuel temperature, and MDNBR. The pressure drop limits were defined as 1.0, 1.5, and 2.0

times the core pressure drop for the reference PWR used in Ferroni's study [23], i.e. the Seabrook PWR [1]. The maximum fuel temperature was set to limit the release of hydrogen from the uranium-zirconium-thorium-hydride fuel, i.e. $UTh_{0.5}Zr_{2.25}H_{5.625}$. The MDNBR limit was imposed by performing a reverse engineering analysis of the Seabrook PWR. The peak cladding temperature was also considered in order to limit the oxidation rate, both during normal operation and during loss of coolant accidents. However, it was never found to be a limiting factor. The bounds on fuel web thickness, shown as t_{web} in Figure 1-1, and the channel diameter are not hard limits, but rather practical limits explored in Ferroni's design work [23]. Finally, the inlet temperature and coolant enthalpy rise were set to match the Seabrook PWR [1, 23].

Table 1.4: IPWR Steady-State Thermal Hydraulic Design Limitations: Adapted from Ferroni [23]

Parameter	Units	Range/Limit
Pressure Drop Across Core	[kPa]	$1.0X = 150$ $1.5X = 225$ $2.0X = 300$
Steady-state Peak Fuel Temperature	$[^oC]$	650
MDNBR	[-]	1.79
Steady-State Peak Clad Inner Temperature	$[^oC]$	370
Fuel Web Thickness	[mm]	2.0 - 6.0
Coolant Channel Diameter	[cm]	0.7 - 1.5
Core Inlet Temperature	$[^oC]$	296.3
Coolant Enthalpy Rise	$[\frac{kJ}{kg}]$	195.2

The design space, i.e. number of MSLTTs, spacing, twist ratio, and length is very broad. Ferroni found that the IPWR performed best without using twisted-tape inserts. The increased pressure drop caused by the MSLTTs resulted in a decreased core flow rate; thereby limiting the channel power in order to maintain a fixed core enthalpy rise. However, as mentioned earlier Ferroni was restricted in his design approach by the choice of three discrete twisted-tape spacings only, and used a CHF correlation more suited to saturated boiling than subcooled boiling. In an attempt to remove these restrictions, this study looks at developing correlations for both pressure drop and CHF for tubes containing MSLTTs at user defined intervals. By removing these restrictions it is hoped that a more optimal result can be derived for the IPWR design in which the MSLTT-equipped reactor out-performs the twisted-tape-free reactor presented in Ferroni's thesis [23].

1.3 Methodology of Investigation

This study was divided into four developmental phases and one applied theory phase. First, a phenomenological model for DNB with MSLTTs was sought by modifying the Usman-Weisman FLTT DNB model [95] which is presented in Chapter 2. However, after finding issues with its derivation this approach was abandoned, but the insights gained from working with this model were used to analyze the existing CHF database for FLTT and short-length twisted-tapes (SLTTs) in Chapter 3. By combining these insights and the observations made when examining the data, a new empirical DNB correlation was developed in Chapter 4. The final developmental part of the study, presented in Chapter 5, consisted of modifying an existing friction factor formula to account for the presence of MSLTTs in order to quantify the trade-off between pressure drop penalty and CHF enhancement.

Finally, some insights regarding the practical application of MSLTTs to the design of the IPWR were developed in Chapter 6. These insights were gained through the extensive two-year study of twisted-tape swirl promoters and should be referenced when implementing MSLTTs in the IPWR design.

Chapter 2

Exploration of Extending the Usman-Weisman DNB Model to MSLTTs

This chapter will cover the origins of the Pei-Weisman model, its basic assumptions, and the phenomenology of DNB. The chapter organization is as follows:

- Historical Modifications of the Pei-Weisman model: Section 2.1.
- Phenomenology of DNB in Axial Flow at Low Quality: Section 2.2
- Modification of the DNB Model for FLTTs: Section 2.3
- Issues with Adapting the FLTT DNB Model for MSLTTs: Section 2.4
- Insights Gained from the FLTT DNB Model: Section 2.5

2.1 Historical Modification of the Pei-Weisman Model

The Pei-Weisman DNB model was originally developed for empty tubes, i.e. pure axial flow, with low or subcooled exit qualities with high velocity flows and is applicable to several fluids other than water including R-113, helium, and nitrogen [94]. Since then, the correlation has been modified to become applicable for a wide range of flow conditions. A time line of these modifications is presented in Table 2.1.

The range of operating conditions over which the model is valid for tubes not containing enhancement devices is given in Table 2.2. The model is intended to be used in the bubbly flow regime where the buoyant force of bubbles can be neglected and the homogeneous approximation for flow velocities is applicable.

Table 2.1: Time line of the Weisman DNB Model

Developer	Ref.	Year	Extension
Pei	[94]	1983	Original Model
Ying	[96]	1985	Rod Bundles
Ying	[102]	1986	$\alpha \leq 0.8$, $V_{SL} > 0.5$m/s
Ileslamlou	[93]	1987	$-0.47 \leq x_e \leq -0.12$
Yang	[101]	1991	Boiling Curves Near DNB and Non-Uniform Heat Flux Bubbly-Layer Effect
Yang, Usman	[95]	1994	Full-length Twisted-Tapes

V_{SL} is the superficial liquid velocity

Table 2.2: Pei-Weisman DNB Model Operating Range for Axial Flow

$0.0045 \leq \left(\frac{\rho_g}{\rho_f}\right) \leq 0.41$
$0.115 < D \leq 3.75$ cm
$3.5 \leq L_h \leq 365$ cm
$0.3G_c \leq G \leq 40,000 \ \frac{kg}{m^2 s}$
$-0.47 \leq x_1$; $\langle\alpha\rangle \leq 0.81$

2.2 Phenomenology of DNB for Tubes with Pure Axial Flow

The basic formulations to predict DNB using the Pei-Weisman model are presented in Equations (2.1) and (2.2), and are applicable to the subcooled and saturated flow regime respectively. This section will cover the general concepts that were used to develop the Pei-Weisman DNB model for tubes without turbulence promoters.

$$q''_{cr} = G i_b \psi (h_2 - h_1) \tag{2.1}$$

$$q''_{cr} = G i_b \psi h_{fg} (x_2 - x_1) \frac{(h_f - h_{1d})}{(h_1 - h_{1d})} \tag{2.2}$$

2.2.1 Mass Balance of the Bubbly Layer

The Pei-Weisman model is based on a mass balance between a thin bubbly layer and the core of the flow, referred to as region 2 and region 1 respectively. The control volume for this calculation is shown in Figure 2-1. The total mass flow rate balance for the differential slice of the bubbly layer can be calculated according to Equation (2.3).

$$\dot{m}_3 = \Delta\dot{m}_2 + \dot{m}_4 \tag{2.3}$$

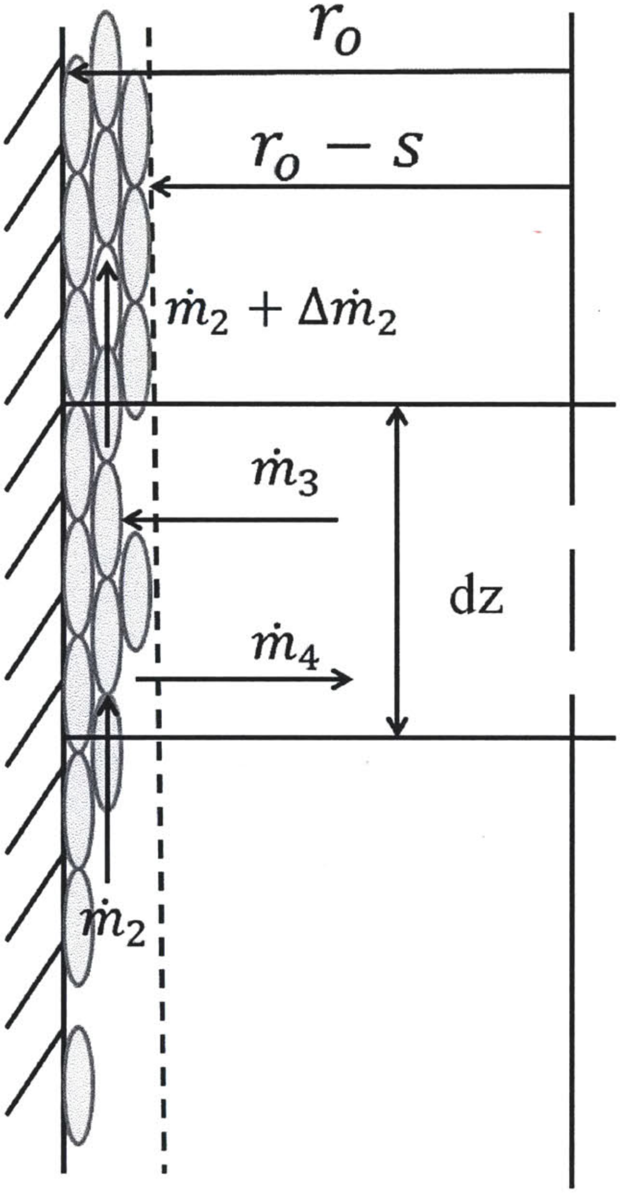

Figure 2-1: Bubbly Layer and Core Mass Flow Rates: Adapted from Pei [73]

Assuming that at the point of DNB the mass flow rates into and out of the bubbly layer are exactly equal, i.e. $\dot{m}_3 = \dot{m}_4$, it is possible to perform a mass balance on the liquid flowing into and out of this control volume. The qualitative expression of the mass balance is shown in Equation (2.4) and the explicit expression is shown in Equation (2.5).

$$Liquid\ in = Liquid\ stored + Liquid\ out \tag{2.4}$$

$$\dot{m}_3 (1 - x_1) = [\Delta\dot{m}_2 (1 - x_2) - \dot{m}_2\Delta x_2 + \Delta\dot{m}_2 (1 - \Delta x_2)] + \dot{m}_3 (1 - x_2) \tag{2.5}$$

By ignoring the higher order term, and dividing through by the differential area that the mass transfer is occurring through, i.e. $2\pi(r_o - s)dz$, the mass flow rate into the bubbly layer can be rewritten as a mass flux such that $G_3 = \frac{\dot{m}_3}{2\pi(r_o-s)dz}$. The change in the liquid flow rate through the bubbly layer is due to the phase transition during boiling as shown in Equation (2.6), where $q_b^{''}$ is the heat flux that is going into boiling according to the Lahey model [58] as shown below.

$$\Delta\dot{m}_2 (1 - x_2) = \frac{q_b^{''}}{h_{fg}} \tag{2.6}$$

$$q_b^{''} = \begin{cases} q_{total}^{''} \left(\frac{h_l - h_{1d}}{h_f - h_{1d}}\right) & if\ h_l \geq h_{1d} \\ 0 & otherwise \end{cases}$$

h_l =liquid phase enthalpy

h_f =saturated liquid enthalpy

h_{1d} =enthalpy of the liquid at bubble departure found using the Levy model [60]

By combining like terms and simplifying, the liquid mass flux balance is expressed as shown in Equation (2.7).

$$G_3 (x_2 - x_1) = \frac{q_b^{''}}{h_{fg}} \left(\frac{r_o}{r_o - s}\right) - \frac{\dot{m}_2}{2\pi (r_o - s)} \left(\frac{\Delta x_2}{dz}\right) \tag{2.7}$$

where, $s(z) = bubbly\ layer\ thickness\ = 6.863 d_b(z)$ *[value taken from computer code in Usman's thesis [88]]*

The mass balance was further simplified by assuming that the bubbly layer thickness is negligible compared to the radius of the pipe. Also, the change in quality of the bubbly layer was assumed to be negligible, eliminating the second term on the right-hand side of Equation (2.7). It will be shown in Section 2.2.6 that the second term in Equation (2.7) cannot be fully neglected in the case of non-uniform heat flux; however, for uniformly heated tubes this term is negligible. By substituting the full expression for the boiling heat flux, the final expression for the liquid mass balance for the bubbly layer is shown in Equation (2.8).

$$G_3\left(x_2-x_1\right)=\frac{q''_{tot}}{h_{fg}}\left(\frac{h_l-h_{1d}}{h_f-h_{1d}}\right) \tag{2.8}$$

An important assumption of this model is that the bubbly layer quality, x_2, corresponds to the maximum void fraction caused by the packing of ellipsoidal bubbles with a length to diameter ratio of approximately 3:1 [73]. This maximum void fraction is set to 82% and the quality is calculated using homogeneous flow approximations.

Since the bubbly layer void is assumed to be 82%, a condition which is only true at CHF, the heat flux must be iterated upon until Equation (2.8) is true. The only term that is not already well defined in Equation (2.8) is the mass flux into the bubbly layer, i.e. G_3. Therefore a derivation for this term needs to be developed, and it will be presented in the next two sections.

2.2.2 Turbulent Intensity Factor

There is an interaction between the bubbly layer and the core of the flow due to radial velocity fluctuations of the turbulent flow near the boundary of these two regions. Physically these fluctuations can be attributed to three causes: interaction of the bulk flow with the bubbles on the pipe wall, shear stress, and disruptions of flow due to the bubbles departing during boiling. The radial velocity fluctuations can expressed as the product of the mean fluid velocity and the root mean square of the radial fluctuating velocity as shown in Equation (2.9).

$$i_b=\frac{\rho_m}{G}\overline{v'^2}^{1/2} \tag{2.9}$$

Pei and Weisman postulated that the root mean square of the radial fluctuating velocity is a function of distance away from the tube wall. This relationship can most clearly be seen when $\overline{v'^2}^{1/2}$ is grouped with the shear velocity, U_τ, and the ratio of the Prandtl mixing length and tube radius as shown in Equation (2.10).

$$\frac{\left[\frac{\overline{v'^2}^{1/2}}{U_\tau}\right]}{\left(\frac{l_e}{r_o}\right)}=F_1 2.9\left(\frac{r}{y}\right)^{0.4} \tag{2.10}$$

where,

y = distance from the tube wall (not twist ratio)

$l_e = 0.4y$

$U_\tau=\sqrt{0.023}Re^{-0.1}\left(\frac{G}{\rho_m}\right)$

F_1 =unknown function that accounts for the presence of bubbles

Now that the turbulent velocity fluctuations have been described as a function of distance from the tube wall, the location of the bubbly layer/bulk flow interface needs to be determined. Pei and Weisman postulated that this distance is related to the bubble diameter as shown in Equation (2.11) [74].

$$F_2 l_e = k d_b \tag{2.11}$$

where,

F_2 =unknown function that accounts for the presence of bubbles

$l_e = 0.4 y_c$

y_c =bubbly layer interface location

k = empirically fit constant

d_b =bubble diameter

By combining Equations (2.9) - (2.11) and assuming the the unknown functions F_1 and F_2 can be related to the fluid properties via an empirically adjusted density ratio, the final expression for the axial flow turbulent intensity factor is shown in Equation (2.12).

$$i_b = 0.462 Re^{-0.1} (k)^{0.6} \left(\frac{d_b}{D}\right)^{0.6} \left[1 + a\left(\frac{\rho_l - \rho_g}{\rho_g}\right)\right] \tag{2.12}$$

$$d_b = 0.015 \left(\frac{8 \rho_m g_c \sigma D}{f G^2}\right) \tag{2.13}$$

where,

k = 2.5

a = 0.135

D = tube diameter

f =Darcy friction factor

2.2.3 Net Rate of Two-Phase Mass Transfer into the Bubbly Layer

It was postulated by Pei and Weisman that the radial fluctuations of the velocity are normally distributed due to the large number of random forces effecting the motion of the fluid in turbulent flow [74]. Since the flow is bounded by the tube walls, the time averaged radial velocity at a given dz must be equal to zero. By assuming that the standard deviation of the fluctuating velocity is equal to the root mean square of these fluctuations, the standard deviation can be defined as shown in Equation (2.14).

$$\sigma_v^{'} = \overline{v'^2}^{1/2} = \left(\frac{G}{\rho_m}\right) i_b \tag{2.14}$$

By using the definition of a normal distribution whose mean value is zero, an expression for the distribution of instantaneous radial velocity can be expressed as shown in Equation (2.15).

$$f(v') = \frac{1}{\sqrt{2\pi}\sigma_v^{'}} exp\left(-\frac{1}{2}\left(\frac{v'}{\sigma_v^{'}}\right)^2\right) \tag{2.15}$$

By assuming that the radial velocity has to overcome some threshold value before the fluid can penetrate the bubbly layer, the net rate of mass flux into the bubbly layer, G_3, can be calculated by integrating the product of the average density and all velocities above the threshold velocity as shown in Equation (2.16).

$$G_3 = \bar{\rho} \int_{v_{11}}^{\infty} (v' - v_{11}) f(v') \, dv \tag{2.16}$$

The integration of this term results in Equation (2.17). By combining this expression with Equation (2.14) and simplifying, the probability of a radial velocity fluctuation actually penetrating the bubbly layer, ψ, is expressed in Equation (2.18).

$$\int_{v_{11}}^{\infty} (v' - v_{11}) f(v') \, dv = \psi \sigma_v^{'} = \sigma_v^{'} \left\{ \frac{1}{\sqrt{2\pi}} exp \left(-\frac{1}{2} \frac{v_{11}}{\sigma_v^{'}} \right)^2 - \frac{1}{2} \left(\frac{v_{11}}{\sigma_v^{'}} \right) erfc \left(\frac{1}{\sqrt{2}} \frac{v_{11}}{\sigma_v^{'}} \right) \right\} \tag{2.17}$$

$$\psi = \frac{1}{\sqrt{2\pi}} exp \left(-\frac{1}{2} \frac{v_{11}}{\sigma_v^{'}} \right)^2 - \frac{1}{2} \left(\frac{v_{11}}{\sigma_v^{'}} \right) erfc \left(\frac{1}{\sqrt{2}} \frac{v_{11}}{\sigma_v^{'}} \right) \tag{2.18}$$

The threshold velocity term, v_{11}, was determined by postulating that all of the bubbles that are produced during boiling are leaving at the same rate they are produced. The expression for the bubble production velocity is shown in Equation (2.19).

$$v_{11} = \frac{q_b^{"}}{\rho_g h_{fg}} \tag{2.19}$$

By combining Equations (2.8), (2.14), and (2.17), the final expression for the CHF is shown in Equation (2.2), which is repeated below for convenience.

$$q_{cr}^{"} = G i_b \psi h_{fg} (x_2 - x_1) \frac{(h_f - h_{1d})}{(h_1 - h_{1d})} \tag{2.20}$$

This equation was found to be valid for slightly subcooled as well as slightly positive equilibrium quality conditions, i.e. $\overline{\alpha} \leq 0.64$, however, under highly subcooled conditions Illeslamlou and Weisman concluded that the model over-predicted CHF because the liquid enthalpy was very close to the departure enthalpy which caused an error in the boiling heat flux calculation [93]. This problem was solved by performing an energy balance on the bubbly layer which resulted in Equation (2.23). In practice, Equation (2.2) is used for saturated boiling, while Equation (2.1) is used for subcooled boiling CHF prediction.

$$E_{inward} = G_3 \left[h_l (1 - x_1) + h_g x_1 \right] = G_3 h_1 \tag{2.21}$$

$$E_{outward} = G_3 \left[h_f (1 - x_2) + h_g x_2 \right] = G_3 h_2 \tag{2.22}$$

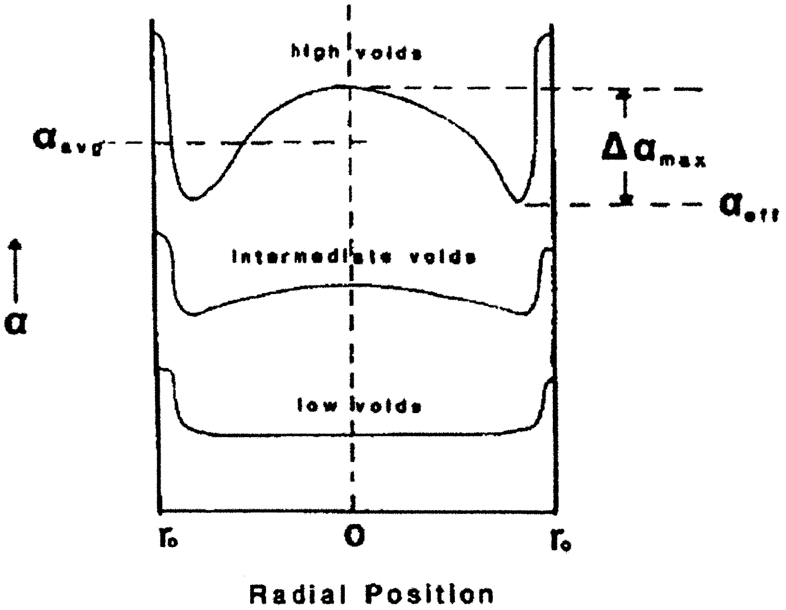

Figure 2-2: Void Profile Distributions [102]

$$q''_{CHF} = (E_{outward} - E_{inward}) = G\psi i_b (h_2 - h_1) \tag{2.23}$$

2.2.4 High Void Fraction

The original Pei-Weisman model was only valid for $\alpha_{avg} \leq 0.64$. Above this point the relative spread of data remained constant; however, the model tended to increasingly under-predict CHF with increasing void fraction. Ying and Weisman postulated that this problem was caused by the assumed void profile [102]. The original void profile was assumed to be flat in the bubbly layer, i.e. Region 1, and core flow regions, i.e Region 2, with $\alpha_2 = 0.82$ and $\alpha_1$being calculated using a homogeneous distribution. At void fractions greater than 64%, the distribution of void begins to transition to a center-peaked shape as annular flow is approached. The distributions of void for these high void fractions are shown in Figure 2-2.

Due to the elevated void fraction in the center of the channel, there was a corresponding decrease in void near the bubbly layer interface, as can be seen in Figure 2-2 when comparing α_{avg} to α_{eff}. As a result, the original formulation was over-predicting the region one quality term, i.e. x_1, in Equation (2.2), causing the predicted CHF to be too low. Therefore, an empirical relationship between the average void and the effective void fraction near the bubbly layer was developed based on experimental data. A piecewise function was created to calculate the effective void fraction, i.e. α_{eff}, and it is shown in Equation (2.24).

$$\alpha_{eff} = \begin{cases} \alpha_{eff} = \alpha_{avg} & if\ \alpha_{avg} \leq 0.642 \\ \alpha_{eff} = 0.642 + 0.37\left(\alpha_{avg} - 0.642\right) & if\ 0.642 < \alpha_{avg} \leq 0.788 \\ \alpha_{eff} = 0.696 + 0.2\left(\alpha_{avg} - 0.788\right) & if\ 0.788 < \alpha_{avg} \leq 0.81 \end{cases} \tag{2.24}$$

2.2.5 Low Mass Flux Correction

In the lower end of the flow velocity range, the buoyancy force becomes non-negligible and must be accounted for in the model. The DNB model accounts for this effect by adjusting the two-phase correction factor in the turbulent intensity factor by altering the "a" term in Equation (2.12) according to the mass flux as shown in Equation (2.25).

$$a = \begin{cases} 0.135 + 1.51\left(1 - \frac{G}{G_c}\right)^2 - 0.25\left(1 - \frac{G}{G_c}\right) & for\ G < G_c \\ 0.135\left(\frac{G}{2700}\right)^{-0.3} & for\ G > 2700\ \frac{kg}{m^2 s} \\ 0.135 & for\ G_c \leq G \leq 2700\ \frac{kg}{m^2 s} \end{cases} \tag{2.25}$$

The critical mass flux, G_c, is calculated using a series of ratios of fluid properties at standard temperature and pressure, as shown in Equation (2.26). It should be noted here that there were two formulations of the first expression in Equation (2.25) in that the coefficient 1.51 was presented as 1.15 in the body of Usman's thesis [88]. However, because it was presented as 1.51 in both the computer code in the appendix of his thesis, as well as in the paper published by Weisman et al. [95], this value was chosen as being accurate.

$$\frac{G_c}{\rho_l} = 2.75\frac{m}{s}\left(\frac{\rho_{SL}}{\rho_l}\right)^{0.33}\left(\frac{D}{D_s}\right)^{0.16}\left(\frac{\mu_{SL}}{\mu_l}\right)^{0.09}\left(\frac{\sigma_l}{\sigma_{SL}}\right)^{0.24} \tag{2.26}$$

All of the properties that have the subscript "SL" are calculated for 20 $°C$ and one bar. D_s corresponds to a diameter of 2.54 cm.

2.2.6 Non-uniform Heat Flux

It was found that the original Pei-Weisman model was capable of predicting CHF for tubes experiencing non-uniform axial heat flux profiles; however, the predictions were slightly too large as discussed by Yang [100]. The original formulation of the Pei-Weisman model was re-evaluated, this time taking into account the change in bubbly layer quality as shown in Equation (2.7). The expression is rewritten below in terms of mass flux and bubbly layer enthalpy instead of quality.

$$q''_{cr} = G\psi i_b\left(h_2 - h_1\right)\frac{\xi_i}{\xi} + \left(\frac{G_2 A_2}{\xi}\right)\left(\frac{dh_2}{dz}\right) \tag{2.27}$$

where,

ξ_i= perimeter of the inner surface of the bubbly layer

ξ= perimeter of the tube

Originally these perimeter terms were left out of the formulation of the Pei-Weisman model [94]; however, in practice these terms improve the accuracy of the model's prediction because they account for the reduced perimeter available for mass transfer due to the thickness of the bubbly layer. The complete derivation is quite involved, and in the interest of keeping this section concise, the important terms have been summarized in Equations (2.28)-(2.30). The full derivation of these terms can be found in Yang's thesis [100].

$$C_1 = \left[1 - \frac{\rho_2 V_2 A_2}{\bar{\rho}\overline{V}A}\right]\frac{\xi}{G\xi_i} \tag{2.28}$$

$$\Phi = C_1 \frac{\left[\frac{dq''_{total}(z)}{dz}\right]}{\psi i_b} \tag{2.29}$$

$$q''_{cr} = G\psi i_b \left(h_2 - h_1\right)\frac{\xi_i}{\xi} + \left(\frac{G_2 A_2}{\xi}\right)\Phi \tag{2.30}$$

The boiling heat flux must also be adjusted for the non-uniform heat flux case. The original expression is shown in Equation (2.31), and the simplified expression is shown in Equation (2.32).

$$q''_b = G\psi i_b h_{fg}\left(x_2 - x_1\right)\frac{\xi_i}{\xi} + \frac{G_2 A_2 h_{fg}\left[dx_2/dz\right]}{\xi} \tag{2.31}$$

$$q''_b = q''_t \left[\frac{G\psi i_b \left(x_2 - x_1\right)\frac{\xi_i}{\xi} + \Omega}{G\psi i_b \left(h_2 - h_1\right)\frac{\xi_i}{\xi} + \Omega}\right] \tag{2.32}$$

where,

$$\Omega = \left(\frac{G_2 A_2}{\xi}\right)\Phi = \left[1 - \frac{\rho_2 V_2 A_2}{\bar{\rho}\overline{V}A}\right]\frac{G_2 A_2}{G\psi i_b \xi_i}\frac{dq''_t}{dz} \tag{2.33}$$

These alterations have no effect on the predicted values of the uniform heat flux data points since all of the non-uniform terms go to zero at that point. The convergence criteria for the non-uniform heat flux case is that the bubbly layer has a maximum void fraction of 82% and the derivative of the bubbly layer enthalpy must also be zero, i.e. $\frac{dh_2}{dz} = 0$. This effect is shown in Figure 2-3 for a cosine shaped heat flux profile.

The reason that the bubbly layer reaches a maximum and begins to fall off is due to the rate that the bubbles are being produced from boiling. As the heat flux decreases after the peak at the mid-point of the channel, so too does the rate of bubble production. The threshold velocity that the turbulent fluctuations must overcome to penetrate the bubbly layer is therefore decreased and the liquid is able to enter at an increasing rate, thereby reducing the void fraction in the bubbly layer.

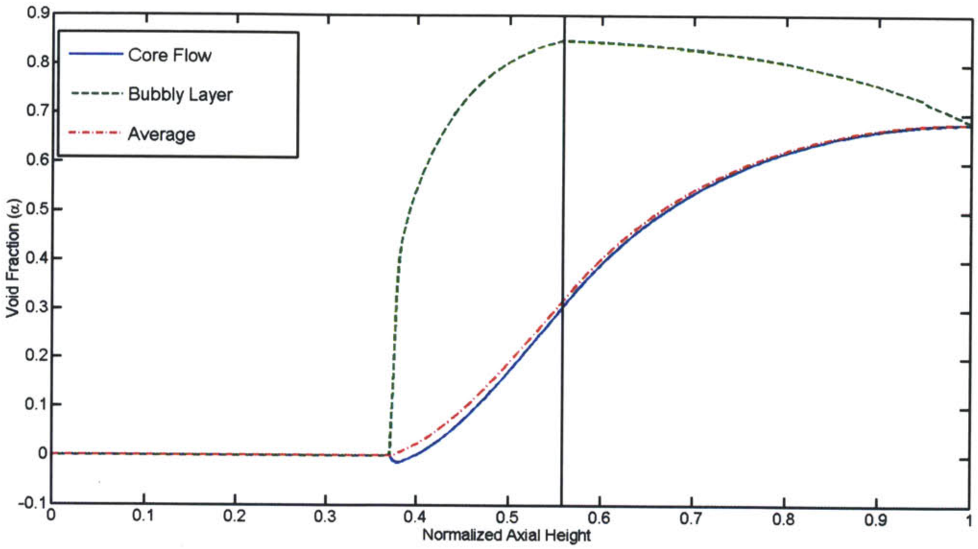

Figure 2-3: Bubbly Layer Void Profile at DNB

2.3 Modification of Model for FLTTs

The original Pei-Weisman DNB model was modified by Usman to account for the added turbulent interchange with the bubbly layer and vapor phase migration caused by twisted-tapes [88]. The major alterations that were implemented in the new model are presented in the following order:

- Revised Turbulent Intensity Factor: Section 2.4.2
- Effective Core Quality: Section 2.3.2

2.3.1 Turbulent Intensity Factor

Usman [88] postulated several modifications to the original turbulent intensity factor that were required to account for the presence of the twisted-tape and the swirling flow. The modifications to the turbulent intensity are best described in the following order:

- Modified Shear Stress Equation
- Revised Bubble Diameter
- Two-Phase Correction Factor
- Summary and Integration of Modifications

Modified Shear Stress for FLTTs In order to account for the increased friction caused by the swirling flow, Usman used a modified version of the Manglik and Bergles friction factor as shown in Equation (2.34).

$$\frac{f_{sw}}{f_{empty}} = \frac{f_{sw}}{f_{y=\infty}} \bullet \frac{f_{y=\infty}}{f_{empty}} = \left(1+\frac{2.752}{y^{1.29}}\right)\left(1+\frac{2}{\pi}\right)^{0.25} \tag{2.34}$$

where,

f_{sw} = friction factor for a given twist ratio

$f_{y=\infty}$ =friction factor for a tube with a twist-free tape inserted, i.e. $y=\infty$

f_{empty} = empty tube friction factor calculated using the tube inside diameter and empty tube mass flux

Usman chose to neglect the effect of the thickness of the twisted tape in the formulation of equivalent diameter reduction, i.e. $\left(1+\frac{2}{\pi}\right)^{0.25}$. The shear stress can now be related to the swirl friction factor as shown in Equation (2.35), where the friction factor shown is the Darcy friction factor.

$$\tau_{w,sw} = \frac{f_{sw}G^2}{8\rho_m} \tag{2.35}$$

Revised Bubble Diameter The bubble diameter is calculated using the same force balance as was used for empty-pipe flow; however, the body force and wall shear stress term needed to be modified to account for the presence of swirl as shown in Equation (2.36).

$$d_b = \frac{C_1\sigma^{1/2}}{\left[\left\{C_2\frac{g_{acc}}{g_c}\left(\rho_L-\rho_g\right)\right\}^2 + \left(\tau_{w,swirl}/D_e\right)^2\right]^{1/4}} \tag{2.36}$$

where,

$C_1 = 0.015$

$C_2 = 0.1$

$D_e = D\left(\frac{\pi}{\pi+2}\right)$

The shear stress term is calculated using Equations (2.34) and (2.35). The body force term needs to be modified to account for the swirling flow. This effect is captured in the term g_{acc}, and is simply the combination of the force of gravity and the centrifugal acceleration field produced by the swirl. Gambill [27] suggested a simplified expression for the acceleration field experienced by the bubble. Gambill's expression is shown in Equation (2.37), where $g_c = 9.81\ m/s^2$, the diameter is in meters, and the velocity is in m/s.

$$\frac{g_{acc}}{g_c} = \frac{0.503}{D}\left(\frac{V_{ax}}{y}\right)^2 \tag{2.37}$$

Two-phase Correction Factor In the Pei-Weisman model [74], a term was added to the turbulent intensity to account for the effect that bubbles would have on the velocity fluctuations near the bubbly layer. This factor was empirical fit to the data. Therefore since the flow conditions are different with a twisted-tape insert, it was determined that the original formulation for the two-phase correction factor had to be altered for implementation with FLTTs [95]. This was done by fitting two new constants to FLTT experimental data. The new expression for this term is shown in Equation (2.38).

$$TPC = 1 + ca\left(\frac{\rho_l - \rho_g}{\rho_g}\right)^n \tag{2.38}$$

where,
c = 1.5
n = 0.9

Summary and Integration of Modifications Taking into account the changes in shear stress, bubble diameter, and equivalent diameter, a new expression was derived for the turbulent intensity factor for FLTTs. If the two-phase correction factor is left off both turbulent intensity terms, the new formulation can be expressed as a ratio of the single-phase turbulent intensity of the swirling flow to the original empty tube turbulent intensity factor as shown in Equation (2.39).

$$\frac{i_{b,sw,1\phi}}{i_{b,1\phi}} = \left(\frac{\tau_{w,swirl}}{\tau_{w,empty}}\right)^{\frac{1}{2}}\left(\frac{d_{b,swirl}}{d_{b,empty}}\right)^{0.6}\left(\frac{D_{e,empty}}{D_{e,swirl}}\right)^{0.6} = \left(1+\frac{2.752}{y^{1.29}}\right)^{\frac{1}{2}}\left(1+\frac{2}{\pi}\right)^{0.725}\left(\frac{d_{b,swirl}}{d_{b,empty}}\right)^{0.6} \tag{2.39}$$

By multiplying the expression for $i_{b,1\phi}$, given by Equation (2.12), the expression for the turbulent intensity factor for FLTTs is shown in Equation (2.40) with the two-phase correction factor added in square brackets.

$$i_{b,sw} = 0.79Re^{-0.1}\left(\frac{d_{b,sw}}{D}\right)^{0.6}\left(1+\frac{2.752}{y^{1.29}}\right)^{\frac{1}{2}}\left(1+\frac{2}{\pi}\right)^{0.725}\left[1+1.5a\left(\frac{\rho_l-\rho_g}{\rho_g}\right)^{0.9}\right] \tag{2.40}$$

where,
D = tube diameter
y = twist ratio
a = velocity correction factor, i.e. Equation (2.25)
Re = empty tube Reynolds number

2.3.2 Effective Core Quality

Due to the density difference between the vapor and liquid phases, it was originally postulated that the bubbles produced during boiling would immediately be transported to the center of the pipe due to the centrifugal force of the swirling flow, causing the quality near the bubbly layer to effectively equal zero. Since this assumption caused an over-prediction of the data, a revised theory about bubble migration was developed by Usman [88]. Weisman and Du postulated that after a bubble departed the tube wall, its diameter grew exponentially according to Equation (2.41) [92]. Usman postulated that once a bubble reached a size that was larger than the turbulent eddies, it would be rapidly transported to the center of the flow.

$$d_b(z) = d_L e^{-\frac{kz}{D}} + d_H\left(1 - e^{-\frac{kz}{D}}\right) \tag{2.41}$$

where,

d_L = the Levy bubble diameter

d_H = the Hinze bubble diameter

Since the Levy bubble diameter is much smaller than the diameter of the Hinze bubble, it can be neglected in Equation (2.41), and the bubble diameter at location z can be expressed as shown in Equation (2.42).

$$d_b(z) = d_H\left(1 - e^{-\frac{kz}{D}}\right) \tag{2.42}$$

The Hinze bubble size is determined by Equation (2.43), and was originally presented in Hinze's work [39].

$$d_H = 0.725\left(\frac{\sigma}{\rho_L}\right)^{3/5}\left(\frac{P}{M}\right)^{-2/5} g_c^{1/5} \tag{2.43}$$

The term $\frac{P}{M}$ is a specific pumping power expression that is the ratio of pumping power per unit mass of fluid being pumped. The simplified expression for this term is shown in Equation (2.44).

$$\frac{P}{M} = \frac{f' G^3}{2 g_c \rho_m^3 D}\left(1 + \frac{2}{\pi}\right) \tag{2.44}$$

where,

$f' = f_{empty}\left(1 + \frac{2.752}{y^{1.29}}\right)\left(1 + \frac{2}{\pi}\right)^{0.25}$

G = empty tube mass flux $\left[\frac{kg}{m^2-s}\right]$

$g_c = 9.81$ $\left[\frac{m}{s^2}\right]$

ρ_m =average density $\left[\frac{kg}{m^3}\right]$

D = empty tube diameter [m]

Now that the equilibrium bubble size has been determined, the distance required for the bubble to grow to a size where it will be transported to the core flow needs to be calculated. Usman postulated that the terminal velocity of the bubble needed to be some multiple of the turbulent velocity fluctuations of the core flow. Therefore an expression for the terminal bubble velocity due to the centrifugal force field was developed as shown in Equation (2.45). This expression was derived by using Stoke's Law and replacing the gravitational acceleration term with the centrifugal acceleration, $\omega^2 r$.

$$U_T = \frac{\omega^2 r \Delta\rho\left(d_b(z)\right)^2}{18\mu_l} \tag{2.45}$$

where,

$\omega = \frac{\pi V_{ax}}{yD}$

$\Delta\rho = \rho_f - \rho_g$

$d_b(z)$ =bubble diameter at location z found using Equation (2.41)

μ_l = liquid phase viscosity

By using the fact that the terminal velocity of a bubble is proportional to the square of its diameter, and postulating that the terminal velocity has to be some multiple of the radial fluctuating velocity, $v"$, the relationship required for bubble migration can be expressed as shown in Equation (2.46).

$$U_T = bv" = C_T d_b^2 \tag{2.46}$$

By assuming that the terminal velocity of the Hinze bubble is the maximum velocity achievable by the growing bubbly, this expression was substituted into Equation (2.42). The equation was then solved for "z", and the distance the bubble needs to travel before it grows to the size required to enter the core of the flow can be calculated using Equation (2.47).

$$L_{mig} = -\frac{D}{k} ln \left[1 - \left(\frac{bv"}{U_{T_H}} \right)^{1/2} \right] \tag{2.47}$$

where,

k=0.035

b=2.50

U_{T_H} = the terminal velocity for a bubble with a Hinze bubble diameter

$v"$ $= 0.106 Re^{-0.1} \left(\frac{G}{\bar{\rho}} \right)$

Using this expression, all of the bubbles produced at a position L meters upstream the current location will migrate to the center of the flow, and the effective quality near the bubbly layer can be expressed according to Equation (2.48).

$$x_{eff,1} = x_1(z) - x_1(z - L_{mig}) \tag{2.48}$$

2.4 Issues with the FLTT Model

The Usman-Weisman FLTT model was evaluated for implementation with MSLTTs; however, several issues were found with the model. This section will address those issues and present some possible solutions in the following order:

- Equivalent Diameter Factor: Section 2.4.1
- Turbulent Intensity Factor: Section 2.4.2
- Two-Phase Correction Factor: Section 2.4.3

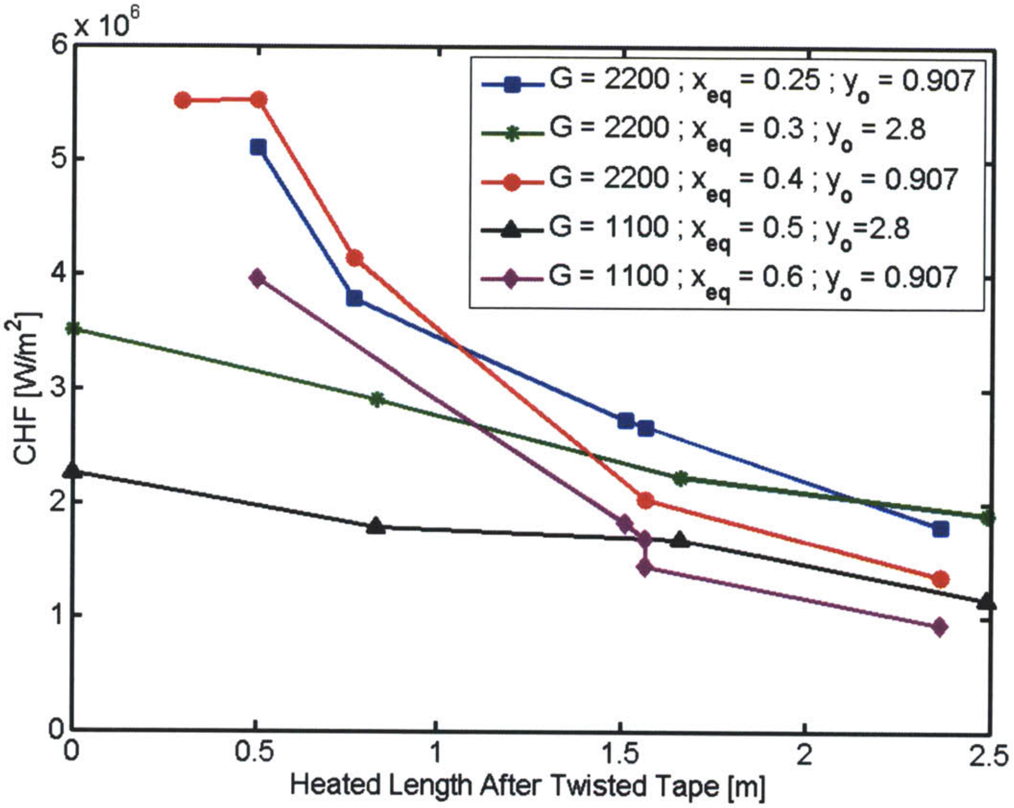

Figure 2-4: Swirl Decay CHF Data Trends
Trends in this figure will be addressed more thoroughly in Chapter 3

2.4.1 Equivalent Diameter Effect

This equivalent diameter term, i.e. the $\left(1+\frac{\pi}{2}\right)$ term in Equation (2.34), is present in two locations in the model that need to be addressed separately. First, it shows up in the the turbulent intensity factor as a shear stress correction, in the bubble diameter calculation, and purely as an equivalent diameter ratio. Second, it shows up in the effective core quality calculation in terms of specific pumping power.

The use of this term in the turbulent intensity calculation is incorrect because it yields non-physical results upon the exit of a SLTT. During the modification of this model for MSLTTs, it was assumed that this equivalent diameter term should be included in the calculation when a twisted-tape was present, and should be removed in regions of swirl decay. When this strategy was implemented it resulted in drastic decreases in the predicted CHF value immediately following the exit of a SLTT, i.e. the predicted CHF value did not smoothly decay upon exiting the SLTT. Upon examination of the data, it was determined that this is not physical as shown in Figure 2-4 where the CHF value is plotted as a function of distance from the exit of a SLTT. Clearly there is a smooth decrease in CHF, not a drastic decrease as originally predicted by the model.

If DNB could occur on the twisted-tape itself, then the formulation of the revised shear stress would be correct; however, since bubbles are only being produced on the tube wall, then only the shear stress at that location should be accounted for in the calculation. By using the equivalent diameter ratio term, the shear stress contribution from the twisted-tape is causing an over-estimation of the shear stress at the tube wall when comparing a location with a SLTT to an area of swirl decay.

The situation is different when calculating the effective core quality. Since the equilibrium bubble diameter depends on the specific pumping power, which is a function of the total pressure drop, the equivalent diameter ratio term is needed in this calculation. Furthermore, when modifying the model to account for MSLTTs, it is necessary to remove the equivalent diameter term when the flow is not going through a SLTT.

In summary, the equivalent diameter term should be removed when calculating any term for the turbulent intensity factor, i.e. shear stress, bubble diameter, and the equivalent diameter ratio explicitly as shown in Equation (2.39). The equivalent diameter term should not be removed when calculating the equilibrium bubble distance inside a SLTT; however, it should be removed when the flow has exited a SLTT. By removing this ratio, the determination of the appropriate numerical values for the empirical constants added during the original model development must be performed again in order to account for the removal of non-negligible terms.

2.4.2 Turbulent Intensity Factor

A contradiction that yields a non-physical result was found when examining the original derivation of the turbulent intensity factor for FLTTs presented in Usman's thesis [88]. Starting with the original formulation for turbulent intensity, and disregarding the equivalent diameter ratio as discussed in the previous section, it can be deduced that the ratio of the turbulent intensity of a pipe with a twisted tape is related to the empty pipe's value through the following expression.

$$\frac{i_{b,sw}}{i_{b,empty}} = \frac{1.16F_1\left(\frac{y}{r}\right)^{0.6}\sqrt{\frac{\tau_{w,sw}g_c}{\bar{\rho}}}\left(\frac{\rho}{G}\right)}{1.16F_1\left(\frac{y}{r}\right)^{0.6}\sqrt{\frac{\tau_{w,empty}g_c}{\bar{\rho}}}\left(\frac{\rho}{G}\right)} = \sqrt{\frac{\tau_{w,sw}}{\tau_{w,empty}}} \tag{2.49}$$

The ratio of the original empty tube turbulent intensity factor ($i_{b,empty}$)to the empty pipe turbulent intensity calculated with the swirl bubble diameter $\left(i'_{b,empty}\right)$, can now be written using Equation (2.12) as shown below.

$$\frac{i_{b,empty}}{i'_{b,empty}} = \frac{0.462Re^{-0.1}k^{0.6}\left(\frac{d_{b,empty}}{D}\right)^{0.6}}{0.462Re^{-0.1}k^{0.6}\left(\frac{d_{b,sw}}{D}\right)^{0.6}} = \left(\frac{d_{b,empty}}{d_{b,sw}}\right)^{0.6} \tag{2.50}$$

By combining Equations (2.49) and (2.50), as shown in Equation (2.51), it is possible to arrive at the expression for $\left[i_{b,sw}/i'_{b,empty}\right]$ shown in Usman's thesis. If this expression is multiplied out to obtain the explicit value of $i_{b,sw}$, the swirl bubble diameter disappears completely from the expression and leaves the empty tube bubble diameter in its place as shown in Equation (2.52). This is a non-physical representation of the system since the bubbles in swirling flow do not have the empty tube diameter.

$$\frac{i_{b,sw}}{i'_{b,empty}} = \frac{i_{b,sw}}{i_{b,empty}} \bullet \frac{i_{b,empty}}{i'_{b,empty}} = \sqrt{\frac{\tau_{w,sw}}{\tau_{w,empty}}} \left(\frac{d_{b,empty}}{d_{b,sw}} \right)^{0.6} \tag{2.51}$$

$$\begin{aligned} i_{b,sw} &= \left(0.462 Re^{-0.1} k^{0.6} \left(\tfrac{d_{b,sw}}{D} \right)^{0.6} \right) \sqrt{\tfrac{\tau_{w,sw}}{\tau_{w,empty}}} \left(\tfrac{d_{b,empty}}{d_{b,sw}} \right)^{0.6} \\ &= \left(0.462 Re^{-0.1} k^{0.6} \left(\tfrac{d_{b,empty}}{D} \right)^{0.6} \right) \sqrt{\tfrac{\tau_{w,sw}}{\tau_{w,empty}}} \end{aligned} \tag{2.52}$$

In order to fix this error, the derivation methodology used by Usman should not be followed, and the original turbulent intensity factor should be adjusted simply by inserting the correct terms for the shear velocity and bubble diameter. The shear velocity must now be expressed as shown in Equation (2.53), which alters the turbulent intensity factor as shown in Equation (2.54). This derivation is much simpler, and maintains a physical result.

$$\begin{aligned} U_\tau &= \sqrt{f} \tfrac{G}{\rho_m} = \sqrt{0.023 Re^{-0.2} \left(1 + \tfrac{2.752}{y^{1.29}} \right) \left(\tfrac{G}{\rho_m} \right)} \\ &= 0.176 Re^{-0.1} \left(1 + \tfrac{2.752}{y^{1.29}} \right)^{1/2} \left(\tfrac{G}{\rho_m} \right) \end{aligned} \tag{2.53}$$

$$i_{b,sw} = 0.790 Re^{-0.1} \left(\frac{d_{b,sw}}{D} \right) \left(1 + ca \left[\frac{\rho_l - \rho_g}{\rho_g} \right]^n \right) \tag{2.54}$$

Again, the coefficients c and n will need to be correlated to the data since they were originally derived with the model including the equivalent diameter ratio.

2.4.3 Two-Phase Correction Factor

There is still an issue with the formulation of the turbulent intensity factor presented in Equation (2.54), specifically the formulation of the two-phase correction factor causes an issue for MSLTTs. In the original Pei-Weisman model [74], the correction factor had the form shown below:

$$Pei - Weisman\ two - phase\ correction\ factor = \left[1 + a \left(\frac{\rho_l - \rho_g}{\rho_g} \right) \right]$$

When the FLTT model was developed by Usman [88], a new two-phase correction factor was developed and correlated to the data as shown below:

$$Usman - Weisman\ two - phase\ correction\ factor = \left[1 + ca \left(\frac{\rho_l - \rho_g}{\rho_g} \right)^n \right]$$

In the case of extreme swirl decay lengths, it is expected that the predicted value of CHF should converge to the axial flow value; however, since the Usman-Weisman formulation does not depend on swirl, there will inevitably be an error in the prediction for the case of extreme swirl decay. This error does depend on

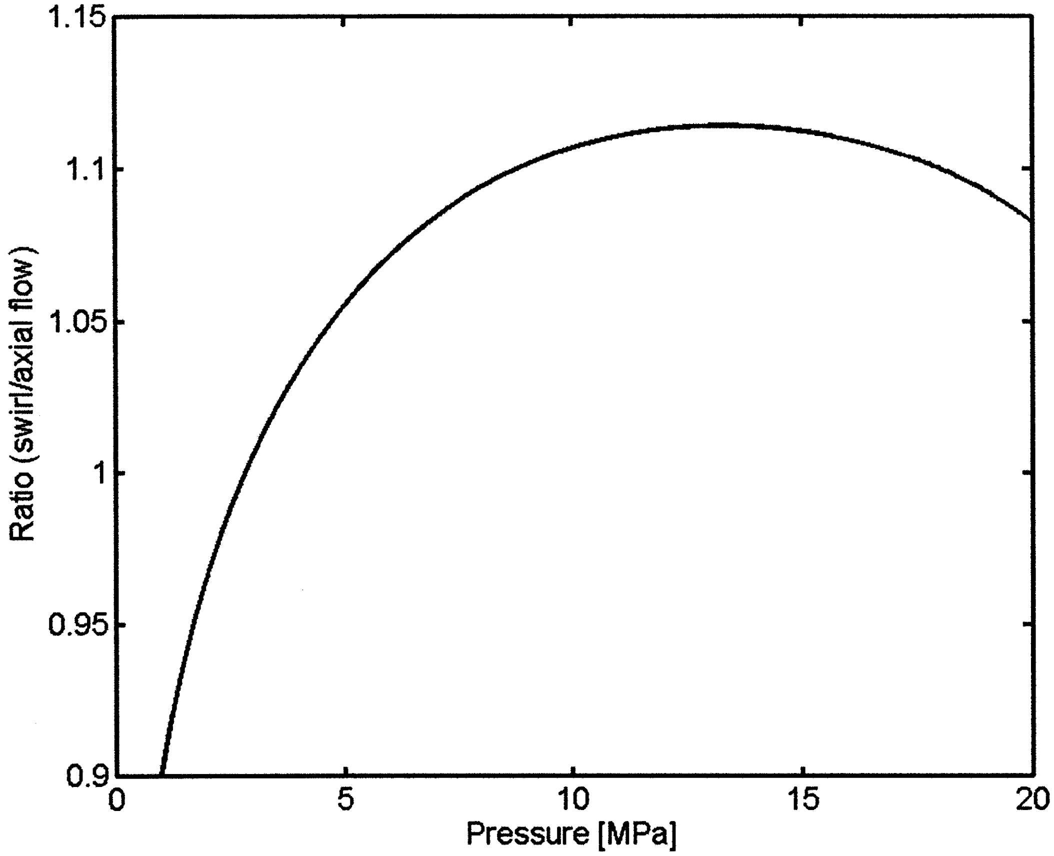

Figure 2-5: Ratio of Two-Phase Correction Factors

pressure as shown in Figure 2-5.

There are two ways that this problem could be overcome. First, a new two-phase correction factor could be derived based on a weighted average of the two terms shown above. In this method a upper bound of twist ratio needs to be defined where the FLTT two-phase correction factor is applicable. Next, the maximum twist ratio that swirl still has an effect on CHF enhancement needs to be defined, i.e. a critical twist ratio (y_{cr}). These two bounds could be used to interpolate the two values either linearly or exponentially. This technique may be difficult to justify physically since the true effect is continuous; therefore a second technique is proposed.

Another way that this problem could be fixed is by using the swirl mass flux value, shown in Equation (2.55) and taken from Kinoshita et al. [51], for the velocity correction term "a". After doing this, then derive the terms c and n such that they are of the form shown in Equation (2.56).

$$G_{sw} = G\frac{\sqrt{4y^2+\pi^2}}{2y} \tag{2.55}$$

$$c = C_1 \left(\frac{y_{cr}}{y_{eff}^{C_2}} \right) \tag{2.56}$$

where,

C_1 *and* C_2 are empirical constants

y_{eff} = effective twist ratio, i.e. either the twist ratio of the SLTT if inside the twisted-tape, or a twist ratio that would produce an equivalent local swirl intensity

The derivation of the critical twist ratio will be shown in Section 2.5.1. This technique for making the two-phase correction factor swirl-dependent is more intensive; however, it will provide a more continuous result from the model.

2.5 Insights from the Usman-Weisman DNB Model

Although the Usman-Weisman FLTT DNB model [95] could not successfully be implemented for the case of MSLTTs, there were some valuable insights gained by working with the model. This section will outline the most important phenomena that will be utilized in the development of the new DNB empirical correlation in the following order:

- The Lower Bound of Swirl Required for Bubble Migration (y_{cr}): Section 2.5.1
- The Importance of Shear Stress on DNB: Section 2.5.2
- Operational Bounds of the DNB Phenomenon: Section 2.5.3

2.5.1 Bubble Migration in Low Swirl Flows

One of the most significant enhancement mechanisms discussed in the Usman-Weisman FLTT model [88, 95] was the effect of bubble migration due to the centrifuging effect. This phenomenon enhances CHF by removing the bubbles near the interface of the bulk flow and the bubbly layer. This increases the liquid density near the bubbly layer, thereby increasing the mass flow rate of liquid into the bubbly layer. In a decaying swirl flow, as is the case with MSLTTs, it is important to know at what swirl intensity this mechanism ceases to exist.

An expression for the lower bound in swirl intensity, known as y_{cr}, can be derived from the bubble migration model developed by Usman [88]. According to this model, bubbles will no longer migrate to the center of the flow when they can no longer overcome the forces imparted on them by the turbulent fluctuations of the fluid in the region near the bubbly layer interface. This occurs when terminal velocity of the Hinze equilibrium bubble is equal to the turbulent velocity fluctuations multiplied by some constant, as shown in Equation (2.57).

$$U_{TH,cr} = bv" \tag{2.57}$$

where,

b=2.5

$v" = 0.106Re^{-0.1}\left(\frac{G}{\rho_m}\right)$

By setting this critical terminal velocity equal to Equation (2.45), the critical angular velocity can be solved for by iterating until the difference of these expressions is approximately zero, as shown in Equation (2.58).

$$0 \approx U_{TH,cr} - \frac{\omega_{cr}^2\,(D/2)\,\Delta\rho d_H^2}{18\mu_l} \tag{2.58}$$

An iterative technique is required since the Hinze bubble diameter, d_H, depends on the friction factor, as shown in Equation (2.43), which in turn depends on the swirl intensity. While the formulation for the specific pumping power shown in Equation (2.44) can be used for locations inside a twisted tape, it is important to note that the friction factor formula should be appropriately adjusted to account for the absence of the twisted-tape in the swirl decay region as shown in Equation (2.59).

$$\frac{P}{M} = \frac{f_{empty}\left(1+\frac{2.752}{y_{eff}^{1.29}}\right)G^3}{2g_c\bar{\rho}^3 D} \tag{2.59}$$

Once ω_{cr} is obtained from this Equation (2.58), the critical twist ratio can be found by using Equation (2.60). This critical twist ratio represents the largest value the effective twist ratio can have before the bubble migration phenomenon ceases to occur. When designing a system using MSLTTs, it is important that the effective twist ratio never exceed this value since any enhancement above the axial flow CHF value is expected to disappear for effective twist ratios greater than this value.

$$y_{cr} = \frac{(G/\rho_m)\,\pi}{\omega_{cr} D} \tag{2.60}$$

An example of the values of y_{cr} are shown in Figure 2-6. Two trends can be seen in this figure. First, y_{cr} decreases as pressure increases. This can be attributed to the decrease in the difference between phase densities, which causes a decrease in the radial buoyant force. Second, y_{cr} decreases as mass flux increases. This effect is caused by an increase in the turbulent radial velocity fluctuations, which necessitate a larger terminal velocity to be overcome and allow the bubble to migrate to the center of the pipe, i.e. $bv"$ increases, therefore U_{T_H} must also increase.

2.5.2 The Effect of Shear Stress on DNB

Another insight gained from this model is the importance of shear stress on CHF. In the Usman-Weisman FLTT model, the increase in shear stress is directly modeled by the turbulent intensity factor and indirectly

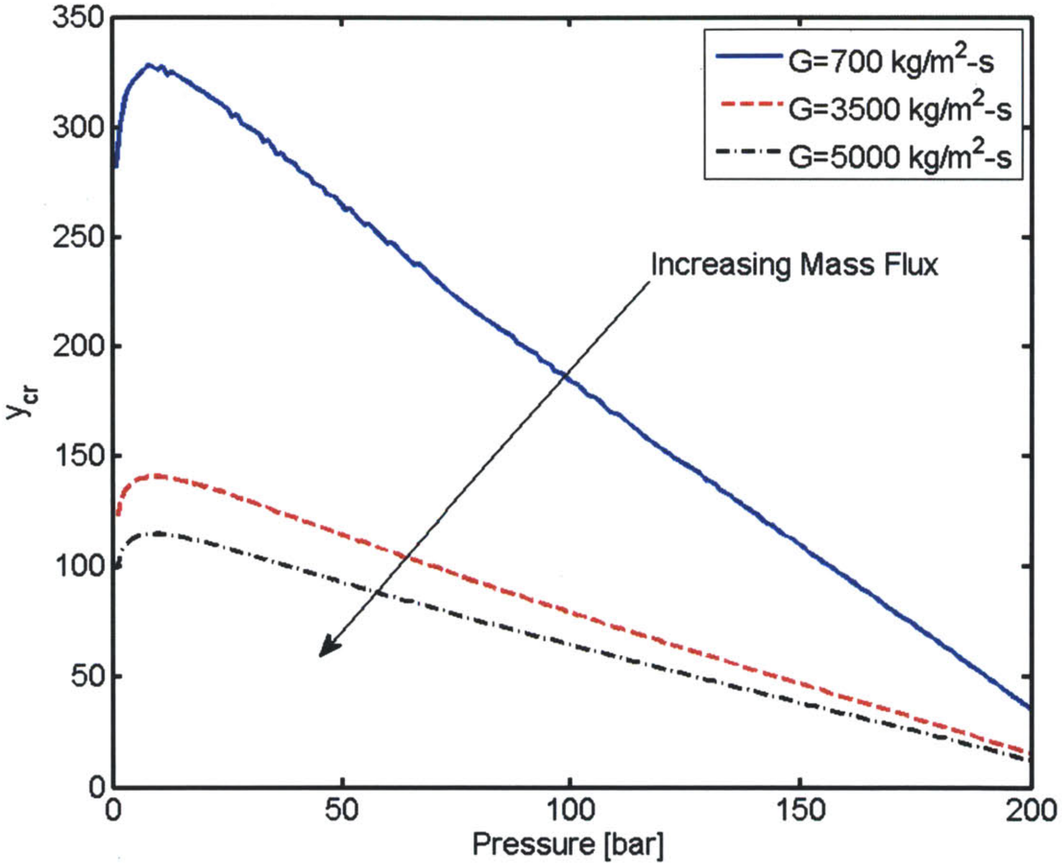

Figure 2-6: Example of the Critical Twist Ratio

by the bubble diameter. An increase in shear stress results in an increase in the intensity of the velocity fluctuations near the tube wall, thereby increasing mass transfer into the bubbly layer. Increasing the shear stress also reduces the bubble diameter size, which indicates that a larger number of smaller bubbles will be required for the critical bubbly layer void fraction to be reached, thereby delaying the onset of DNB.

With these observations in mind, it is important that the new empirical DNB correlation have a term that relates CHF enhancement to an increase in shear stress, proportional to flow velocity and inversely proportional to twist ratio.

2.5.3 Operational Bounds of the DNB Phenomenon

Possibly the most important insight gained from working with the Usman-Weisman FLTT model is the operation bounds at which DNB is expected to occur. Since there is a wide range of data available for the development of an empirical correlation, it is important to restrict the bounds enough that the accuracy is high while maintaining a simple formulation. At the same time, it is important not to restrict the bounds of the data too much otherwise the valid operating range is unnecessarily restricted. Therefore, the bounds of data that will be examined initially in the development of the new correlation will be restricted to the operational bounds of the Usman-Weisman FLTT model [95] as shown in Table 2.3.

Table 2.3: Operation Bounds of the Usman-Weisman FLTT DNB Model [95]

$0.0045 \leq \left(\frac{\rho_g}{\rho_f}\right) \leq 0.41$
$0.115 < D \leq 3.75$ cm
$3.5 \leq L_h \leq 365$ cm
$694 \leq G \leq 40,000\ \frac{kg}{m^2 s}$
$-0.3 \leq x_1$; $\langle\alpha\rangle \leq 0.64$

Chapter 3

Twisted-Tape CHF Enhancement Mechanisms and Parametric Trends

This chapter will cover the characteristics of all available twisted-tape CHF data both for FLTTs and SLTTs. The goal of this chapter is to illustrate some of the basic phenomena identified in the Usman-Weisman model that can also be used in the development of an empirical DNB correlation for MSLTTs. These ideas will be presented in the following order:

- Non-Uniform Circumferential Heating with FLTT Inserts: Section 3.1
- Uniform Circumferential Heating with FLTT Inserts: Section 3.2
- Uniform Circumferential Heating with SLTT Inserts: Section 3.3

3.1 Non-Uniform Circumferential Heating with FLTT Inserts

Although non-uniform circumferential (NUC) heating data was not considered in this study, this section briefly discusses some of the studies that have been performed using this technique and the basic phenomenological differences between one-sided and uniformly heated twisted-tape CHF enhancement. A summary is given of how Kinoshita et al. [51] implemented these phenomenon in the original Pei-Weisman model [74] to predict CHF under these conditions.

In order to remove heat from the primary divertor in fusion reactors such as ITER (International Thermonuclear Experimental Reactor), where the heat flux affects only one side of the cooling tubes, several authors have conducted experiments for low pressure, high mass flux, highly subcooled flows with FLTT inserts under NUC heating conditions [5, 11, 28, 43, 52, 55, 89]. In general these experiments yield very high CHF values, on the order of tens of megawatts.

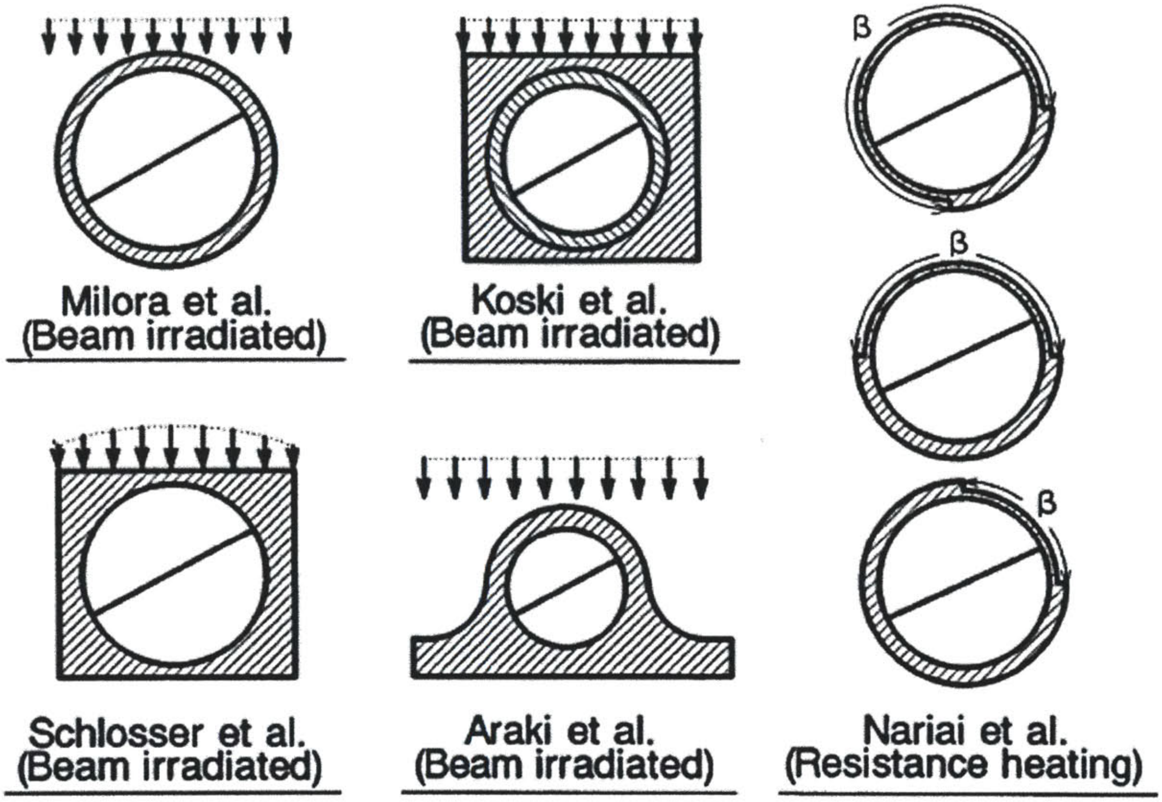

Figure 3-1: One-sided Heating Heat Flux Profiles: Taken from Inasaka et al. [43]

The experimental setups for one-sided CHF tests are shown in Figure 3-1. This figure was taken from Inasaka et al. [43], where they attempted to quantify the heat flux distribution on the inner surface of the tube wall by performing a transient two-dimensional heat diffusion analysis using a finite element technique. The two techniques used to heat the test sections in these studies are electron beam irradiation and resistance heating. In electron beam irradiation an electron gun is used to scan a test section rapidly to produce an average heat flux over the heated length [5, 55]. In the resistance heating technique, also known as the Joule effect, electricity is passed through the tube, producing heat due to electrical resistance. This technique is used extensively for uniform circumferentially heated test sections; however, studies by Nariai et al. **[72]** and Kinoshita et al. [52] used this technique for NUC heating. NUC heating was obtained using this technique by machining the tube outer surface to create thin regions of tube wall where the heat flux was higher.

Kinoshita et al. [52] found that when the heat flux on the tube perimeter of lower heat flux, i.e. the thicker walled portion covering an angle of $360^o - \beta$ in Figure 3-1, dipped below the heat flux of net vapor generation, q''_{NVG}, the CHF of the tube was increased noticeably compared to uniformly heated tubes with FLTTs at those same local conditions. Conversely, if the lower heat flux portion did not dip below q''_{NVG}, the CHF for that tube was nearly identical to the CHF of a uniformly heated tube. Enhancement in CHF for NUC heating condition was attributed to disruption in the bubbly layer for tubes where the lower heat flux area falls below q''_{NVG} [43, 52, 51].

As previously mentioned, Inasaka et al. [43] attempted to quantify the angular heat flux profile for these NUC heated tubes using a transient finite element model for heat conduction. The heat flux and wall temperature distribution for half the circumference at the exit of a test section during a typical electron beam heated CHF experiment is shown in Figure 3-2. Assuming symmetry, the heat flux profile of the other half of the circumference is identical. The x-axis in this figure represents the angular position as measured from the peak heat flux. The important thing to note here is that even though the peak heat flux is over 70 $\frac{MW}{m^2}$, the local heat flux at angular positions past $\sim \frac{\pi}{4}$ falls below q''_{NVG} indicating that bubbles are not departing the tube surface in this angular range. Therefore, since the path of the coolant is helical due to the twisted-tape, the flow is periodically passing through areas of boiling and non-boiling. This is not the case for axial flow NUC heated tubes where boiling is sustained once it develops.

The process of passing through regions of boiling and non-boiling occurs throughout the tube with increasing intensity. This is due to the rise in the bulk enthalpy as the flow passes through the tube. Therefore, it can be said that the angle of the tube where $q'' > q''_{NVG}$ is increasing since the fluid conditions required for bubble departure are reached at a greater angular distance from the peak heat flux upon each rotation. In the case of uniform axial heat flux, the point where CHF occurs is still at the tube exit since this location corresponds to the largest angle of boiling, i.e. the largest impediment to mass transfer with the bubbly layer.

In the original Usman-Weisman model [95], the point of bubble departure was found using the Levy model [60], and it was assumed that once boiling was initiated, it continued throughout the tube. This is true in the case of uniformly heated tubes both with and without twisted-tapes, NUC heated tubes in pure axial flow, and NUC heated tubes with twisted-tapes where the minimum of the circumferential heat flux never falls below q''_{NVG}. However, in the case of NUC heated tubes with twisted-tape inserts where the heat flux does fall below q''_{NVG}, the boiling length corresponds to the length of the helical path of the fluid as it travels through an area of heat flux above q''_{NVG}. For the case of resistance heating, where the circumferential heat flux profile is much more sharply defined, the effective boiling length is expressed in Equation (3.1). For cases where the circumferential heat flux profile is known, it is simply the helical distance where the heat flux is above q_{NVG}.

$$L_{eff} = \frac{D_i}{2}\sqrt{4y^2+\pi^2}\left(\frac{360-\beta}{180}\right) \tag{3.1}$$

where,

β =low heat flux angle of the test section corresponding to part that was machined to be physically thinner [deg]

This idea was taken a step further by Kinoshita et al. [51] when they developed a phenomenological model to describe NUC heated CHF for tubes with and without twisted-tape inserts. The model was a

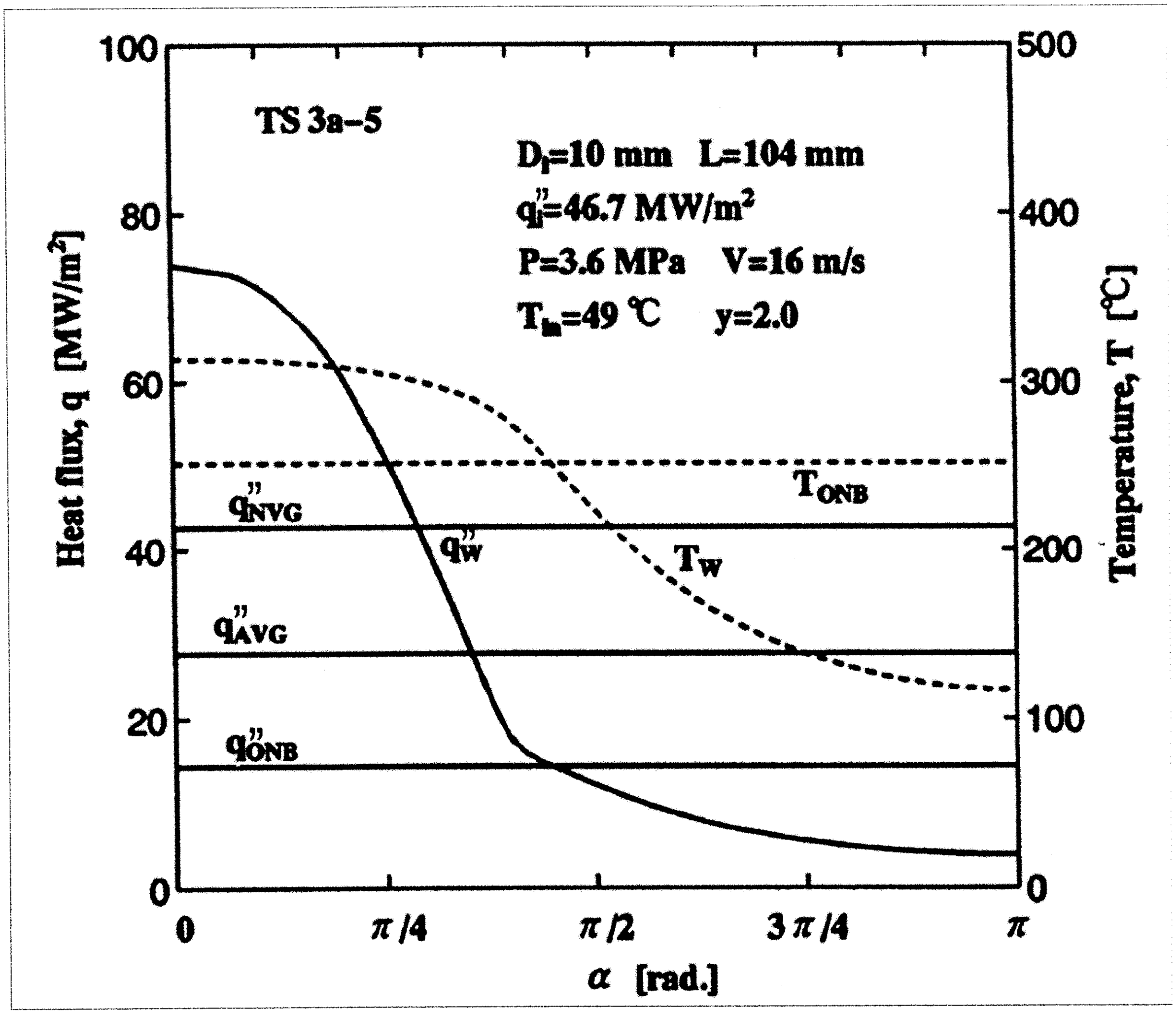

Figure 3-2: Heat Flux and Wall Temperature Distribution at the Test Section Exit for a NUC Heated Tube: Taken from Inasaka et al. [43]
q_i'' corresponds to the average incoming heat flux on the side facing the electron beam

modification of the original Pei-Weisman CHF model [74]. In their model, Kinoshita et al. modified the critical void fraction in order to account for the difference in bubble geometry at the lower pressures and high subcoolings characterizing their experiments as compared to the original operating range the Pei-Weisman model was developed to cover. More importantly, the boiling and condensation heat flux expressions were altered to take into account the effective boiling length given in Equation (3.1).

This effective boiling length is used to adjust the condensation heat flux, which was redefined in this model as shown in Equation (3.2).

$$q''_{cond} = H_l \left(T_{sat} - T_l \right) \frac{A_h}{\pi D L_{eff}} \tag{3.2}$$

where,

H_l =Dittus-Boelter single-phase heat transfer coefficient [20]

T_l =bulk liquid temperature

$A_h = \pi D L_{eff} \frac{\pi}{4}$

The term A_h is the heat transfer area of the bubbles. Since there was little information regarding the frequency and bubble number density for the operating conditions Kinoshita et al. were interested in, they assumed that the heat transfer area corresponded to the projected area of spherical bubbles when they are in contact with each other as shown in Figure 3-3 [51]. This figure shows a small section of the pipe wall covered in spherical bubbles that are just in contact with each other. The variable L_h in this case is the length of one unit cell such that $L_{eff} = N_{cells} L_h$. In this case, since the bubbles are considered spherical, $L_h = D_b$. On a unit cell basis, i.e. the expanded view, the ratio of the pipe wall covered by bubbles to the total pipe wall area is found to be $\frac{\pi}{4}$.

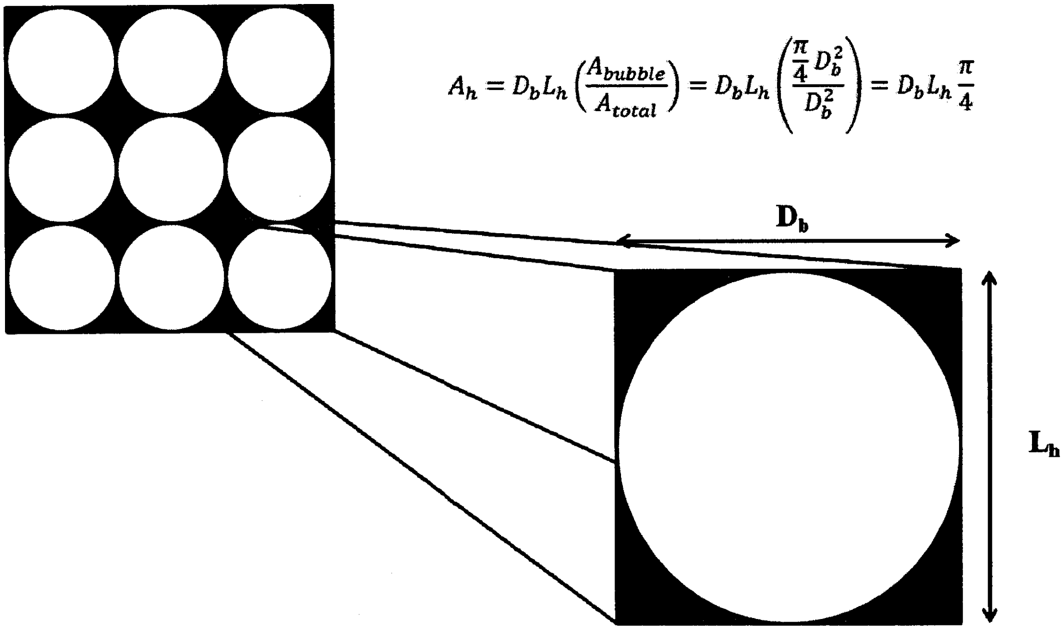

Figure 3-3: Projected Condensation Heat Transfer Area for Bubbles at Low Pressure and High Subcooling

The boiling heat flux was also altered and is shown in Equation (3.3), where q''_{NVG} is calculated using the Levy model [60].

$$q''_b = q''_{total} - q''_{NVG} \tag{3.3}$$

The only other modification made to the original Pei-Weisman model was to use a swirl mass flux term as shown in Equation (3.4). This term was used instead of incorporating any changes to the shear stress calculation through use of the Manglik-Bergles friction factor [63] as was done by Usman [88]. Furthermore, the Kinoshita et al. model did not account for bubble migration or the centrifugal acceleration effect on bubble departure. It can be hypothesized that they did not need to account for bubble migration because the flow quality is nearly zero due to the high degree of subcooling of the bulk flow and the very small boiling length.

$$G_{sw} = G_{empty} \frac{\sqrt{4y^2 + \pi^2}}{2y} \tag{3.4}$$

3.2 Uniform Circumferential Heating with FLTT Inserts

The complete body of data for uniform circumferentially heated FLTTs with water as the working fluid is presented in Table 3.1. Since NUC heated experiments will not be addressed from this point forward, circumferentially uniformly heated experiments will simply be addressed as FLTT experiments. A table of the FLTT and SLTT data is presented in Appendix A. While both the axial and swirl flow versions of the Weisman model have been shown to be applicable to other fluids, the empirical correlation that will be developed in Chapter 4 will only be valid for water. If the reader would like more information on CHF tests using other fluids, Staub [79] and Usman [88] contain data for refrigerant cooled pipes. Also Weisman et al. [95] present some helium data, although the source is not specifically cited; therefore it is difficult to tell where this data originated.

3.2.1 Visualization of the Data

Of the data sources presented in Table 3.1, only a few were actually used in the development of the empirical DNB correlation that is presented in the next chapter. The data that could be used for the Usman-Weisman model validation are shown in Figure 3-4. The theoretical operating range of the IPWR is outlined with the rectangular box. Note that the design pressure is also 15.51 MPa. Also note that the only applicable SLTT data are circled on the plot. SLTT data will be discussed at length in Section 3.3; however, it is briefly presented here to give a concise picture of the data available.

The only data close to the operating conditions of the IPWR, i.e. high pressure, mass flux less than $\sim 10,000\ \frac{kg}{m^2-s}$, and subcooled, are those of Viskanta [91]. However, even this data is at too low a mass flux for the design study. There are a few subcooled data points in the right range of mass flux; however, these data correspond to low operating pressure, i.e. 0.77-3.4 MPa. Furthermore, the most critical point, known as the minimum departure from nucleate boiling ratio (MDNBR), in the IPWR operation typically falls at or above an equilibrium quality of about (-0.15). In the case of a perfect chopped-cosine flux shape, this quality corresponds to the location of peak heat flux. At the end of the cycle, the power shape tends to flatten, therefore the critical point approaches the top of the core. This effect is illustrated in Figure 3-5

Table 3.1: FLTT CHF Data

Author	Ref.	Mass Flux [$\frac{kg}{m^2-s}$]	Pressure [MPa]	Exit Quality	Heated Length [cm]	Diameter [mm]	Twist Ratio	# Data Points
Subcooled Boiling								
Viskanta	[91]	678-2712	13.8	(-0.091) - 0.532	45.72	7.93	2.5 - 5	51
Gambill et al.	[27]	4476 - 47555	0.101 - 3.758	(-0.383) - 0.113	3.454 - 44.12	3.45 - 10.21	2.08 - 12.03	40
Drizius et al.	[21]	4500 - 24800	0.393 - 1.335	(-0.157) - (-0.046)	3.7 - 14.1	1.6	1.25 - 10.25	25
Tong et al.	[87]	5049 - 18290	0.392 - 1.398	(-0.306) - (-0.129)	0.664 - 15.7	2.44 - 6.54	1.9 - ∞	32
Hata et al.	[34]	3845 - 13498	~0.8	(-0.283) - (-0.113)	5.95	6	2.39 - 4.45	134
Nariai et al.	[71]	5300 - 7400	0.101 - 1.47	(-0.256) - (-0.054)	10	6	2.61 - ∞	35
Feinstein et al.	[22]	15476 - 68094	0.344	(-0.183) - (-0.129)	10.2	6.35	2 - 6	27
Saturated Boiling								
Moussez et al.	[67]	4450, 5850	7.0	0.116, 0.165	80	10	3	2
Moeck et al.	[66]	391 - 1145	6.91 - 7.0	0.742 - 0.953	101.6	11.43	5.55 - 34.5	29
Matzner et al.	[64]	1261 - 4598	6.895	0.33 - 0.88	487.7	10.16	15	27
Brevi et al.	[12]	758 - 1038	5.07	0.795 - 0.880	20	10	3	37
Kisina et al.	[53]	1400 - 2800	14.7	0.218 - 0.825	200	8 - 14.3	5 - 15.91	23

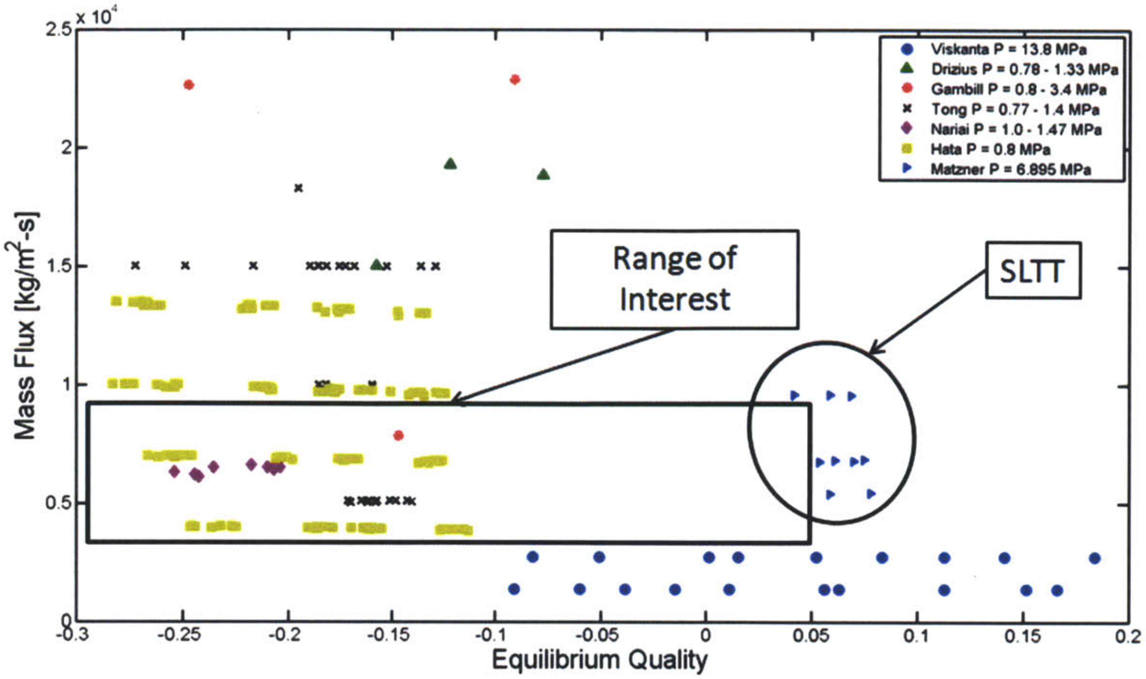

Figure 3-4: FLTT Data Applicable to the Usman-Weisman Model Validation

where a channel analysis was performed for typical PWR operating conditions using a chopped cosine to approximate the heat flux shape of the core. The flattening of the operating flux shape was simulated by decreasing the peak to average heat flux ratio from 1.515 at the beginning of life, to 1.3 at the mid-point, and 1.1 at the end of life. These peaking values are only meant for qualitative comparison and are not based on a depletion analysis.

To summarize, there is a large gap in the data in terms of pressure, mass flux, and equilibrium quality for the range of interest for the IPWR design. This gap was one of the main reasons that the phenomenological model of Weisman and Usman was pursued. It was hoped that once an understanding of the mechanism of DNB for tubes containing twisted-tapes was solidified through the model, it could then be applied to operations outside the range that the model was validated against.

3.2.2 Comparison Technique and Enhancement Phenomena

One convenient way to view twisted-tape CHF data is as a ratio of the experimental twisted-tape CHF value compared to an empty tube at those same local conditions, as shown in Equation (3.5). Here, the empty tube CHF value is calculated using the same pressure, equilibrium quality, tube geometry, and mass flow rate. This ratio is known as the twisted-tape critical heat flux ratio (TTCHFR). This ratio easily illustrates where the use of twisted-tape inserts is most beneficial.

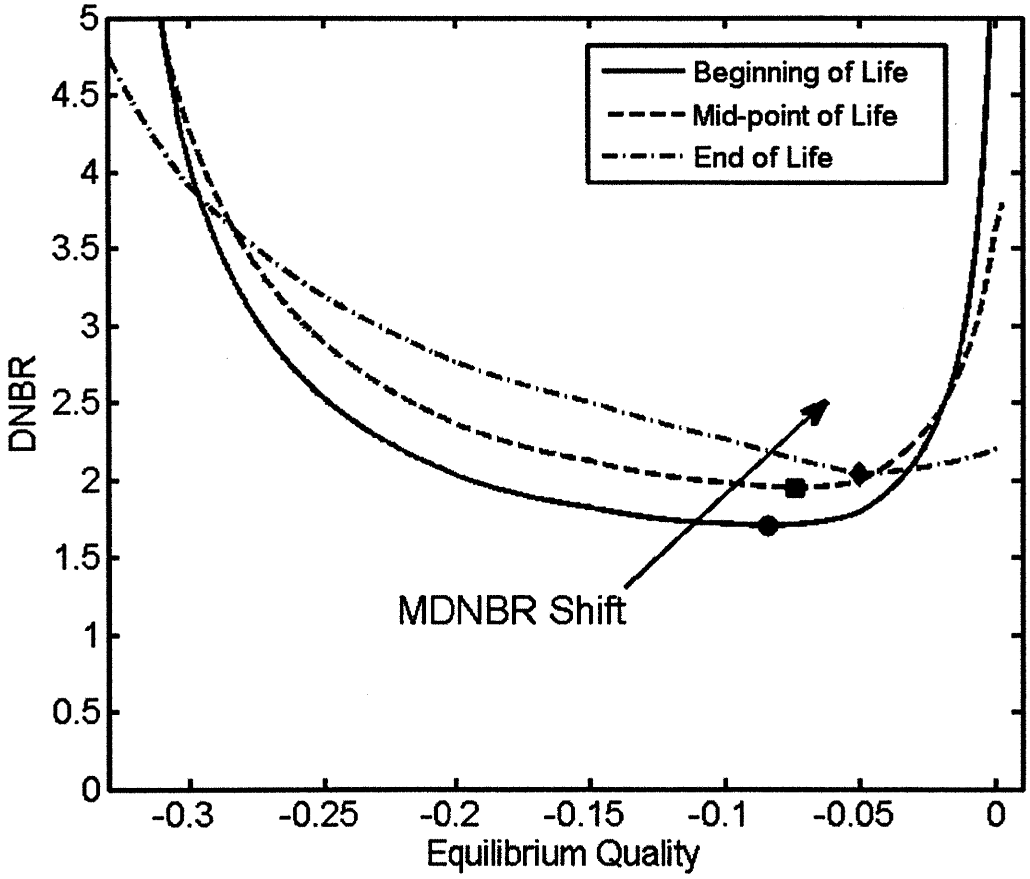

Figure 3-5: MDNBR Shift

$$TTCHFR = \frac{CHF_{sw}}{CHF_{empty}} \tag{3.5}$$

In the strictest sense, it is important to take into account the physical space occupied by the twisted-tape in order to calculate an equivalent mass flow rate; however, for the majority of the studies and for most practical design cases, the twisted-tape occupies only a small fraction of the overall flow area, i.e. $< 10\%$. The distribution of flow area fraction occupied by the twisted-tape is shown in Figure 3-6. Because the twisted-tape takes up a small fraction of the flow area, it is possible to ignore its presence by using the same mass flux value for the empty tube CHF. This idea can be further validated by comparing the $y=\infty$ data of Nariai et al. [71] to the value predicted by the modified Tong correlation for empty tubes [70], as shown in Figure 3-7. In this figure, the predicted value of CHF was calculated as if the tube did not have a twisted tape present, using the same mass flux that was reported for the tube with the twisted-tape insert. While physically the presence of the twisted-tape insert does have an effect on the velocity profile of the flow, this effect is not significant enough to be segregated from the noise of the experimental data and the error of the correlations that are used to describe it. Therefore it is appropriate to use the empty tube mass flux values when comparing the TTCHF values to the empty tube values. This finding is consistent with the formulation of the correlations of Nariai et al. [72], Jensen [44], and Kisina et al. [53].

Enhancement of CHF for tubes containing twisted-tape inserts can be attributed to two main mechanisms:

- The twisted-tape increases the liquid radial velocity gradient near the wall and hence the wall shear stress compared to an empty tube at the same mass flux. This helps increase mass exchange between the liquid in the center of the flow and that in the bubbly layer while also decreasing the bubble diameter. Therefore, it takes a larger number of small bubbles to reach the critical void fraction of 82% in the bubbly layer.

- The centrifugal force field developed by the swirling flow acts to centrifuge the more dense, cool liquid phase toward the tube wall while also forcing the vapor phase to migrate to the center of the tube. Also, at very high void fractions, the centrifuging effect redeposits entrained droplets to the liquid film. This effect delays the onset of Dryout.

With these two mechanisms in mind, it can be expected that the TTCHFR will increase with an increase in mass flow rate and a decrease in twist ratio due to the effect these parameters have on increasing the shear stress and the centrifuging effect. An increase in TTCHFR can also be expected for increasing void fraction since the centrifuging effect redeposits the entrained droplets which maintains a thicker liquid film compared to an empty tube, thereby delaying the onset of Dryout. This is not to say that the magnitude of CHF will increase with increasing void fraction. This effect is shown qualitatively in Figure 3-8 where the magnitude of the CHF value for both the empty tube and twisted-tape equipped tube decrease with increasing quality while the ratio between the two tends to increase.

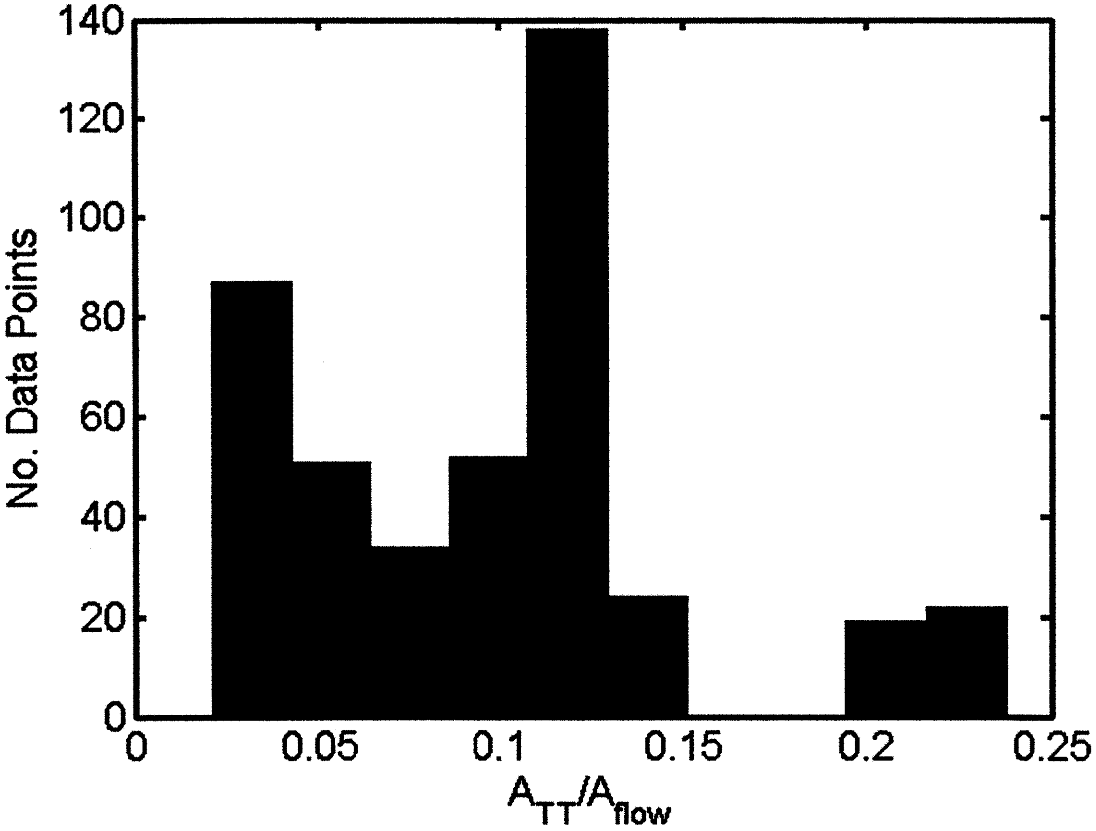

Figure 3-6: Fraction of Flow Area Occupied by the Twisted-Tape

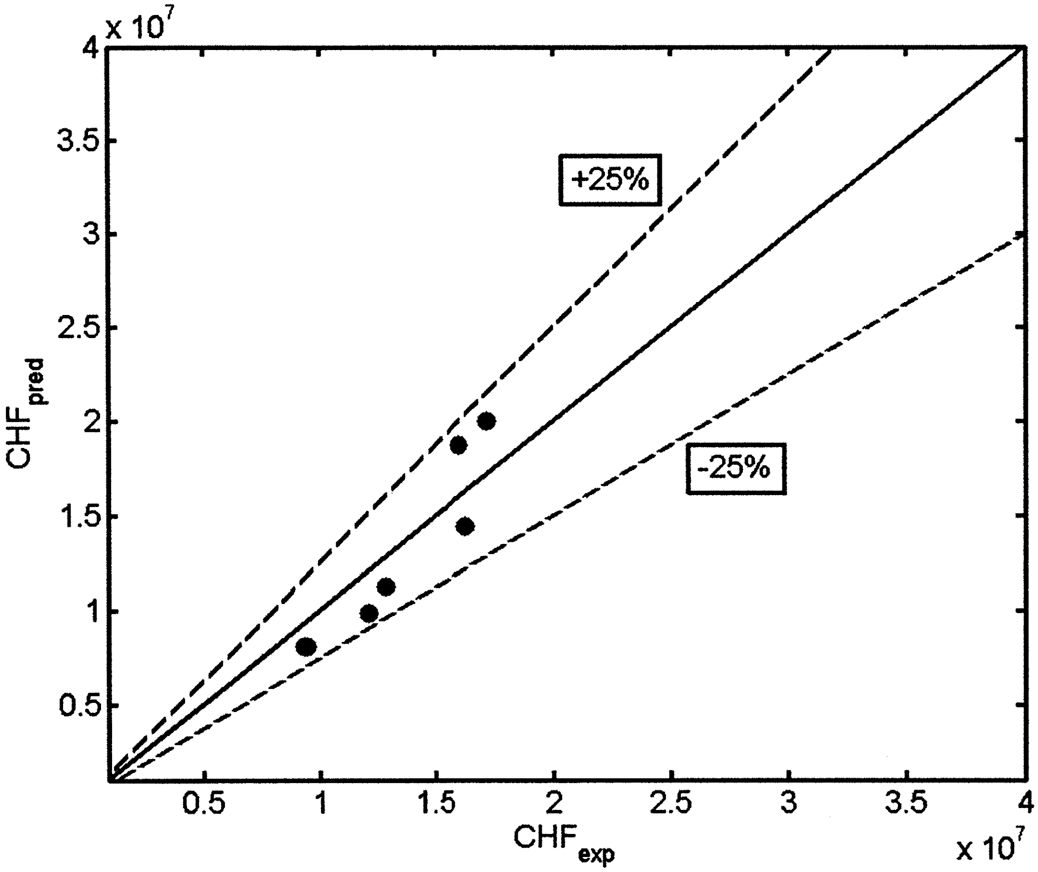

Figure 3-7: Comparison of $y=\infty$ and Empty Tube CHF Values

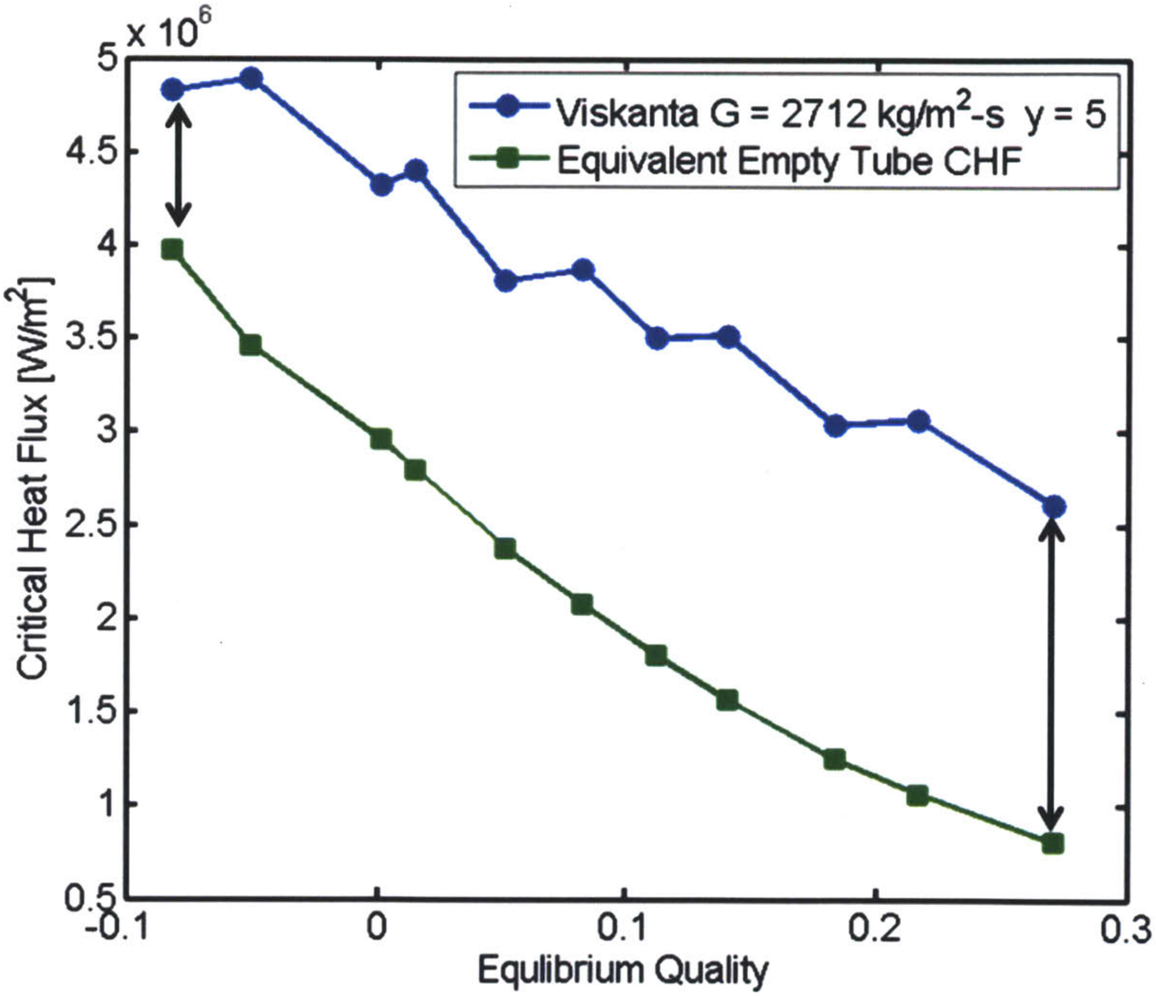

Figure 3-8: Viskanta Critical Heat Flux vs. Equilibrium Quality

Table 3.2: Empty Tube Comparison Correlation Operating Range

Parameter	Units	Modified Tong	Groeneveld LUT
Mass Flux	$\left[\frac{kg}{m^2-s}\right]$	1300 - 40000	0 - 8000
Pressure	$[MPa]$	0.1 - 20	0.1 - 21
Equilibrium Quality	[-]	(-0.01) - (-0.46)	(-0.50) - 0.90
Heated Length	[mm]	3 - 200	$(\frac{L_h}{D}) > 5$
Diameter	[mm]	2 - 20	>3

It should be noted which correlations are being used to compare the empty tube to the twisted-tape CHF experimental values. In order to cover a wide range of data, two empty tube correlations had to be utilized. The first correlation is the modified Tong correlation, as presented in Nariai et al. [70, 71]. This correlation was used primarily for the high mass flux data. The second correlation used was the Groeneveld Look-up Tables (LUT) [30]. The operating ranges of each of these correlations are listed in Table 3.2. If the data fell into a range that was covered by both correlations, then the Groeneveld LUT was the default correlation for comparison.

The increase in TTCHFR due to increased shear stress, i.e. an increase in mass flux, is illustrated by the trends in the data gathered by Viskanta [91] in Figure 3-9. Notice how the TTCHFR increases when the twist ratio decreases at constant mass flux, as can be seen when comparing the two lowest lines. Also notice how the ratio increases at fixed twist ratio, but increasing mass flux, as is evident by comparing the top three lines in this figure. The huge increase in CHF at high quality motivated design applications under these conditions and hence a large collection of data exist at conditions similar to the BWR operating range, i.e. ~7 MPa and high quality.

3.2.3 CHF Depression for Tubes Containing Twisted-Tape Inserts

There are some instances where the presence of the twisted-tape insert cause either no increase in CHF, or in some cases CHF depression. This is particularly prevalent for three operating conditions which will be discussed in the following order:

- Low mass flux/large twist ratio at high quality
- Insulating effect of the twisted tape
- Very low void at CHF

Low Mass Flux/Large Twist Ratio at High Void First, for high quality flows in tubes equipped with a FLTT, it is possible that if the centrifugal field is not strong enough, i.e. large twist ratio or small mass flux, the entrained liquid droplets will actually follow along the twisted-tape instead of being redeposited on the pipe wall. This effect was pointed out in Moeck et al. [66] and can be seen in Figure 3-10, which shows the dependence of the boiling efficiency on mass flux, for different values of the steam quality at the

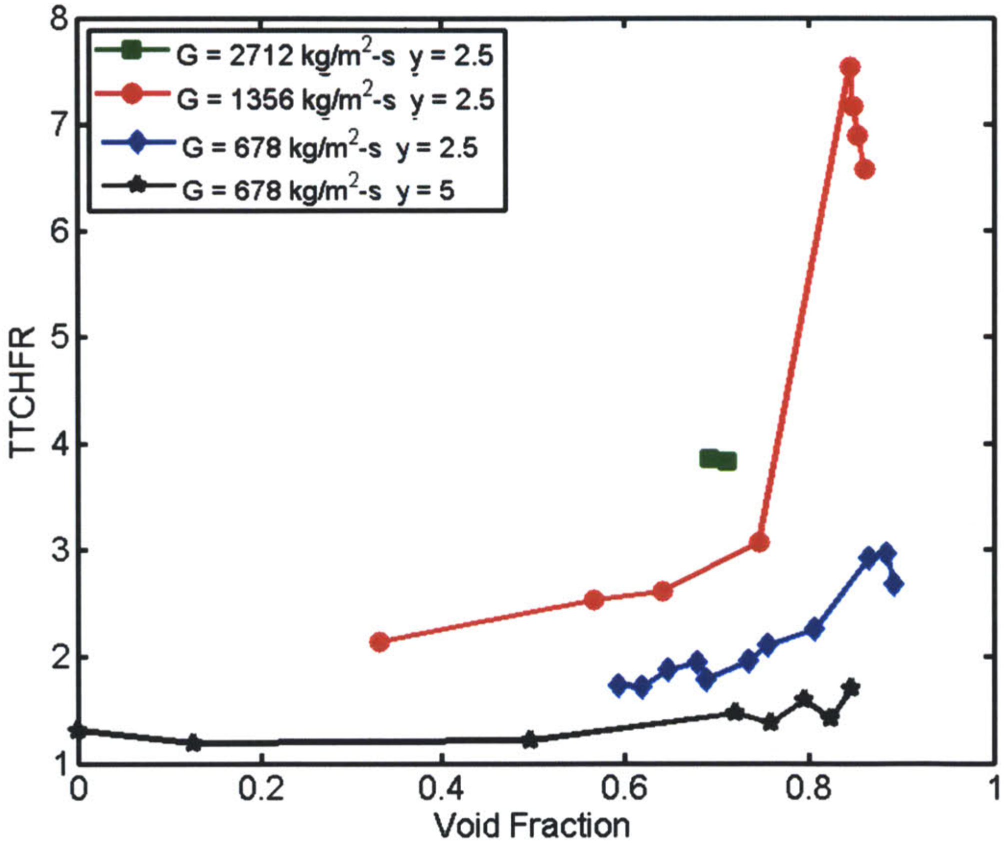

Figure 3-9: TTCHFR vs. Equilibrium Quality: Viskanta [91]

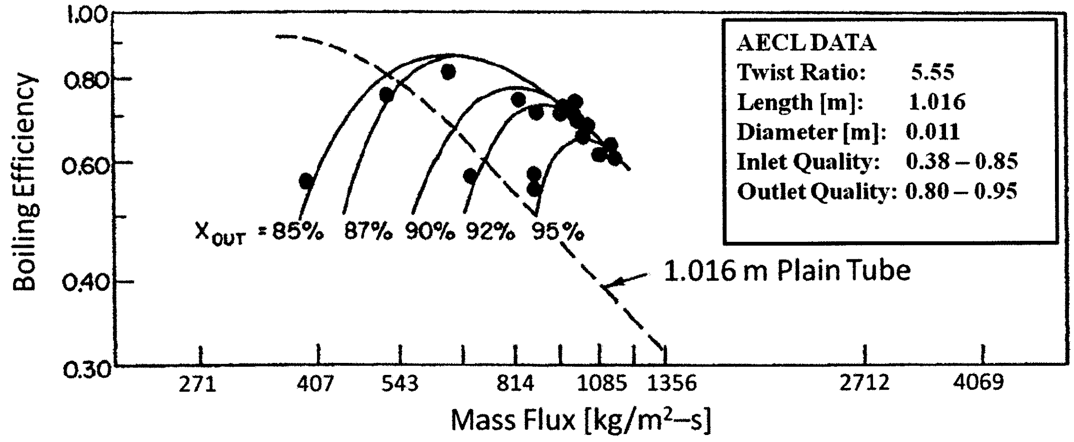

Figure 3-10: CHF Depression Due to High Void-Low Swirl Conditions: Adapted from Moeck et al. [66]

tube exit. The boiling efficiency is a parameter sometimes used for high flow quality heat exchangers, and is defined as Equation (3.6). The term in the numerator is the heat flux yielding Dryout, while the term in the denominator is the heat flux required for the flow to exit the tube at 100% quality.

$$\eta_b = \frac{q''_{exp}}{q''_{max}} \tag{3.6}$$

Insulating Effect of the Twisted-Tape The second condition that can cause CHF depression in tubes containing twisted-tapes is the insulating effect. This effect was discussed at length in Tong et al. [87]. The insulating effect refers to the reduction in heat transfer near the intersection of the tube wall and the twisted-tape. There is a minimum thickness that twisted-tapes can be manufactured due to the mechanical properties of the metal that they are fabricated from; therefore, insulating effect becomes a significant problem for very small diameter tubes since the twisted-tape occupies a large portion of the tube perimeter as shown in Figure 3-11. Even if the tape is not in direct contact with the tube wall, but has a small diametral gap, the low velocity of the flow at the intersection of the twisted-tape and the tube wall creates a region of inefficient heat transfer, thereby creating a region of locally high boiling. This effect would be lessened in the IPWR compared to laboratory experiments because the heat would be able to diffuse through the fuel; however, it is important to avoid this effect if possible.

If small diameter tubes must be implemented, this problem can be circumvented using one of two techniques. First, the insulating effect can be eliminated by increasing the gap between the twisted-tape and the tube wall to allow coolant to flow through the gap; however, this large gap could cause the insert to vibrate at high flow velocities, resulting in flow induced fretting. Second, for tightly-fit twisted-tapes, the heat transfer coefficient can be increased by either decreasing the twist ratio or increasing the mass flux to

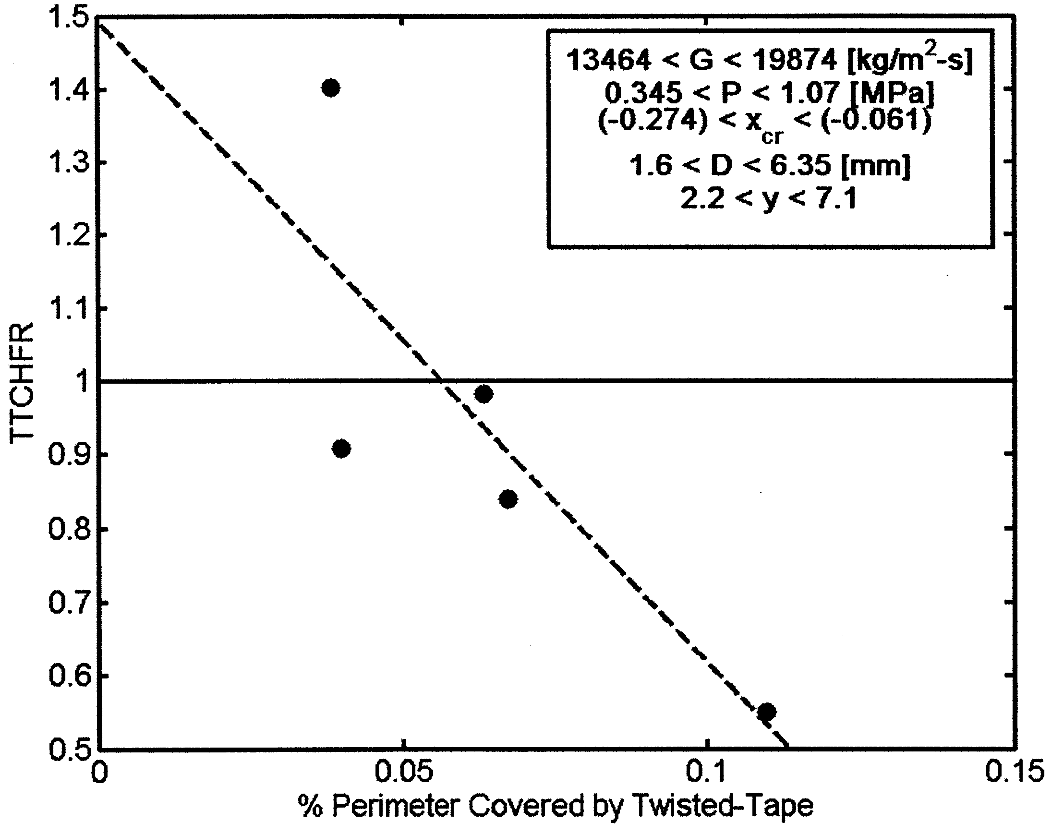

Figure 3-11: Insulation Effect for Subcooled Tests

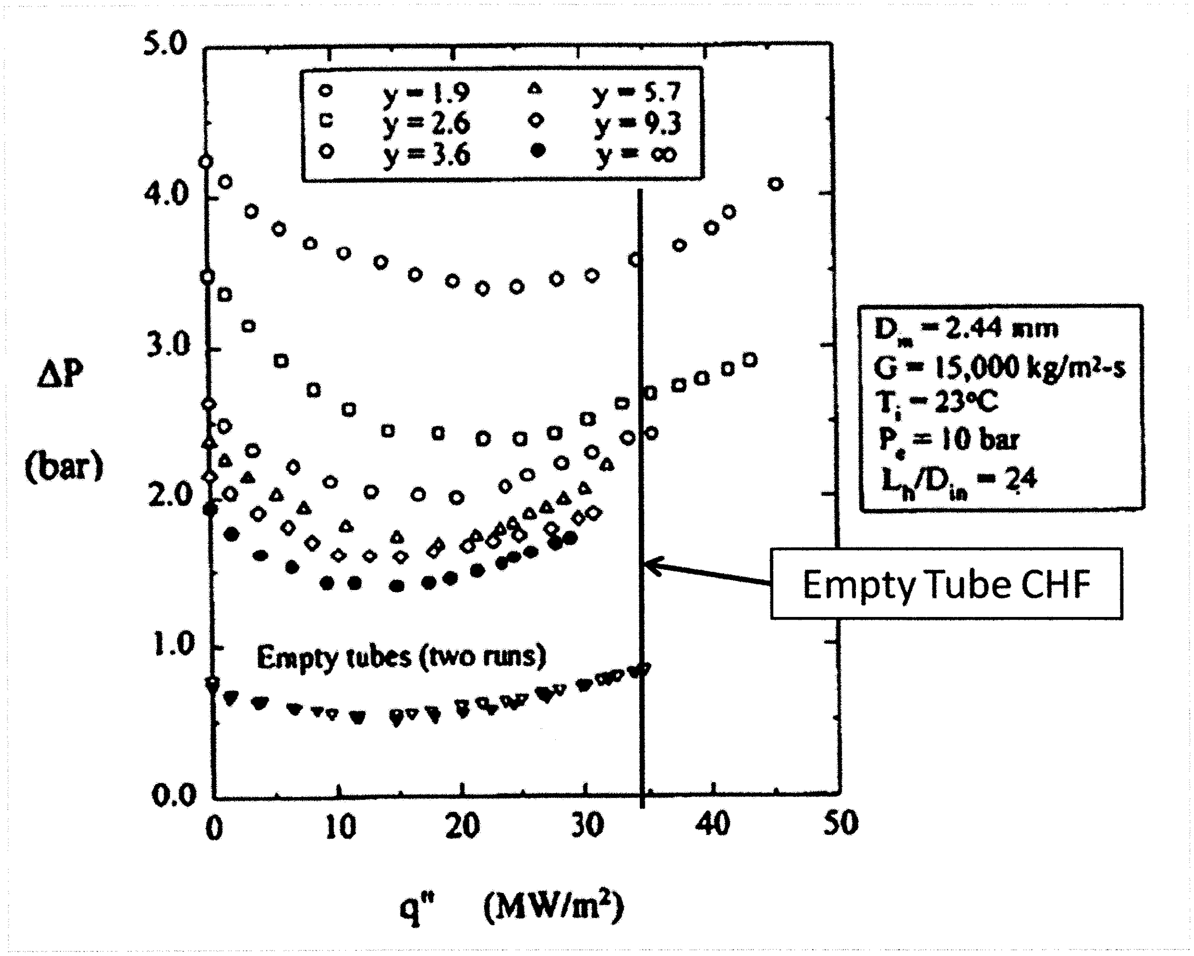

Figure 3-12: Insulation Effect: Adapted from Tong et al. [87]

offset the insulating effect of the tape.

A plot of pressure drop vs. heat flux from Tong et al. [87] is shown in Figure 3-12 where the last point on the right side of each curve represents the CHF for that tube. The diametral gap for these experiments was between 0.05 - 0.1 mm. Here it can be seen that for tubes with $y > 3.6$ the CHF is actually lower than the empty tube value because the poor heat transfer at the intersection of the twisted-tape and tube wall is not offset by a sufficiently high swirl intensity. Therefore, in this case of extremely small inner tube diameter, i.e. 2.44 mm, the twist ratio must be below about $y=3.6$ in order for any CHF enhancement to occur.

Low Void at CHF The final effect that could cause a TTCHFR of close to unity is the absence of void in the channel. This is only a problem for very highly subcooled conditions. This effect can be seen in Figure 3-13 where the TTCHFR for the subcooled data was plotted against shear stress and void fraction. The dots in this figure are the data points while the surface is a simple interpolation between the data. The local void fraction was calculated by finding the bubble departure using the modified Levy model, then the flow

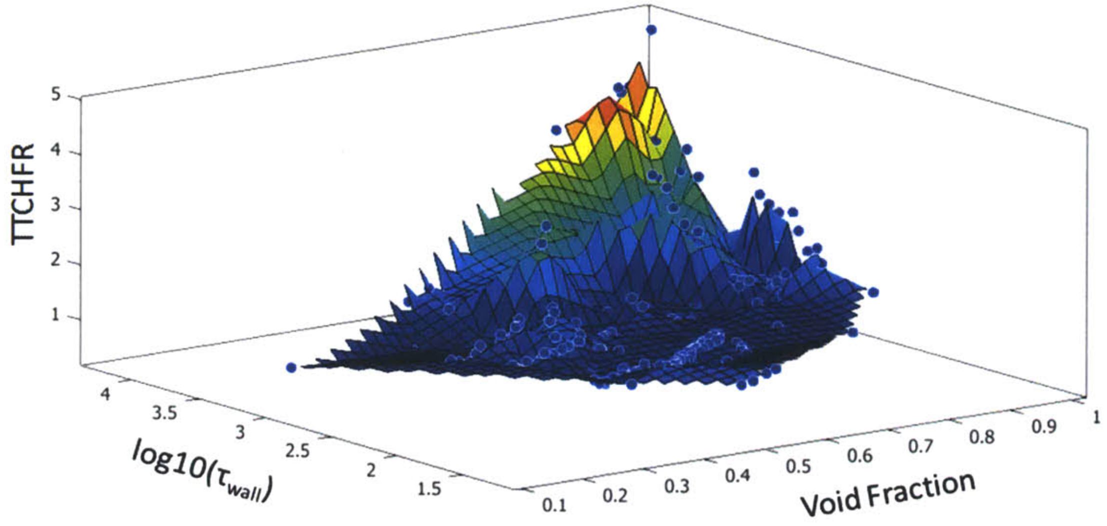

Figure 3-13: Subcooled Data Trends
This data is all subcooled CHF data from the papers in Table (3.1)

quality was calculated using the Levy profile fit method [60].

This figure shows the two enhancement effects discussed earlier, where the TTCHFR increases as the shear stress increases due to the bubbles being stripped from the tube wall. The ratio also increases due to increasing void because of the bubbles migrating away from the bubbly layer, while the entrained droplets are being redeposited on the tube wall. Conversely, the TTCHFR tends to go to unity for near-zero void fraction in subcooled boiling before the bubbles have detached. When CHF occurs with almost no void, the mechanism changes for two reasons. First, the liquid is so highly subcooled that the subcooled boiling heat transfer is very large, preventing bubbles from growing to a size that could be removed by the swirling flow. Secondly, without bubbles detached from the tube wall and present in the bulk of the flow, the centrifugal force field produced by the twisted-tape inserts has nothing to act upon. There are no bubbles to remove from the bubbly layer interface, and there are no entrained liquid droplets to redeposit on the liquid film. Therefore, it can be hypothesized that in the attached bubble regime of DNB, there is little benefit to including a twisted-tape insert for the purpose of CHF enhancement.

3.3 Uniform Circumferential Heating with SLTTs

As mentioned at the beginning of the previous section, there is very little data for SLTTs corresponding to conditions resulting in DNB that can be used for developing and benchmarking a new empirical DNB correlation; however, when looking at the entire body of data, there are actually quite a few data points at high quality, i.e. Dryout conditions, that can be used for discussion of parametric trends. A summary of the authors and the operating ranges for these data sets is shown in Table 3.3.

Table 3.3: SLTT CHF Data

Author	Ref.	Mass Flux $\left[\frac{kg}{m^2-s}\right]$	Pressure $[MPa]$	Exit Quality	Heated Length After TT [cm]	Diameter [mm]	Twist Ratio	# Data Points
Hassid et al.	[33]	1100 - 3800	5.0 - 6.96	0.097 - 0.727	29 - 236.6	15.1	0.572 - 1.02	248
Peterlongo et al.	[75]	1050 - 4050	4.97 - 6.49	0.085 - 0.639	83.2 - 249.2	15.1	2.8	91
Matzner et al.	[64]	1343 - 9792	6.895	0.04 - 0.65	122 - 244	10	5	69

In general these studies were focused on improving margin to Dryout in BWR operating conditions, therefore nearly all of the data points are at very high quality, making them inapplicable to this study. Also, the majority of the swirl decay lengths are far too large, i.e. 55-244 diameters, to be of interest in a practical design sense considering that it has been indicated that the effect of swirl nearly disappears after 50 diameters [56, 97]. Despite these two major problems with the data, a few of the general trends will be briefly covered in this section in the following order:

- SLTT CHF Enhancement Phenomena
- The Effect of Bubble Migration on CHF Enhancement

3.3.1 CHF Enhancement with SLTTs

This section will only cover the issues that differ compared to FLTT CHF enhancement, since the basic phenomenology remains the same. The topics that will be covered are the following:

- CHF vs. Swirl Decay Length
- Developing Swirl
- Channel History Effect

CHF vs. Swirl Decay As was discussed in Section 4.2.2, after the flow exits a SLTT, the magnitude of swirl immediately begins decaying. This reduction in swirl corresponds to a reduction in CHF due to the reduced centrifugal force field, as well as a reduction in shear stress due to a lower resultant coolant velocity near the tube wall. These effects can be seen in Figure 3-14, where experimental CHF data for similar conditions were plotted as a function of swirl decay length. It is important to note that the values for mass flux, equilibrium quality at CHF location, and twist ratio given in the figure legend are approximate values, and the real values fluctuate around these values slightly. Also, the points corresponding to zero heated length were CHF values taken from FLTT data collected by Viskanta [91] at similar operating conditions.

This figure also shows how CHF in the decaying swirl region tends to increase with decreasing quality, decreasing twist ratio, and increasing mass flux. Specifically, if the three lines with $y_o = 0.907$ are examined, the CHF value for these curves at the largest decay length show that CHF decreases with increasing quality as expected. The three curves with G = 2200 illustrate the point that CHF increases with a decrease in twist ratio. Finally, if the points corresponding to G = 2200, $y_o = 0.907$; and G=1100, $y_o = 0.907$ with a decay length of about 0.5 meters are compared, the increase in CHF with increasing mass flux can be seen.

Developing Swirl One of the most important design parameters of SLTTs is the number of turns required for swirl to become fully developed. If too few twists of the tape are made, then the full effect of that twist ratio is not realized. Conversely, if too many twists are made, the swirl will reach a steady state value

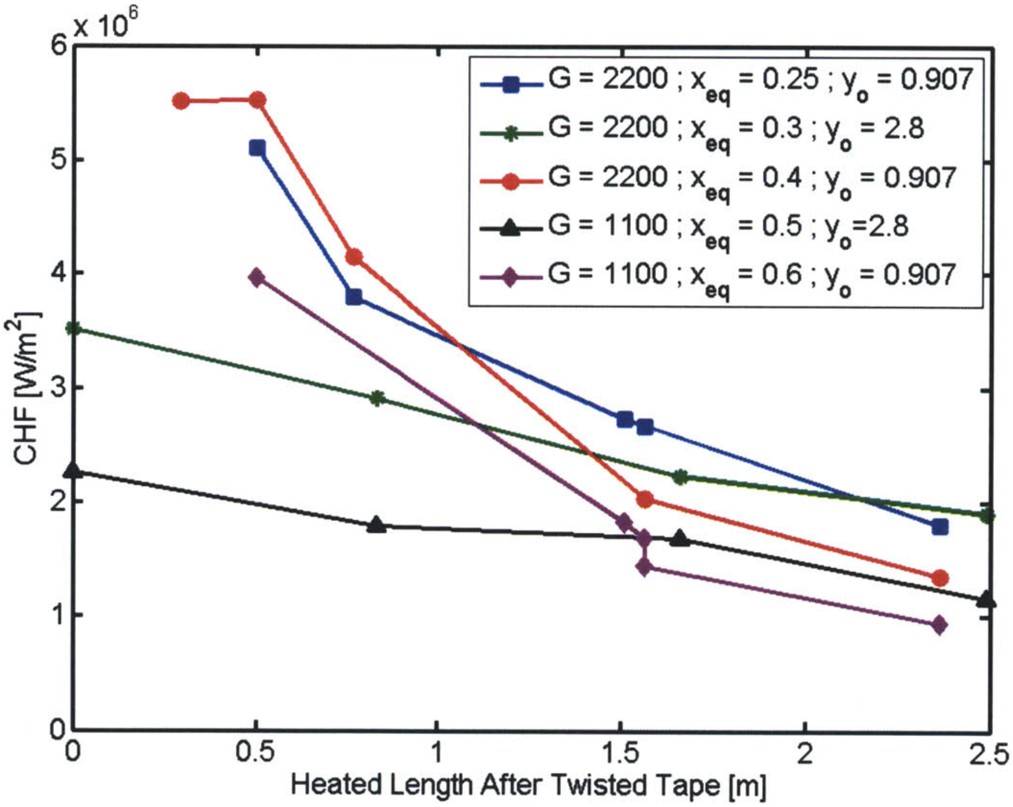

Figure 3-14: SLTT CHF vs. Swirl Decay Length

before the exit of the SLTT and the channel will perform worse in terms of pumping power due to the excess twisted-tape length.

As a result of their extensive studies, Hassid et al. [33] determined that swirl appears to be fully developed after only 1-1.5 360^o rotations. Any number of turns beyond this value appeared to have no further enhancement effect on the CHF values recorded in their study.

Channel History Effect In pure axial flow, high quality conditions, reaching Dryout can be correlated to the hydrodynamic conditions upstream of the location of Dryout. This is often termed the channel history effect, i.e. Dryout depends on the following phenomena in the liquid film along the tube upstream of the Dryout location, evaporation, liquid droplet entrainment and redeposition of liquid droplets from the vapor core. In the case of twisted-tape inserts, the flow disruption caused by the twisted-tape is so large that the hydrodynamic conditions upstream of the promoter are not translated through twisted-tapes as discussed by Matzner et al. [64] and Hassid et al. [33]. The reason for this effect is that most of liquid droplets present in the vapor core of the flow before the SLTT are centrifuged to the tube wall upon passing through the insert, creating a thicker liquid film than would be present under equilibrium conditions. This can be seen in Figure 3-15 where Fryer et al. [26] show the liquid film flow rate fraction after the flow passes through a SLTT. Clearly it takes some time for all of the liquid droplets to redeposit in the liquid film. Then as the swirl intensity decays, the rate of entrainment overtakes the enhanced deposition rate caused by swirl, and the liquid film begins to approach its pre-swirl promoter thickness. Therefore, the flow conditions downstream of a twisted-tape are related to the upstream conditions only through the quality of the flow at the entrance of the twisted-tape as shown by Hassid et al. [33].

3.3.2 Bubble Migration and Critical Twist Ratio

One of the mechanisms that aid in CHF enhancement is the migration of bubbles away from the bubbly layer due to the twisted-tape induced centrifugal field. The lower limit of swirl where this effect can still occur was addressed in Section 2.5.1, and is represented as the critical twist ratio, y_{cr}. In theory, when the effective twist ratio falls below y_{cr} any enhancement due to the presence of swirl should disappear and the TTCHFR should tend to unity. This effect can be observed by using the SLTT data of Refs. [33, 64, 75], as shown in Figure 3-16. It is clear from this figure that as the effective twist ratio approaches the critical twist ratio, then enhancement due to the twisted tape disappears. Therefore, it is important when designing systems with SLTTs not to allow the effective twist ratio to exceed y_{cr} in a location where CHF enhancement is needed to provide a safety margin to the operating heat flux, otherwise there is no point in installing the SLTTs.

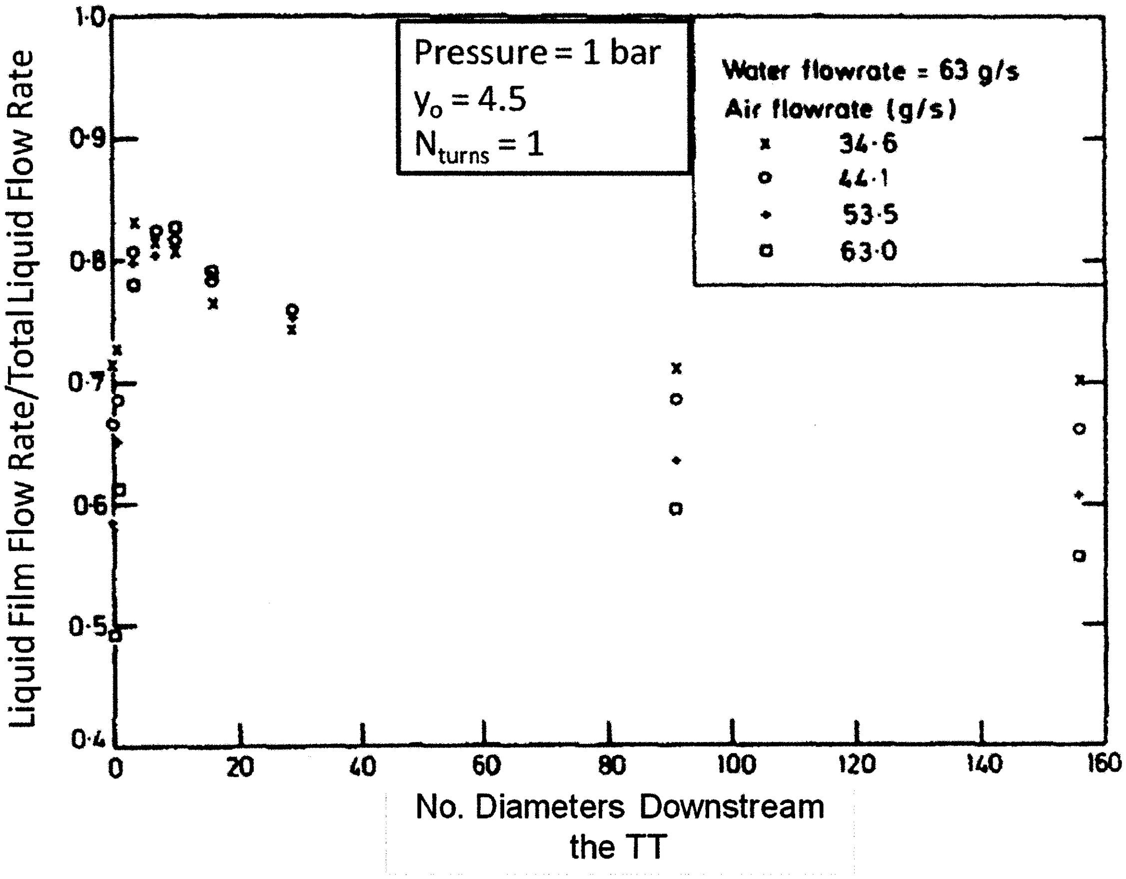

Figure 3-15: Liquid Film Thickness of an Annular Flow After Passing Through a SLTT: Adapted from Fryer et al. [26]

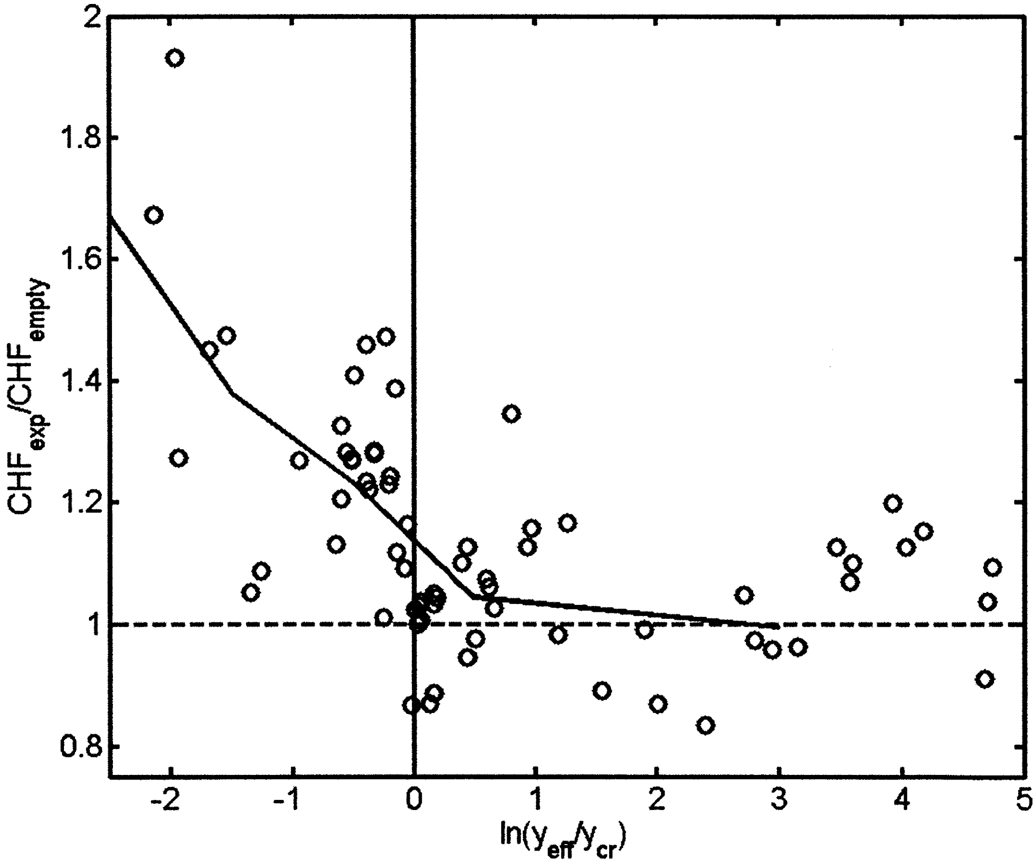

Figure 3-16: TTCHFR vs. $\frac{y_{eff}}{y_{cr}}$ ratio for SLTT-Provided Channels: Data from Hassid et al. [33], Matzner et al. [64], and Peterlongo et al. [75]

Chapter 4

Empirical DNB Correlation Development

This section will cover the development of a correlation that describes the ratio of CHF for a tube with swirling flow compared to a tube in pure axial flow under the same local conditions. As stated in Chapter 1, and qualitatively shown below in Figure D-1 as the DNBR, this correlation is needed to describe the behavior of the CHF enhancement in both axial and swirl flows.

While this correlation is primarily intended for use in a scoping study of the IPWR design, it should also be valid over a wide range of pressures in order to not only capture as many data points as possible, but also so that it is useful in other, more general design projects.

This Chapter is organized as follows:

- Background on DNB Correlation Development: Section 4.1
- Methodology for DNB Correlation Development: Section 4.2
- Validation of New DNB Correlation: Section 4.3

4.1 Evaluation of Existing Empirical DNB Correlations

There are a wide range of correlations specifically derived for FLTT CHF evaluation; however, there are no existing correlations that exactly fit the criteria that are required for a design study of the IPWR using MSLTTs. Since a useful correlation must be applicable to the IPWR design while also describing as much of the existing data as possible, it must cover a wide range of operating conditions. Since the Usman-Weisman model [95] was developed to describe the range of operating conditions in which DNB occurs, the bounds of the model provide an initial range of conditions that should be considered for the new empirical DNB correlation. The hypothetical operating conditions of the IPWR and the bounds of the Usman-Weisman

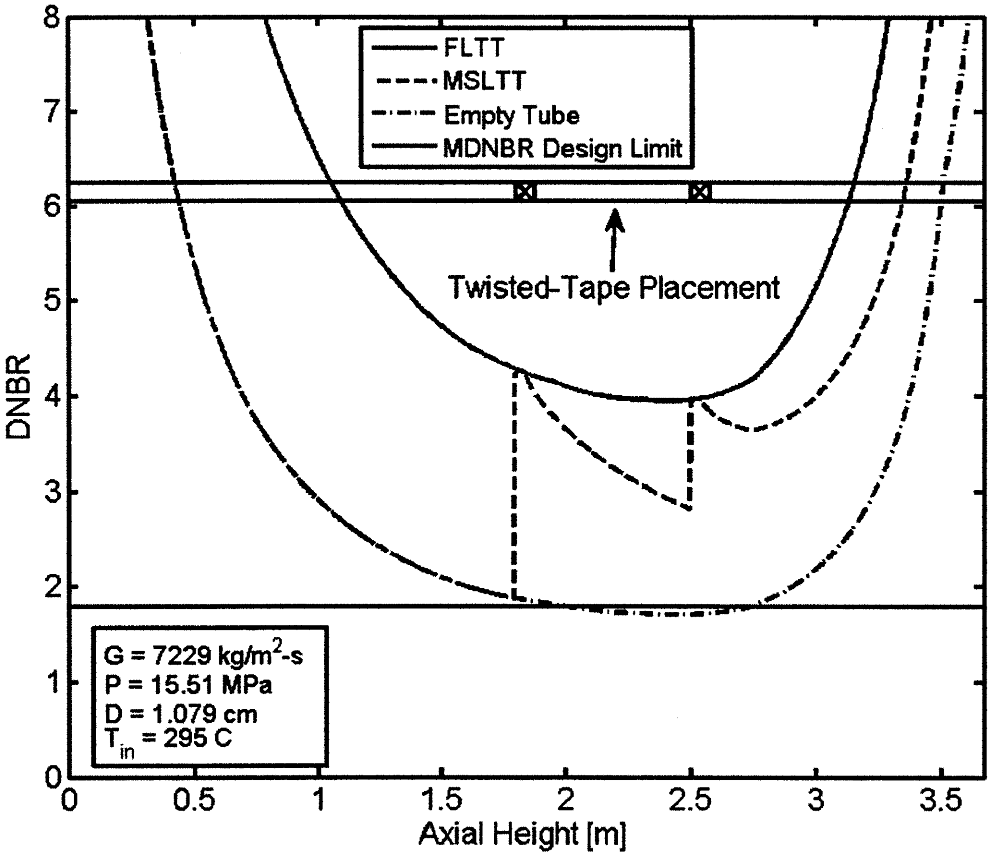

Figure 4-1: DNBR vs. Axial Height

Table 4.1: Desired TTCHF Correlation Bounds

Parameter	Units	Usman-Weisman Model	IPWR Operating Conditions	Combined Range
Mass Flux	$\frac{kg}{m^2-s}$	$0.3G_c$ - 40,000	< 10,000	0 - 40,000
Pressure	[MPa]	0.777 - 20.75	< 16.0	0.777 - 20.75
Quality	[-]	$x_{eq} = (-0.47) \rightarrow \alpha_{HEM} = 0.64$	(-0.35) - 0.05	$x_{eq} = (-0.47) \rightarrow \alpha_{HEM} = 0.64$
Heated Length	[m]	0.035 - 3.65	3.67	0.035 - 3.65
Diameter	[cm]	0.115-3.75	0.7 - 1.5	0.115 - 3.75
Twist Ratio	[-]	all	all	all

model are listed in Table 4.1. These bounds were combined to produce the requirements for a useful DNB correlation. Not all of these bounds will necessarily be met in the new DNB correlation since there are real limitations in terms of the body of data that can be used to validate any DNB correlation over this range of operating conditions.

It is also important to keep in mind that the heat flux in the IPWR is not axially uniform, therefore there must be a technique to determine the effect this will have on DNB. With these parameters in mind, a critical analysis of the existing DNB correlations for swirl flow was performed.

The existing twisted-tape CHF correlations are listed in Table 4.2. This table also indicates whether or not the correlation was developed to describe ratio of CHF that occurs in an empty tube compared to a tube containing a twisted-tape insert, also known as the twisted-tape CHF ratio (TTCHFR), as shown in Equation (4.1), i.e. Yes, or simply a twisted-tape CHF value, i.e. No. All of these TTCHF correlations and their operating ranges are given explicitly in Appendix C; however, they will be briefly discussed here.

$$TTCHFR = \frac{CHF_{sw}}{CHF_{empty}} \tag{4.1}$$

Subcooled TTCHF Correlations Overall these correlations perform well when describing the data from which they were derived. All of these correlations are disqualified for use in this study for several reasons. First, the Gambill and Drizius equations completely neglect the effect of pressure. They are also for very high mass flux conditions over a very narrow range of pressures.

The Nariai correlation [71] was developed for near-atmospheric conditions and is difficult to scale with pressure. The base correlation upon which it is built is also only valid for heated lengths up to 0.2 meters, which is much too short for the IPWR design. This correlation did show promise in terms of its general formulation, therefore it will be discussed further in Section 4.2.1.

The Tong correlation [87] was developed for low pressure and high mass flux operation as well. The tubes

Table 4.2: Existing Twisted-Tape CHF Correlations

Author	Ref	Ratio (Y/N)
Subcooled		
Gambill et al.	[27]	N
Drizius et al.	[21]	N
Nariai et al.	[71]	Y
Tong et al.	[87]	N
Hata et al.	[34]	N
Saturated		
Matzner et al.	[64]	N
Brevi et al.	[12]	N
Jensen	[44]	Y
Kisina et al.	[53]	Y
Both		
Krug et al.	[57]	N
Modified Jensen	[23]	Y

in the test were very small, on the order of a few millimeters both in terms of length and diameter. As is the case with many empirically derived expressions, this correlation is prone to large errors when extrapolated outside its advertised data range.

The Hata correlation [34] is formulated primarily with non-dimensional numbers, which showed promise for extrapolation outside its original data range; however, the correlation was developed for tubes less than 6 cm long. This issue caused some problems when trying to adapt the correlation to be applicable to reactor design since the total height of the IPWR core is approximately 60 times this length.

Saturated TTCHF Correlations None of these correlations qualify since they were derived specifically for saturated boiling conditions; however, a brief discussion of each is given to illustrate why they were not chosen as a base for the new correlation.

The Matzner correlation [64] was geometry specific, therefore it is impossible to use this correlation for any variations in twisted-tape configuration, i.e. twist ratio, twisted tape spacing, number of twisted tapes other than the ones used in their study. Also this correlation was developed for operating conditions well above the upper bound of void fraction that is of interest for the IPWR design.

The Brevi correlation [12] was also developed using very high flow quality data. Furthermore, it only is applicable over a very narrow range of operating conditions, i.e. one pressure, one twist ratio, and three mass flux values. Therefore, any parametric trends could not be fully derived from this study.

The Jensen correlation [44] presents non-physical phenomena under certain operating conditions. Particularly the predicted value of CHF will increase once the twist ratio increases beyond a certain value, i.e. y_{max}=4.7 for a system pressure of 15.51 MPa. This problem was first cited in Ferroni et al. [23], and was dealt with by deriving an analytic expression for the maximum twist ratio allowed to be used with this correlation. The Jensen correlation is an expression that describes the TTCHFR using the Katto correlation as the empty tube CHF reference value [48]. This correlation is based on a non-dimensional map of flow

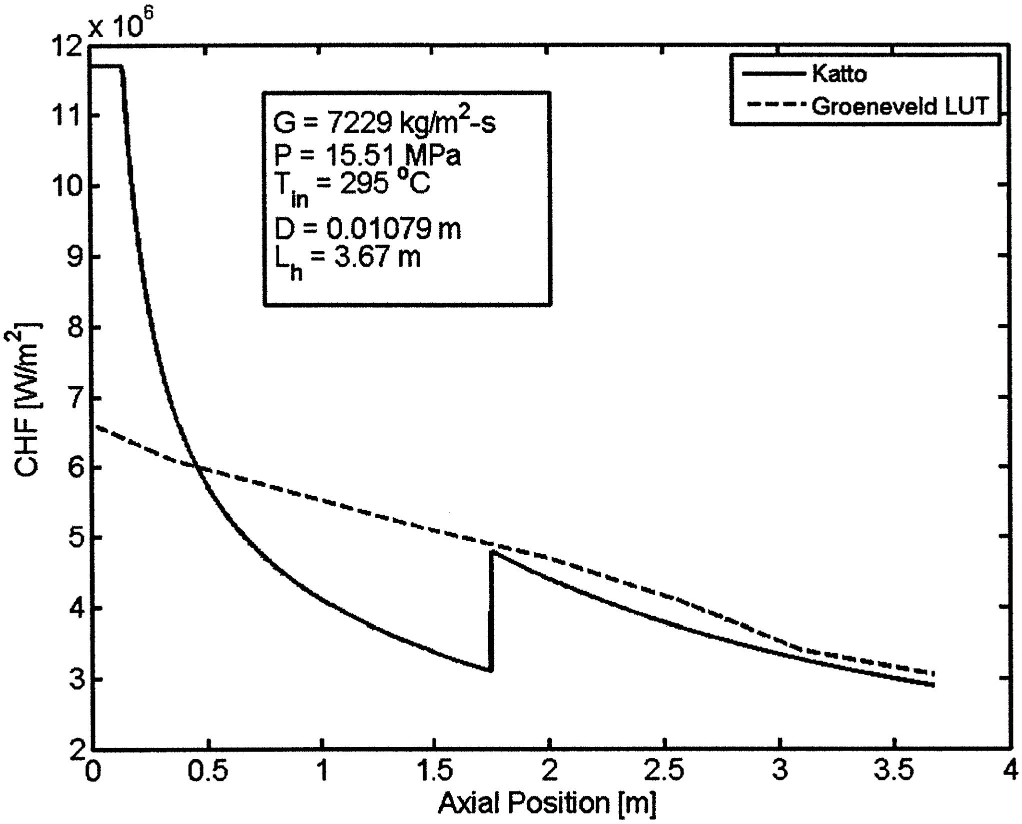

Figure 4-2: Katto Correlation Discontinuity for an Empty Tube

conditions used to determine the CHF mechanism at local conditions, i.e. high or low pressure DNB, high or low pressure dryout, or an intermediate zone between these conditions. The Katto correlation has good data prediction accuracy; however, it shows large discontinuities when these non-dimensional CHF regime boundaries are crossed, as shown in Figure 4-2, where the Katto correlation is compared to the Groeneveld LUT values under the same operating conditions. This problem presents a serious issue with reactor design since these discontinuities can drastically effect the reported MDNBR value as well as raise concerns with the validity of the reported value.

The Kisina correlation [53] was developed using data with high void fraction. It is based on a non-dimensional flow regime map also developed by Kisina [54]. Overall this correlation is complicated to interpret, and is highly piecewise. It could provide some insight to the effect of void fraction on Dryout conditions in swirling flow; however, high void operations are outside the scope of this study.

Subcooled and Saturated TTCHF Correlations Considering that the correlation needs to be valid for both subcooled and saturated conditions, it is clear that only the Krug correlation [57] and the Ferroni correlation [23] are valid for this study; however, there are issues with these correlations as well.

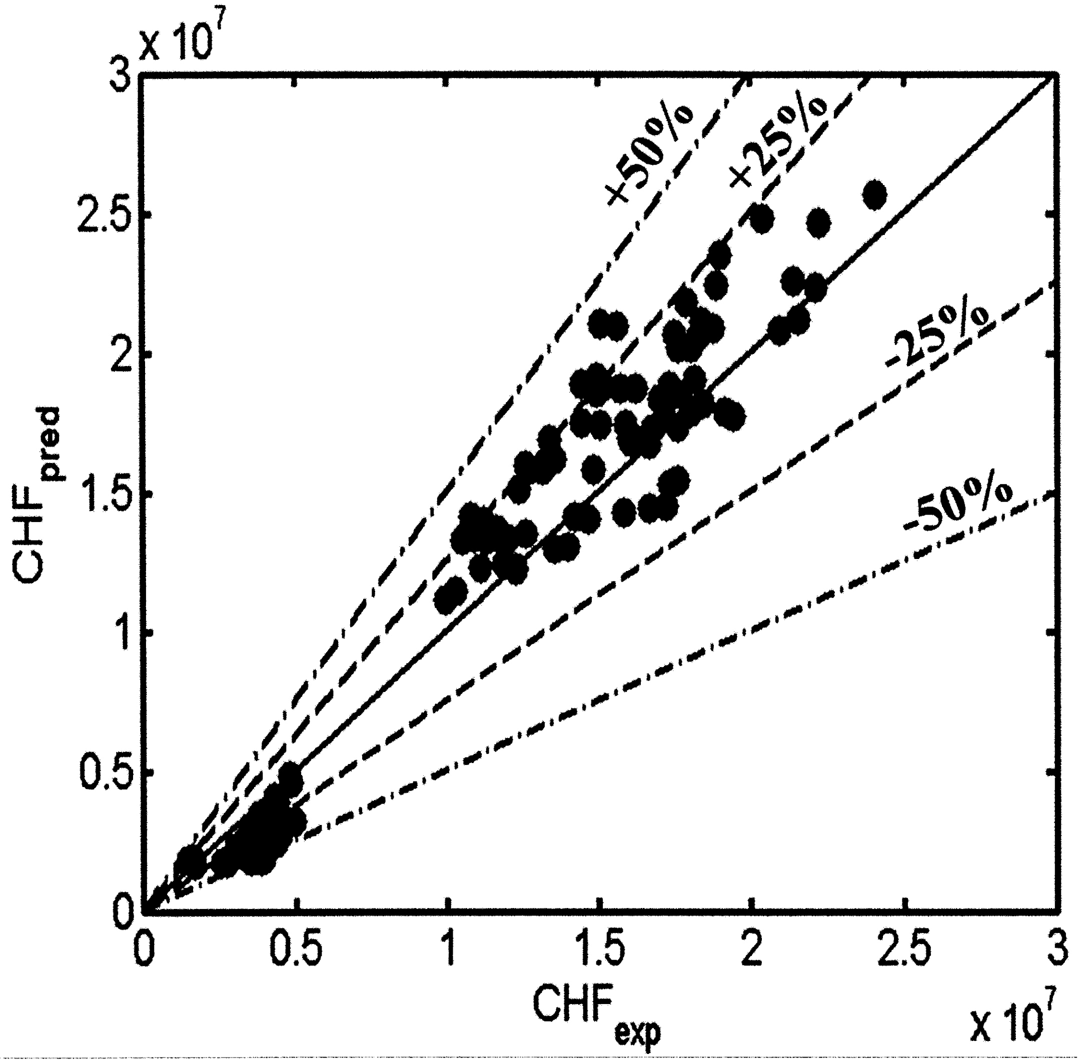

Figure 4-3: Krug Correlation Accuracy

The Krug correlation attempted to capture too broad a range of data, which resulted in poor prediction accuracy. Figure 4-3 shows the performance of the Krug correlation over the operating range of interest. The inner dashed lines on the scatter plot represent ±25%, whereas the outer dashed lines represent ±50%. It should be noted that most of the outliers are for saturated boiling conditions. Since this correlation represents a fairly large range of errors in prediction, it was decided not to use this correlation.

The Ferroni correlation is simply an extension of the Jensen correlation [44] for use with MSLTTs. Ferroni was able to solve the non-physical behavior of the correlation by applying a limit on the maximum twist ratio that could be used as a function of pressure. However, the issue of discontinuities still exist. Furthermore, the Jensen correlation was originally developed for saturated boiling conditions only, therefore its application to subcooled boiling is an extension that could potentially introduce errors.

With all of these correlations discounted for a variety of reasons, it is clear that a new correlation needs to be developed for this study that is capable of spanning subcooled as well as slightly positive equilibrium quality conditions in addition to a large range of mass flux, quality, and decaying swirl. Section 4.2 will now describe the basic methodology of how this new correlation was developed.

4.2 Methodology for DNB Correlation Development

This section presents the general approach to developing the new empirical DNB correlation for swirl flows. Generally, there are two possible approaches to perform this task. The first is a direct correlation method, which is very common for experimental studies. It consists of determining a standard form of the correlation, then adjusting the coefficients through a least-square analysis to match the existing data. An example of this approach can be found in Krug et al. [57]. Generally this method is quite accurate; however, there are a few issues to overcome. First, it can be difficult to choose the proper form of the correlation, e.g. should the terms be exponential, multiplicative, or additive. Second, specifically for this study, relatively few swirl flow CHF data are available for the operating conditions of interest, as shown in Section 3.2.1. Gaps in the data could lead to biases in non-physical directions. Furthermore, these correlations generally diverge quickly when they are applied outside the bounds of the database from which they were derived as found in the assessment of empty tube correlations by Hall et al. [31].

In a case where a technique is being implemented to enhance an understood phenomenon, a ratio correlation method can be followed, consisting of developing a correlation for the enhancement factor only, while keeping an existing correlation for the base case. Since this is the case with the twisted-tape swirl promoters, this method has been chosen for this study. Specifically, the differences between the empty tube CHF and that of the tube with a swirl promoter are correlated as an expression that is multiplied by an existing empty tube CHF correlation to calculate the swirl flow CHF value. Several correlations have been developed using this approach, [23, 44, 53, 71] with good results. This approach has the benefit of having a distinct lower bound, i.e. the empty tube CHF value. There are some instances where a tube with a twisted-tape can have a lower CHF value than that of a empty tube [87], as discussed in Section 3.2.3; however, if the conditions of low mass flux with a high twist ratio and high void, or small diameter tubes are avoided, the CHF of a tube with a twisted-tape will perform the same, if not better than the empty tube. Having the predicted CHF of the empty tube as a base value is also beneficial in the case of MSLTTs because in the case of extreme swirl decay lengths, the amount of swirl in the pipe is nearly zero. In this case, the flow can be considered purely axial, so it should have the same CHF value as an empty tube, as shown in Figure 4-4.

In this study, the formulation of an accurate correlation identifies the CHF enhancement mechanism in swirl flow using insights gained while analyzing the Usman-Weisman model. Once this mechanism is identified and correlated with the existing data, the empty tube correlation can help bridge the gap for

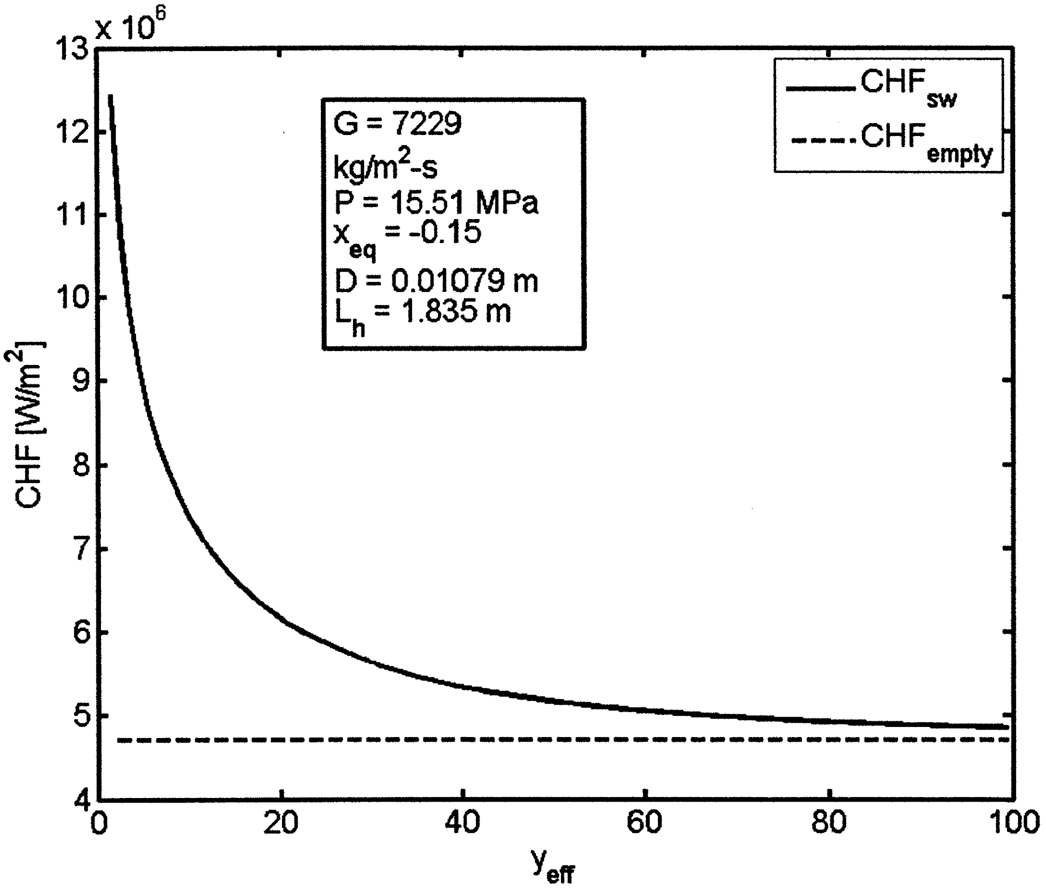

Figure 4-4: Decay of CHF for Swirling Flow to CHF for Axial Flow at High Effective Twist Ratio

ranges of pressure, mass flux, or quality that do not exist in the twisted-tape database.

However, using a ratio correlation does have a drawback. Since there is some error inevitably built into the empty tube CHF correlation, this error could be compounded by the error introduced when correlating the ratio term. This issue is not present in the first method of correlation development; however, the overall benefits of using a ratio correlation outweigh this negative aspect.

The remainder of Section 4.2 presents the development of the new empirical DNB correlation for swirling flow, i.e. either FLTTs or MSLTTs. The development of the new correlation will be presented in the following order:

- Selection of Empty Tube CHF Base Correlation: Section 4.2.1
- Swirl Decay Model for MSLTT CHF Calculation: Section 4.2.2
- Formulation of Correlation: Section 4.2.3
- Presentation of the New Empirical DNB Correlation: Section 4.2.4

4.2.1 Selection of the Base Empty-Tube Correlation

The criteria particularly applicable to the empty tube CHF correlation set forth at the beginning of this chapter require that this correlation must be valid for subcooled as well as slightly positive equilibrium quality conditions, be accurate over the wide range of pressure and mass flux that could exist in the reactor, and have a correction factor for non-uniform heat flux.

Since there are a wide range of empty tube CHF correlations to choose from, only two of the most notable correlations for both subcooled and saturated conditions were selected for evaluation. The first correlation of interest is the W-3 correlation, which was developed originally for uniform axial heat flux profiles [83, 85], but then was extended to account for the effect of non-uniform heating [84]. The operating range of the W-3 correlation is given in Table 4.3. This correlation is convenient for our purposes because it was developed to cover the normal operating conditions of a PWR. It is also convenient because it has a correction factor for axially non-uniform heat flux. Therefore, this correlation does meet all of the criteria set forth at the beginning of this section for the empty tube correlation; however, it is slightly limiting in the pressure range and it would be advantageous to capture more of the existing low pressure data in the validation of the new correlation. Also, while the W-3 correlation covers subcooled and saturated conditions, the lower bound of the correlation is not as subcooled as desired. The upper bound of the mass flux is also below the current mass flux of the proposed IPWR concept reactor [23], therefore its accuracy may be poor if used for the IPWR design study.

Because of these issues, the W-3 correlation was disregarded as an option for the base correlation of the new TTCHF ratio correlation. The next correlation that was considered was the latest version of the Groeneveld Look-up Table (LUT) [30]. The operating range covered by this correlation is listed in Table 4.4.

Table 4.3: W-3 Correlation Operating Parameters

Parameter	Range
Pressure	5.5 - 16 MPa
Mass Flux	1356 - 6800 $\frac{kg}{m^2-s}$
Equivalent Diameter	0.005 - 0.018 m
Equilibrium Quality	(-0.15) - 0.15
Heated Length	0.254 - 3.70 m
Ratio of Heated to Wetted Perimeter	0.88 - 1.0

Table 4.4: Groeneveld LUT Operating Parameters

Parameter	Range
Pressure	0.1 - 21 MPa
Mass Flux	0 - 8000 $\frac{kg}{m^2-s}$
Equivalent Diameter	> 0.003 m
Equilibrium Quality	(-0.50) - 0.90
Heated Length to Diameter Ratio	$if\ x_{in} < 0\ ;\ \frac{L_h}{D} > 50$ $if\ x_{in} > 0\ ;\ \frac{L_h}{D} > 100$

This correlation was developed by examining the world database of CHF data. In all, over 30,000 data points were considered in the construction of the table and extensive work was performed to minimize discontinuities and non-physical parametric trends. The parametric error distribution for the LUT is presented in Figure 4-5. The LUT also has a correction factor for non-uniform heat flux, therefore it is applicable to the IPWR design. The complete listing of correction factors for the Groeneveld LUT will be presented in Section 4.2.4 along with the complete formulation of the new DNB correlation.

4.2.2 Swirl Decay Model

In order to calculate CHF for the decaying swirl region of a tube containing MSLTTs, it is necessary to find an appropriate swirl decay model. This model will be used to quantify the swirl intensity of a decaying swirl flow which will be used as an input to the new DNB correlation. Ideally this swirl decay model would take into account the presence of two-phase flow; however, there is no data that a model could be directly validated against. Therefore, a single-phase swirl decay model was used to approximate the effective twist ratio downstream of a SLTT.

In order to quantify the swirl intensity downstream of a SLTT, the idea of an effective twist ratio must be used. This term, denoted as y_{eff}, is defined as the theoretical twist ratio that a twisted-tape would have in order to induce a steady state swirl equivalent to the local swirl value. In other words, decaying swirl is treated as swirl in a FLTT equipped tube where the twist ratio of the promoter is gradually increasing.

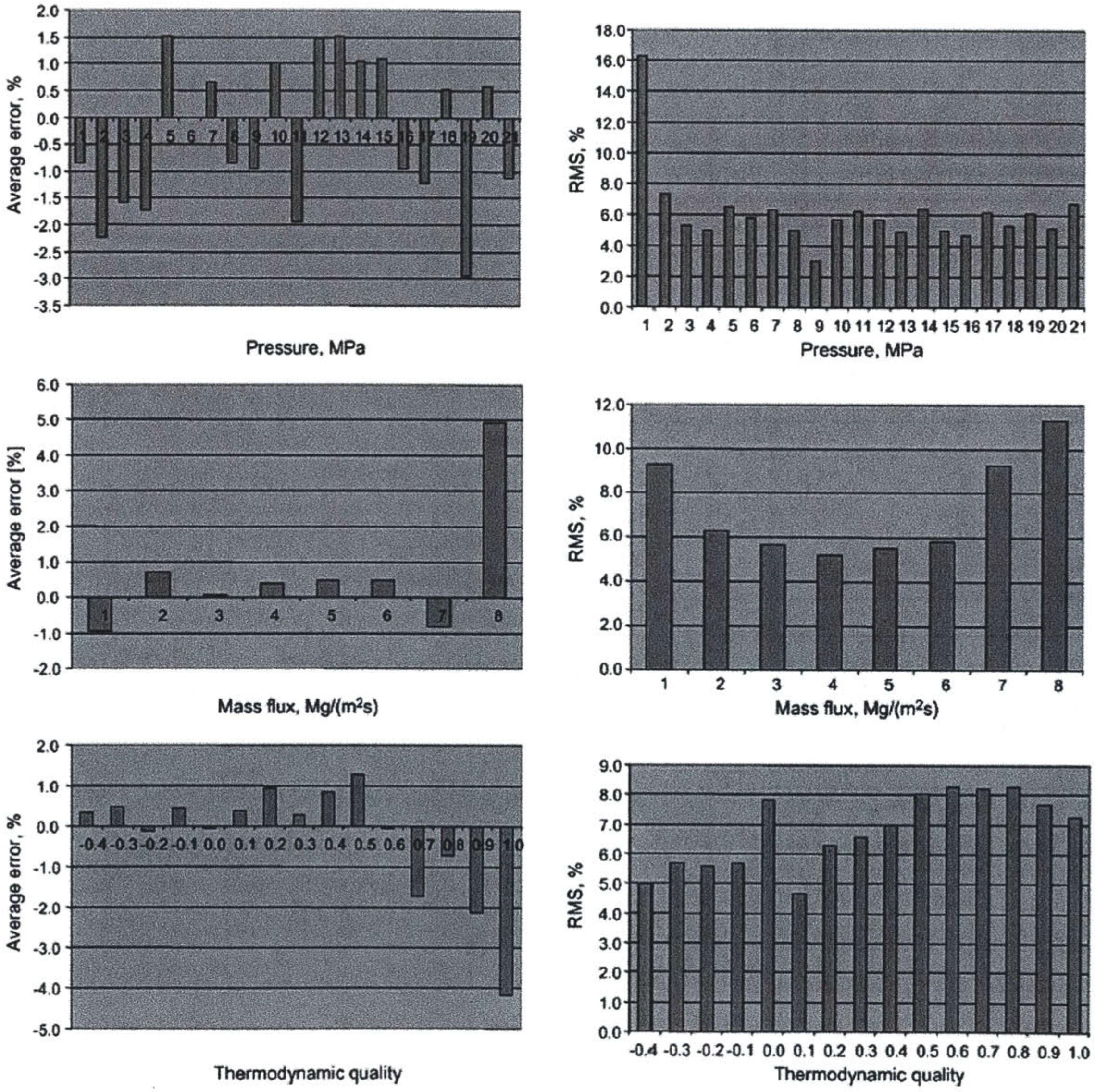

Figure 4-5: Groeneveld LUT Parametric Error: Adapted from [30]

The previous work of Ferroni [23] utilized the swirl decay model developed first by Kreith et al. [56], then independently confirmed and improved by Algifri et al. [4]. The full presentation of this swirl decay model can be found in Appendix C. This model was not used for two reasons. First, it is complex and computationally intensive. Second, and more importantly, the presentation of this model in Kreith et al. [56] was convoluted and the data that was used to validate the model was also described in a convoluted manner, leading to doubts in the formulation of the model and subsequent abandonment of this approach.

A more simple model of swirl decay was developed by Wu et al. [99]. This model performs a momentum balance on the fluid due to shear stress and boundary layer development as the fluid flows downstream of a swirl promoter. The formulation of the model is shown in Equation (4.2), where λ_s is the friction factor.

$$ln\left(\frac{6+2z^2+2\sqrt{3}\sqrt{z^4+3z^2+3}}{2\sqrt{3}+2\sqrt{3}z^2-2\sqrt{z^4+3z^2+3}}\right) = 2\sqrt{3}\cdot f\cdot(\overline{x}-6exp\left(-0.25\overline{x}\right)+6)+C_o \tag{4.2}$$

where,

$\overline{x} = \frac{L}{D}$

$z = \frac{V_{tan}}{V_{ax}} = \frac{\pi}{2y_{eff}}$

$f = \begin{cases} \frac{0.3164}{Re^{0.25}} & if \quad smooth \\ 0.0096+\sqrt{\frac{\xi}{D}}+\sqrt{\frac{2.88}{Re}} & if \quad rough \end{cases}$

$C_o = ln\left(\frac{6+2z_o^2+2\sqrt{3}\sqrt{z_o^4+3z_o^2+3}}{2\sqrt{3}+2\sqrt{3}z_o^2-2\sqrt{z_o^4+3z_o^2+3}}\right)$

z_o= the ratio of tangential to axial velocity at the exit of the swirl promoter

It is possible to numerically solve for "z" at each node after the exit of the twisted-tape. This value can then be used to find the effective twist ratio using Equation (4.3), assuming that the fluid behaves as a rigid disc, i.e. the fluid is rotating with the same angular velocity at every radial location.

$$z = \frac{\pi}{2y_{eff}} \tag{4.3}$$

Wu et al. [99] validated this model using data from Migay et al. [65]. The data for the hydraulically smooth pipe is shown in Figure 4-6. When this model was implemented for Migay et al. [65] rough tube cases presented in Wu's paper [99], there were large errors in the predictions as shown in Figure 4-7.

Since Migay et al. [65] used a glass tube for the smooth tube data, which is perfectly smooth, it is necessary to quantify smooth vs. rough for the use of this model in the IPWR design. By assuming that the Zircaloy cladding has a roughness of drawn tubing, i.e. 1.5e-6 meters [82], it has a non-dimensional roughness of $\sim 1.5e-4$. This is approximately an order of magnitude smoother than the data used by Wu et al. [99] in validation of the rough tube model. Furthermore, the VIPRE subchannel analysis code [17] has a default setting to use the smooth tube approximation for core analysis. Therefore, the smooth tube model should be valid for IPWR design application and the errors in the rough tube model can be neglected for this study.

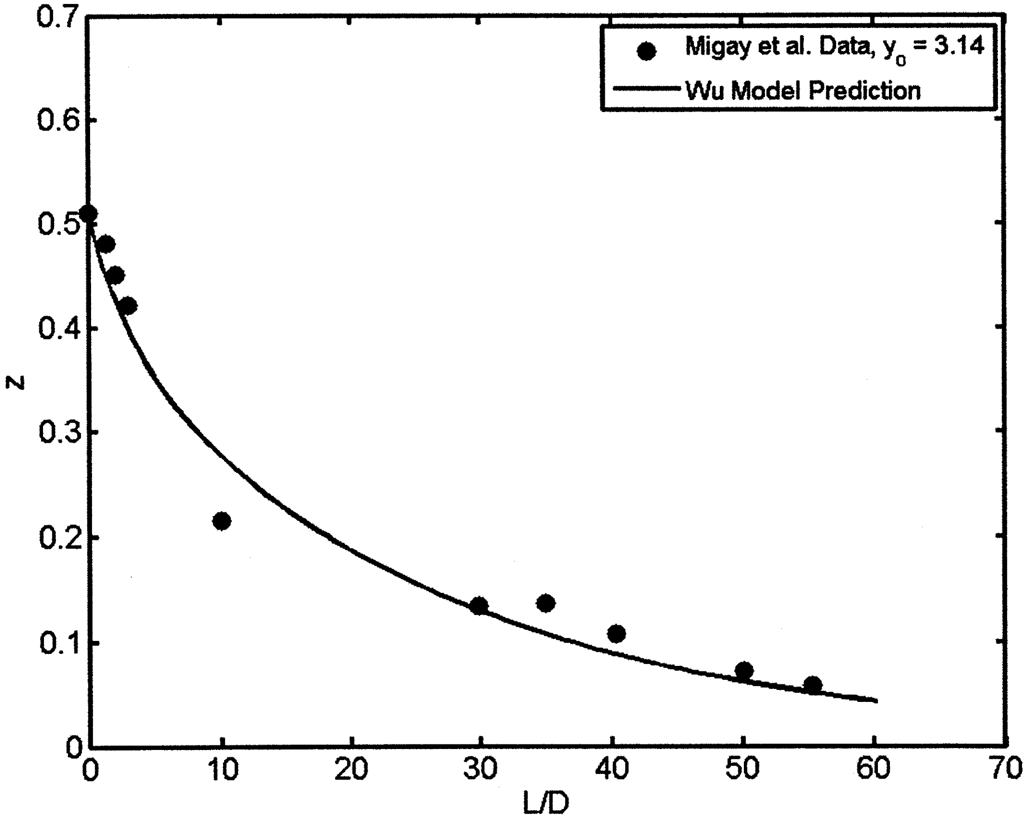

Figure 4-6: Wu Swirl Decay Model Compared to Smooth Tube Swirl Decay Data of Migay et al. [65]

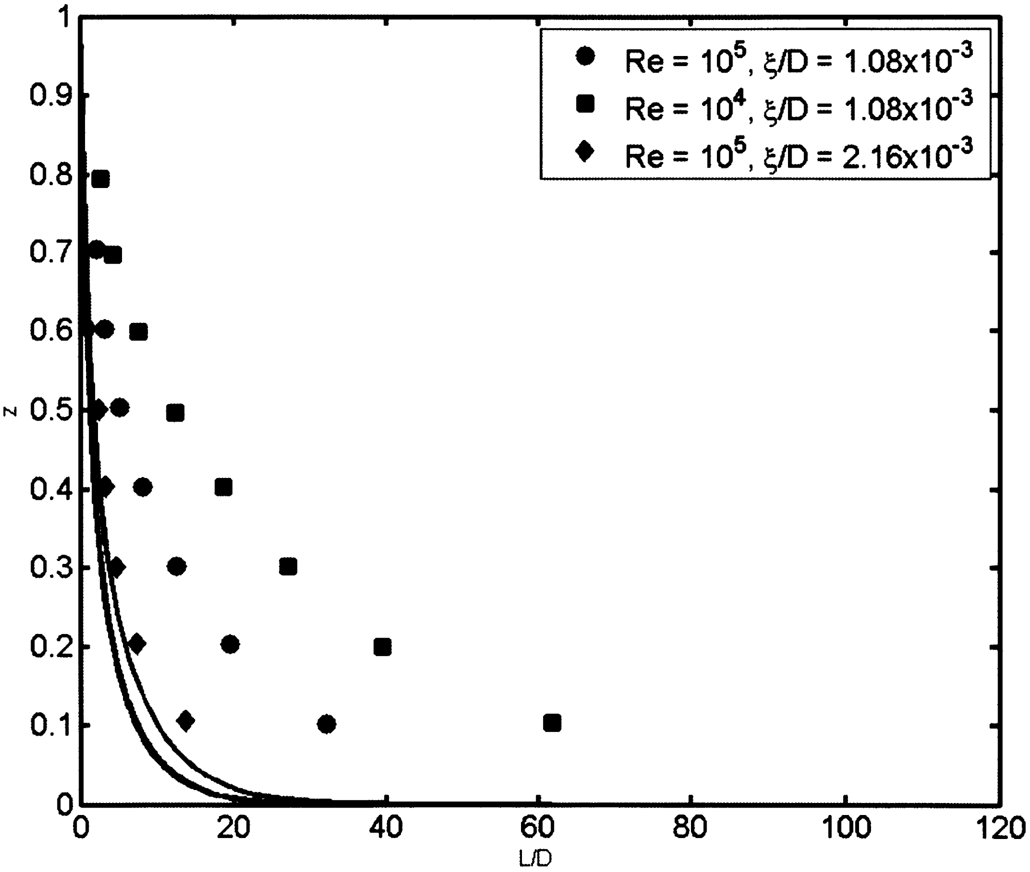

Figure 4-7: Wu Swirl Decay Model Compared to Rough Tube Swirl Decay Data of Migay et al. [65]

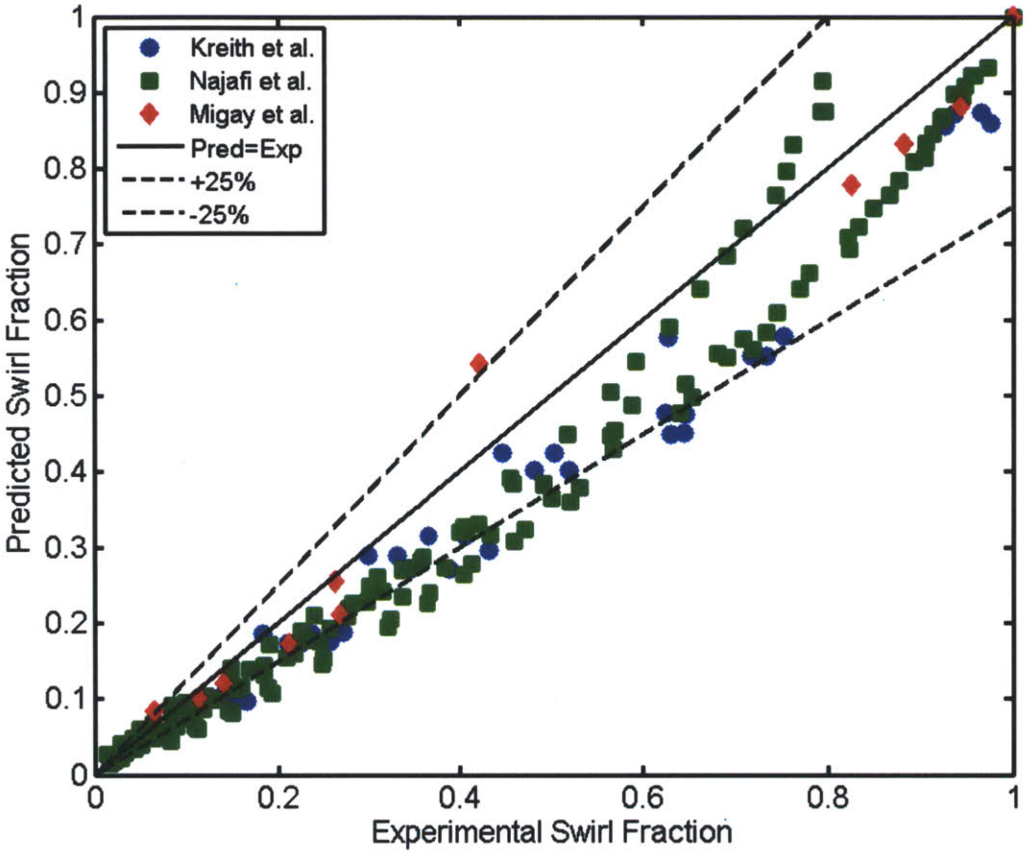

Figure 4-8: Validation of Wu et al. Swirl Decay Model

In order to more thoroughly validate this model, it was used to predict the data of Kreith et al. [56], Najafi et al. [69], and the remainder of the Migay et al. smooth tube data [65]. This swirl decay data can be found in Appendix A. The results of this validation are shown in Figure 4-8 where the metric compared is the swirl fraction which is defined in Equation (4.4).

$$S_f = \frac{z}{z_o} = \frac{y_o}{y_{eff}} \tag{4.4}$$

In general the model tends to under-predict the swirl fraction, making it conservative in CHF calculation. The performance of this swirl decay model is presented in Table 4.5 as the mean and standard deviation of the error (R). This method of calculating the effective twist ratio will also be used for the pressure drop correlation that will be presented in Section 5.3.

Table 4.5: Wu et al. [99] Swirl Decay Model Performance

Author	Ref	$\mu(R)$	$\sigma(R)$	No. Data
Wu et al.	[99]	0.9729	0.1670	11
Kreith et al.	[56]	0.7930	0.1031	34
Najafi et al.	[69]	0.8433	0.1697	144

4.2.3 Formulation of the Correlation

Since the relationship between the empty tube DNB and that of a tube with twisted-tapes could depend on all local variables of the flow, the expression that relates them should be a function of these local conditions. Explicitly, this expression should be a function of flow rate, pressure, quality, pipe diameter, and swirl intensity. Since the correlation is meant to be used for DNB, the heated length and inlet enthalpy is not needed for the formulation.

As shown in Table (4.2) at the beginning of this chapter, there were several formulations for FLTTs to choose from as the basis for the new correlation. Since the new DNB correlation is primarily focused on subcooled boiling, the expressions proposed by Jensen [44] and Kisina et al. [53] which were designed for saturated boiling conditions were disregarded. This only leaves the formulation proposed by Nariai et al. [71], shown in Equation (4.5).

$$\frac{q''_{cr,sw}}{q''_{cr,empty}} = \left(1 + 0.01\theta exp\left(-P^2\right)\right)^{1/6} \tag{4.5}$$

where,

$\theta = \frac{a_T}{g}$

$a_T = \frac{\pi^2 V_{ax}^2}{2y^2 D}$ = tangential acceleration

g = gravitational acceleration, 9.81 $\left[\frac{m}{s^2}\right]$

D = tube inner diameter [m]

V_{ax} = axial velocity of the coolant $\left[\frac{m}{s}\right]$

y = twist ratio

P = system pressure [MPa]

This formulation is convenient because it takes into account all of the parameters noted at the beginning of this section, but it also goes to the correct limit in the case of very large twist ratios, as illustrated previously in Figure 4-4. It should be noted that Equation (4.5) does not account for the flow area reduction due to the presence of the tape, and therefore it indicates that a tube with a non-twisted insert, i.e. y=∞, has the same CHF value as that of an empty tube. While this is not necessarily the case, an analysis of the data given in Nariai et al. [71] shows that the y=∞ data does not differ significantly from the prediction of the empty tube correlation that was used as the formulation basis, as shown previously in Section 3.2.2. In other words, the effect of the straight tape is smaller than the error bands of the correlation, and quite likely, the experimental error of the study.

Since the Equation (4.5) was derived for very low pressure data, it was necessary to reformulate the coefficients to include data from a wide range of pressures. The general form of the expression that was correlated to the data is shown in Equation (4.6), with the ratio of twisted-tape CHF to empty tube CHF denoted by gamma as it was in the Nariai et al. correlation [72]. The process of correlation will be discussed in the next section.

$$\gamma = \left(1 + C_1 \theta exp\left[C_2\left(\frac{\rho_f}{\rho_g}\right)\right]\right)^{C_3} \tag{4.6}$$

This expression can be directly tied to the mechanisms shown to cause CHF enhancement in the Usman-Weisman model. One of the main causes of increased CHF in the Usman-Weisman model was an increase in shear stress, both due to increasing flow velocity and decreasing twist ratio. This effect is taken in to account in the formulation of the θ term in this expression. The system pressure is also taken into account with the density ratio just as it is in the turbulent intensity term in the Usman-Weisman DNB model.

4.2.4 New Empirical DNB Correlation

The empty tube correlation used as the base for the new correlation is the Groeneveld LUT and the appropriate correction factors [30, 59, 80]. The correction factors shown below were taken from Todreas et al. [82] since some errors exist in open literature and these factors were confirmed to be correct in personal communications with Groeneveld. Correction factors, shown in Equation (4.7), are needed since the CHF values reported in the LUT are presented as a function of only mass flux, pressure, and quality for a uniformly heated tube of 8 mm in diameter, a series of correction factors need to be applied to the base CHF value, as shown in Equation (4.7). The Groeneveld LUT also has correction factors for rod bundles and mid-plane spacers; however, neither of these are relevant to this study since the flow is always internal.

$$q''_{cr,empty} = f\left(G, P, x_{eq}\right) K_D K_{L_b} K_{q''_{non,u}} \tag{4.7}$$

where,

$f\left(G, P, x_{eq}\right)$ =CHF from LUT, eventually interpolated, linearly, between the values of G, P and x_{eq}

$$K_D = diameter\ correction = \begin{cases} \left(\frac{D}{0.008}\right)^{-0.5} & if \quad 0.003 < D \leq 0.025\ m \\ 0.57 & if \qquad D > 0.025\ m \end{cases}$$

$$K_{L_b} = boiling\ length\ correction = \begin{cases} exp\left[\left(\frac{D}{L_h}\right) exp\left(2\alpha_{HEM}\right)\right] & if \qquad \left(\frac{L_h}{D}\right) \geq 5 \\ 1 & otherwise \end{cases}$$

$$K_{q''_{non,u}} = non - uniform\ heat\ flux\ correction = \begin{cases} 1 & if \qquad x_{eq} \leq 0 \\ \frac{q''(z)}{\overline{q''_{BLA}}} & otherwise \end{cases}$$

α_{HEM} =void fraction calculated using the homogeneous equilibrium model

$\overline{q''_{BLA}}$ =average heat flux from the onset of saturated boiling to the present location

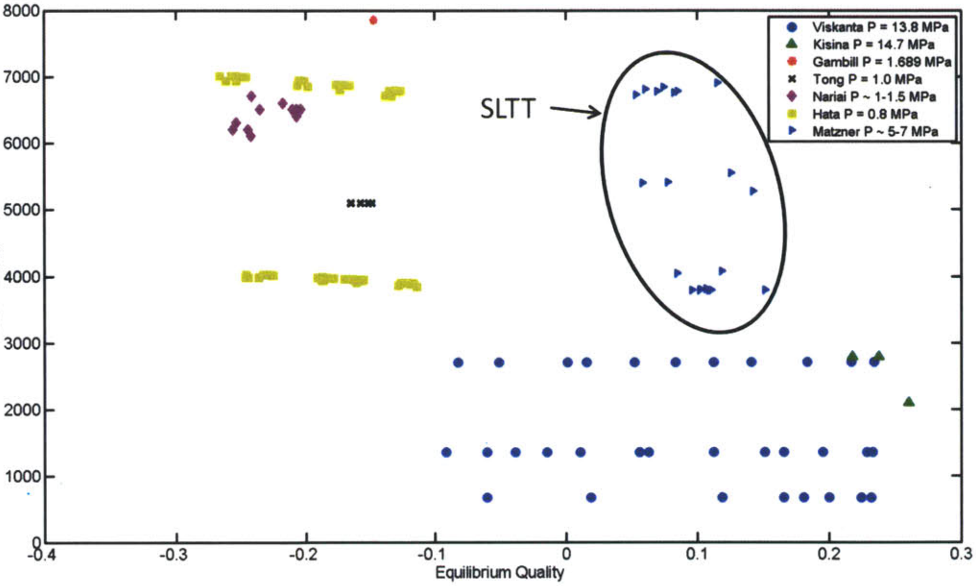

Figure 4-9: TTCHF Data Used for DNB Correlation Development

Using a least squares analysis approach, coefficients $C_1 - C_3$ of Equation (4.6) were fit to the data shown in Figure 4-9. This correlation was used to analyze the available twisted-tape CHF data that fell into both the operating parameters of the Usman-Weisman model and the Groeneveld LUT. While the Usman-Weisman model is only capable of accurate predictions for an average void of up to 64%, it was found that this correlation could accurately predict the data up to $\sim$ 70% void fraction. Because a higher cutoff for void fraction was achieved with the correlation as compared to the model, Figure 4-9 includes data points of SLTTs from Matzner et al. [64], as well as a few data from Kisina et al. [53].

The final form of the correlation is shown in Equation (4.8). The final operating range of this correlation is shown in Table 4.6. Clearly the range of operating conditions originally proposed in Table 4.1 were not met; however, this correlation covers a very large range of pressure, mass flux, quality, and effective twist ratio. It also has a non-uniform axial heat flux correction factor built-in, so the application of this correlation to the IPWR design case should be performed quite easily and accurately.

$$\frac{q''_{cr,sw}}{q''_{cr,st}} = \left(1 + 0.7\theta exp\left[-0.09\left(\frac{\rho_f}{\rho_g}\right)\right]\right)^{0.14} \tag{4.8}$$

where,

$\theta = \frac{\pi^2 V_{ax}^2}{2 g y_{eff}^2 D}$

g = gravitational acceleration, 9.81 $\left[\frac{m}{s^2}\right]$

$V_{ax} = \frac{G}{\rho_m}$

$\rho_m = \left(\frac{x}{\rho_g} + \frac{1-x}{\rho_l}\right)^{-1}$

Table 4.6: Operating Range of the New Twisted-Tape DNB Correlation

Parameter	**Units**	**Desired Range**	**Actual Theoretical Range**	**Data Range**$^+$
Mass Flux	$\frac{kg}{m^2-s}$	0 - 40,000	0 - 8,000	678 - 7845
Pressure	[MPa]	0.777 - 20.75	0.777 - 20.75	0.8 - 14.7
Quality	[-]	$x_{eq} = (-0.47) \rightarrow$ $\alpha_{HEM} = 0.64$	$x_{eq} = (-0.47) \rightarrow$ $\alpha_{HEM} = 0.70$	$x_{eq} = (-0.27) \rightarrow$ $\alpha_{HEM} = 0.696$
Heated Length	[m]	0.035 - 3.65	0.035 - 3.65	0.0595 - 2.438
Diameter	[cm]	0.115 - 3.75	0.115 - 3.75	0.44 - 1.151
Twist Ratio	[-]	all	all	1.93 - 445*

+Data set includes 113 FLTT data and 10 SLTT data

****Calculated effective twist ratio for SLTT data***

y_{eff} =effective twist ratio, i.e. if inside a SLTT use the twisted-tape y, if downstream a SLTT use y_{eff} as calculated by the Wu model [99]

The effective twist ratio is either the twist ratio of the SLTT if it is inside the twisted-tape, or the effective twist ratio calculated using the swirl decay model presented in Section 4.2.2 if in a decaying swirl region.

4.3 DNB Correlation Validation

The performance of the new correlation over the range of data shown in Table 4.6 for FLTTs is shown in Figure 4-11, while its performance for SLTTs is shown in Figure 4-12. The data that was used for this comparison is tabulated in Appendix A.

The comparison for both the FLTT and SLTT data was performed using a direct substitution method (DSM), instead of using the energy balance method (EBM) that was used with the Usman-Weisman model. In the DSM method, the local conditions at the tube outlet are used as inputs to the correlation. The EBM is an iterative technique where the inlet conditions are fixed and channel power is adjusted such that the operating heat flux causes DNB at the critical location. In the case of uniform heat flux this location is at the tube exit. These methods are shown in Figure 4-10 where q_m represents the CHF calculated by the DSM, EBM, and the measured value respectively moving from top to bottom on the figure.

One item to note in Figure 4-10 is that the error, calculated as shown in Equation (4.9), in the predicted value of CHF for the EBM is often lower due to the negative slope of CHF with increasing quality, therefore it is important to distinguish which method is used for the advertised error.

$$error = \frac{CHF_{predicted} - CHF_{measured}}{CHF_{measured}} \tag{4.9}$$

As seen in Table 4.7, the performance of the correlation has been shown to be satisfactory over a wide

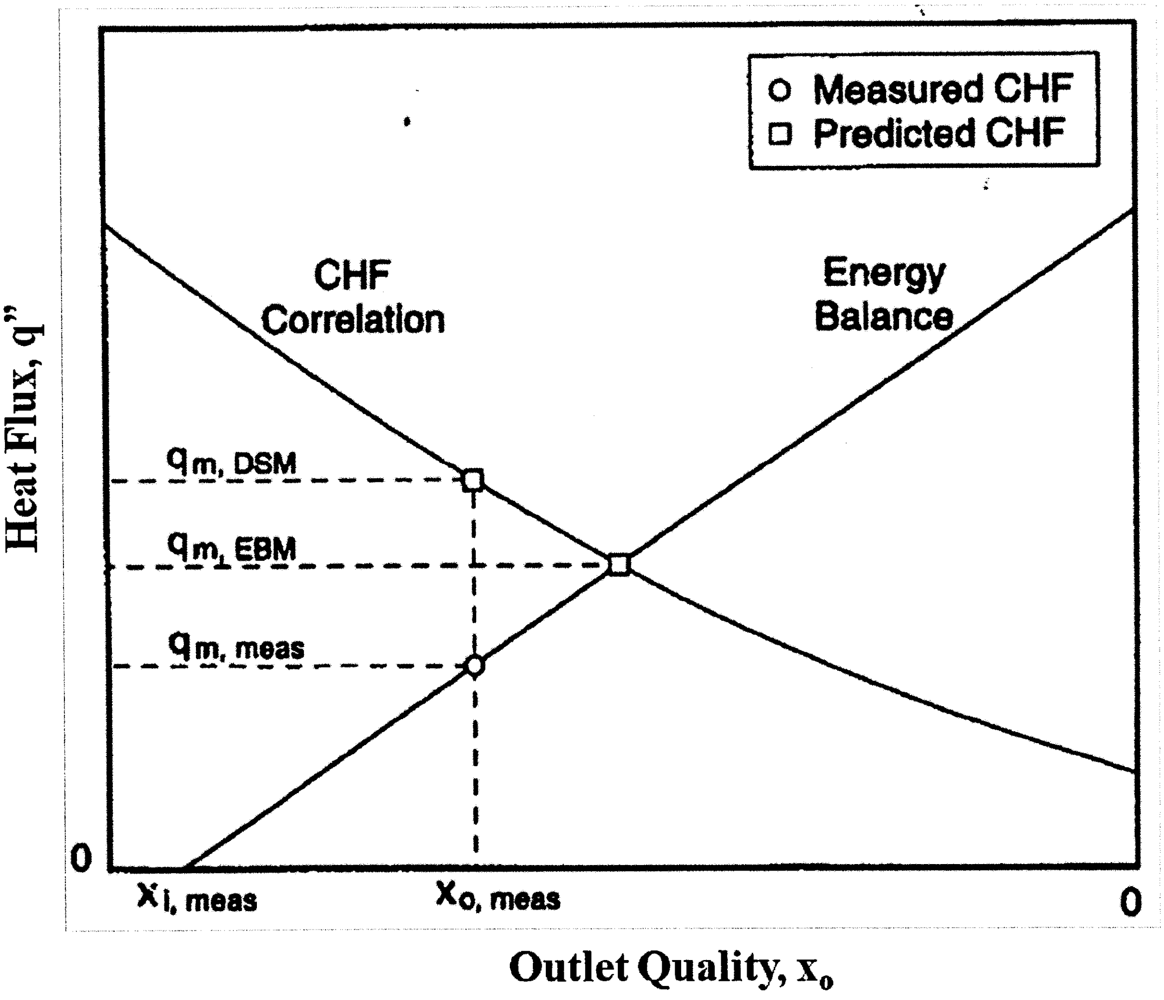

Figure 4-10: CHF Prediction and Error Evaluation Methods: Adapted from Hall et al. [31]

Table 4.7: Correlation Accuracy

Twisted-Tape Configuration	$\mu(R)$	$\sigma(R)$
SLTT	0.997	0.0614
FLTT	1.0221	0.1290

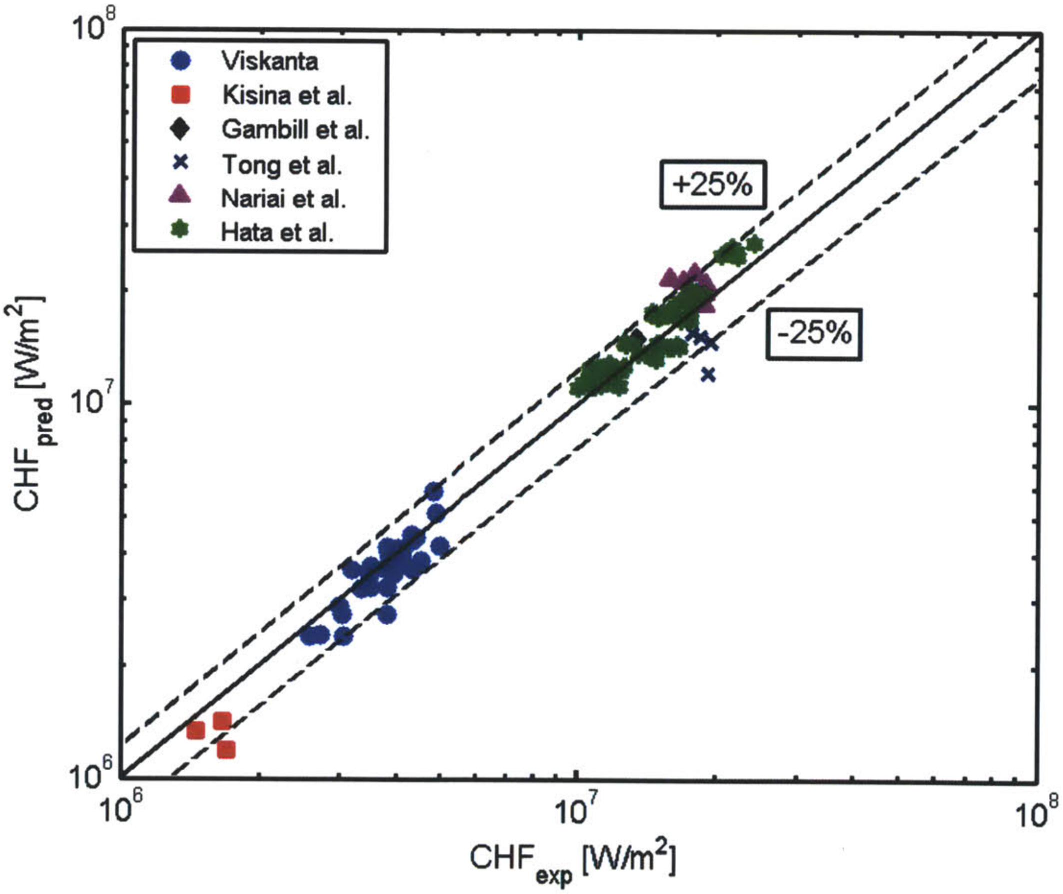

Figure 4-11: FLTT DNB Correlation Validation

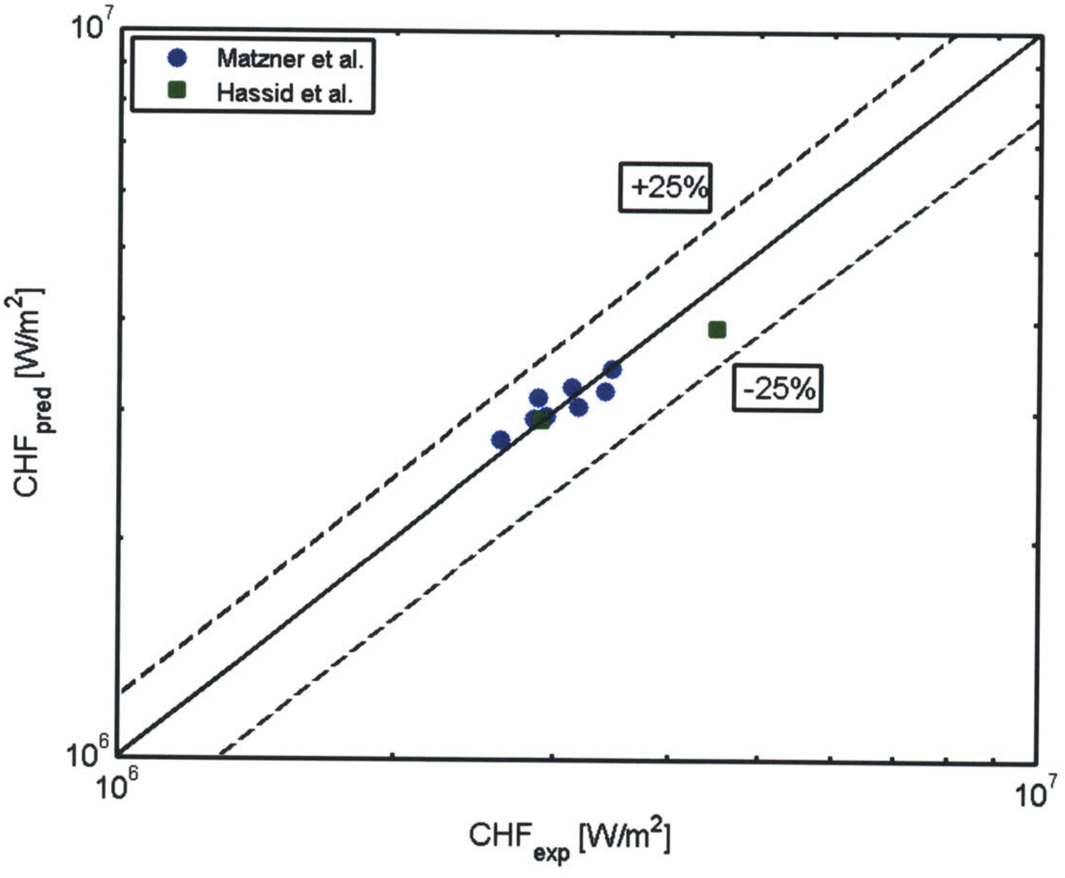

Figure 4-12: SLTT DNB Correlation Validation

range of operating conditions. The performance of the correlation is measured in the same fashion as was typical of the Usman-Weisman model using mean and standard deviation of the ratio of predicted to experimental values.

Although this correlation presents the possibility of using other empty tube CHF correlations as its base, it is not recommended that this be practiced since the correlation was derived specifically for the Groeneveld LUT.

4.4 Flow Regime Limitation on DNB Prediction

The upper bound of void fraction (and hence quality for an assumed slip of unity) of the new DNB correlation was set at first to match the upper bound suggested by the Weisman et al. DNB model for FLTTs [95], i.e. 64%; however, it was found upon comparison with the data that it was applicable up to a void fraction of approximately 70%. It is interesting to note that although this limit is different than the Usman-Weisman model's limit, it is not drastically so; therefore, in order to gain an understanding of why there is a breakdown in prediction method around the 64-81% void fraction range, the upper bound of the correlation and model was compared to the flow regime map of Hewitt et al. [38] as shown in Figure 4-13.

Three lines of varying void fraction and pressure were plotted as a function of mass flux ranging from 2700-8000 $\frac{kg}{m^2s}$. The line corresponding to $\alpha = 0.81$ is the upper bound of the Pei-Weisman axial flow model after it was modified to take into account the assumed increase in void fraction profile in the center of the tube as discussed in Section 2.2.4, while the other two lines correspond to the upper void fraction bound of the FLTT DNB model.

Two trends in CHF can be observed from examining this plot. In both cases changes in either void fraction for a given pressure or pressure for a given void fraction cause transition into the annular regime. First, the magnitude of CHF can be expected to decrease for increasing void at a fixed pressure since the liquid film thickness decreases and cannot support bubble agglomeration as will be discussed in Section 8.1.3. Second, for a fixed void fraction, a decrease in CHF can be expected for an increase in pressure since again a thinning of the liquid film occurs. These transitions toward annular flow are illustrated by the black dots on Figure (4-13) which show conditions all at a mass flux of 7000 $\frac{kg}{m^2s}$.

The reason that a DNB model is valid for the wispy-annular flow regime can be substantiated through the work of Collier et al. [16], who states that the liquid film in wispy-annular flow is relatively thick and contains small gas bubbles. It can be postulated that these statements indicate the thickness of the liquid film is large enough to support bubble agglomeration, and therefore DNB can occur. A more in-depth analysis of the flow regime map on CHF mechanism is outside the scope of this study; however, an interested reader can find more information on annular flow in the book by Hewitt [37].

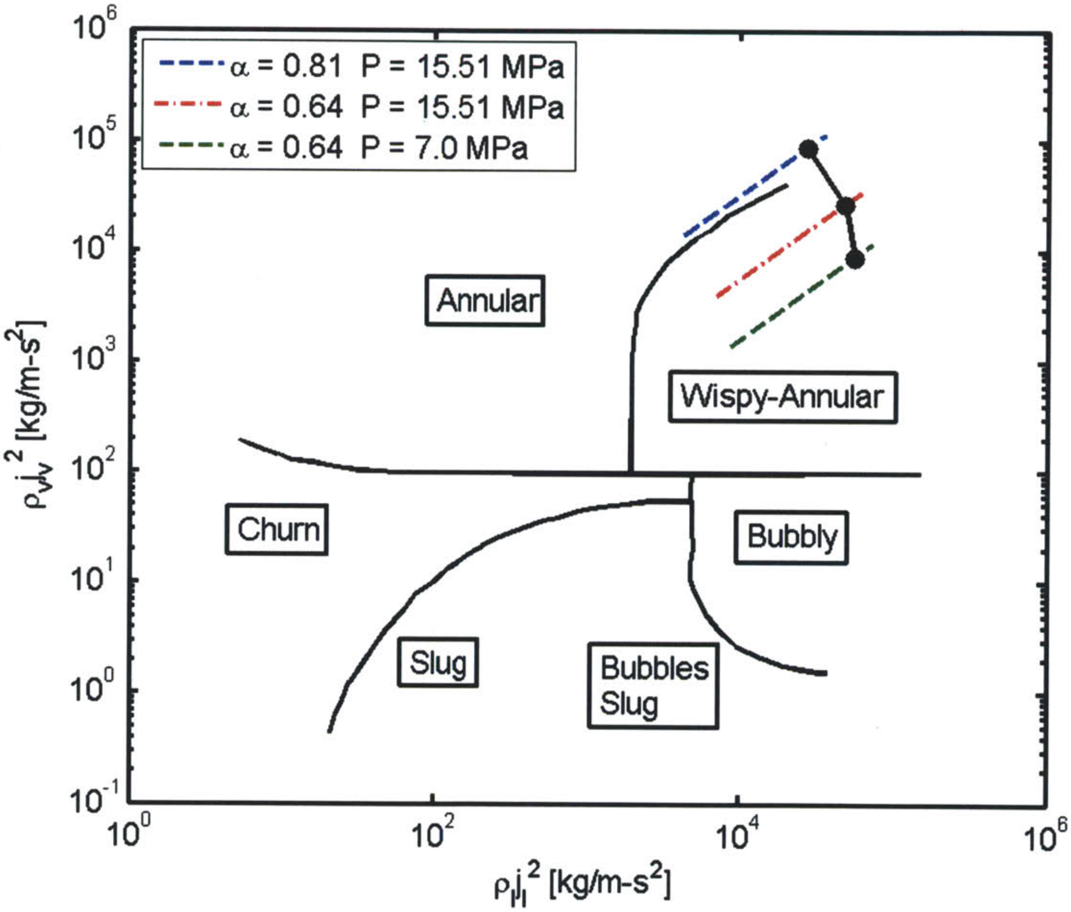

Figure 4-13: Relationship of the Upper Bound to the Flow Regime Map: Adapted from Hewitt et al. [38]

Chapter 5

Pressure Drop

The pressure drop of flow through a reactor coolant channel can be calculated as the sum of four components: gravity losses, acceleration losses, friction losses, and form losses. In the case of flow boiling, there are several thermodynamic regimes that must be considered: single-phase flow, subcooled boiling, and saturated boiling. Additionally, since the presence of twisted-tapes must be taken into account, there are four hydrodynamic conditions that must be considered: pure axial flow, developing swirl (entrance to a twisted tape), fully developed swirl (flow inside a tape after more than 1.5 revolutions), and decaying swirl (after the exit of a short-length twisted tape). This chapter presents the development of a technique to describe each of these phenomena in order to accurately describe the plot of pressure vs. axial height for a tube containing MSLTTs which was mentioned in Chapter 1, and is shown in Figure 5-1.

Because the correlation needs to take into account the local boiling and swirl conditions, the total pressure drop is most easily calculated numerically such that the pressure drop across a node of length dz is found by:

$$dP_{total,i} = P_{i-1} - P_i = (dP_{grav})_i + (dP_{acc})_i + (dP_{fric})_i + (dP_{form})_i \tag{5.1}$$

Note the sign convention for pressure drop, where a positive value indicates a loss in pressure. This is consistent with how pressure drop is normally presented. This chapter will discuss the calculation of each of these components in the order that they are listed in Equation (5.1). Then the chosen methodology is validated at the end of the chapter.

5.1 Gravity Pressure Drop

The gravity pressure drop for a given axial location is calculated the same regardless of boiling regime or swirl condition. It is defined by the following equation:

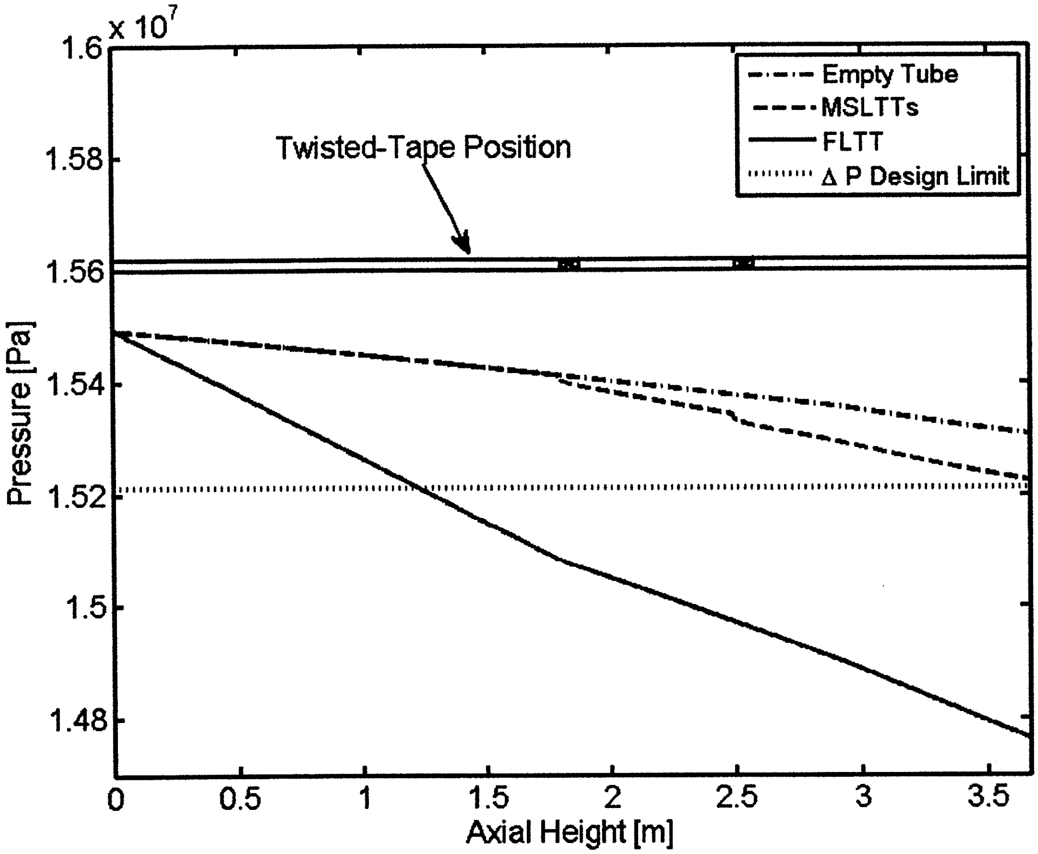

Figure 5-1: Pressure vs. Axial Height

$$(dP_{grav})_i = (\rho_m)_i \, g dz \tag{5.2}$$

where,

g = 9.81 m/s^2; acceleration due to gravity

$(\rho_m)_i = \frac{x_i}{\rho_g} + \frac{(1-x_i)}{(\rho_l)_i}$; mean coolant density

dz =node length [m]

The flow quality is calculated using the Levy profile-fit method [60] as shown in Equation (5.3), where $x_{eq}(z_D)$ is the equilibrium quality at the location of bubble departure.

$$x_i = x_{eq}(z_i) - x_{eq}(z_d) \, exp\left(\frac{x_{eq}(z_i)}{x_{eq}(z_D)} - 1\right) \tag{5.3}$$

5.2 Acceleration Pressure Drop

The pressure drop due to acceleration must take into account both flow area constrictions/expansions and changes in coolant density. Acceleration losses due to changes in flow area are only considered at the inlet and exit of the flow channel. Since the coolant density change across the length of a SLTT, i.e. on the order of a few centimeters, can be considered negligible, the acceleration of the flow at the inlet and exit of the twisted tape can be assumed to cancel out. The expression for acceleration pressure drop is given in Equation (5.4).

$$(dP_{acc})_i = \left(\frac{G_m^2}{\rho_m^+}\right)_i - \left(\frac{G_m^2}{\rho_m^+}\right)_{i-1} \tag{5.4}$$

where,

G_m =the mass flux of node i calculated as the mass flow rate divided by the actual flow area $\left[\frac{kg}{m^2-s}\right]$

$(\rho_m^+)_i = \left(\frac{x_i^2}{\{\rho_g \alpha_i\}} + \frac{(1-x_i)^2}{\{\rho_l(1-\alpha_i)\}}\right)^{-1}$; the dynamic density $\left[\frac{kg}{m^3}\right]$

It is important to note that for a flow entering a small channel from a large plenum, or vice versa, the flow velocity of the plenum can be considered negligible, therefore there is an acceleration pressure drop at the entrance and a pressure gain at the exit of such a channel as shown in Equation (5.5).

$$\begin{aligned} (dP_{acc})_{inlet} &= \left(\frac{G_m^2}{\rho_m^+}\right)_{i=1} - 0 \\ (dP_{acc})_{outlet} &= 0 - \left(\frac{G_m^2}{\rho_m^+}\right)_{i=N_{nodes}} \end{aligned} \tag{5.5}$$

5.3 Friction Pressure Drop

This section will describe the calculation of the friction pressure drop in the following order:

- Isothermal Friction Factor: Section 5.3.1
- Heat Transfer Coefficient: Section 5.3.2
- Wall Viscosity Correction Factor: Section 5.3.3

5.3.1 Isothermal Friction Factor

The friction pressure drop must be calculated differently according to the local heat transfer and swirl conditions. A previous method for dealing with the friction pressure loss was developed by Ferroni et al. [23, 24]; however, this method involves the piece-wise splicing of several pre-existing correlations. The method also involved a lumped parameter approach for dealing with MSLTTs, i.e. a swirl friction factor multiplier that was a function of twisted-tape spacing and the SLTT twist ratio was applied uniformly across a twisted-tape module regardless of fluid property variations. The twisted-tape module is defined as the section of tube including the SLTT its the swirl decay region. While the previous method was reasonably accurate for all swirl and boiling conditions, it does not distinguish the pressure drop contributions associated with the different regions of a twisted tape unit section, i.e. twisted tape entrance, taped region and swirl decay region. Therefore, a discrete method of friction factor calculation was developed in this study and has the following benefits:

- Uses one friction factor correlation for all swirl and boiling conditions, therefore it is continuous
- Allows discrete calculations for each node, accounting for fluid property variation
- Treats the form loss at the entrance to the twisted-tape separately, presented in Section 5.4
- Allows for any length of twisted-tape segment, provided that the twisted-tape goes through at least 1.5 360^0 revolutions
- Allows for any swirl decay length

A correlation for the friction factor of both single- and two-phase flow for tubes with FLTTs was recently published by Kanizawa et al. [47]. This correlation was validated for air, water, and refrigerant in horizontal and vertical flows, and has prediction accuracy of ±30% for 81.5% of all single- and two-phase swirl data, with 98% of the single-phase swirl data falling within this range.

The Kanizawa friction factor correlation extended the axial flow friction pressure drop correlation developed by Müller-Steinhagen et al. [68] to be applicable to tubes containing FLTTs. The original friction factor correlation involved a simple empirical interpolation of the liquid- and vapor-only Darcy friction factors to account for two-phase flows such that:

$$\left(\frac{dP_{fric}}{dz}\right)_{tp} = \beta\left(1-x\right)^{1/3} + Bx^3 \tag{5.6}$$

where,

$\beta = A + 2\left(B - A\right)x$

$A = \left(\frac{dP_{fric}}{dz}\right)_l = f_{lo}\frac{G^2}{2\rho_l D_e}$

$B = \left(\frac{dP_{fric}}{dz}\right)_v = f_{vo}\frac{G^2}{2\rho_v D_e}$

tp = two-phase

The liquid- and vapor-only friction factors were given by the piecewise expression shown in Equation (5.7), where "j" represents the appropriate phase. As noted below, the Reynolds number is calculated using the equivalent diameter. Therefore, for an empty tube this is the tube diameter, whereas for a tube with a twisted-tape insert, the reduction in equivalent diameter must be taken into account as shown below.

$$f_{jo} = \begin{cases} \frac{64}{Re_j} & if \quad Re_j \leq 1187 \\ \frac{0.316}{Re_j^{0.25}} & if \quad Re_j > 1187 \end{cases} \tag{5.7}$$

where,

Table 5.1: Friction Factor Calculation

Location	No Swirl (upstream of the first TT)	Swirl (FLTTs and MSLTTs)
$z_i \leq z_D$	Eq. 5.7	Eqs. 5.7, and 5.9-5.10
$z_i > z_D$	Eqs. 5.6-5.8	Eqs. 5.6-5.10

$Re_j = \frac{GD_e}{\mu_j}$

$$D_e = \begin{cases} D\frac{\pi}{\pi+2} & if\ TT\ present \\ D & if\ no\ TT \end{cases}$$

G = total mass flux using the empty tube flow area

In calculating the equivalent diameter, this correlation does not take into account the thickness of the twisted-tape. From the preceding equations, it is possible to calculate the two-phase friction factor as shown in Equation (5.8).

$$f_{tp} = \left(\frac{dP_{fric}}{dz}\right)_{tp,p} \frac{2\rho_m D_e}{G^2} \tag{5.8}$$

This friction factor can then be corrected for swirl by using the ratio developed by Kanizawa et al. [47] that is presented in Equation (5.9). Again, note that when calculating the empty tube friction factor for the denominator of this ratio, the twisted-tape equivalent diameter is used to find the Reynolds number.

$$\frac{f_{sw}}{f_{empty}} = \left(1 + 2y^{-0.4} Fr_h^{-0.1}\right)^{1.5} \tag{5.9}$$

where,

$Fr_h = \frac{G^2}{gD_e\rho_m^2}$

y = twist ratio $= \frac{Length\ for\ 180^\circ\ turn\ of\ twisted-tape}{Tube\ diameter}$

Note that the mean density is calculated the same way as it is presented in Section 5.1. By implementing Equations (5.6)-(5.9), it is possible to define the friction pressure drop for single- and two-phase flow in a tube with a FLTT as shown in Equation (5.10).

$$(dP_{fric})_i = (f_{sw})_i \frac{G^2 dz}{2(\rho_m)_i (D_e)_i} \tag{5.10}$$

In theory it is possible to extend this correlation to MSLTT situations by using the swirl decay model presented in Section 4.2.2 to derive an effective twist ratio. This effective twist ratio can be entered directly into Equation (5.9), i.e. replace y with y_{eff}, to obtain the friction factor ratio for a given nodal location.

The results of the correlation validation will be shown in Section 5.5; however, a summary of the friction factor formulation is shown in Table 5.1.

5.3.2 Heat Transfer Coefficient

For diabatic flow, it is necessary to correct the friction factors to account for the viscosity difference present at the tube wall compared to the average, or bulk, viscosity. This is due to the fact that viscosity depends on temperature. If the lower viscosity of the water at the tube wall were not taken into account, an over-prediction of pressure drop could occur.

In order to obtain the viscosity at the tube wall it is necessary to calculate the tube surface temperature by using heat transfer coefficients. Unlike the friction factor formula presented in the previous section, there is no single heat transfer coefficient correlation that covers all swirl and boiling conditions; therefore a piecewise treatment of the calculation is performed, as shown in Table 5.2. With the exception of the correlation for single-phase, no swirl flow, the heat transfer coefficient correlations chosen are the same as those selected in Ferroni [23], where details on the rationale behind the various choices can be found. For single-phase, no swirl flow, the Gnielinski heat transfer coefficient correlation was used because it accounts for not only the temperature gradient in the fluid, but can also account for the entrance region effect on heat transfer. The Gnielinski correlation is presented in Equations (5.11)-(5.12) for liquids with $0.05 < \frac{Pr}{Pr_w} < 20$.

$$Nu = \left[\frac{(f/8)(Re-1000)\,Pr}{1+12.7\sqrt{f/8}\,(Pr^{2/3}-1)}\right]\left[1+\left(\frac{D}{L}\right)^{2/3}\right]\left(\frac{Pr}{Pr_w}\right)^{0.11} \tag{5.11}$$

$$f = \frac{1}{(1.82 log_{10}(Re) - 1.64)^2} \tag{5.12}$$

where,

Pr = Prandtl number using properties evaluated at the bulk average temperature

Pr_w =Prandtl number using properties evaluated at the wall temperature

L = length measured from the entrance of the tube to the current location

Table 5.2 presents the authors of the correlations for each boiling and swirl condition and the reference tied to that correlation.

As will be discussed in the next section, the wall temperature is only important for pressure drop calculations in the single-phase heat transfer region. However, a complete presentation of the heat transfer correlation calculation methodology was given in this section because the wall temperature is needed for maximum fuel temperature calculation. In some cases, the fuel temperature can be a limiting parameter to the IPWR design due to hydrogen release.

5.3.3 Wall Viscosity Correction Factor

As mentioned in Section 5.3.2, the difference in fluid properties must be taken into account when calculating the diabatic friction factor. This correction is usually performed by the use of a simple viscosity ratio term,

Table 5.2: Heat Transfer Correlations

Boiling Condition	**Author(s)**	**Ref.**
Axial Flow		
Single-phase	Gnielinski	[29]
Subcooled Boiling	Collier and Thome (modified Chen)	[15]
Saturated Boiling	Chen	[14, 82]
Swirling Flow Inside a TT		
Single-phase	Manglik and Bergles	[63]
Subcooled Boiling	None Available, used Collier and Thome	[15]
Saturated Boiling	Jensen and Bensler	[45]
Swirling Flow in Decaying Swirl		
Single-phase	Modified Jensen and Bensler	[23, 45]
Subcooled Boiling	None Available, used Collier and Thome	[15]
Saturated Boiling	Modified Jensen and Bensler	[23, 45]

as shown in Equation (5.13).

$$V_{visc} = K\left(\frac{\mu_w}{\mu_b}\right)^{n\left(\frac{D_e}{D}\right)} \tag{5.13}$$

where,

K = 1

$D_e = \frac{4 \times A_{flow}}{P_{wetted}} = D\left(\frac{\pi}{\pi+2}\right)$

$n = \begin{cases} 0.28 & where\ TTs\ are\ not\ present \\ 0.35 & where\ TTs\ are\ present \end{cases}$

The value for the empty tube n-factor was developed by Leung et al. [59], while the twisted-tape value was proposed by Lopina and Bergles [61]. Lopina and Bergles also suggested that the diameter ratio for single-phase flow also be included in this correction factor since the viscosity of the fluid along the twisted-tape is equal to the bulk viscosity. Therefore, the twisted-tape surface does not reduce the viscosity of the fluid drastically; however, it does provide added perimeter to increase the overall shear stress acting on the fluid.

The viscosity correction factor is applied to the single-phase regime as shown in Equation (5.14). According to Ferroni [23], the viscosity correction factor should not be applied after boiling incipience due to the increased friction caused by the bubbles attached to the tube wall.

$$V_{visc} = \begin{cases} \left(\frac{\mu_w}{\mu_b}\right)^{0.28} & if \quad TTs\ are\ not\ present \\ \left(\frac{\mu_w}{\mu_b}\right)^{0.35\left(\frac{\pi}{\pi+2}\right)} & if \quad TTs\ are\ present \end{cases} \tag{5.14}$$

5.4 Form Pressure Drop

There are three form losses that need to be considered in the pressure drop calculation for the case of core pressure drop with MSLTTs. The first two form losses are entrance and exit losses caused by the rapid constriction and expansion of the flow at the inlet and exit of the core respectively [82]. The third form loss is caused by the build-up of swirl in the entrance region of a twisted-tape [27]. In general, form losses take the form shown in Equation (5.15). The addition of the two-phase multiplier to the form loss in the presence of boiling was suggested by the heat exchanger handbook written by Hewitt [35].

$$(dP_{form})_i = \begin{cases} K_i \frac{G^2}{2(\rho_l)_i} & if \quad z_i \leq z_{OSV} \\ K_i \frac{G^2}{2\rho_f} \left(\phi_{lo}^2\right)_i & if \quad z_i > z_{OSV} \end{cases} \tag{5.15}$$

Entrance and exit losses characterize all geometries regardless of whether twisted-tapes are present. The form loss coefficient "K" for abrupt changes in area is given in Equation (5.16), as suggested by Todreas and Kazimi [82].

$$K = \begin{cases} 0.5 & if \quad abrupt\ constriction \\ 1 & if \quad abrupt\ expansion \end{cases} \tag{5.16}$$

In the case of FLTTs or at the entrance of each SLTT, the form factor suggested by Gambill et al. [27] is applied. This factor accounts for the form loss due to swirl formation, and is given by Equation (5.17).

$$K_{TT} = \frac{1}{8}\left(\frac{\pi}{y}\right)^2 \left(\frac{0.25\pi D^2}{0.25\pi D^2 - t_{TT}D}\right)^2 \tag{5.17}$$

where,

t_{TT} =twisted tape thickness [m]

Since the Kanizawa et al. [47] correlation presented in Section 5.3 does not explicitly give a two-phase multiplier, one must be derived. The two-phase multiplier is defined as the ratio of the pressure drop gradients for two-phase flow and saturated single-phase flow as shown in Equation (5.18).

$$\phi_{lo}^2 = \frac{\left(\frac{dP}{dz}\right)_{tp}}{\left(\frac{dP}{dz}\right)_{lo}} \tag{5.18}$$

The numerator for this expression is given by Equation (5.6), and the denominator is given by the expression for "A" that is shown directly below Equation (5.6). "A" must be solved for using saturated liquid conditions. Substituting these two expressions into Equation (5.18), the two-phase multiplier for axial flow is shown in Equation (5.19).

$$\phi_{lo}^2 = \frac{\left(\beta\left(1-x\right)^{1/3} + Bx^3\right)}{A_{sat}} \tag{5.19}$$

Equation (5.19) can be used for the entrance of the first twisted-tape since there is no swirl at that location. However, since some swirl may exist from the previous twisted-tape, swirl must be taken into account for any subsequent twisted-tapes as shown in Equation (5.20).

$$\phi_{lo}^2 = \frac{\left(\beta\left(1-x\right)^{1/3} + Bx^3\right)}{A_{sat}} \frac{\left(\frac{f_{sw}}{f_{empty}}\right)_{tp}}{\left(\frac{f_{sw}}{f_{empty}}\right)_{lo}} \tag{5.20}$$

By entering the expression for the friction factor ratio, given by Equation (5.9), and using the local mean density to calculate the Froude number in the numerator, and saturated liquid conditions in the denominator, the final expression for the two-phase multiplier for the twisted-tape form loss is shown in Equation (5.21). The effective twist ratio is used here since the multiplier is calculated using local conditions in the entrance of the twisted-tape where only the swirl from a previous twisted tape exists, i.e. the swirl has not been developed by the current twisted-tape at this location.

$$\phi_{lo}^2 = \frac{\left(\beta\left(1-x\right)^{1/3} + Bx^3\right)}{A_{sat}} \frac{\left(1 + 2y_{eff}^{-0.4} Fr_h^{-0.1}\right)^{1.5}}{\left(1 + 2y_{eff}^{-0.4} Fr_{sat}^{-0.1}\right)^{1.5}} \tag{5.21}$$

5.5 Validation of Pressure Drop Correlation

The pressure drop calculation method was validated against four sets of experimental data. Of these sets, three came from the two-phase tests performed by Matzner et al. [64] on empty tubes and tubes provided with FLTT or MSLTTs, while the fourth set came from the adiabatic single-phase tests performed by Ferroni [24] on empty and MSLTT-provided tubes. Validation against Matzner experimental results is shown in Figure 5-2.

The new pressure drop calculation method was also tested against the original adiabatic single-phase pressure drop data of Ferroni et al. [24]. Before discussing the results of the validation for this data set, it is important to define how the friction factor was calculated in the Ferroni et al. study. The unit length for one twisted-tape section, or module, was defined as either the distance from the entrance of one twisted-tape to the entrance to the next twisted-tape, or equivalently as the distance from the mid-points of two subsequent twisted-tape sections. This length is defined explicitly as:

$$L_{mod} = L_{TT} + L_{decay} = 2yDN_{rev} + sD \tag{5.22}$$

where,

$N_{rev} = 1.5$; considering that Hassid et al. [33] determined that fully developed swirl is present after this many 360° rotations of the TT

s = swirl decay region length, expressed in tube inner diameters

The friction factor was thereby defined by Equation (5.23). This definition treated the form loss and

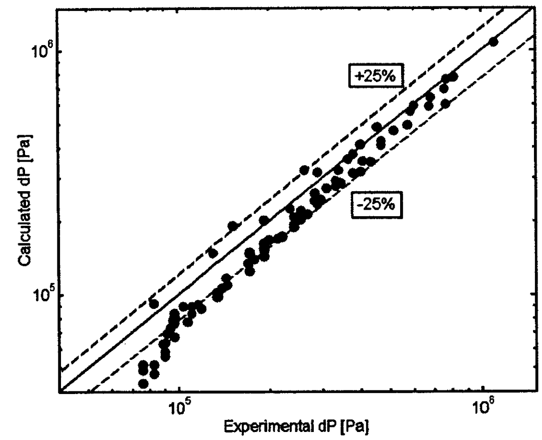

(a) Empty Tube Data

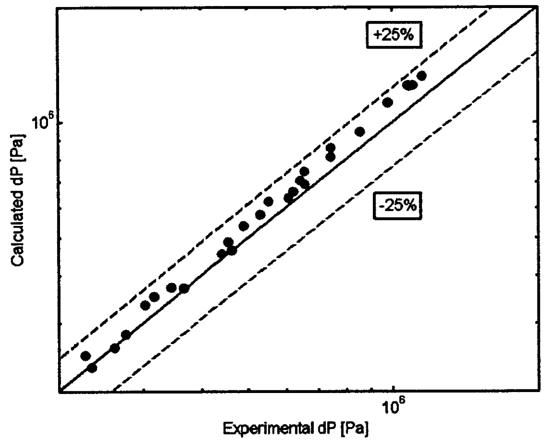

(b) FLTT Data

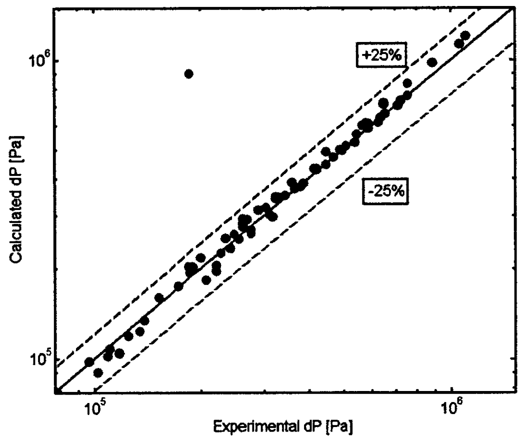

(c) MSLTT Data

Figure 5-2: Comparison of Correlation Predictions with Matzner et al. Experimental Pressure Drop Data [64] friction pressure drop as a lumped parameter.

$$f = \Delta P_{mod} \frac{D}{L_{mod}} \frac{2\rho_l}{G^2} \tag{5.23}$$

where,

D = tube inner diameter

G = mass flux using the empty tube area

The new friction pressure drop method presented in Section 5.3 and 5.4 was implemented over a theoretical test section that, in order to minimize the numerical errors associated with discrete calculations of pressure drop, consisted of two modules. In order to calculate the friction pressure drop, an effective twist ratio was calculated for the swirl decay region using the model developed in Section 4.2.2. The total pressure drop was calculated as shown below, where the form loss is multiplied by 2 to account for the number of twisted-tape modules:

$$\Delta P = 2K_{TT} \frac{G^2}{2(\rho_l)_i} + \sum_{i=1}^{N_{nodes}} (dP_{fric})_i$$

This pressure drop was then input as the ΔP_{mod} value in Equation (5.23), where $2L_{mod}$ was used for the length. The results of this comparison are shown in Figure 5-3. The correlation tends to slightly over-predict the experimental data; however, the accuracy tends to increase with increasing Reynolds number, decreasing tape spacing, and decreasing twist ratio.

The mean ratio and standard deviation of the error is presented in Table 5.3. Overall, the correlation does slightly over-predict the data, but the errors are within an acceptable range. The benefits of using this correlation as compared to the methodology that was proposed by Ferroni et al. [24] are the following:

- One friction factor correlation is used over all values of flow quality and swirl intensity
- Since the mechanism for friction factor has been confirmed with this model, it can be applied outside the experimental range of the data used to develop the Ferroni et al. correlation

Table 5.3: Statistical Evaluation of Pressure Drop Predictions

Data Description	No. Data Points	$\mu(R)$	$\sigma(R)$
Matzner et al. Empty Tube [64]	87	0.841	0.130
Matzner et al. FLTT [64]	27	1.068	0.063
Matzner et al. MSLTT[1] [64]	68	1.000	0.059
Ferroni et al. Empty Tube [24]	67	0.995	0.065
Ferroni et al. MSLTT [24]	201	1.273	0.130

1. These statistics exclude the one outlier data point

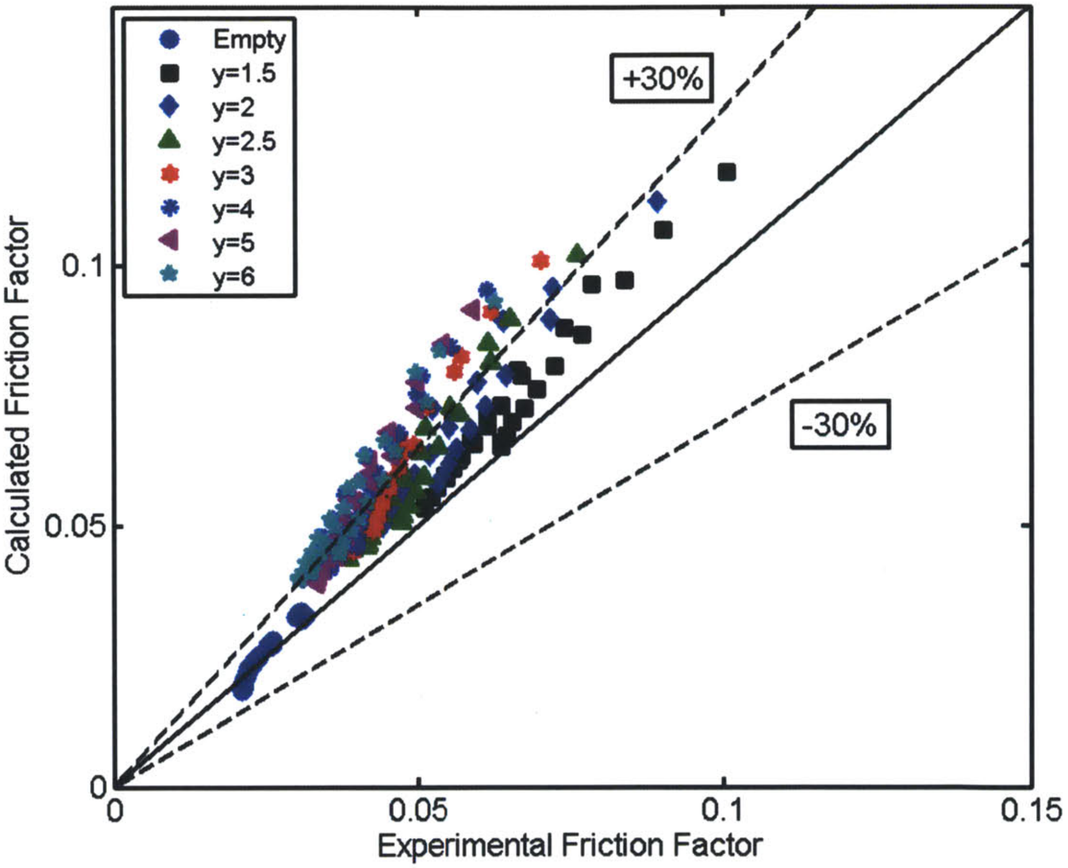

Figure 5-3: Comparison of Correlation Predictions with Ferroni et al. Experimental Pressure Drop Data [24]

Chapter 6

Design Insights

This section is a continuation of the optimization of the IPWR design first presented in the doctoral thesis by Ferroni [23]. The thermal hydraulic constraints originally developed in that study are listed in Table 6.1. These same limitations should be applied to the IPWR design in any future studies, along with some new constraint on effective twist ratio as discussed in Section 3.3.2. A full discussion of how these limits were set can be found in Ferroni [23], so that it is not provided here; however, it is worth mentioning that the three limits for core pressure drop refer to 1.0, 1.5, and 2.0 times core pressure drop of a typical four loop PWR.

The previous attempt at implementing SLTTs in the IPWR design performed by Ferroni et al. [23] concluded that a core with empty tubes actually performed better than one with tubes containing MSLTTs. That study consisted of examining an empty tube configuration (E-IPWR) and two twisted-tape configurations: a core with a twisted-tape spanning the upper half of the channel with a twist ratio of 2.5 (H-IPWR), and a core containing MSLTTs (S-IPWR). The MSLTT equipped core had twisted-tapes with a twist ratio of 1.5 that went through 1.5 360^o turns. The entrance of the last tape was exactly 50 diameters from the exit of the tube, then the other tapes were spaced 50 diameters apart with the number of tapes varying depending on diameter, such that the top 1.6 meters of the core were equipped with swirl promoters. All three of these configurations are shown in Figure 6-1. Note that note all of the MSLTT designs in Ferroni's study [23] had three SLTTs. Some cases had a higher number if the channel diameter was small.

The maximum power cases for the three design cases are presented in Table 6.2. These are the values for the fuel web thickness of 2 mm, even though it was determined that this geometry is difficult to manufacture and a case with a larger web thickness ($\sim 3mm$) was therefore considered. In each of the maximum power S-IPWR designs, there were three twisted-tapes in the upper half of the core.

Increasing the power of a reactor by using MSLTTs involves a tradeoff between the increased pressure drop due to each additional tape and the elevation in CHF provided by these twisted tapes. When a SLTT is added to a channel, the flow rate at which the pressure drop limit is reach decreases. If the increase in CHF due to the SLTT at this low flow rate does not exceed the CHF in an empty tube at the higher flow

Table 6.1: IPWR Steady-State Thermal Hydraulic and Swirl Intensity Constraints: Adapted from [23] and This Study

Parameter	Units	Range/Limit
From Ferroni [23]		
Pressure Drop Across Core	[kPa]	$1.0X = 150$ $1.5X = 225$ $2.0X = 300$
MDNBR	[-]	1.79
Steady-state Peak Fuel Temperature	$[^oC]$	650
Peak Clad Inner Temperature	$[^oC]$	370
Core Inlet Temperature	$[^oC]$	296.3
Coolant Enthalpy Rise	$\left[\frac{kJ}{kg}\right]$	195.2
Coolant Channel Diameter	[cm]	0.7 - 1.5
Fuel Web Thickness	[mm]	2.0 - 6.0
Active Core Height	[m]	3.67
From This Study		
Maximum Effective Twist Ratio	[-]	y_{cr}

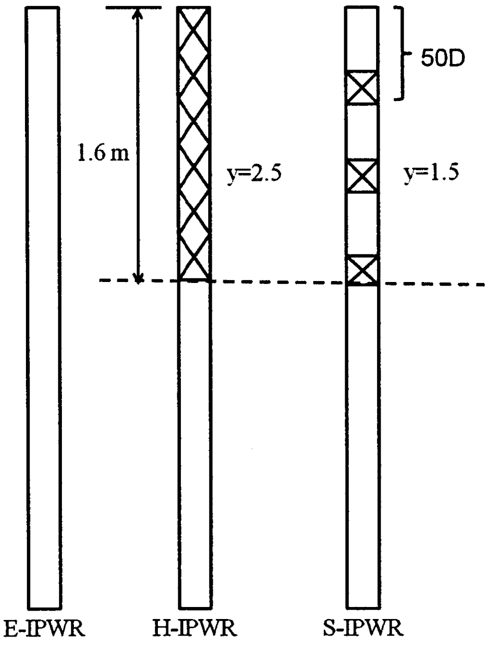

Figure 6-1: Twisted-Tape Configurations for the Previous IPWR Design Study (Not to Scale) [25]

Table 6.2: Maximum Achievable Power $[GW_{th}]$ of the IPWR in Ferroni et al. [23]

Core Pressure Drop Limit $[kPa]$	E-IPWR	H-IPWR	S-IPWR
150	3.703	2.992	3.250
225	4.328	3.672	3.906
300	5.047	4.188	4.391

Reference PWR Reactor had a Power of 3.411 GW_{th} [1]

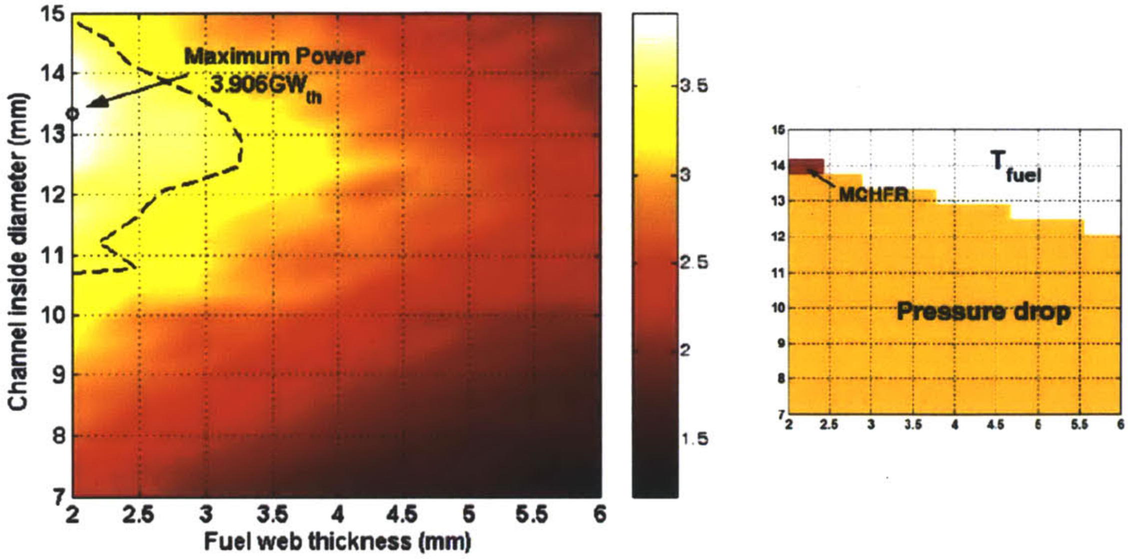

Figure 6-2: Power and Limiting Parameter Map for the S-IPWR 1.5X Pressure Drop Case: From [25]

rate, then there is no point in adding the swirl promoters.

The achievable power and limiting parameter maps developed by Ferroni et al. [23] for the 1.5X pressure drop S-IPWR is shown in Figure 6-2. There are two conclusions that can be taken from these maps. First, since the limiting factor is nearly always pressure drop, the number of twisted tapes used in the design should decrease. In Ferroni's maximum power cases there are always three SLTTs, therefore this number should be reduced to two. Second, since CHF is almost never a limiting factor, the twisted-tapes should be placed further apart. Therefore a methodology for placing these two SLTTs needs to be developed.

One of the major constraints of the Ferroni et al. study [23] was that the twisted-tape spacing was limited to a maximum spacing of 50 diameters due to the pressure drop calculation methodology that was being implemented [23]. Ferroni also uses swirl decay lengths, "s", of integral lengths, i.e. 30, 40, or 50, in order to be used with the pressure drop calculation methodology implemented in the design [23]. Therefore, with the new twisted-tape DNB correlation, pressure drop calculation methodology, and twisted-tape placement optimization, the power of the twisted-tape equipped core may be increased to a level at or above the E-IPWR maximum achievable power level.

Since the limitations of twisted-tape placement have been relaxed, the design space for this reactor is much broader; however, the following paragraphs will discuss ways to limit the design space to a more manageable size. The overall process can be described by the following five steps:

1. Determine the optimal twist ratio to use in each SLTT.

2. Determine the maximum mass flux as a function of channel diameter and number of twisted tapes.

3. Use the beginning of life (BOL) flux shape to determine the placement of the first twisted-tape.

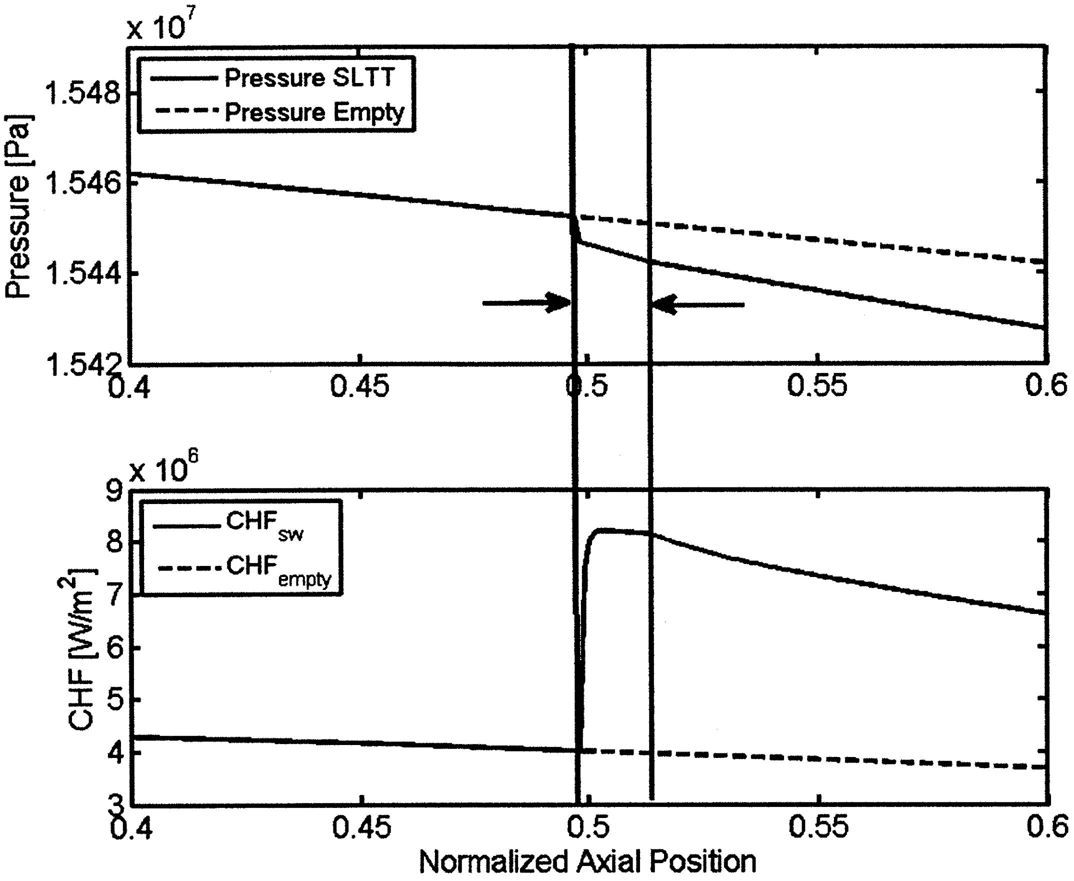

Figure 6-3: SLTT Pressure Drop vs. CHF Enhancement Length of Comparison

4. Use the end of life (EOL) flux shape to determine the placement of the second twisted-tape.

5. Evaluate whether a twisted-tape should be added or removed from the design.

6.1 Twist Ratio of the SLTTs

Previously the twist ratio had been set to a fixed value of 1.5. This was done to maximize the amount of swirl for a given twisted-tape while minimizing the amount of excess material in the core [23]; however, this might not be the optimal twist ratio for a SLTT due to the large pressure drop associated with small twist ratios. In order to characterize the best twist ratio for use in the IPWR design, a scoping comparison of the ratio of the pressure drop increase and the CHF enhancement was performed. The increased pressure drop and the increase in CHF within a single SLTT, i.e. the ratio of CHF and pressure drop for the empty tube and twisted-tape equipped region between the arrows in Figure 6-3 were compared.

The increased pressure drop consisted of the form pressure drop of Gambill et al. [27], originally shown in Equation (5.17), and the friction pressure drop as if the swirl was fully developed using the Kanizawa et al. correlation [47], as shown in Equations (5.7) - 5.10. The empty tube friction pressure drop was compared to the twisted-tape pressure drop shown in Equation (6.1) by using Equation (6.2). This expression simply represents the ratio of pressure drop for a twisted-tape equipped pipe over the length of the SLTT and the pressure drop over the same length of a tube with no twisted-tape.

$$dP_{TT} = dP_{TT,friction} + dP_{TT,form} \tag{6.1}$$

$$\epsilon_{\Delta P} = \frac{dP_{TT}}{dP_{empty}} \tag{6.2}$$

The CHF enhancement was calculated using the ratio of the swirl to axial flow CHF as developed for the new DNB correlation presented in Equation (4.8), and also shown below in Equation (6.3).

$$\gamma = \left(1 + 0.7\theta exp\left[-0.09\left(\frac{\rho_f}{\rho_g}\right)\right]\right)^{0.14} \tag{6.3}$$

The gain in CHF compared to the gain in pressure drop was compared via a non-dimensional metric as shown in Equation (6.4). For values greater than one, this metric indicates that there is a larger increase in CHF as compared to the increase in pressure drop over a given twisted-tape. In theory, the maximum value of this metric corresponds to the best value of twist ratio to use for IPWR design.

$$\epsilon = \frac{\left(\frac{CHF_{TT}}{CHF_{empty}}\right)}{\left(\frac{dP_{TT}}{dP_{empty}}\right)} = \frac{\gamma}{\epsilon_{\Delta P}} \tag{6.4}$$

The results of this study are shown in Figure 6-4 for a channel diameter of one centimeter, and all fluid properties are fixed and are taken as bulk values at the mid-point in the IPWR. Since this analysis does not take into account the swirl decay portion of the pressure drop and CHF enhancement the complete characterization of the channel performance is not represented by this calculation. However, there are a few important points that can be drawn from this figure:

- The rise in pressure drop increases dramatically as the twist ratio approaches 1.5
- This pressure drop gradient is flatter above a twist ratio of about 2
- Large gains in CHF can still be achieved at twist ratios larger than y=1.5 with smaller pressure drop penalties, indicating that a twist ratio larger than 1.5 should be used in the design strategy

In order to balance these results with the need to maintain swirl downstream of the twisted-tape, a moderate value of twist ratio should be chosen somewhere between y=2 and y=3.5. The value suggested from this analysis is y=2.5. This value maintains a large gain in CHF and provides enough swirl intensity

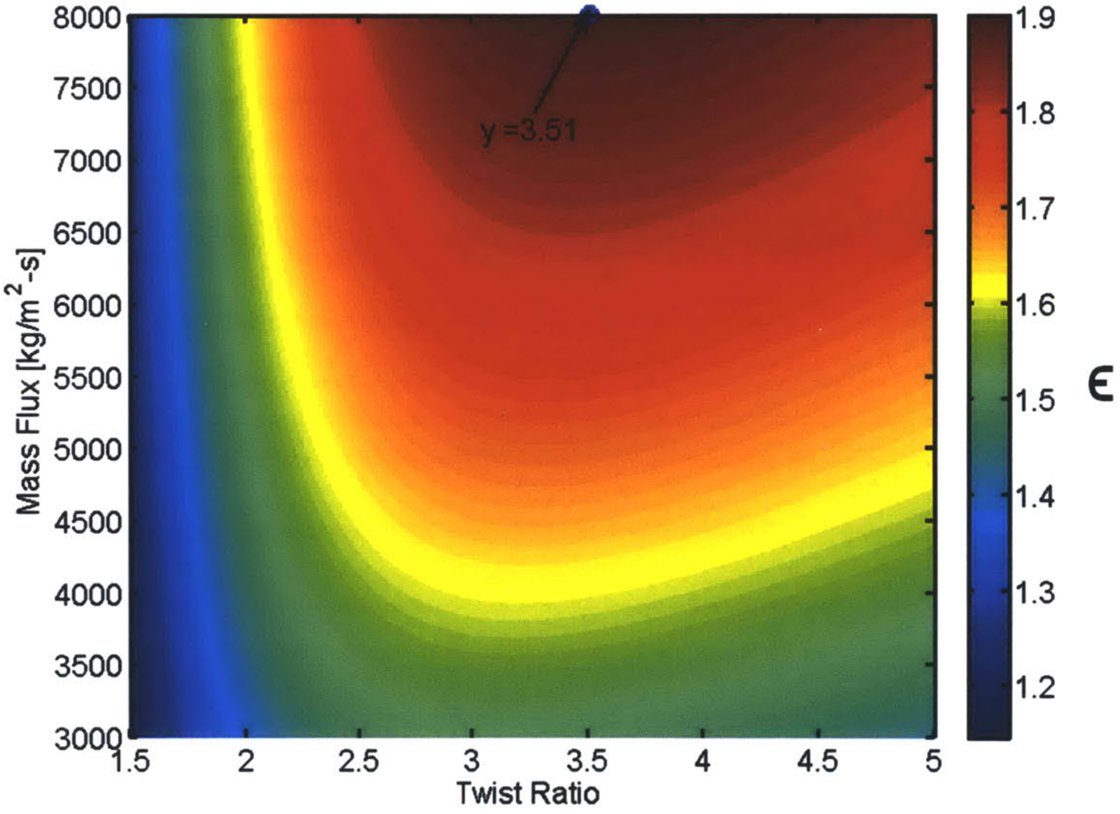

Figure 6-4: Optimal Twist Ratio for IPWR Design

to provide significant CHF enhancement downstream of the twisted-tape, while also reducing the pressure drop seen at a very low twist ratio, i.e. y=1.5.

6.2 Maximum Mass Flux

Since the flow quality in the IPWR is relatively small, the coolant density does not vary drastically. Therefore, the placement location of a fixed number of twisted-tapes in the channel has very little effect on the total channel pressure drop. This effect can be seen in Figure 6-5, where a single twisted-tape of twist ratio 1.5 undergoing 1.5 full turns was placed at various heights in a channel operating at typical IPWR conditions. The average pressure drop channel was taken as the mean pressure drop for all cases where the SLTT was in the top half of the core. It is clear from this figure that the channel pressure drop only varies by about ±8% depending on TT placement; however, it is important to notice that the channel pressure drop does decrease as the twisted-tape approaches the top of the core. This is due to the reduction in the amount of swirl in the channel, i.e. as the twisted-tape approaches the top of the core there is a larger axial flow region upstream of the twisted tape that experiences a lower pressure drop.

Because of this small variance in pressure drop with twisted-tape placement, it is possible to approximate the maximum achievable mass flux for an average channel for a given core pressure drop limit. This mass flux value is then used to find the optimal placement of the twisted-tapes. Since the twisted-tape placement has very little effect on pressure drop, this limit is much more convenient than trying to design using the MDNBR since the margin to DNB can change drastically based on twisted-tape location.

The maximum mass flux is found by performing a thermal hydraulic analysis on an average power channel. The average channel is used to approximate the core pressure drop because the IPWR core consists of thousands of parallel channels only connected at the plena. Because of this, the pressure drop across each channel must be equal. While the actual pressure drop will not necessarily be the pressure drop of the average channel, it is a reasonable approximation.

This analysis was performed on four channels of 0.7, 1.0, 1.3, and 1.5 cm in diameter with two SLTTs each having a twist ratio of 2.5 placed at 1.84 m and 2.75 m from the bottom of the core. This placement of the SLTTs was selected because these positions represent the mid-core height and the location halfway between the mid-core height and the top of the core. The average enthalpy rise through the tube was maintained at 195.2 kJ/kg and the mass flux was increased until the pressure drop limit was reached. The results of this analysis are shown in Figure 6-6 where the three horizontal lines represent the three pressure drop limits presented in Table 6.1. As expected, the maximum achievable mass flux increases with an increasing channel diameter. In order to simplify the discussion in the next two sub-sections, only the channel with a diameter of 1.5 cm will be discussed further because this case best illustrates the design methodology for two SLTTs.

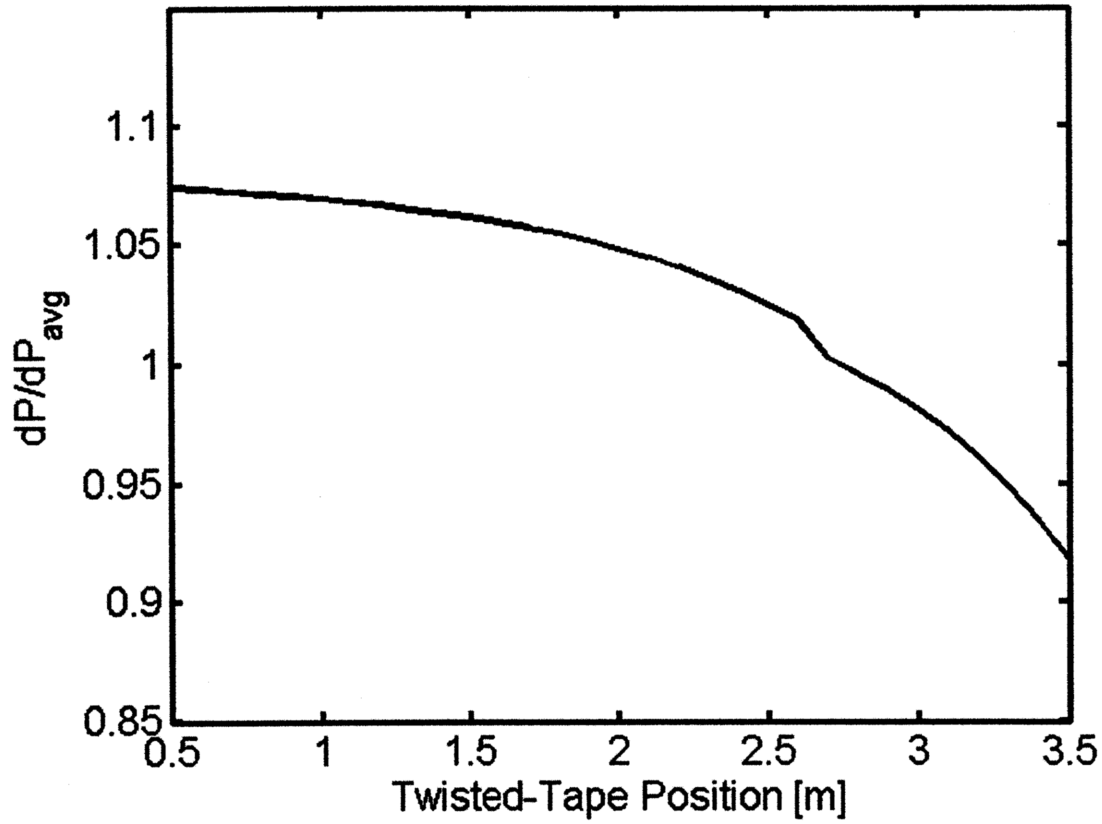

Figure 6-5: Channel Pressure Drop as a Function of Twisted-Tape Position as Measured from the Bottom of the Core

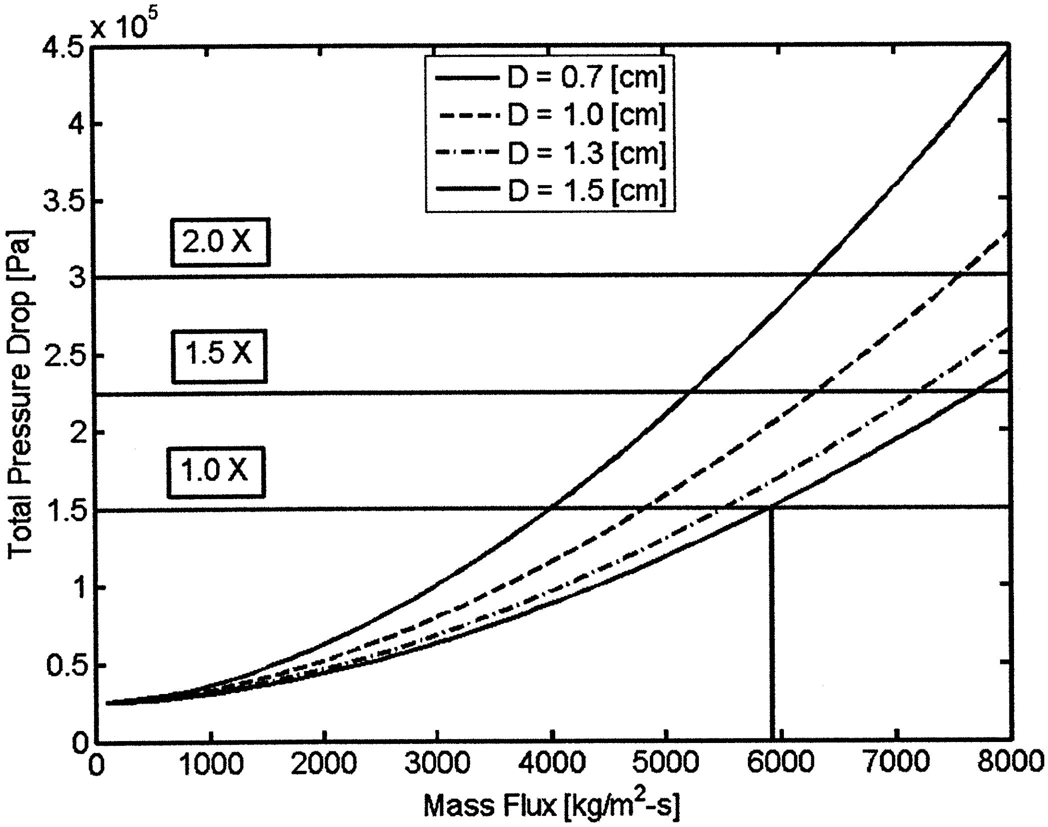

Figure 6-6: Limiting Mass Flux for Two Twisted-Tapes of y=2.5 and Varying Channel Diameter

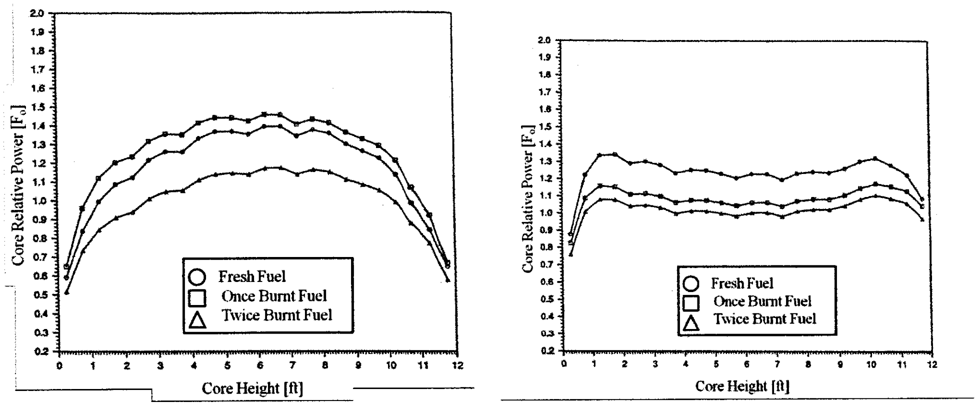

(a) BOL Heat Flux Profiles

(b) EOL Heat Flux Profiles

Figure 6-7: Axial Heat Flux Profile for the Seabrook PWR [1]

6.3 BOL Twisted-Tape Placement

Now that an approximate value of the limiting mass flux has been found to be equal to 5900 $\left[\frac{kg}{m^2-s}\right]$, it is possible to approximate the best location for the first twisted-tape in the channel. In order to optimize the placement of this twisted-tape, it is important to understand the evolution of the heat flux profile over time. In a freshly refueled core, the heat flux shape can be approximated by a chopped cosine with a large peak at the mid-plane of the core. In the case of the IPWR, this peak is equal to 1.515 times the average heat flux. As the cycle progresses, the heat flux tends to flatten due to more of the fissionable material being consumed in the areas of high power. This effect can is shown in Figure 6-7, where the normalized heat flux profiles of the Seabrook PWR are plotted at the beginning and end of the refueling cycle. The flattening of the heat flux profile shifts the point of MDNBR from around 2/3 the core height toward the channel exit. Therefore, the placement of the twisted-tapes needs to take into account this flux shape evolution.

The first twisted-tape can be placed by using the BOL heat flux profile and will deal with increasing the margin to DNB for a freshly refueled core. The hottest sub-channel has been used for this analysis, since this is the limiting case. The placement of this twisted-tape was determined by performing a channel analysis using the chopped-cosine heat flux profile and using one twisted-tape starting at the entrance of the channel then moving the swirl promoter down the length of the channel. In general, the MDNBR trace vs. twisted-tape placement has a peak as seen in Figure 6-8.

The reason for this peak in MDNBR is illustrated in Figure 6-9. This figure shows the DNBR trace for four cases, i.e. an empty tube and three cases with a SLTT at positions increasingly higher in the core. For the empty tube, the point of MDNBR falls around 60% of the way up the core. When a SLTT is placed low in the core, represented by the "A" curve in this figure, the point of MDNBR is shifted to a location higher in the core, but its magnitude is also increased. This increase in MDNBR can be seen as the initial rise in Figure 6-8, i.e. before the MDNBR peak. As the SLTT continues to move up the core, the point of MDNBR shifts to the inlet of the twisted-tape as shown by Curve B in Figure 6-9. This shift corresponds to the peak in the MDNBR plot in Figure 6-8. The MDNBR value continues to decrease as the SLTT is moved up the core until it is placed so high that the location and value of MDNBR returns to the original empty tube value as shown by Curve C in Figure 6-9.

In the case that the MDNBR limit is crossed twice, it is important to choose the crossing with the twisted-tape higher in the core as the design case. The first time the design limit is crossed, the location of MDNBR corresponds to the extreme end of the swirl decay region. Strictly in terms of the design constraints, the limit is met; however, the swirl intensity beyond this point is nearly zero. As the heat flux profile flattens, the margin decreases.

The second time the limit is reached, MDNBR is occurring at the entrance of the twisted-tape. This is desirable because the effect of swirl produced by this twisted-tape will extend further down the channel where DNB is more of a concern with no decrease in MDNBR. By using this technique, the margin to DNB is largest in the high heat flux area. According to Figure 6-8, the first twisted-tape should be place at 1.3 meters from the bottom of the core. Next, the heat flux at the end of the refueling cycle needs to be taken into account for the placement of the second twisted-tape.

6.4 EOL Twisted-Tape Placement

The second twisted tape can be placed near the end of the channel in order to protect against DNB at the end of the cycle, when the axial heat flux profile is nearly flat. The tape might not be able to be placed the end of the channel due to the need of maintaining the effective twist ratio upstream of this SLTT below the critical twist ratio as discussed in Section 3.3.2. If the effective twist ratio of the flow exceeds this value, any enhancement due to the twisted-tape should be neglected. A comparison of the effective twist ratio and the critical twist ratio are shown in Figure 6-10. These lines intersect at 3.5 m; therefore, the upper bound for the location of the second twisted-tape is set at this location. Note that this location is 0.17 meters from the top of the core, i.e. 3.67-3.5=0.17.

This analysis is performed using an axially uniform heat flux profile and moving a twisted-tape starting at the end of the channel and moving downward. Again, there are two points that the twisted-tapes could be placed at to meet the MDNBR limit as shown in Figure 6-11. The first time the MDNBR limit is met approximately corresponds to the upper bound of where the twisted-tape can be placed, i.e. $y_{eff} = y_{cr}$ (0.17 m from TOC). Therefore, because the critical twist ratio is nearly exceeded and because this location is very near the TOC, i.e. minimal benefit to the channel during BOL operations, the twisted-tape should be placed further down the core than where the MDNBR limit is first met. Besides this constraint, the placement of the second SLTT is not a clear-cut decision since placing the tape anywhere between about 0.3-1.95 meters from the top of the core would satisfy the EOL MDNBR limit.

Therefore it is best to choose the location of maximum MDNBR, in this case 2.87 meters from the bottom

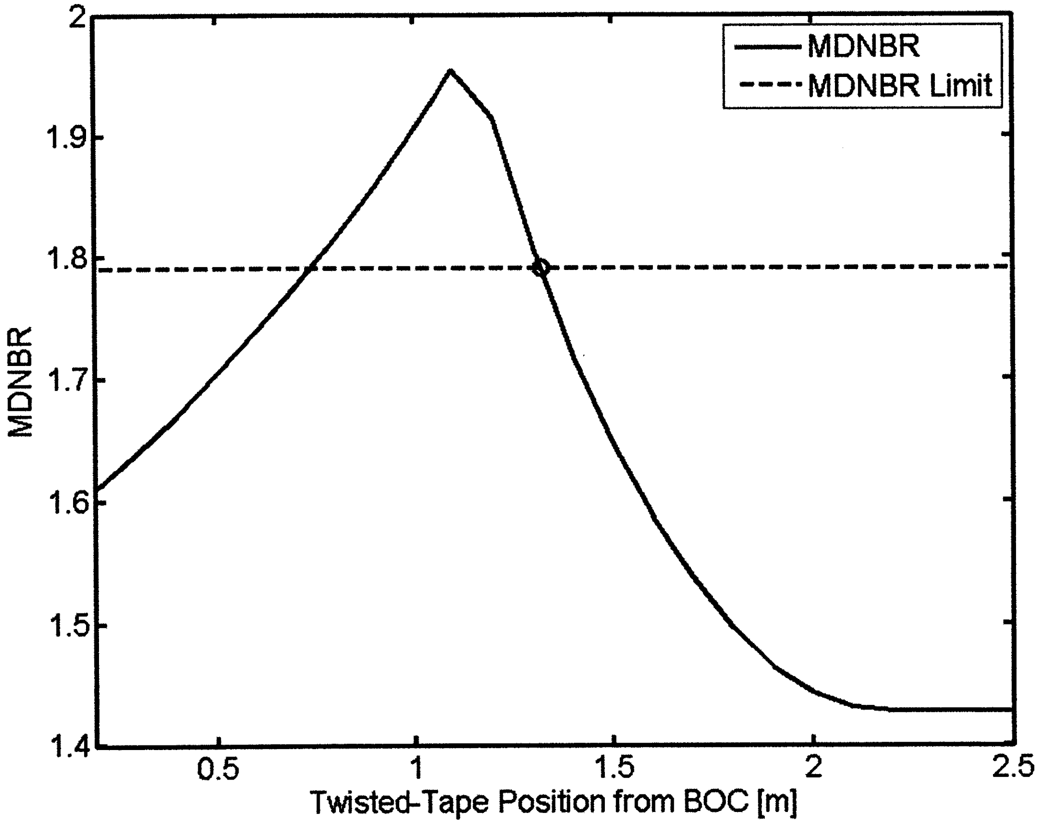

Figure 6-8: MDNBR as the First Twisted-Tape is Moved Up the Channel

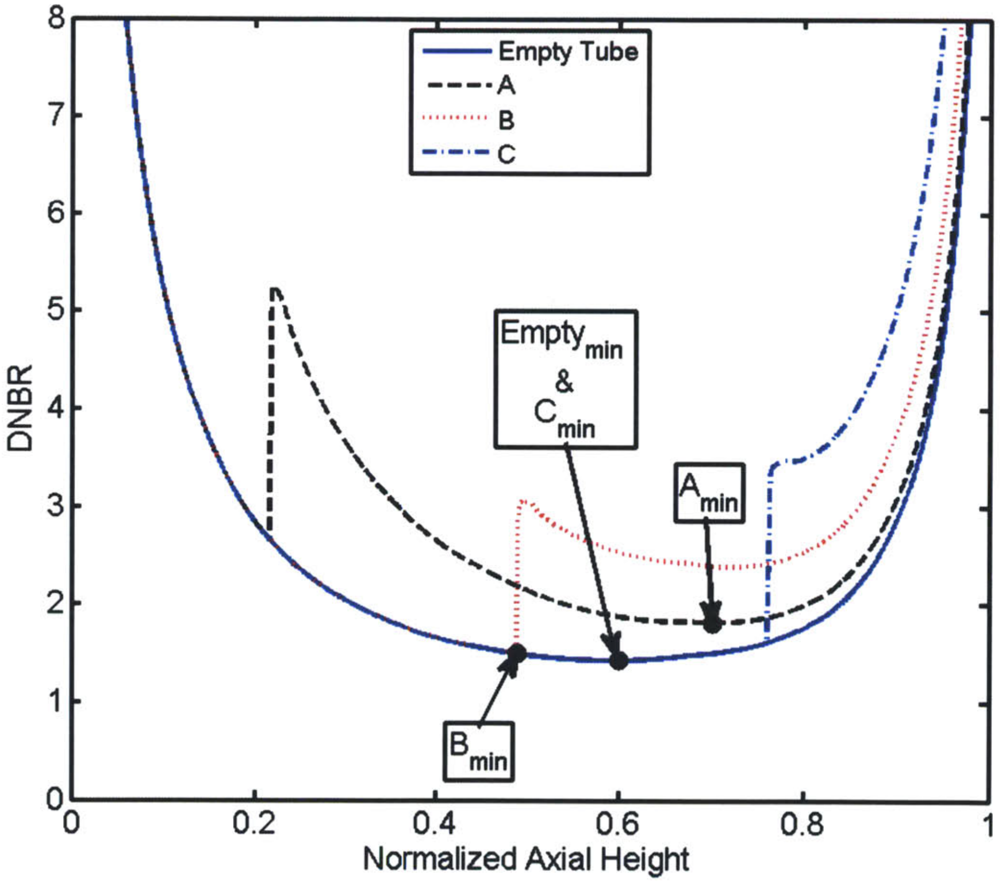

Figure 6-9: MDNBR Shift as Twisted-Tape is Moved Up the Core

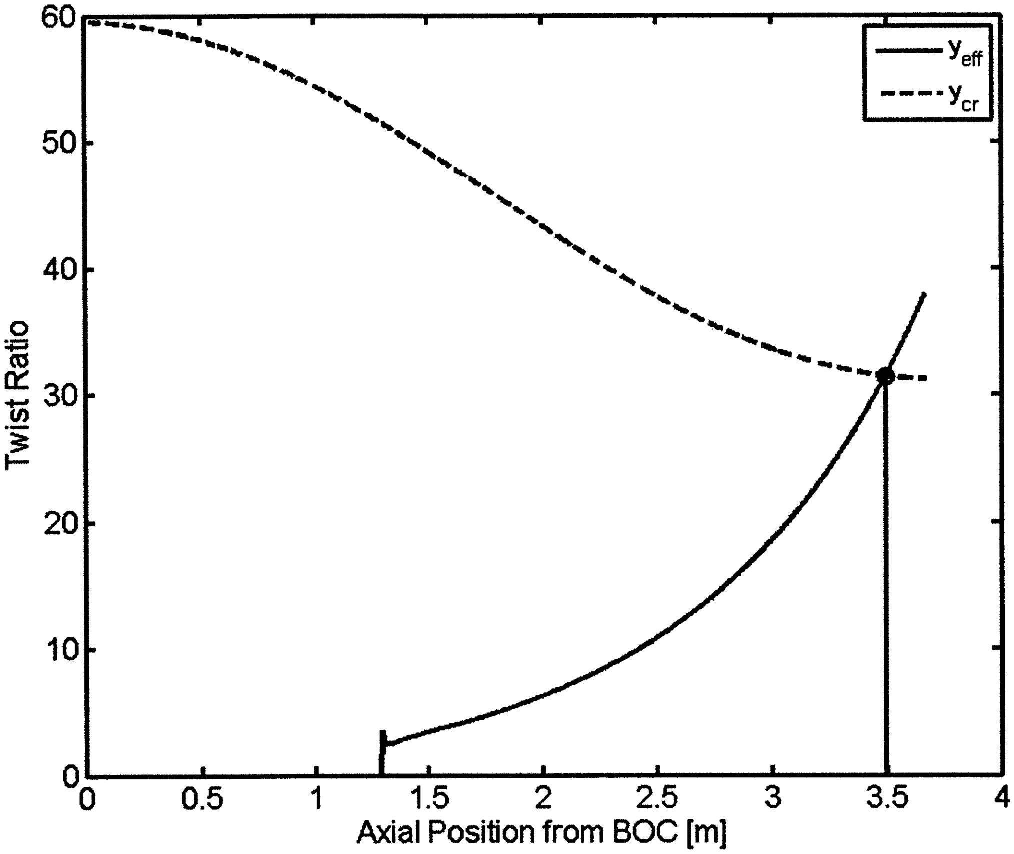

Figure 6-10: Finding the Upper Bound of the Second Twisted-Tape Placement Using y_{cr}

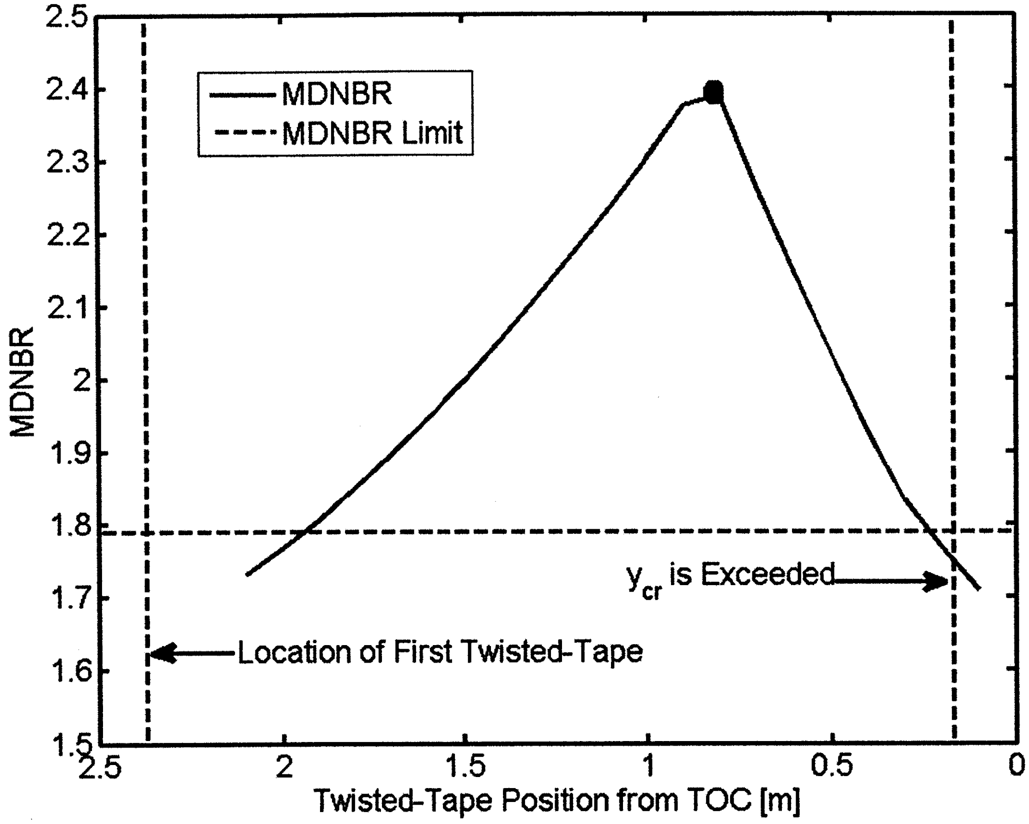

Figure 6-11: MDNBR as the Second Twisted-Tape is Moved Down the Channel

of the core, i.e. 0.8 meters from TOC. Since the actual heat flux profile at EOL is slightly peaked at the core exit, this placement will give more margin at the end of the channel while also being far enough up the channel to provide significant DNBR margin with the mid-life flux shape.

6.5 Adding or Removing a SLTT

When optimizing the placement of the twisted-tapes, there are some instances when it is necessary to add or remove a twisted-tape in order to maximize power. These cases are best described by examining Figure 6-12. This figure represents the MDNBR trace for the first twisted-tape placement, similar to Figure 6-8. For Case A, the DNBR is always below the MDNBR limit. This breach of the MDNBR limit indicates that the core does not meet the design specifications and is CHF limited. In this case there are two possible solutions. First, a twisted-tape can added to the design. By adding another SLTT, the pressure drop will increase and the limiting mass flux will be lower. Because the enthalpy rise across the core is fixed as indicated by the design criteria, a lower mass flux results in a lower total channel power and therefore a lower heat flux. By

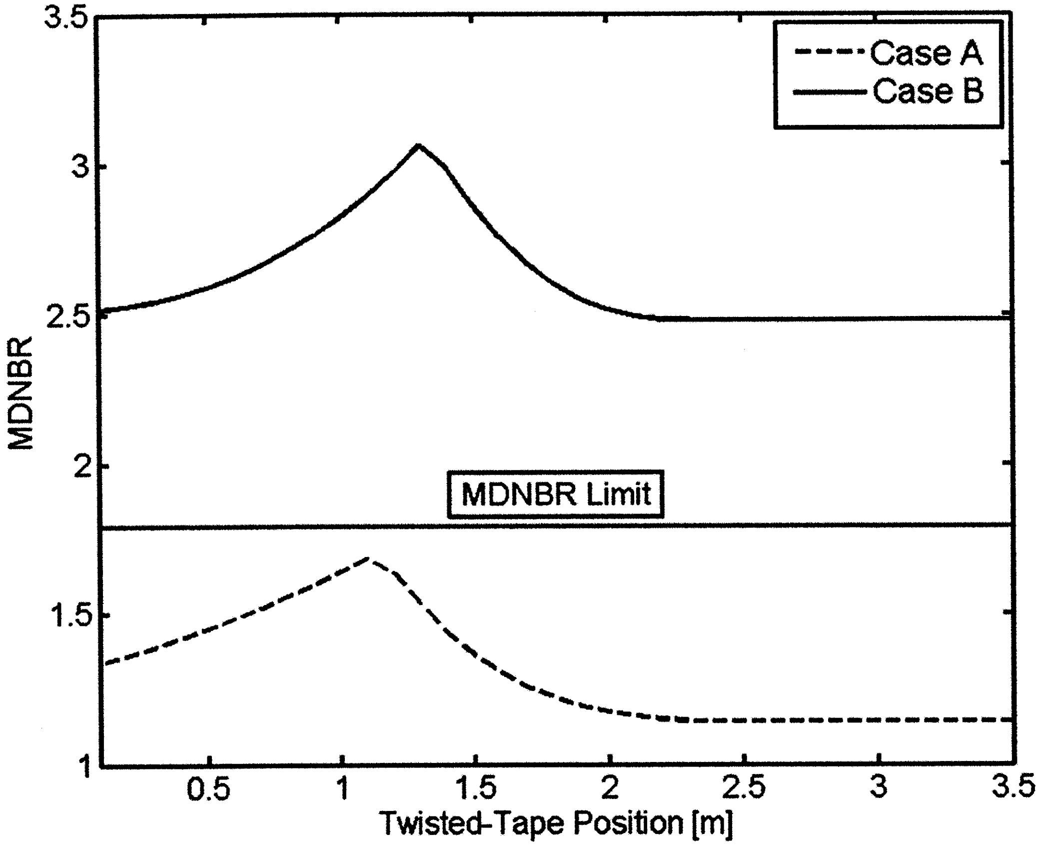

Figure 6-12: Cases when SLTTs should be added or removed

lowering the heat flux, the MDNBR limit can now be met.

The second possible solution is to decrease the twist ratio of the SLTTs while holding the number of SLTTs constant. This can be done as long as the twist ratio does not drop below y=1.5, since this is considered a lower bound for the manufacture of twisted-tapes. Below this value the tapes tend to buckle during manufacture as indicated by Ferroni [23].

Conversely, if the MDNBR trace never drops below the MDNBR limit as is the case with Case B, then a SLTT should either be removed, or the twist ratio increased for the opposite reasons presented in the previous case. Removing a twisted-tape or increasing its twist ratio will allow the limiting mass flux to increase, thereby increasing the heat flux and decreasing MDNBR.

Typically the number of SLTTs used will increase with increasing diameter due to the negative gradient of pressure drop and CHF with increasing diameter.

Chapter 7

Conclusions

This chapter summarizes the conclusions that were derived from this study in the following order:

- DNB Model Summary: Section 7.1
- DNB Correlation Summary: Section 7.2
- Pressure Drop Correlation Summary: Section 7.3
- Design Methodology Summary: Section 7.4

7.1 DNB Model Summary

The Pei-Weisman DNB model [73, 74], as modified by Usman [88, 95] was analyzed in Chapter 2 in an attempt to create a phenomenological model of DNB for tubes containing MSLTTs. Although this model had to be abandoned due to issues found with the derivation of the FLTT model, three insights were gained that were used to develop the new empirical DNB correlation:

1. There is a lower limit of swirl intensity that is expected to enhance CHF with respect to non-swirl flow. This lower bound was associated to a critical twist ratio, i.e. y_{cr}. This insight was used to set a design limitation recommending that SLTTs not be placed at distances greater than the length required for the effective twist ratio to exceed the critical twist ratio, i.e. $y_{cr} > y_{eff}$.
2. Shear stress is an important factor for DNB enhancement. The Usman-Weisman model indicates that CHF is enhanced with twisted-tape inserts due to the increased shear stress caused by the swirling flow. Therefore, it was concluded that an empirical correlation should include terms that increase CHF proportional to an increase in flow velocity and a decrease in twist ratio.
3. The operational bounds of the Usman-Weisman model were considered for the development of the empirical correlation. This insight helped to produce a simple correlation that encompasses as large a

range of operating conditions as could be described by one formulation.

7.2 DNB Correlation Summary

Drawing from the insights gained by working with the Usman-Weisman DNB model [95], a new empirical correlation was developed in Chapter 4, capable of predicting DNB for tubes containing MSLTTs at user-defined intervals. This correlation was developed by formulating an expression to describe the ratio of the twisted-tape DNB value as compared to an empty tube operating at the same conditions, as shown in Equation (4.8).

The Groeneveld LUT [30] was used as the reference empty tube correlation for the new MSLTT DNB correlation. The Wu swirl decay model [99] was used to calculate the local swirl intensity in regions of decaying swirl. This swirl intensity was expressed by means of an effective twist ratio, i.e. the twist ratio of a hypothetical FLTT with the same swirl intensity, which was used as an input to the correlation.

The new DNB correlation was validated over the range of data shown in Table 7.1. Its performance was satisfactory, predicting 95% of the 123 data points within ±25% for both FLTT and SLTT conditions. While other correlations are also accurate for the prediction of CHF in non-swirl conditions, their use in the correlation developed in this study is not recommended because the new correlation was developed specifically for the Groeneveld LUT. The data that was used to validate the new correlation can be found in Appendix A, along with all of the other experimental data that was gathered during the literature review.

Table 7.1: Bounds of the New Empirical DNB Correlation

Parameter	**Units**	**Theoretical Range**[1]	**Data Range**
Mass Flux	$\frac{kg}{m^2-s}$	0 - 8,000	678 - 7845
Pressure	[MPa]	0.777 - 20.75	0.8 - 14.7
Quality	[-]	$x_{eq} = (-0.47) \rightarrow \alpha_{HEM} = 0.70$	$x_{eq} = (-0.27) \rightarrow \alpha_{HEM} = 0.696$
Heated Length	[m]	0.035 - 3.65	0.0595 - 2.438
Diameter	[cm]	0.115 - 3.75	0.44 - 1.151
Twist Ratio	[-]	all	1.93 - 445[2]

1. The theoretical range refers to the bounds that this correlation is believed to valid under; however, the range that has been validated with data is listed in the "Data Range" column.
2. The twist ratio of 445 refers to the maximum effective twist ratio calculated for the SLTT CHF data.

7.3 Pressure Drop Correlation Summary

In an attempt to increase the flexibility of the IPWR design in terms of pressure drop characteristics, the Kanizawa FLTT friction pressure drop correlation [47], shown in Equations (5.6) - (5.10), was modified in

Chapter 5 to account for regions of decaying swirl by using the Wu swirl decay model [99], shown in Equations (4.2) and (4.3), to calculate a local swirl intensity. Form pressure losses were calculated using the form loss coefficient presented by Gambill et al. [27], as shown in Equation (5.17). A wall viscosity correction factor was applied to the friction pressure drop up to the point of boiling incipience, shown in Equation (5.13).

The modified friction factor correlation performed well over a wide range of single-phase adiabatic, and diabatic two-phase conditions. Data from Matzner et al. [64] and Ferroni et al. [24] were used to validate the modified correlation. Overall, the modified correlation predicted 73% of the 451 data points within ±25%, and 81% of the data within ±30%.

While the methodology for the friction pressure drop discussed above can be used, a sensitivity analysis shown in Appendix B revealed that removal of the viscosity correction factor and the two-phase multiplier for the twisted tape form loss coefficient resulted in negligible errors. Therefore, the friction pressure drop should be calculated using Equation (7.1) below.

$$dP_{fric} = \begin{cases} f_l \frac{dz}{D} \frac{G^2}{2\rho_l} & if\ z_i < z_D\ without\ swirl \\ f_{tp} \frac{dz}{D} \frac{G^2}{2\rho_m} & if\ z_i \geq z_D\ without\ swirl \\ f_l \frac{dz}{D} \frac{G^2}{2\rho_l} \left(1 + 2y_{eff}^{-0.4} Fr_h^{-0.1}\right)^{1.5} & if\ z_i < z_D\ with\ swirl \\ f_{tp} \frac{dz}{D} \frac{G^2}{2\rho_m} \left(1 + 2y_{eff}^{-0.4} Fr_h^{-0.1}\right)^{1.5} & if\ z_i \geq z_D\ with\ swirl \end{cases} \tag{7.1}$$

where,

dP_{fric} =friction pressure drop for node i

f_l =single-phase liquid friction factor, Equation (5.7)

dz = axial step size

G = mass flux calculated using the empty tube cross-sectional area

D = tube inner diameter

ρ_l =density of the liquid

f_{tp} =two-phase liquid friction factor, Equation (5.8)

ρ_m =mean two-phase density

y_{eff} = twist ratio of the SLTT if inside a twisted-tape, or the effective twist ratio calculated using the Wu swirl decay model [99] downstream a SLTT

$Fr_h = \frac{G^2}{gD_e\rho_m^2}$ =Froude number

g = gravitational acceleration, 9.81 $\frac{m}{s^2}$

Since the wall viscosity correction is not performed, there is no need to calculate the wall temperature, which greatly simplifies the process. Furthermore, Equation (7.2) can be used to calculate the form loss coefficient for each SLTT without accounting for the two-phase multiplier that was derived from the Kanizawa correlation [47].

Table 7.2: Maximum Achievable Power (GW_{th}) from Ferroni [23]

Core Pressure Drop Limit [kPa]	E-IPWR	H-IPWR	S-IPWR
150	3.703	2.992	3.250
225	4.328	3.672	3.906
300	5.047	4.188	4.391

$$K_{TT} = \frac{1}{8}\left(\frac{\pi}{y}\right)^2 \left(\frac{0.25\pi D^2}{0.25\pi D^2 - t_{TT}D}\right)^2 \tag{7.2}$$

where,

t_{TT} =thickness of the twisted-tape insert

D = tube inner diameter

y = twist ratio of the twisted-tape

The change in average error that resulted from removal of both the two-phase multiplier for the form loss coefficient and the viscosity correction term were less than 1%. Therefore, these terms can be disregarded for the range of data that was tested using this methodology, i.e. a single-phase length up to 2.6 meters for the viscosity correction factor and up to a flow quality of 30% for the two-phase multiplier.

7.4 Design Methodology Summary

With the flexibility of the new empirical DNB correlation and pressure drop calculation methodology, the design space for the IPWR using MSLTTs is vast. Therefore, in an attempt to make the task of optimizing its design more manageable, a methodology was developed in Chapter 6.

This design methodology involves a four step process where the designer first finds the approximate maximum mass flux for a channel with two twisted-tapes as a function of channel diameter. In step two, this mass flux is used as an input to the DNB correlation for the case of a channel with one SLTT placed such that the MDNBR limit is met at the SLTT inlet for a chopped cosine heat flux shape. This flux shape approximates the beginning of life heat flux profile. In step three, the mass flux is held constant while second SLTT is placed in the location that gives the channel the maximum MDNBR for a uniform heat flux profile. This heat flux profile represents the end of life profile. Finally, the number of SLTTs is appropriately adjusted considering two eventualities: if the DNBR is less than the design limit a SLTT needs to be added; or, the DNBR is greater than the design limit and therefore a SLTT can be removed.

In an attempt to illustrate the improvements that could be made using the flexibility of the new techniques, the S-IPWR maximum power for 225 kPa core pressure drop limit, shown in Table 7.2, was selected for modification.

In Ferroni's design case, each channel contained three SLTTs with a twist ratio of 1.5. By removing one of these SLTTs, increasing the twist ratio to 2.5, and optimizing the placement of these SLTTs, a new core power of 4.491 GW_{th} was achieved. The subchannel analysis code that was used to analyze this case is presented in Appendix D using this geometry as an example case. This is an improvement of 3.8% over the maximum power E-IPWR configuration and a 31.7% increase over the Seabrook PWR. Further optimization of the core design by investigating changes in design variables such as channel diameter and twist ratio likely should yield at least a nominal 5% improvement over the maximum power of the E-IPWR.

This design strategy attempts to minimize the number of SLTTs required to achieve maximum channel power, while also accounting for the flattening of the heat flux profile as the core approaches the end of its refueling cycle. While this design methodology is still complicated, it reduces the search space for the maximum power IPWR design by applying physically based heuristics for the placement and number of SLTTs. It is hoped that through the use of the new DNB correlation, pressure drop methodology, and SLTT placement strategy that an IPWR design utilizing MSLTTs will outperform the empty tube configuration proposed in Ferroni's study [23].

Chapter 8

Future Work

This chapter presents the suggested future work that would further the understanding of the boiling crisis phenomenon for tubes containing SLTTs and advance the design of the IPWR concept. The suggested future work is presented in the following order:

- Experimental Studies: Section 8.1
- Modeling Work: Section 8.2
- Design Work: Section 8.3

8.1 Experimental Studies

The DNB and pressure drop correlations developed in this thesis are based on available but significantly limited experimental data, particularly at IPWR operating conditions. Hence acquisition of test data at these operating conditions for channels with MSLTTs of geometries of design interest is of pressing need to validate the proposed correlations. Additionally this section covers the proposed experimental work that could be used to develop more accurate models or correlations to better describe DNB for tubes containing MSLTTs. The section is divided into three sub-sections that will be presented in the following order:

- Diabatic Pressure Drop and CHF for Tubes Containing Twisted-Tape Inserts: Section 8.1.1
- Two-Phase Swirl Decay for Better Characterization of y_{eff}: Section 8.1.2
- The Effect of Liquid Film Thickness on Boiling Crisis Mechanism: Section 8.1.3

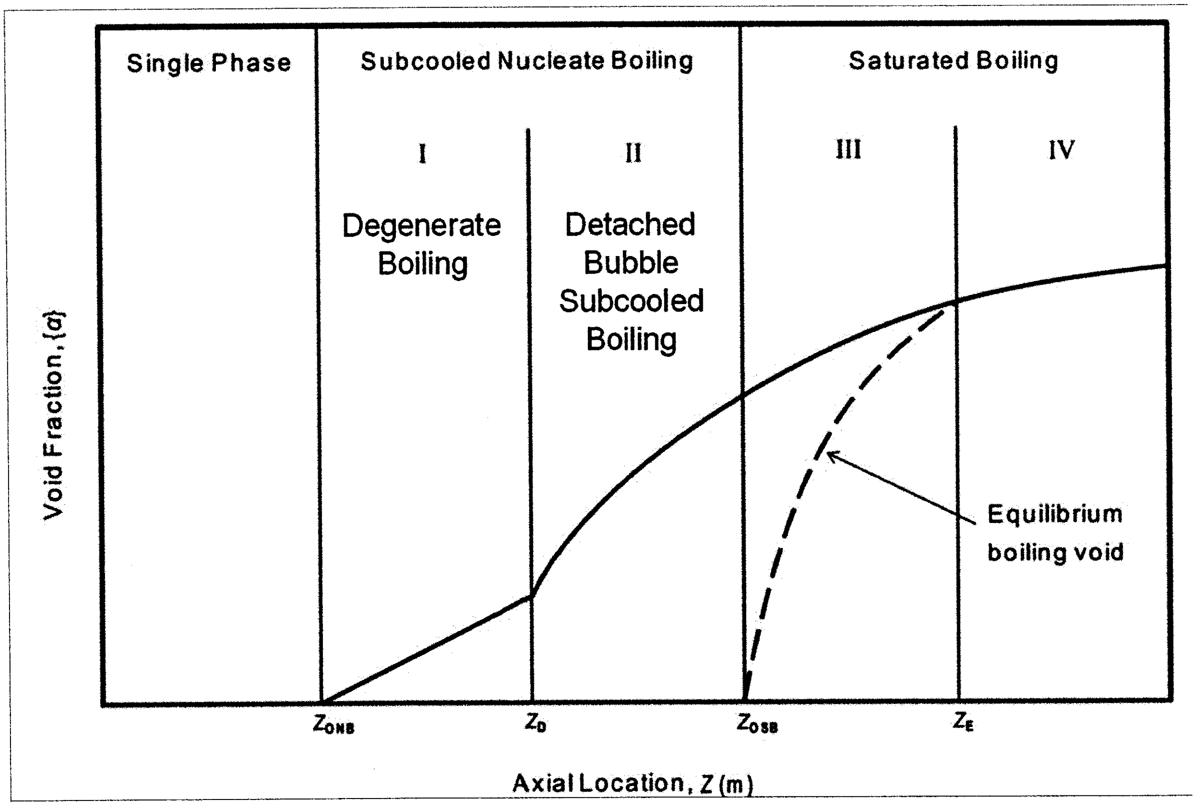

Figure 8-1: Subcooled Boiling Development: Taken from [82]

8.1.1 Diabatic Pressure Drop and CHF for Tubes Containing Twisted-Tape Inserts

There are two regions of subcooled nucleate boiling, the surface boiling region, and the detached bubble region as shown qualitatively in Figure 8-1. The surface boiling regime begins at boiling incipience, also known as the onset of nucleate boiling (ONB), i.e. z_{ONB}, and ends at bubble departure, i.e. z_D. The ONB location can be found through the use of an appropriate heat transfer coefficient correlation along with a boiling incipience wall superheat correlation such as those developed by Davis and Anderson [18], or Bergles and Rohsenow [9], which is shown in Equation (8.1). It should be noted that Equation (8.1) is a dimensional correlation only valid for

$$(q")_i = 15.6P^{1.156}\left(T_{wall} - T_{sat}\right)_i^{2.3/P^{0.0234}} \tag{8.1}$$

where,

$(q")_i$= heat flux $\left[\frac{Btu}{hr-ft^2}\right]$

P = pressure [psi]

T_{wall}, T_{sat}=temperature of the wall and fluid saturation temperature respectively, $[^oF]$

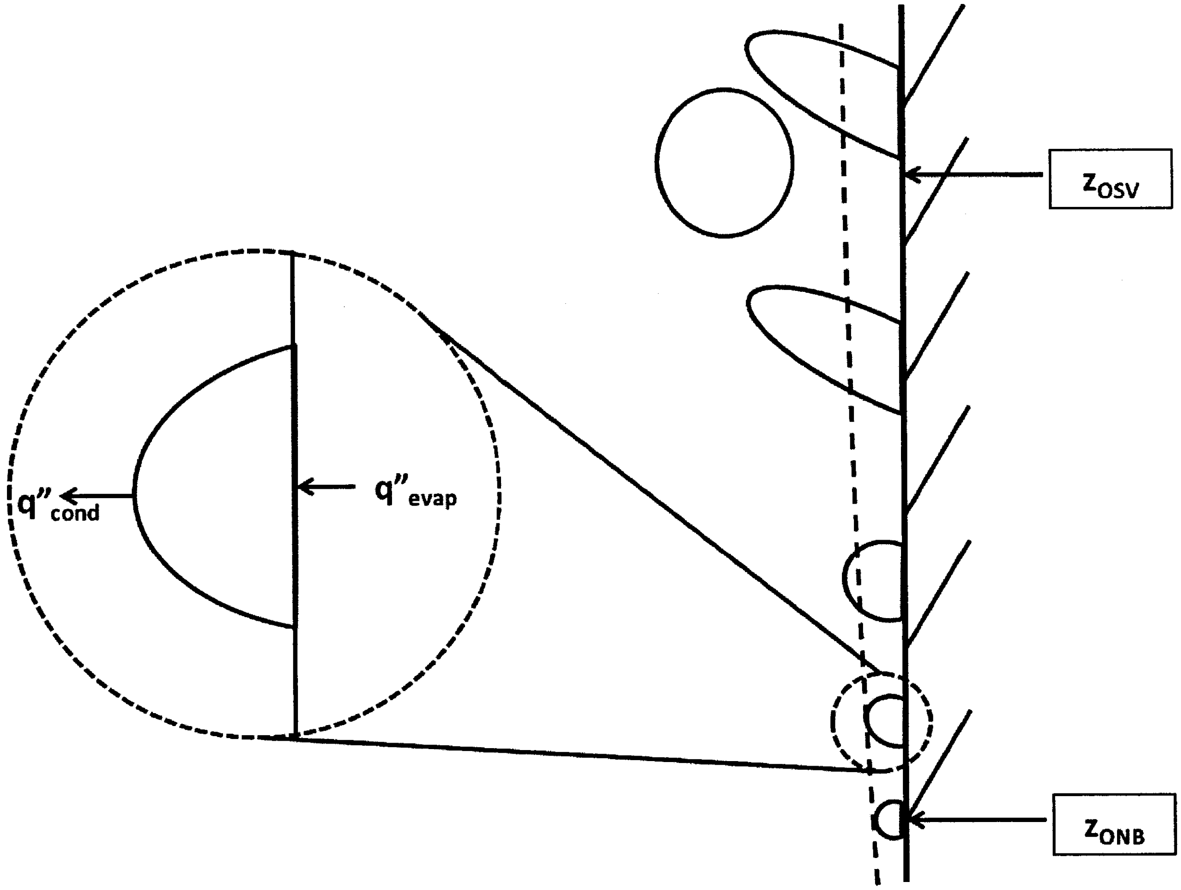

Figure 8-2: Boiling Incipience and Bubble Departure

In the surface boiling regime, the evaporation of the liquid phase at the base of the bubble is exactly balanced by the condensation of the vapor phase at the bubble tip, as shown in the expanded view portion of Figure 8-2. The dashed line in this figure represents the laminar boundary layer.

The bubbles continue to grow in size downstream of z_{ONB} because the bulk temperature of the fluid is increasing axially, thereby reducing the rate of heat transfer at the bubble tip. This reduction in heat transfer causes the equilibrium bubble size to increase until a combination of shear stress, buoyancy, and in the case of swirling flows, the centrifugal force combine to remove the bubble from the tube wall. At this point the tube is now in the detached bubble region of subcooled boiling.

Surface boiling friction pressure drop is composed of several competing mechanisms. Downstream of z_{ONB}, the cross-sectional flow area of the tube is slightly constricted due to the formation of a bubbly layer. At first this effect has minimal effect on the friction factor since the bubbles are smaller than the laminar boundary layer surrounding them as shown in Figure 8-2. The viscosity of the fluid near the bubbly layer continues to decrease at this time as the fluid approaches its saturation temperature.

As the bubbles continue to grow, the tips of the bubbles begin protruding into the bulk of the flow. This

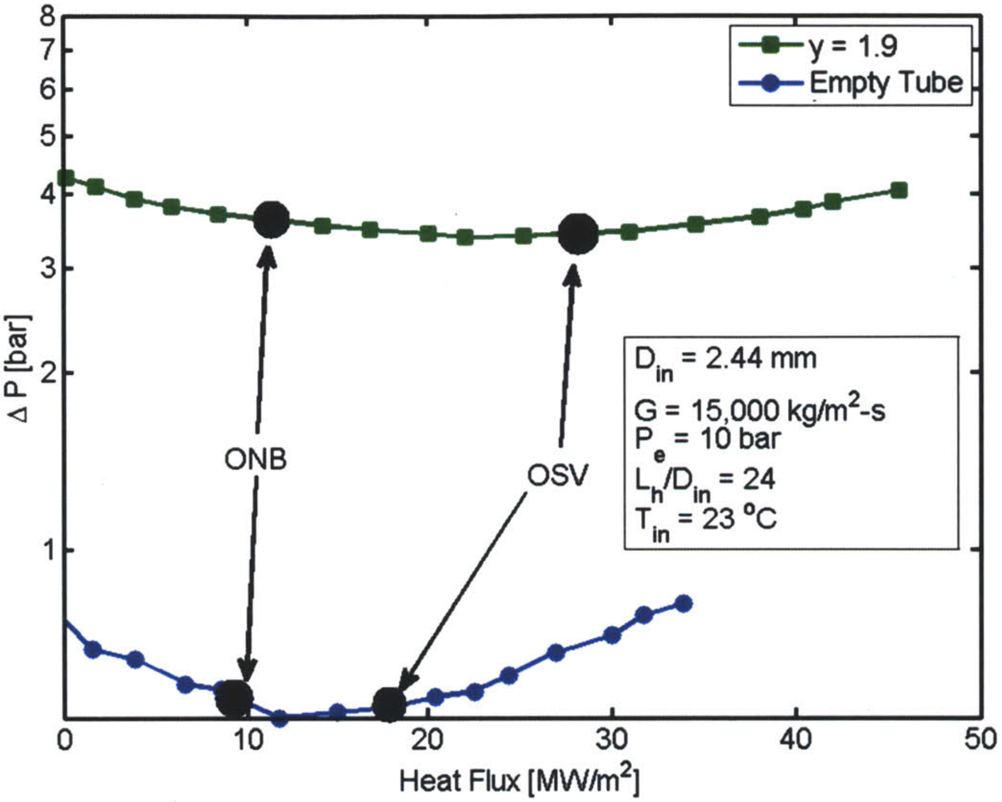

Figure 8-3: Pressure Drop in Developing Boiling: Taken from [87]

artificial roughening of the tube wall increases the turbulence of the fluid near the bubbly layer, resulting in a higher loss in momentum. Meanwhile, the continual decrease in flow area due to bubble growth results in a steadily increasing mass flux. These effects combine to result in a higher pressure drop, which can only partially be offset by the lower fluid viscosity near the bubbly layer.

A combination of these effects is shown in the heat flux vs. pressure drop plot in Figure 8-3 adapted from Tong et al. [87]. The points of ONB and OSV are shown qualitatively on this figure. The decrease in pressure drop for both curves to the left of ONB is due to the decrease in viscosity of the fluid as its temperature increases. After ONB, the curve continues to slightly decrease due to the continued decrease in liquid viscosity; however, the curve begins to flatten due to the increased pressure drop from the growth of the bubbly layer. After OSV, the presence of bubbles has significant effects on the flow and the pressure drop begins to rise again until CHF is achieved at the final data point.

There have been very few data points gathered for surface boiling in swirl conditions. A few of these data are presented in Tong et al. [87], as was just discussed. Some data also exist in Dedov [19]; however, these data refer to one-sided heating experiments. Despite not having a large database, Dedov was able to make some conclusions about the basic trends of subcooled boiling pressure drop for swirling flows. The

Table 8.1: Parametric Study Limits for Surface Boiling in Swirl Flow

Parameter	Units	Range
Re	[-]	10,000 - 1,000,000
Diameter	[cm]	0.5-1.5
Heated Length	[m]	5.0 - 150
Twist Ratio (y) for both FLTT and SLTT	[-]	1.5 - 15
Swirl Decay Length for SLTT	$[\frac{L_h}{D}]$	10 - 100
Exit Equilibrium Quality	[-]	(-0.4) - (-0.1)

phenomena for swirling flows do follow that of an empty tube; however, the flat portion of the boiling curve appear to lengthen, as can be seen in Figure 8-3. This simply indicates that the region of surface boiling can be sustained longer due to the increase in convective heat transfer rate at the interface between the bubble tips and the liquid core which reduces the bubble growth rate. Dedov also suggested that the surface boiling region is most prevalent for mass flux values above 2100 $\left[\frac{kg}{m^2-s}\right]$, and equilibrium qualities less than (-0.1) [19].

There is no generalized correlation for friction factor for the surface boiling region for swirling flows. Therefore, it is suggested that an experimental study be performed to cover this gap in the the correlation database. The suggested operating ranges that should be studied are listed in Table 8.1. It would be beneficial to perform these studies at both low and high pressure; however, similitude may be enough to allow a low pressure correlation to be applied to high pressure conditions. Also, the heated length should be short enough for the surface boiling region to occupy a significant portion of the channel. If this is not the case, it can be difficult to distinguish the effect that surface boiling has on friction pressure drop from the effect of the detached bubble region.

It is suggested that the new friction factor correlation take the form of a friction factor ratio based upon the empty tube value. A surface boiling friction factor correlation for empty tubes that could be used as a reference correlation is the Bergles-Dormer correlation [7], shown in Equation (8.2) as the Darcy friction factor.

$$f_{empty} = 0.428Re^{-0.28}\left(\frac{\mu_w}{\mu_b}\right)^{0.35} \tag{8.2}$$

Furthermore, the ratio of the axial to swirl flow friction factor could take the same form as the Kanizawa et al. correlation [47], as shown in Equation (8.3). Data from the proposed parametric study could be used to fit coefficients $C_1 - C_4$.

$$\frac{f_{sw}}{f_{empty}} = \left(1 + C_1 y^{C_2} Fr^{C_3}\right)^{C_4} \tag{8.3}$$

8.1.2 Two-Phase Swirl Decay

While there is a reasonable amount of data for single-phase swirl decay [56, 69, 99], there is no reported swirl intensity measurements for two-phase flows. This lack of data was the reason that the swirl decay model of Wu et al. [99] was used as an approximation of the swirl intensity at a given location even though it was developed only for single-phase flows. There are ways to infer the rate of swirl decay from experimental data, particularly CHF data for SLTTs as previously discussed in Section 3.3.1; however, this is not a direct measurement of the swirl intensity since Dryout may be delayed due to the history of the channel instead of local effects.

The same argument can be made for the pressure drop data of Matzner et al. [64]. Reasonable estimates of pressure drop were obtained using the single-phase swirl decay model to calculate the decaying swirl of the two-phase flow; however, there is uncertainty in the exact value of the form pressure loss due to the twisted-tape. Therefore, the only way to gain direct insight to the phenomena of two-phase swirl decay is to perform an experimental study. This study can be performed with air-water, or steam-water flows, but should cover the same range of parameters shown in Table 8.1 as discussed in the previous section.

Two-phase swirl intensity is difficult to quantify with a convenient metric; however, Najafi et al. [69] suggest two ways to do so. The first way is through the use of non-dimensional numbers. In addition to the Reynolds number defined in its traditional fashion, the Rossby number, as shown in Equation (8.4) can be used to characterize swirling flows. This number is only appropriate inside the twisted-tape because it assumes that the entire fluid is rotating with the same angular velocity, i.e. the fluid acts as a rigid disc.

$$Ro = \frac{W_o}{R\omega} \tag{8.4}$$

where,
W_o =bulk axial velocity [m/s]
R = tube diameter [m]
ω =angular velocity [rad/s]

Swirl intensity can be more accurately be described by the term Ω, which is formulated in Equation (8.5). For single-phase flow at thermal equilibrium, the density terms cancel; however, for two-phase flows, it is important to adjust the density by using a time-averaged local void fraction, as shown in Equation (8.6). A no-slip condition is assumed since the local vapor and liquid velocities should be nearly equal if the region under investigation is small enough.

$$\Omega = \frac{(axial\ flux\ of\ angular\ momentum)}{(axial\ flux\ of\ linear\ momentum)} = \frac{\int_0^R 2\pi\rho(r)W(r)\,V(r)\,r^2dr}{\int_0^R 2\pi\rho(r)W(r)^2\,r^2dr} \tag{8.5}$$

$$\rho(r) = \langle\alpha(r)\rangle\,\rho_g + (1 - \langle\alpha(r)\rangle)\,\rho_l \tag{8.6}$$

The local, time-averaged void fraction, $\langle \alpha(r) \rangle$, can be determined experimentally through a variety of techniques including but not limited to electronic probes, photography, or through neutron tomography. Several authors have discussed the range of experimental techniques available to experimenters today. If the reader is interested in learning more about these techniques, further reading can be found in Refs. [6, 49, 50, 78].

Whether the experimental swirl intensity is quantified using the Rossby number or by the more intensive method shown in Equation (8.5), this information should be compared to the swirl decay model used in this study in order to assess the current method's viability for use in two-phase flow conditions. If the swirl intensity is found to decay differently than how it is currently predicted, it is recommended that the new information gained by this experimental work be used to update the current prediction methodology in order to more accurately predict pressure drop and CHF in the decaying swirl region for tubes equipped with MSLTTs.

8.1.3 Effect of Liquid Film Thickness on CHF Mechanism

For axial flow cases, it can be said that the property of the flow that determines the mechanism of boiling crisis, i.e. DNB or Dryout, is the flow regime. After all, two of the most prominent mechanistic models for boiling crisis were developed for specific flow regimes. Namely, the original Pei-Weisman model [74] was developed for DNB in the bubbly flow regime, while the liquid film Dryout model of Hewitt et al. [36] was developed specifically for annular flow. While the Usman DNB model [88] for tubes containing FLTTs is a modification of the original Pei-Weisman model, the flow pattern of a swirling flow is not the same as the bubbly flow regime that both models were based on.

Shakutsui et al. [77] attempted to make a flow regime map for low pressure swirling flows. In their work, they determined that the presence of any bubbles in the channel resulted in the formation of a central vapor column. Photographic results of their study are shown in Figure 8-4. Therefore, it appears that swirling flows can be classified as annular flow for any vapor content; however, not all swirling flows undergo Dryout as the boiling crisis phenomenon, as is evidenced by this study and the work by Usman [88].

Therefore, it is clear that CHF in annular flow is not analogous to Dryout, so there must be another mechanism at work that determines which mechanism of boiling crisis will occur. The answer might come from analyzing the differences between an axial flow that undergoes Dryout and a swirling flow that undergoes DNB. In annular flow when no swirl is present, the liquid film is maintained on the wall by the impingement of the high velocity vapor core. Because this force is intrinsically small, the thickness of the liquid film must also be small. Because this liquid film is very thin, it is not capable of providing enough resistance to the flow of bubbles away from the tube wall for a vapor blanket to form.

In swirling flow, the centrifugal force aids in holding up the liquid film. Therefore the thickness of the liquid film can be much larger than the liquid film in axial annular flow. Since the only difference between the annular regime of axial and swirl flow is the thickness of the liquid film, the mechanism of boiling crisis

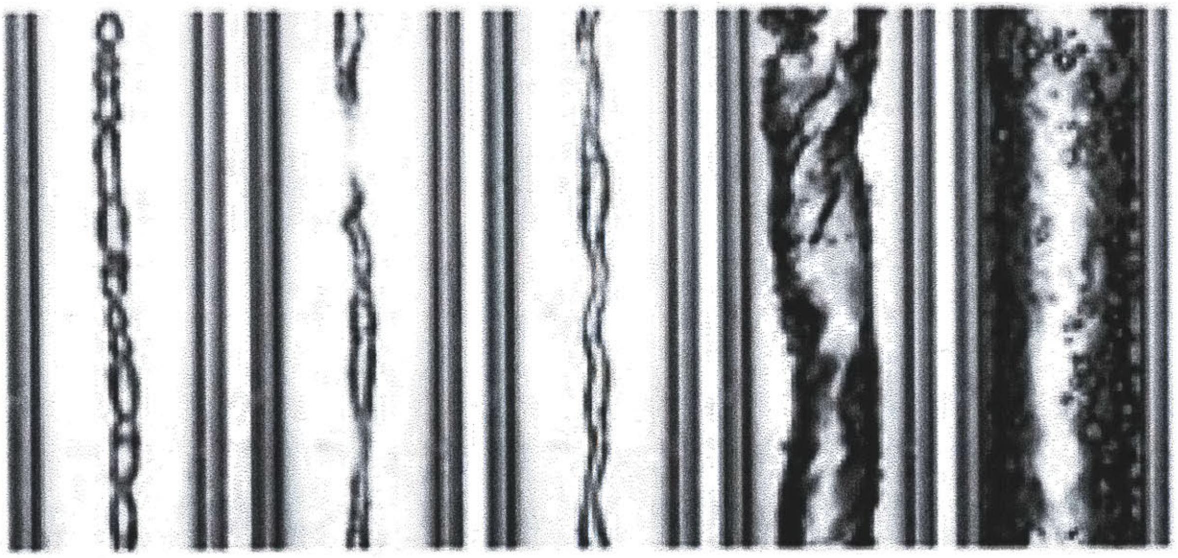

Figure 8-4: Flow Patterns for Two-Phase, Low Pressure Swirling Flow: Adapted from [77]

must depend on this variable. Therefore, a series of tests should be performed to characterize this critical liquid film thickness. A possible starting point to explain the mechanism may be to correlate the ratio of the liquid film thickness to the bubbly layer thickness required for DNB to occur.

This idea is shown qualitatively in Figure 8-5 where the dashed line represents the minimum thickness of liquid film required to support DNB. The horizontal line represents the location where the boiling crisis mechanism transitions from DNB to Dryout. The Usman-Weisman model [95] assumes that the bubbly layer thickness required for DNB is about 5.5 times the bubble diameter; however, this assumption is based on homogeneous flow velocities for the liquid and vapor phases. Near the transition point, where the void fraction is high, the slip ratio between the vapor and liquid phases could be quite large, causing a low velocity liquid region to form near the bubbly layer, thereby lowering the shear stress and possibly altering the bubbly layer thickness.

The experimental study required to test the idea that there is a minimum liquid film thickness required to support DNB would involve conducting a series of boiling crisis tests that cover the range of parameters in Table 8.2. The range of void fraction was selected since it has been shown that the Usman-Weisman model [95], and the empirical DNB correlation (developed in this study), tend to break down at void fractions above approximately 64%; therefore the transition to Dryout should occur at or slightly above this point. Both FLTTs and SLTTs should be tested since the presence of the twisted-tape could have an effect on the bubbly layer thickness at the transition of phenomenon. It is suggested that neutron or gamma ray tomography be used to measure the flow structure since these techniques do not disturb the flow as a cold viewing pane or electronic probe would. Information on how to conduct such an experiment can be found in Refs. [10, 13, 32, 41, 50, 103].

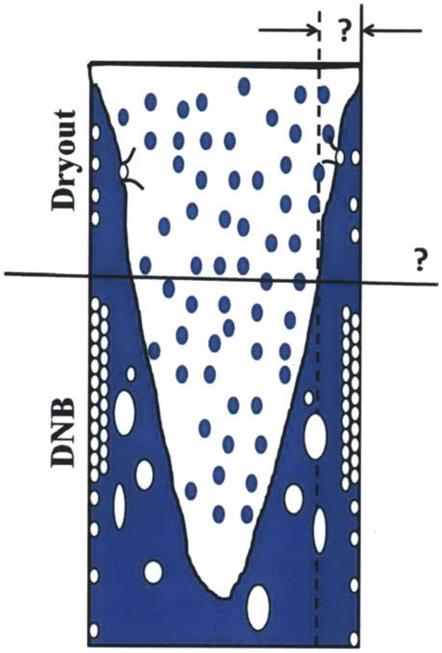

Figure 8-5: Transition from DNB to Dryout

Table 8.2: Parametric Ranges for DNB to Dryout Swirl Flow Transition Experiments

Parameter	Units	Range
Mass Flux	$\left[\frac{kg}{m^2-s}\right]$	1500 - 10,000
Pressure	[MPa]	5.0 - 16.0
Void Fraction	[-]	0.60 - 0.90
Twist Ratio	[-]	1.5 - 15
Diameter	[cm]	0.5 - 1.5
Heated Length	[cm]	5.0 - 1.5

8.2 Modeling Development

This section covers the development of a phenomenological model for Dryout in tubes containing MSLTTs.

Previous work by Whalley [97] has shown that a liquid film dryout model can be used to predict boiling crisis for high quality swirling flows. In this model, Whalley used a simplified swirl decay model to estimate how long the swirl would persist in a tube after exiting a SLTT. He found that swirl would have a significant effect on boiling crisis for a distance of about 50 diameters after the exit of the twisted-tape insert. In this zone of swirl, he assumed that 100% of the entrained liquid droplets were redeposited in the liquid film, and once redeposited these droplets were not re-entrained. The results of Whalley's Dryout model are shown in Figure 8-6, where the CHF enhancement as compared to an empty tube in annular flow is shown as a function of twisted-tape position. While the results of this model were good, the assumption he made could be improved.

Fryer et al. [26] performed an experiment on a 3.2 cm diameter channel with a swirl promoter with y=4.5 twisted 180° at its entrance. They measured the liquid film flow rate fraction, mass flow rate of the liquid film divided by the total liquid flow rate, as a function of distance after the swirl promoter for a fixed air flow rate of 53.5 g/s and pressure of about 1.5 bar. As seen in Figure 8-7, the fraction of liquid in the film does not increase to 100% at any point, and in most cases is much less than unity. Therefore, the assumption that there is no entrainment from the liquid film for 50 diameters after the twisted-tape is not true, which prompts the need for an investigation to find a way to take into account the dynamic nature of the phenomena.

Upon further analysis of Fryer's data subsequently described, the fraction of liquid in the liquid film at 50 diameters is actually a function of the void fraction of the channel. The Martinelli-Lockhart relationship, shown in Equations (8.7)-(8.8), was used to calculate the void fraction of the flows shown in Figure 8-7, and the liquid film flow fraction at 50 diameters downstream of the twisted-tape was found by linearly interpolating the values bounding the location indicated by the vertical black line in the figure.

$$\alpha = \frac{1}{\left[1 + \left(\frac{1-x}{x}\right)^{0.72} C(P)\right]^{0.378}} \tag{8.7}$$

$$C\left(P\right)^{1/0.8} = \left(\frac{\rho_v}{\rho_l}\right)^{0.5} \left(\frac{\mu_l}{\mu_v}\right)^{0.1} \tag{8.8}$$

The results of this analysis are shown in Figure 8-8. This trend suggests that the liquid film thickness can be directly correlated to the void fraction of the channel. It also suggests that there is potential for development of a more accurate model of the Dryout phenomenon in swirling flow. This could be done by adjusting the deposition coefficient in the model suggested by Hewitt et al. [36] in order to account for the effect of swirl. Their model is simply a mass balance on the liquid film layer and states that Dryout is reached when the film thickness reaches zero. Explicitly, the mass balance of the liquid film according to

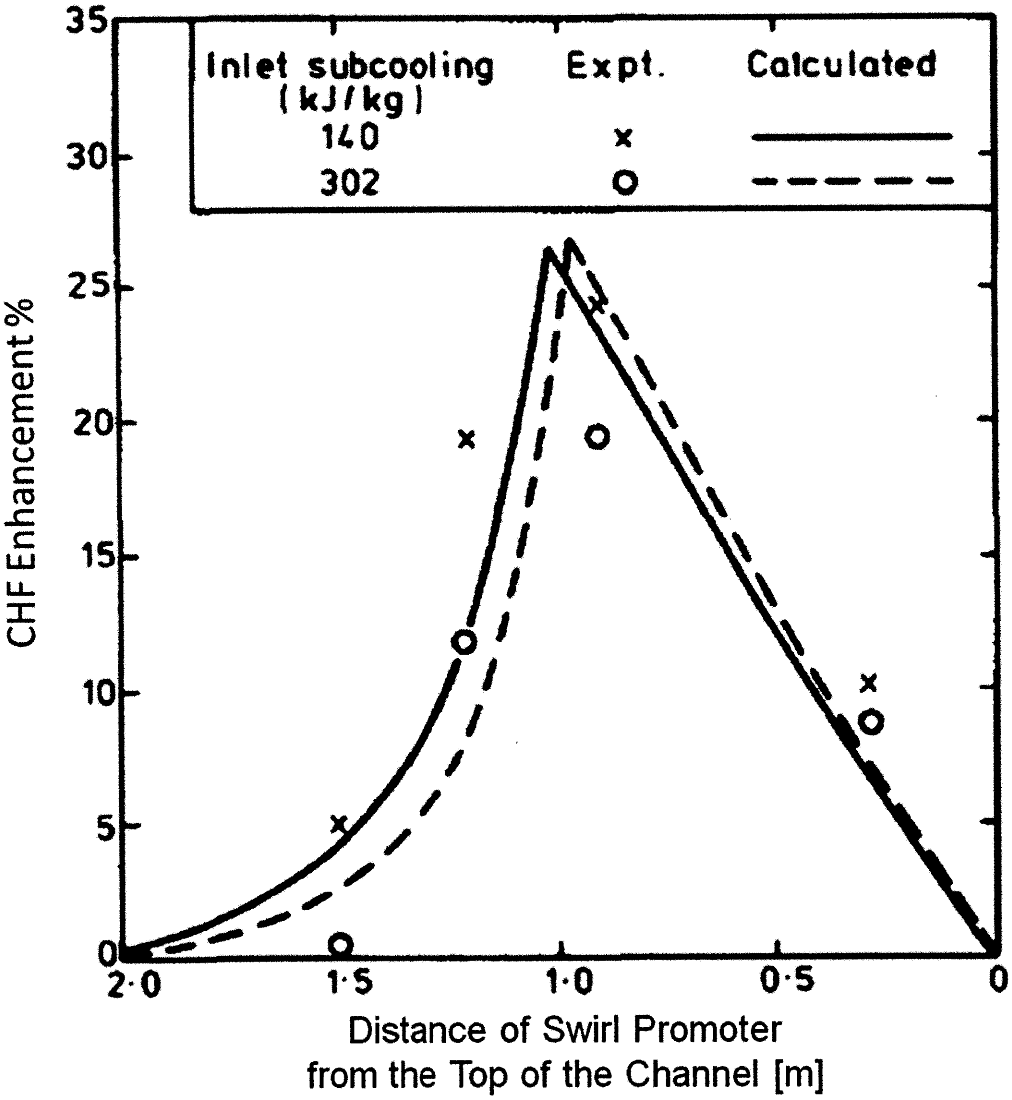

Figure 8-6: Dryout Under Swirl Flow Conditions: Adapted from Whalley [97]

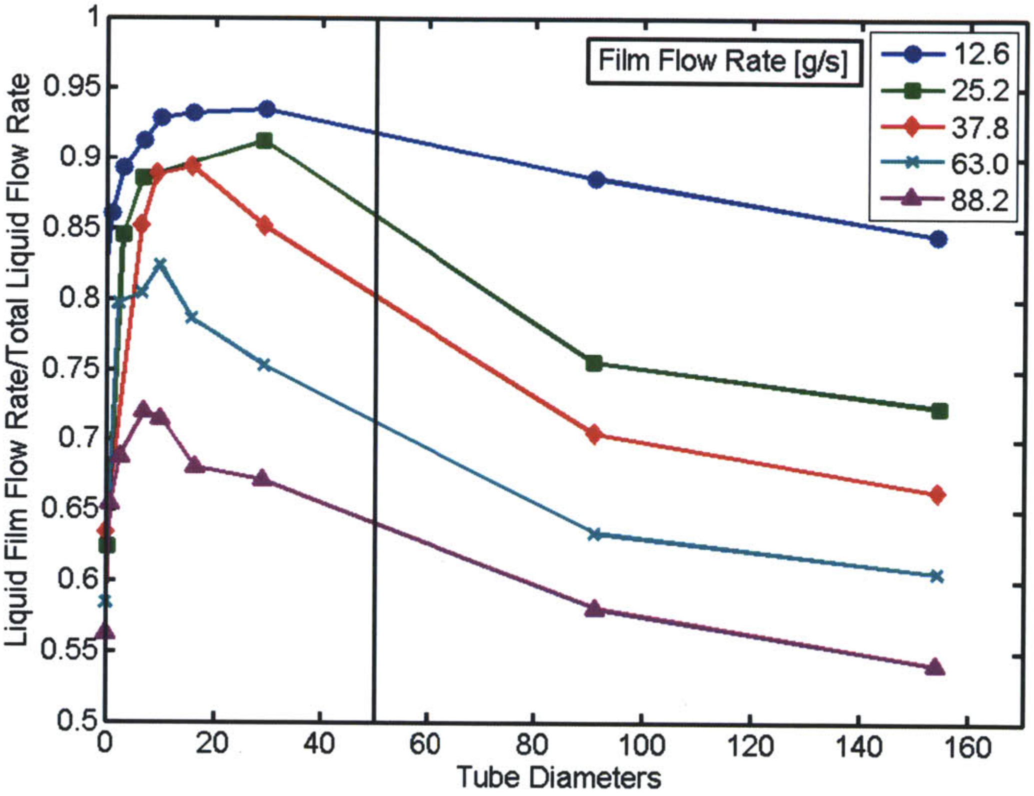

Figure 8-7: Liquid Film Flow Fraction After a Twisted-Tape Insert: Adapted from [26]

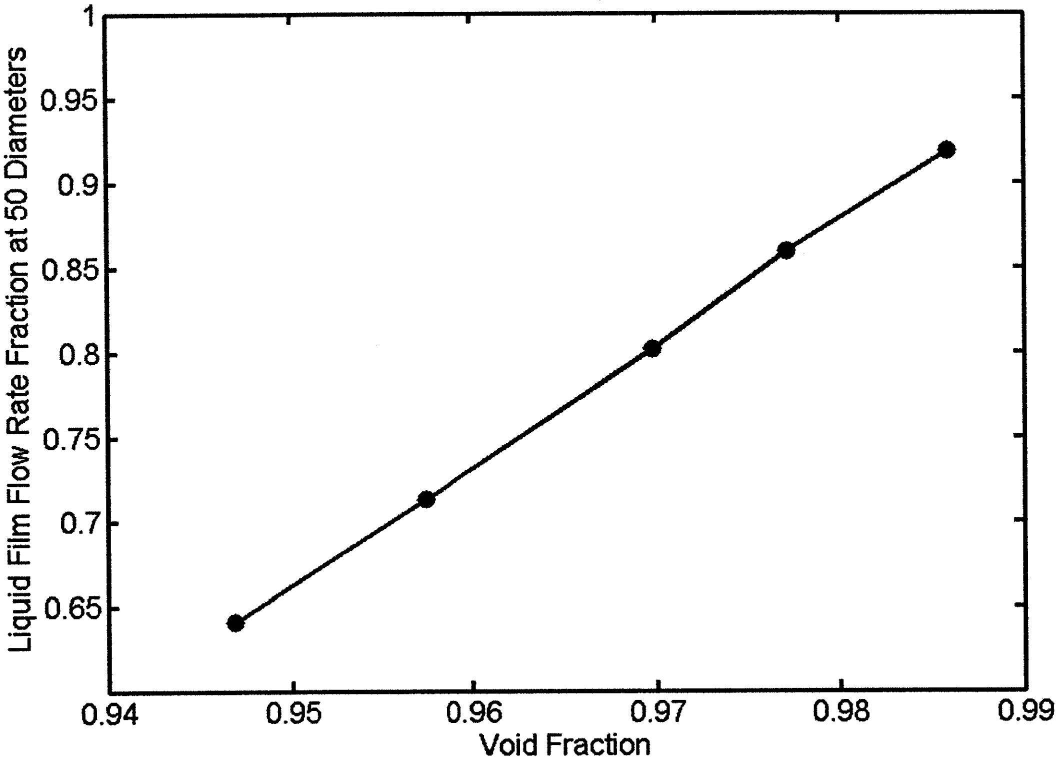

Figure 8-8: Dependence of Liquid Film Flow Rate Fraction on Void Fraction

their model is shown in Equation (8.9).

$$\frac{d\dot{m}_{LF}}{dz} = \frac{4}{d}\left(D - E - \frac{q"}{h_{fg}}\right) \tag{8.9}$$

where,

$\dot{m}_{LF}$ =liquid film flow rate

d = tube diameter

D = liquid droplet deposition rate on the tube wall

E = entrainment of liquid droplets in the vapor core

$\frac{q"}{h_{fg}}$ = rate of evaporation of liquid from the film

The deposition coefficient is directly related to the concentration of droplets in the vapor core in the center of the tube, as shown in Equation (8.10). This concentration, C, is a cross-section averaged value. A potential way to account for swirl would be to adjust the concentration based on local swirl conditions to account for the higher concentration of liquid droplets near the liquid film. This is shown qualitatively in Figure 8-9 where the concentration of the liquid droplet near the liquid film is much higher than the uniform concentration due to swirl.

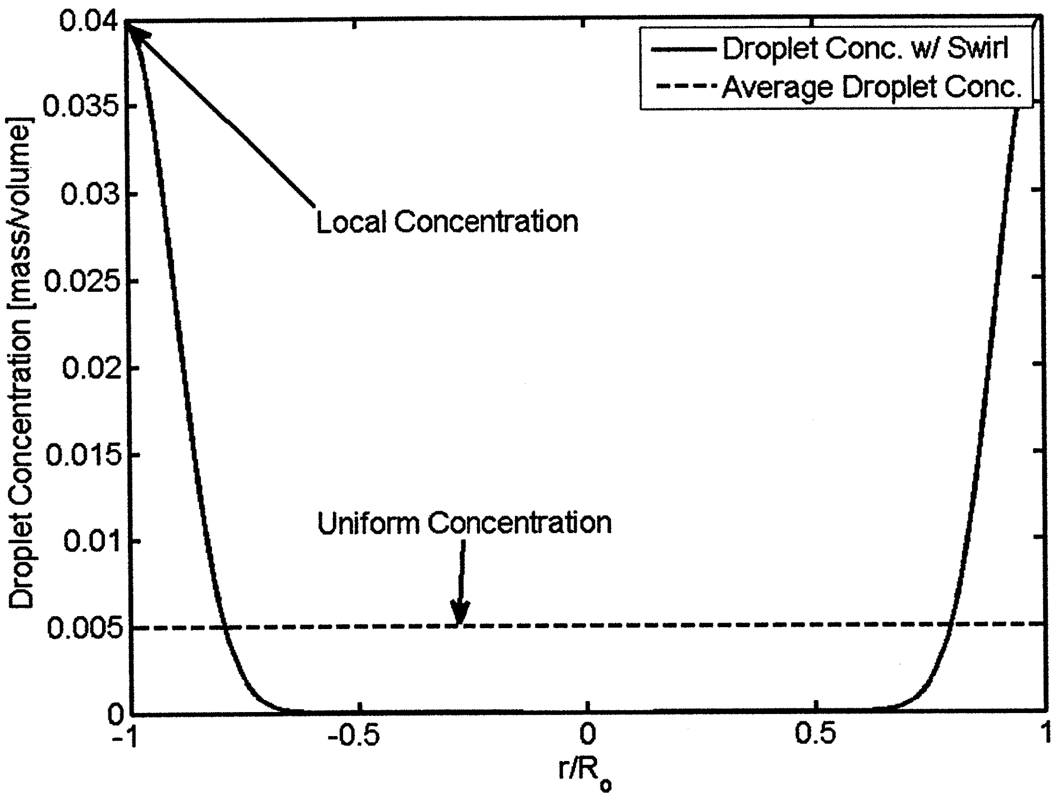

Figure 8-9: Qualitative Liquid Droplet Concentration Under Swirl Conditions

$$D = kC \tag{8.10}$$

By using the technique described in this section, it is hoped that a mechanical model could be derived to describe Dryout in tubes equipped with MSLTTs.

8.3 Design Application

This section covers the proposed design work that is meant to explore the potential design benefits of MSLTTs in the IPWR design. Section 8.3.1 covers a brief description of the optimization strategy for implementing SLTTs in the IPWR. Section 8.3.2 covers the concept of Ledinegg flow instabilities. Section 8.3.3 covers parallel channel flow instabilities. In addition, means to effectively install MSLTTs in flow channels should be developed which ensure secure fitting at accurately positioned locations.

8.3.1 IPWR Optimization Strategy

Optimization of the IPWR for maximum power output should be performed using the design methodology outlined in Chapter 6. This design methodology involves a four step process where the designer first finds the approximate maximum mass flux for a channel with two twisted-tapes as a function of channel diameter. In step two, this mass flux is used as an input to the DNB correlation for the case of a channel with one SLTT placed such that the MDNBR limit is met at the SLTT inlet for a chopped cosine heat flux shape. This flux shape approximates the beginning of life heat flux profile. In step three, the mass flux is held constant while second SLTT is placed in the location that gives the channel the maximum MDNBR for a uniform heat flux profile. This heat flux profile represents the end of life profile. Finally, the number of SLTTs is appropriately adjusted considering two eventualities: the DNBR is always less than the design limit resulting in the addition of a SLTT; or, the DNBR is always greater than the design limit and a SLTT is removed.

8.3.2 Ledinegg Flow Instability

A condition may arise for a single heated channel, or a series of parallel heated channels in which flow oscillations are caused by the external pressure drop gradient exceeding the internal gradient. This condition is caused by the condition shown in Equation (8.11), and is refered to as the Ledinegg instability [86].

$$\left(\frac{\delta \Delta P}{\delta G}\right)_{internal} \leq \left(\frac{\delta \Delta P}{\delta G}\right)_{external} \tag{8.11}$$

In this equation, the internal condition refers to the pressure drop and mass flux in the core, while the external conditions refer to the pump capacity. This instability is illustrated in Figure 8-10, where two pump head curves are illustrated by the red and blue lines. In Case 1, the criteria shown in Equation (8.11) is met at point B. At this point, the flow is unstable because two possible states fulfill the core pressure drop requirement, i.e. the flow could either be all vapor, or all liquid. In Case 2, the pump head derivative is always more negative than the internal derivative. Therefore, this system is inherently stable, and flow oscillations will not occur. Furthermore, the hump in the curve, i.e. the transition from point B to point C becomes smaller as the channel pressure drop becomes larger. An increase in pressure drop can be supplied through three mechanisms: orificing at the channel inlet, insertion of twisted-tape inserts, or reduction in channel diameter.

Once the channel geometry, twisted-tape placement, and core power are fully characterized, an analysis should be performed to ensure that a sufficient margin exists to the onset of Ledinegg flow instabilities.

8.3.3 Parallel-Channel Flow Instability

In a configuration of parallel flow channels connected with common plena as in the IPWR, the potential for parallel channel flow instability exists. In the IPWR configuration with its flow channels of identical geometry and twisted-tape inserts, the core radial power profile is the predominant factor which creates variability

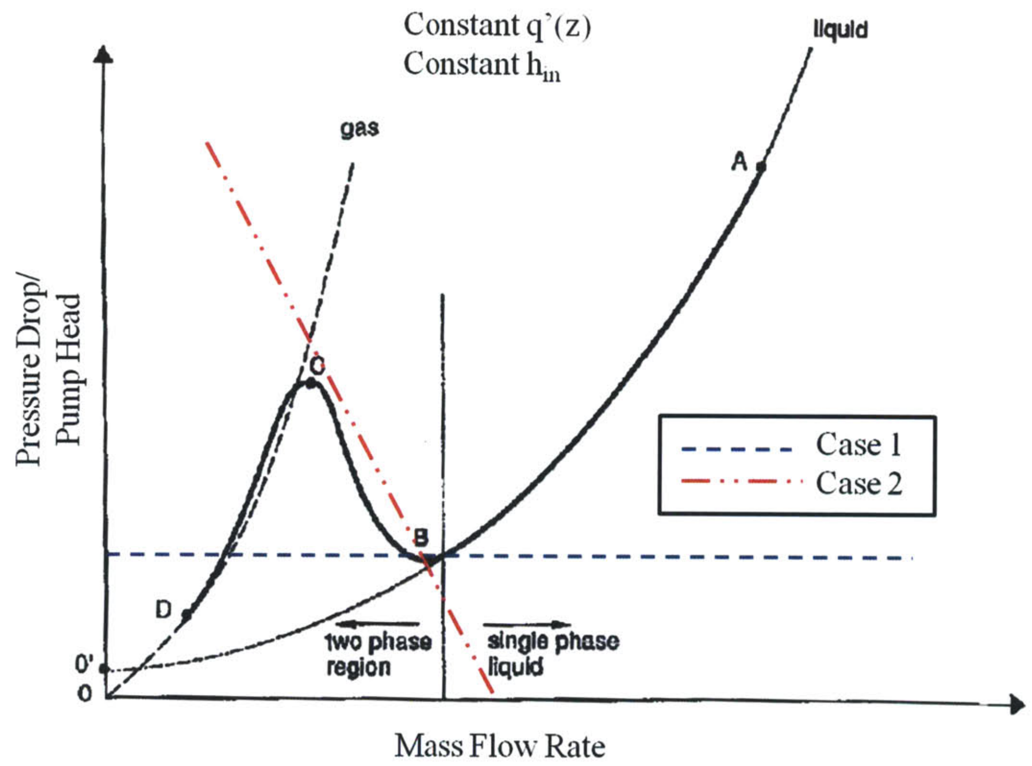

Figure 8-10: Ledinegg Instability Criteria: Adapted from Todreas et al. [82]

of coolant conditions among flow channels. It is this variability combined with the constant channel outlet radial pressure profile imposed by the multiple array of cooling channels that gives rise to the potential for parallel channel instability [90, 81].

Once the IPWR channel and twisted-tape configuration is fixed and characteristic axial and radial power profiles are established by core design, the core configuration should be checked to assure a satisfactory margin to the onset of parallel channel instability exists.

Bibliography

[1] *Seabrook, Revision 11 to Updated Final Safety Analysis Report, Chapter 4, U.S. Nuclear Regulatory Commission*, accession no. ml071430575 edition, 2007.

[2] K.N. Agrawal, H.K. Varma, and S. Lal. Pressure drop during forced convection boiling of R-12 under swirl flow. *Transactions of the ASME*, 104:758–762, 1982.

[3] Akhavan-Behabadi, M.A. Kumar, and M. Jamali. Investigation of heat transfer and pressure drop during swirl flow boiling of R-134a in a horizontal tube. *International Journal of Heat and Mass Transfer*, 52:1918–1927, 2009.

[4] A.H. Algifri and R.K. Bhardwaj. Prediction of the heat transfer for decaying turbulent swirl flow in a tube. *International Journal of Heat and Mass Transfer*, 28(9):1637–1643, 1985.

[5] M. Araki, K. Sato, S. Suzuki, and M. Akiba. Critical-heat-flux experiment on the screw tube under one-side-heating conditions. *Fusion Technology*, 29:519–528, 1996.

[6] W.D. Bachalo. Experimental methods in multiphase flows. *International Journal of Multiphase Flow*, 20:261–295, 1994.

[7] A. E. Bergles and T. Dormer. Subcooled boiling pressure drop with water at low pressure. *International Journal of Heat and Mass Transfer*, 12:459–470, 1969.

[8] A. E. Bergles, A.S. Komendantov, A.F. Krug, Y.A. Kuzma-Kichta, and Fedorovich E.D. Investigation of boiling crisis in swirling flows. *Presented at International Conference on Heat and Mass Transfer and Hydrodynamics of Swirling Flows*, Moscow, Russia:UDC 536.248.2, 2011.

[9] A. E. Bergles and W.M. Rohsenow. The determination of forced convection boiling heat transfer data. *Journal of Heat Transfer*, 86:363, 1964.

[10] A. Bieberle, D. Hoppe, E. Schleicher, and U. Hampel. Void measurement using high-resolution gamma-ray computed tomography. *Nuclear Engineering and Design*, 241:2086–2092, 2011.

[11] J. Boscary, J. Fabre, and J. Schlosser. Critical heat flux of water subcooled flow in one-side heated swirl tubes. *International Journal of Heat and Mass Transfer*, 42:287–301, 1999.

[12] R. Brevi, M. Cumo, A Palmieri, and D. Pitimada. Forced convection heat transfer and burnout measurements with twisted tapes. *La Termotecnica*, 25(2):619–625, 1971.

[13] E. Calzada, B. Schillinger, and F. Grunauer. Construction and assembly of the neutron radiography and tomography facility antares at frm ii. *Nuclear Instruments and Methods in Physics Research*, A 542:38–44, 2005.

[14] J.C. Chen. Correlation for boiling heat transfer to saturated fluids in convective flow. *Industrial and Engineering Chemistry Process Design and Development*, 5(3):322–329, 1966.

[15] J.G. Collier and J.R. Thome. *Convective Boiling and Condensation 3rd. Edition.* Oxford University Press, 1994.

[16] J.G. Collier and J.R. Thome. *Convective Boiling and Condensation.* Oxford University Press, 1996.

[17] J.M. Cuta, A.S. Koontz, C.W. Stewart, S.D. Montgomery, and K.K. Nomura. *VIPRE-01: A Thermal Hydraulic Code for Reactor Cores. Volume 2: User's Manual. Revision 2.* EPRI-NP-2511-CCM-A, 1985.

[18] E.J. Davis and G.H. Anderson. The incipience of nucleate boiling in forced convection flow. *American Institute of Chemical Engineers Journal*, 12:774–780, 1966.

[19] A.V. Dedov. Peculiarities of boiling in subcooled flow. *Thermal Engineering*, 56(8):691–699, 2009.

[20] F.W. Dittus and L.M.K Boelter. Heat transfer in automobile radiators of the tubular type. *International Communications in Heat and Mass Transfer*, 12:3–22, 1985.

[21] M.R. Drizius, R.K. Shkema, and A.A. Shlanciauskas. Boiling crisis in swirled flow of water in pipes. *Heat Transfer Soviet Research*, 10:1–7, 1978.

[22] L. Feinstein and R.E. Lundberg. Fluid friction and boiling heat transfer with water in vortex flow in tubes containing an internal twisted tape. Technical Report RADC-TDR-63-451, U.S. Air Force Research and Technology Division, 1963. Unclassified Report AD 430889.

[23] P. Ferroni. *An Inverted Hydride-fueled Pressurized Water Reactor Concept.* PhD thesis, Massachusetts Institute of Technology, 2010.

[24] P. Ferroni, R.E. Block, N. Todreas, and A. E. Bergles. Experimental evaluation of pressure drop in round tubes provided with physically separated, multiple, short-length twisted tapes. *Experimental Thermal and Fluid Science*, 35:1357–1369, 2011.

[25] P. Ferroni and N. Todreas. An inverted hydride-fueled pressurized water reactor concept. Technical Report MIT-ANP-TR-126, Massachusetts Institute of Technology, 2009.

[26] P.J. Fryer and P.B. Whalley. The effect of swirl on the liquid distribution in annular two-phase flow. *International Journal of Multiphase Flow*, 8(3):285–289, 1982.

[27] W.R. Gambill, R.D. Bundy, and R.W. Wansbrough. Heat transfer, burnout, and pressure drop for water in swirl flow through tubes with internal twisted tapes. *Chemical Engineering Progress Symposium Series*, 57(32):127–137, 1961.

[28] G.P. Gaspari and G Cattadori, editors. *Subcooled Flow Boiling in Tubes with and without Turbulence Promoters*, volume 3, Honolulu, HI, Oct. 31-Nov. 5 1993. World Conference on Experimental Heat Transfer.

[29] V. Gnielinski. Neue gleichungen fur den warme- und den stoffubergang in turbulent durchstromten rohren und kanalen (new equations for heat and mass transfer in turbulent pipe and channel flow). *International Journal of Chemical Engineering*, 16:359–368, 1976.

[30] D. Groeneveld, Shan. J.Q., A.Z. Vasic, L.K.H. Leung, A. Durmayaz, J. Yang, S.C. Cheng, and A. Tanase. The 2006 chf look-up table. *Nuclear Engineering and Design*, 237:1909–1922, 2007.

[31] D.D. Hall and I. Mudawar. Evaluation of subcooled critical heat flux correlations using the pu-btpfl chf database for vertical upflow of water in a uniformly heated round tube. *Nuclear Technology*, 117:234–247, 1997.

[32] G.D. Harvel, K. Hori, K. Kawanishi, and J.S. Chang. Real-time cross-sectional averaged void fraction measurements in vertical annulus gas-liquid two-phase flow by neutron radiography and x-ray tomography techniques. *Nuclear Instruments and Methods in Physics Research*, A 371:544–552, 1996.

[33] A. Hassid, G.C. Manzoni, and R. Ravetta. Heat transfer crisis with steam-water mixtures: An experimental study on the increase of critical power with local swirl promoters in round tubes. *Energia Nucleare*, 13(11):589–610, 1966.

[34] K. Hata and S. Masuzaki, editors. *Heat Transfer and Critical Heat Flux of Subcooled Water Flow Boiling in a SUS304-Tube with Twisted-tape Insert*, number IHTC14-22225, Washington, D.C., 2010. International Heat Transfer Conference.

[35] G.F. Hewitt. *Heat Exchanger Design Handbook*, volume 2. Begell House Inc., New York, NY, 2008.

[36] G.F. Hewitt and A.H. Govan. Phenomena and prediction in annular two-phase flow. In J.H. Kim, U.S. Rohatgi, and A. Hashemi, editors, *Advances in Gas-liquid flows*, volume FED-99 HTD-155, Dallas, TX, November 1990. ASME.

[37] G.F. Hewitt and N.S. Hall-Taylor. *Annular Two-Phase Flow*. Pergamon Press, 1970.

[38] G.F. Hewitt and D.N. Roberts. Studies of two-phase flow patterns by simultaneous x-ray and flash photography. Technical report, AERE-M2159, 1969.

[39] J.O Hinze. Fundamentals of the hydrodynamic mechanism of splitting in dispersion processes. *American Institute of Chemical Engineers Journal*, 1(3):289–295, 1955.

[40] M. www.x-eng.com Holmgren. *IAPWS IF-97 Water and Steam Properties.*

[41] E.M.A. Hussein and D.A. Meneley. Single exposure neutron tomography of two-phase flow. *International Journal of Multiphase Flow*, 12(1):1–34, 1986.

[42] F. Inasaka and H Nariai. Critical heat flux and flow characteristics of subcooled flow boiling in narrow tubes. *JSME International Journal*, 30:1595–1600, 1987.

[43] F. Inasaka and H Nariai. Enhancement of subcooled flow boiling critical heat flux for water in tubes with internal twisted tapes under one-sided-heating conditions. *Fusion Engineering and Design*, 39-40:347–354, 1998.

[44] M.K. Jensen. A correlation for predicting the critical heat flux condition with twisted-tape swirl generators. *International Journal of Heat and Mass Transfer*, 27(11):2171–2173, 1984.

[45] M.K. Jensen and H.P. Bensler. Saturated forced convective boiling heat transfer with twisted-tape inserts. *ASME Journal of Heat Transfer*, 108:93–99, 1986.

[46] M.K. Jensen, M. Pourdashti, and H. Bensler. Two-phase pressure drop with twisted-tape swirl generators. *International Journal of Multiphase Flow*, 11(2):201–211, 1985.

[47] F.T. Kanizawa, R.S. Hernandes, A.A.U. Moraes, and G. Ribatski. A new correlation for single and two-phase flow pressure drop in round tubes with twisted-tape inserts. *Brazillian Society of Mechanical Science and Engineering*, 33:243–250, 2011.

[48] Y. Katto. Critical heat flux of forced convection boiling in uniformly heated vertical tubes (correlation of chf in hp-regime and determination of chf and determination of chf-regime map). *International Journal of Heat and Mass Transfer*, 23:1573–1580, 1980.

[49] J.K. Keska and B.E. Williams. Experimental comparison of flow pattern detection techniques for air-water mixture flow. *Experimental Thermal and Fluid Science*, 19:1–12, 1999.

[50] J.L. Kickhofel, R. Zboray, M. Damsohn, A. Kaestner, E.H. Lehmann, and H.M. Prasser. Cold neutron tomography of annular coolant flow in a double subchannel model of a boiling water reactor. *Nuclear Instruments and Methods in Physics Research*, A 651:297–304, 2011.

[51] H. Kinoshita, H Nariai, and F. Inasaka. Study of critical heat flux mechanism in flow boiling using bubble crowding model (Application to CHF in short tube and in tube with twisted tape under non-uniform heating conditions). *JSME International Journal*, 44(1):81–89, 2001.

[52] H. Kinoshita and T. Yoshida. Study on the mechanism of critical heat flux enhancement for subcooled flow boiling in a tube with internal twisted tape under nonuniform heating conditions. *Heat Transfer - Japanese Research*, 25:293–307, 1996.

[53] V.I. Kisina and A.I. Leont'ev. Burnout during upward flow of steam-water mixture through vertical tubes with spiral inserts. *Teploenergetika (Thermal Engineering)*, 1:65–70, 2006.

[54] V.I. Kisina and N.V. Tarasova. Structure of an adiabatic two-phase flow under the upward motion of a steam-water mixture in vertical tubes. *Teploenergetika (Thermal Engineering)*, 12:60–72 (Russian) 1006–1018 (English), 2004.

[55] J.A. Koski and C.D. Croessmann. Critical heat flux investigations for fusion-relevant conditions with the use of a rastered electron beam apparatus. In *ASME 88-WA/NE-3-Eng*, pages 1–7, Chicago, IL, December 1988. ASME.

[56] F. Kreith and O.K. Sonju. The decay of a turbulent swirl in a pipe. *Journal of Fluid Mechanics*, 22:257–271, 1965.

[57] A.F. Krug, Y.A. Kuzma-Kichta, and A.S. Komendantov. Generalization of data on critical heat fluxes for flow swirled using a tape. *Thermal Engineering*, 57(3):232–237, 2010.

[58] R.T. Jr. Lahey. *The Thermal Hydraulics of a Boiling Water Nuclear Reactor.* American Nuclear Society, 1977.

[59] L.K.H. Leung, D.C. Groeneveld, A. Teyssedou, and F. Aube. Pressure drop for steam and water flow in heated tubes. *Nuclear Engineering and Design*, 235:53–65, 2005.

[60] S. Levy. Forced convection subcooled boiling prediction of vapor volumetric fraction. *International Journal of Heat and Mass Transfer*, 10:951–965, 1967.

[61] R.F. Lopina and A. E. Bergles. Heat transfer and pressure drop in tape-generated swirl flow of single-phase water. *ASME Journal of Heat Transfer*, 91:434–442, 1969.

[62] J.A. Malen, N.E. Todreas, P. Hejzlar, P. Ferroni, and A. E. Bergles. Thermal hydraulic design of a hydride-fueled inverted PWR core. *Nuclear Engineering and Design*, 239:1471–1480, 2009.

[63] R. M. Manglik and A. E. Bergles. Heat transfer and pressure drop correlations for twisted-tape inserts in isothermal tubes: Part II -Transition and turbulent flows. *Transaction of the ASME*, 115:890–896, 1993.

[64] B. Matzner, J. Casterline, E.O. Moeck, and G.A. Wikhammer. Critical heat flux in long tubes at 1000 psia with and without swirl promoters. *ASME Paper*, No.65-WA/HT-30:–, 1965.

[65] V.K. Migay and L.K. Golubev. Friction and heat transfer in turbulent swirl flow with a variable swirl generator in a pipe. *Heat Transfer-Soviet Research*, 2(3):68–73, 1970.

[66] E.O. Moeck, G.A. Wikhammer, I.P.I MacDonald, and J.G. Collier, editors. *Two Methods of Improving the Dryout Heat Flux for High Pressure Steam/Water Flow*, number 2109, Chalk River, Ontario, 1964. AECL.

[67] C. Moussez, A. Rosuel, G. Sourioux, G. du Boucheron, and D. Eidelman. Ecoulements giratoires dans l'eau bouillante. *EURAEC Report*, 1114(Euratom Contract No. 058-61-7 RDF):1–98, 1965.

[68] H. Muller-Steinhagen and K. Heck. A simple friction pressure drop correlation for two-phase flow in pipes. *Chemical Engineering and Processing*, 20:297–308, 1986.

[69] A.F. Najafi, S.M. Mousavian, and K. Amini. Numerical investigations on swirl intensity decay rate for turbulent swirling flow in a fixed pipe. *International Journal of Mechanical Sciences*, 53:801–811, 2011.

[70] H Nariai and F. Inasaka, editors. *Critical Heat Flux of Subcooled Flow Boiling with Water*, Fourth International Topical Meeting on Nuclear Reactor Thermal-Hydraulics, 1989.

[71] H Nariai and F. Inasaka, editors. *Critical Heat Flux of Subcooled Flow Boiling in Tubes with Internal Twisted Tapes*, volume 7, San Francisco, 1991. Nuclear Thermal Hydraulics Conference.

[72] H Nariai, F. Inasaka, A. Ishikawa, and H. Kinoshita. Effect of internal twisted tape on critical heat flux of subcooled flow boiling under non-uniform heating condition. In *Proceedings of the 10th International Heat Transfer Conference*, volume 7, pages 521–526, Brighton, 1994.

[73] B. Pei. *Prediction of Critical Heat Flux in Flow Boiling at Low Qualities.* PhD thesis, University of Cincinnati, 1981.

[74] B.S. Pei and J. Weisman. Prediction of critical heat flux in flow boiling at low qualities. *International Journal of Heat and Mass Transfer*, 26(10):1463–1477, 1983.

[75] G. Peterlongo, R. Ravetta, B. Riva, L. Rubiera, and F.A. Tacconi. Large scale experiments on heat transfer and hydrodynamics with steam-water mixtures: Further critical power and pressure drop measurements in round vertical tubes with and without internal obstacles. *CISE Report*, R122:–, 1964.

[76] S.K. Saha, U.N. Gaitonde, and A.W. Date. Heat transfer and pressure drop characteristics of turbulent flow in circular tube fitted with regularly spaced twisted-tape elements. *Experimental Thermal and Fluid Science*, 3:632–640, 1990.

[77] H. Shakutsui, T. Suzuki, S. Takagaki, K. Yamashita, and K. Hayashi. Flow patterns in swirling gas-liquid two-phase flow in a vertical pipe. In *7th International Conference on Multiphase Flow*, pages 1–6, Tampa, FL USA, May 30-June 4 2010. ICMF.

[78] C.W. Snoek. A selection of new developments in multiphase flow measurement techniques. *Experimental Thermal and Fluid Science*, 3:60–73, 1990.

[79] F.W. Staub. Two-phase fluid modeling-the critical heat flux. *Nuclear Science and Engineering*, 35:190–199, 1969.

[80] A. Tanase, S.C. Cheng, D. Groeneveld, and Shan. J.Q. Diameter effect on critical heat flux. *Nuclear Engineering and Design*, 239:289–294, 2009.

[81] N.E. Todreas and M.S. Kazimi. *Nuclear Systems II: Elements of Thermal Hydraulic Design.* CRC Press, 2001.

[82] N.E. Todreas and M.S. Kazimi. *Nuclear Systems I: Thermal Hydraulic Fundamentals.* CRC Press, 2nd edition, 2012.

[83] L.S. Tong. Heat transfer in water-cooled nuclear reactors. *Nuclear Engineering and Design*, 6:301–324, 1967.

[84] L.S. Tong. Prediction of departure from nucleate boiling for an axially non-uniform heat flux distribution. *Journal of Nuclear Energy*, 21:241–248, 1967.

[85] L.S. Tong. Boiling crisis and critical heat flux. Technical Report TID-25887, USAEC Critical Review Series, 1972.

[86] L.S. Tong and Y.S. Tang. *Boiling Heat Transfer and Two-Phase Flow.* CRC Press, 2nd edition, 1997.

[87] W. Tong, A. E. Bergles, and M.K. Jensen. Critical heat flux and pressure drop of subcooled flow boiling in small-diameter tubes with twisted-tape inserts. *Journal of Enhanced Heat Transfer*, 3(2):95–108, 1996.

[88] S. Usman. Development of a phenomenological model for prediction of chf under low-quality and subcooled swirl flow conditions. Master's thesis, University of Cincinnati, 1993.

[89] A.N. Varava, A.V. Dedov, A.T. Komov, and S.A. Malakhovskii. Experimental investigation of critical heat flux under boiling in subcooled swirling flow under conditions of one-sided heating. *High Temperature*, 47(6):843–848, 2009.

[90] P.K. Vijayan. Introduction to instabilities in natural circulation systems, ictp. In *Lecture: T-6*, Trieste, Italy, June 2007.

[91] R. Viskanta. Critical heat flux for water in swirling flow. *Nuclear Science and Engineering*, 10:202–203, 1961.

[92] J. Weisman and L. Du. Computation of the effect of heat addition on interfacial shear in bubbly flow. *International Journal of Multiphase Flow*, 18(4):623–631, 1992.

[93] J. Weisman and S Ileslamlou. A phenomenological model for prediction of critical heat flux under highly subcooled conditions. *Fusion Technology*, 13:654–659, 1988.

[94] J. Weisman and B.S. Pei. Prediction of critical heat flux in flow boiling at low qualities. *International Journal of Heat and Mass Transfer*, 26(10):1463–1477, 1983.

[95] J. Weisman, J.Y. Yang, and S. Usman. A phenomenological model for boiling heat transfer and the critical heat flux in tubes containing twisted tapes. *International Journal of Heat and Mass Transfer*, 37(1):69–80, 1994.

[96] J. Weisman and S.H. Ying. A theoretically based critical heat flux prediction for rod bundles at PWR conditions. *Nuclear Engineering and Design*, 85:239–250, 1984.

[97] P.B. Whalley. The effect of swirl on critical heat flux in annular two-phase flow. *International Journal of Multiphase Flow*, 5:211–217, 1979.

[98] P.B. Whalley, P. Hutchinson, and G.F. Hewitt. The calculation of critical heat flux in forced convection boiling. In *5th International Heat Transfer Conference*, number B6.11, Tokyo, 1974.

[99] H.Y. Wu, H.E. Cheng, R.J. Shuai, and Q.T Zhou. An analytical model for decaying swirl flow and heat transfer inside a tube. *ASME Journal of Heat Transfer*, 122:204–208, 2000.

[100] J. Yang. *A Study of Heat Transfer Rates and the Critical Heat Flux under Subcooled Boiling Conditions.* PhD thesis, University of Cincinnati, 1990.

[101] J.Y. Yang and J. Weisman. A phenomenological model of subcooled flow boiling in the detached bubble region. *International Journal of Multiphase Flow*, 17(1):77–94, 1991.

[102] S.H. Ying and J. Weisman. Prediction of the critical heat flux in flow boiling at intermediate qualities. *International Journal of Heat and Mass Transfer*, 29(11):1639–1648, 1986.

[103] R. Zboray, J. Kickhofel, M. Damsohn, and H.M. Prasser. Cold-neutron tomography of annular flow and functional spacer performance in a model of a boiling water reactor fuel rod bundle. *Nuclear Engineering and Design*, 241:3201–3215, 2011.

Appendix A

Data

This section presents all of the data used for validating the original Usman model, as well as its extension to SLTTs. Also included in this section is the two-phase pressure drop data from Matzner et al. [64] , as well as all of the single-phase adiabatic swirl decay data that was used to validate the swirl decay model by Wu et al. [99]. The data appears in the following order:

- FLTT and SLTT data that was used to validate the new DNB model: Appendix A.1
- All FLTT and SLTT data outside the range of the new DNB model: Appendix A.2
- Two-phase pressure drop data: Appendix A.3
- Swirl decay data: Appendix A.4

A.1 Validation Data

The following tables present all of the data that was used to validate the new empirical DNB correlation. The FLTT data is shown in Table A.1 while the SLTT data is shown in Table A.3. The inlet enthalpy and heated length for SLTT data correspond to the enthalpy at and location of the downstream end of the last SLTT in the test section respectively.

Table A.1: FLTT CHF Data Used for Model Validation

Mass Flux [kg/m^2-s]	**Pressure [Pa]**	**Inlet Enthalpy [J/kg]**	**Heated Length [m]**	**Diameter [m]**	**Twist Ratio**	**Exp. CHF [W/m^2]**	**Pred. CHF [W/m^2]**
Viskanta							
678	13790000	368889	0.4572	0.00793	2.5	4036160	4109088.4
678	13790000	447494	0.4572	0.00793	2.5	3851371.6	4019489.1
678	13790000	422267	0.4572	0.00793	2.5	3986878.9	3884097.3
678	13790000	485013	0.4572	0.00793	2.5	3879861.3	3736465.4
678	13790000	620205	0.4572	0.00793	2.5	3506088.4	3687083.7
1356	13790000	783826	0.4572	0.00793	2.5	4978148.3	4179892.8
1356	13790000	985581	0.4572	0.00793	2.5	4351628.4	3609111.3
1356	13790000	1124000	0.4572	0.00793	2.5	3817297.6	3223322.1
2712	13790000	1490000	0.4572	0.00793	2.5	3826920.4	2742519.7
678	13790000	-46576	0.4572	0.00793	5	4538972.3	3809802.0
678	13790000	306047	0.4572	0.00793	5	3754071.4	3643361.3
678	13790000	607499	0.4572	0.00793	5	3184720.1	3594447.9
1356	13790000	723034	0.4572	0.00793	5	4356329.3	4340445.5
1356	13790000	795797	0.4572	0.00793	5	4126897.8	4056873.7
1356	13790000	820064	0.4572	0.00793	5	4121124.1	3854616.3
1356	13790000	870780	0.4572	0.00793	5	3974069.5	3625263.3
1356	13790000	901443	0.4572	0.00793	5	3957127.2	3504117.5
1356	13790000	1029000	0.4572	0.00793	5	3492869	3488055.8
1356	13790000	1115000	0.4572	0.00793	5	3347139.5	3214926.6
1356	13790000	1231000	0.4572	0.00793	5	3001269.5	2881792.7
1356	13790000	1346000	0.4572	0.00793	5	2723127.8	2422987.5
1356	13790000	1375000	0.4572	0.00793	5	2581279	2390781.6
2712	13790000	1063000	0.4572	0.00793	5	4826140.4	5862788.9
2712	13790000	1092000	0.4572	0.00793	5	4888104.6	5134344.4
2712	13790000	1196000	0.4572	0.00793	5	4321466.6	4466049.3

2712	13790000	1205000	0.4572	0.00793	5	4398070	4416879.8
2712	13790000	1295000	0.4572	0.00793	5	3805434.8	4149454
2712	13790000	1324000	0.4572	0.00793	5	3867399	3882044.9
2712	13790000	1387000	0.4572	0.00793	5	3497853.9	3569722.5
2712	13790000	1416000	0.4572	0.00793	5	3510347.6	3240372.2
2712	13790000	1503000	0.4572	0.00793	5	3036674.9	2726564.6
2712	13790000	1535000	0.4572	0.00793	5	3068032.4	2394921.3
Kisina et al.							
2100	14700000	1276000	2	0.011	11.35	1697540	1187803.1
2800	14700000	1464000	2	0.011	15.91	1450640	1334049.8
2800	14700000	1389000	2	0.011	15.91	1659700	1420004.4
Gambill et al.							
7845	1689000	109858	0.441198	0.006325	12.03	13430000	14876607
Tong et al.							
5100	1000000	97314	0.10512	0.00438	1.93	17712100	15544331
5100	1000000	97314	0.10512	0.00438	1.93	18495200	15150843
5100	1000000	97314	0.10512	0.00438	1.93	19492300	14682561
5100	1000000	97314	0.15696	0.00654	1.93	19181400	12116572
Nariai et al.							
6500	1080000	176813	0.1	0.006	2.61	18800000	18616086
6600	1080000	151733	0.1	0.006	2.94	18800000	20086686
6500	1080000	143373	0.1	0.006	9.44	15900000	21741639
6500	1080000	176813	0.1	0.006	3.62	18200000	18922481
6400	1080000	172633	0.1	0.006	2.71	18300000	18763671
6500	1080000	168453	0.1	0.006	2.64	18400000	19239330
6200	1470000	181335	0.1	0.006	9.44	17000000	21429281
6300	1470000	156262	0.1	0.006	3.91	17900000	22484171
6100	1470000	160441	0.1	0.006	2.61	19000000	21100749
Hata et al.							
3904	800000	359483	0.0595	0.006	3.39	12284800	11144574

3910	800000	350786	0.0595	0.006	3.39	12284800	11253683
3913	800000	345552	0.0595	0.006	3.39	11937100	11362610
3949	800000	282187	0.0595	0.006	3.39	12053000	12220984
3946	800000	287618	0.0595	0.006	3.39	11357600	12258690
3943	800000	292761	0.0595	0.006	3.39	10546400	12323015
3951	800000	278398	0.0595	0.006	3.39	11705300	12379290
3954	800000	273518	0.0595	0.006	3.39	12053000	12408167
3948	800000	283531	0.0595	0.006	3.39	10894000	12448051
3950	800000	279792	0.0595	0.006	3.39	11125800	12477659
3950	800000	281486	0.0595	0.006	3.39	10662300	12539793
3961	800000	259136	0.0595	0.006	3.39	12632500	12593947
3962	800000	256727	0.0595	0.006	3.39	11705300	12850710
3989	800000	199709	0.0595	0.006	3.39	14718500	13435472
3990	800000	197042	0.0595	0.006	3.39	14255000	13590259
4025	800000	85675	0.0595	0.006	3.39	17384100	17027332
4028	800000	71833	0.0595	0.006	3.39	17615900	17636321
6791	800000	366134	0.0595	0.006	3.39	16688700	14159384
6791	800000	366561	0.0595	0.006	3.39	16109300	14230690
6799	800000	358750	0.0595	0.006	3.39	16457000	14386706
6870	800000	289054	0.0595	0.006	3.39	14950300	17008637
6882	800000	275996	0.0595	0.006	3.39	16225200	17247545
6882	800000	276146	0.0595	0.006	3.39	15182100	17479771
6881	800000	277212	0.0595	0.006	3.39	14486800	17590682
6945	800000	200426	0.0595	0.006	3.39	18079500	20019846
6945	800000	200156	0.0595	0.006	3.39	17615900	20176496
7012	800000	77805	0.0595	0.006	3.39	22135800	25610858
7013	800000	73017	0.0595	0.006	3.39	21440400	26094731
3887	800000	373433	0.0595	0.006	2.39	10894000	11141088
3893	800000	364119	0.0595	0.006	2.39	11241700	11215421
3899	800000	354125	0.0595	0.006	2.39	10778100	11402268
3943	800000	276840	0.0595	0.006	2.39	12400700	12265330
3977	800000	207932	0.0595	0.006	2.39	14834400	13230745

3982	800000	195721	0.0595	0.006	2.39	13559600	13769084
4015	800000	94324	0.0595	0.006	2.39	16804600	16838198
4017	800000	83501	0.0595	0.006	2.39	17615900	16988628
4023	800000	39566	0.0595	0.006	2.39	18079500	19056559
6778	800000	368767	0.0595	0.006	2.39	15761600	14207518
6773	800000	373414	0.0595	0.006	2.39	14950300	14202523
6789	800000	358771	0.0595	0.006	2.39	14950300	14590127
6868	800000	280031	0.0595	0.006	2.39	17500000	16781825
6870	800000	277409	0.0595	0.006	2.39	15645700	17305095
6869	800000	279234	0.0595	0.006	2.39	15066200	17359974
6933	800000	202339	0.0595	0.006	2.39	18890700	19637286
6996	800000	91833	0.0595	0.006	2.39	22251700	24765154
6994	800000	96366	0.0595	0.006	2.39	20397400	25087686
7010	800000	39082	0.0595	0.006	2.39	24106000	27120964
3845	800000	386323	0.0595	0.006	4.45	9966890	11086334
3865	800000	354931	0.0595	0.006	4.45	10314600	11448918
3908	800000	279507	0.0595	0.006	4.45	11125800	12486090
3944	800000	204190	0.0595	0.006	4.45	13559600	13582517
3947	800000	196666	0.0595	0.006	4.45	14023200	13646981
3983	800000	79193	0.0595	0.006	4.45	15877500	18019270
3987	800000	55043	0.0595	0.006	4.45	16688700	18855521
3988	800000	44885	0.0595	0.006	4.45	17268200	19088639
6704	800000	374833	0.0595	0.006	4.45	12748300	14397584
6707	800000	372105	0.0595	0.006	4.45	13211900	14400786
6714	800000	365229	0.0595	0.006	4.45	12632500	14662951
6800	800000	279227	0.0595	0.006	4.45	15066200	17244497
6799	800000	281131	0.0595	0.006	4.45	14486800	17299562
6855	800000	214724	0.0595	0.006	4.45	17384100	19339546
6867	800000	198680	0.0595	0.006	4.45	17384100	20177299
6930	800000	81706	0.0595	0.006	4.45	20976800	25560279
6936	800000	62276	0.0595	0.006	4.45	21556300	26452135

Table A.3: SLTT CHF Data Used for Model Validation

Mass Flux [kg/m^2-s]	Pressure [Pa]	Inlet Enthalpy [J/kg]	Heated Length [m]	Diameter [m]	Initial Twist Ratio	Exp. CHF [W/m^2]	Pred. CHF [W/m^2]
Matzner et al.							
6835	6895000	1155000	1.219	0.01016	5	3133000	3248268.3
5411	6895000	1119000	1.219	0.01016	5	2940000	2956118.6
6727	6895000	1096000	1.219	0.01016	5	3464000	3442212.1
5398	6895000	1047000	1.219	0.01016	5	3407000	3199617.9
6754	6895000	1182000	1.219	0.01016	5	2883000	3135355.9
6781	6895000	1020000	2.438	0.01016	5	2625000	2742696.7
6781	6895000	963642	2.438	0.01016	5	2852000	2932108.0
6808	6895000	904496	2.438	0.01016	5	3186000	3043062.0
Hassid et al.							
3800	6963000	1094000	1.566	0.0151	0.907	2898000	2921003.6
3800	6963000	1180000	0.766	0.0151	0.907	4487000	3912600.2

A.2 Additional CHF Data

The following tables present all additional FLTT and SLTT data that was not used to validate the new model. All of this data falls outside the range of the new correlation.

Table A.5: Other FLTT CHF Data

Mass Flux [kg/m^2-s]	**Pressure [Pa]**	**Inlet Enthalpy [J/kg]**	**Heated Length [m]**	**Diameter [m]**	**Twist Ratio**	**Exp. CHF [W/m^2]**
Matzner et al.						
2889	6895000	1281000	4.877	0.01016	15	1347000
2780	6895000	1161000	4.877	0.01016	15	1486000
2848	6895000	1048000	4.877	0.01016	15	1659000
2862	6895000	915226	4.877	0.01016	15	1861000
1451	6895000	1298000	4.877	0.01016	15	981100
1465	6895000	1177000	4.877	0.01016	15	1076000
1533	6895000	1055000	4.877	0.01016	15	1148000
1424	6895000	946007	4.877	0.01016	15	1139000
1397	6895000	856008	4.877	0.01016	15	1167000
1261	6895000	832630	4.877	0.01016	15	1120000
1410	6895000	623576	4.877	0.01016	15	1366000
2875	6895000	875865	4.877	0.01016	15	1893000
2726	6895000	572488	4.877	0.01016	15	2161000
2102	6895000	1279000	4.877	0.01016	15	1284000
2129	6895000	1139000	4.877	0.01016	15	1420000
2156	6895000	1013000	4.877	0.01016	15	1552000
2089	6895000	881529	4.877	0.01016	15	1609000
2129	6895000	815644	4.877	0.01016	15	1681000
2034	6895000	587917	4.877	0.01016	15	1801000
4272	6895000	1259000	4.877	0.01016	15	1454000
4286	6895000	1159000	4.877	0.01016	15	1852000
4245	6895000	1064000	4.877	0.01016	15	2215000

4218	6895000	982697	4.877	0.01016	15	2303000
4299	6895000	846212	4.877	0.01016	15	2423000
4326	6895000	721638	4.877	0.01016	15	2555000
4516	6895000	458502	4.877	0.01016	15	3069000
4598	6895000	947819	4.877	0.01016	15	2662000
Viskanta						
678	13790000	699911	0.4572	0.00793	2.5	3404434
678	13790000	715435	0.4572	0.00793	2.5	3428665
678	13790000	924571	0.4572	0.00793	2.5	3028702
678	13790000	1142000	0.4572	0.00793	2.5	2719556
678	13790000	1365000	0.4572	0.00793	2.5	2195839
678	13790000	1556000	0.4572	0.00793	2.5	1707347
1356	13790000	1334000	0.4572	0.00793	2.5	3150185
1356	13790000	1519000	0.4572	0.00793	2.5	2951881
1356	13790000	1557000	0.4572	0.00793	2.5	2769421
1356	13790000	1597000	0.4572	0.00793	2.5	2595811
1356	13790000	1673000	0.4572	0.00793	2.5	2259759
2712	13790000	1535000	0.4572	0.00793	2.5	3510884
678	13790000	940711	0.4572	0.00793	5	2654402
678	13790000	1136000	0.4572	0.00793	5	2201897
678	13790000	1167000	0.4572	0.00793	5	2259810
678	13790000	1399000	0.4572	0.00793	5	1715497
678	13790000	1409000	0.4572	0.00793	5	1815176
1356	13790000	1533000	0.4572	0.00793	5	2167826
2712	13790000	1632000	0.4572	0.00793	5	2611479
Kisina et al.						
2000	14700000	1232000	2	0.008	15.625	1747750
2000	14700000	1624000	2	0.008	15.625	1165160
2000	14700000	2200000	2	0.008	15.625	479913
1400	14700000	1465000	2	0.011	11.35	1207340
1400	14700000	1686000	2	0.011	11.35	945318

2100	14700000	1718000	2	0.011	11.35	1198520
2650	14700000	1495000	2	0.011	13.635	1783180
2650	14700000	1689000	2	0.011	13.635	1229520
2800	14700000	1616000	2	0.011	13.635	1702730
2800	14700000	1789000	2	0.011	13.635	1245530
1400	14700000	1438000	2	0.011	15.91	940906
1400	14700000	1410000	2	0.011	15.91	1055630
1400	14700000	1590000	2	0.011	15.91	862664
1400	14700000	1861000	2	0.011	15.91	514682
2800	14700000	1596000	2	0.011	15.91	1197010
2000	14700000	1878000	2	0.01427	5	1320020
2000	14700000	2062000	2	0.01427	5	817934
2600	14700000	1854000	2	0.01427	5	1665180
2600	14700000	1966000	2	0.01427	5	1360420
2600	14700000	2191000	2	0.01427	5	845141
Gambill et al.						
4476	131700	69813	0.266192	0.010211	2.99	11420000
4870	135800	74705	0.20447	0.010211	2.99	14980000
7376	134400	37137	0.41148	0.007747	2.42	11230000
11703	206200	42390	0.20701	0.007747	2.42	21610000
18501	379200	46905	0.1016	0.007747	2.42	52740000
18501	379200	45989	0.051308	0.007747	2.42	59310000
32816	139300	90638	0.09652	0.004597	2.08	64350000
33503	158600	80399	0.062992	0.004597	2.08	78710000
33508	148900	76166	0.037846	0.004597	2.08	88330000
24652	118600	90419	0.09652	0.004597	2.08	53380000
25751	122000	87578	0.0635	0.004597	2.08	65460000
24443	120700	87170	0.0381	0.004597	2.08	78140000
16072	103400	78735	0.09652	0.004597	2.08	31920000
16802	104100	80110	0.062738	0.004597	2.08	36210000
16740	103400	80570	0.0381	0.004597	2.08	45960000

45067	204800	97199	0.03683	0.004597	2.08	1.2E+008
45453	192400	75682	0.09525	0.004597	2.08	98490000
47555	204800	74094	0.0635	0.004597	2.08	1.0E+008
10777	108200	75856	0.305562	0.006325	2.3	10560000
10354	3758000	104073	0.3048	0.006325	2.3	16210000
20493	240600	104732	0.3048	0.004801	7.7	21770000
20509	3241000	116125	0.3048	0.004801	7.7	21510000
22602	3413000	145074	0.304038	0.003454	2.46	29680000
21116	101400	102528	0.3048	0.003454	2.46	34130000
9466	322000	79619	0.290576	0.006325	2.3	18900000
8916	232400	83207	0.287274	0.006325	4.94	15230000
9972	250300	99474	0.290576	0.006325	8.03	14220000
22863	848100	85639	0.290576	0.004801	2.49	43530000
22482	208900	93450	0.290576	0.004801	4.98	28860000
8278	655000	247349	0.289052	0.006325	2.3	16120000
22425	3068000	91469	0.288544	0.004801	2.49	34450000
21681	197900	77433	0.290068	0.004801	2.49	34700000
41197	199900	106212	0.278892	0.003454	7.84	41360000
16221	584000	86669	0.2794	0.006325	4.95	24010000
8443	322000	117131	0.440436	0.006325	12.03	11480000
7852	308200	80922	0.292608	0.006325	8.03	14030000
27307	1551000	90953	0.14859	0.006325	4.95	37950000
4494	166200	85403	0.292608	0.006325	2.47	8738000
14141	390900	76944	0.28956	0.006325	8.03	21420000
Moeck et al.						
873	6944000	1874000	1.016	0.01143	5.55	2031000
1004	6998000	1836000	1.016	0.01143	5.55	2336000
1043	6924000	1798000	1.016	0.01143	5.55	2425000
1138	6912000	1738000	1.016	0.01143	5.55	2647000
1005	6928000	1817000	1.016	0.01143	5.55	2338000
869.1	6948000	1839000	1.016	0.01143	5.55	2021000

877.8	6948000	1831000	1.016	0.01143	5.55	2042000
1012	6928000	1815000	1.016	0.01143	5.55	2353000
1145	6912000	1726000	1.016	0.01143	5.55	2663000
391.3	6985000	1715000	1.016	0.01143	5.55	910100
519.7	6975000	1748000	1.016	0.01143	5.55	1209000
647.2	6963000	1765000	1.016	0.01143	5.55	1505000
701.8	6964000	1814000	1.016	0.01143	5.55	1633000
830.4	6945000	1814000	1.016	0.01143	5.55	1932000
963.3	6930000	1756000	1.016	0.01143	5.55	2241000
1029	6923000	1698000	1.016	0.01143	5.55	2394000
1094	6917000	1650000	1.016	0.01143	5.55	2545000
964	6998000	1764000	1.016	0.01143	5.55	2242000
871.6	6959000	1851000	1.016	0.01143	34.5	2027000
1004	6948000	1751000	1.016	0.01143	34.5	2336000
1136	6940000	1642000	1.016	0.01143	34.5	2642000
392	6986000	1832000	1.016	0.01143	34.5	911677
518.2	6977000	1815000	1.016	0.01143	34.5	1205000
645.8	6969000	1725000	1.016	0.01143	34.5	1502000
702.5	6972000	1835000	1.016	0.01143	34.5	1634000
836.1	6961000	1778000	1.016	0.01143	34.5	1945000
966.7	6952000	1678000	1.016	0.01143	34.5	2249000
1093	6946000	1557000	1.016	0.01143	34.5	2543000
877.5	6998000	1838000	1.016	0.01143	34.5	2041000
Brevi et al.						
758	5066250	832612	0.2	0.01	3	1567000
758	5066250	847319	0.2	0.01	3	1548000
758	5066250	870853	0.2	0.01	3	1516000
758	5066250	892420	0.2	0.01	3	1483000
758	5066250	920883	0.2	0.01	3	1471000
758	5066250	946387	0.2	0.01	3	1446000
758	5066250	974836	0.2	0.01	3	1420000

758	5066250	996415	0.2	0.01	3	1399000
758	5066250	1013000	0.2	0.01	3	1381000
758	5066250	1039000	0.2	0.01	3	1353000
758	5066250	1059000	0.2	0.01	3	1344000
758	5066250	1084000	0.2	0.01	3	1326000
758	5066250	1110000	0.2	0.01	3	1314000
758	5066250	1129000	0.2	0.01	3	1305000
915	5066250	868237	0.2	0.01	3	1838000
915	5066250	882944	0.2	0.01	3	1816000
915	5066250	906503	0.2	0.01	3	1810000
915	5066250	931046	0.2	0.01	3	1805000
915	5066250	952623	0.2	0.01	3	1781000
915	5066250	975177	0.2	0.01	3	1752000
915	5066250	997738	0.2	0.01	3	1730000
915	5066250	1017000	0.2	0.01	3	1702000
915	5066250	1040000	0.2	0.01	3	1677000
915	5066250	1061000	0.2	0.01	3	1648000
915	5066250	1090000	0.2	0.01	3	1600000
1038	5066250	846099	0.2	0.01	3	2272000
1038	5066250	858835	0.2	0.01	3	2242000
1038	5066250	882374	0.2	0.01	3	2217000
1038	5066250	903908	0.2	0.01	3	2152000
1038	5066250	929373	0.2	0.01	3	2089000
1038	5066250	953885	0.2	0.01	3	2053000
1038	5066250	976435	0.2	0.01	3	2020000
1038	5066250	1002000	0.2	0.01	3	2004000
1038	5066250	1025000	0.2	0.01	3	1985000
1038	5066250	1049000	0.2	0.01	3	1955000
1038	5066250	1073000	0.2	0.01	3	1930000
1038	5066250	1094000	0.2	0.01	3	1904000

Moussez et al.

4450	7000000	1327200	0.8	0.01	3	2610000
5850	7000000	1282050	0.8	0.01	3	2915000
Tong et al.						
5049.42	1000000	97314	0.05856	0.00244	1.93	17000000
5051.91	1000000	97314	0.05856	0.00244	1.93	17857100
5053.16	1000000	97314	0.05856	0.00244	1.93	18285700
5058.55	1000000	97314	0.05856	0.00244	1.93	20142900
9928.99	1000000	97314	0.05856	0.00244	1.93	35571400
15016.2	1000000	97314	0.05856	0.00244	1.93	45571400
18290.3	1000000	97314	0.05856	0.00244	1.93	51857100
5100	1000000	97314	0.05856	0.00244	1.93	18090900
5100	1000000	97314	0.05856	0.00244	1.93	20085100
5100	1000000	97314	0.05856	0.00244	1.93	17022300
10000	1000000	97314	0.05856	0.00244	1.93	35825900
10000	1000000	97314	0.10512	0.00438	1.93	30390000
10000	1000000	97314	0.10512	0.00438	1.93	31173400
15000	391963	96748	0.05856	0.00244	7.1	23118300
15000	776465	97106	0.05856	0.00244	7.1	27132600
15000	1070820	97380	0.05856	0.00244	7.1	28100400
15000	1397940	97684	0.05856	0.00244	7.1	31075300
15000	1000000	96834	0.05856	0.00244	1.93	45650700
15000	1000000	181104	0.05856	0.00244	1.93	36575000
15000	1000000	188455	0.05856	0.00244	1.93	32570700
15000	1000000	272517	0.05856	0.00244	1.93	28558500
15000	1000000	313367	0.05856	0.00244	1.93	27267500
15000	1000000	337457	0.05856	0.00244	1.93	25766400
15000	1000000	97314	0.0066426	0.00244	1.93	67755500
15000	1000000	97314	0.0316319	0.00244	1.93	52177400
15000	1000000	97314	0.0568715	0.00244	1.93	45565700
15000	1000000	97314	0.0936496	0.00244	1.93	31936500
15000	1000000	97314	0.0938861	0.00244	1.93	30401400

Drizius et al.						
4500	471000	-60246	0.141	0.0016	2.56	5580000
7770	503000	88187	0.141	0.0016	2.73	9350000
11620	548000	86098	0.141	0.0016	2.27	15100000
14020	685000	99498	0.141	0.0016	2.2	18600000
18870	781000	99295	0.141	0.0016	2.24	24600000
5400	442000	11773	0.141	0.0016	5.07	6150000
9590	478000	45590	0.141	0.0016	5.12	11900000
13990	526000	96960	0.141	0.0016	5.17	17500000
17320	643000	101551	0.141	0.0016	4.92	20900000
22560	581000	100821	0.141	0.0016	4.92	27900000
6060	421000	64726	0.141	0.0016	9.49	6660000
9700	430000	103953	0.141	0.0016	9.66	10300000
13510	479000	76498	0.141	0.0016	9.4	15300000
17570	620000	69661	0.141	0.0016	10.25	20200000
24800	511000	99733	0.141	0.0016	9.87	29000000
4750	484000	29877	0.037	0.0016	2.37	20200000
9670	591000	69072	0.037	0.0016	1.25	43500000
13760	711000	83110	0.037	0.0016	2.23	62500000
19300	794000	80255	0.037	0.0016	2.25	81300000
14390	460000	166320	0.037	0.0016	2.19	54000000
15040	1335000	109132	0.037	0.0016	2.3	65300000
15840	393000	102255	0.037	0.0016	5.11	59700000
15840	709000	94342	0.037	0.0016	10.12	53000000
15840	605000	70113	0.09	0.0016	9.88	30600000
15840	609000	106916	0.09	0.0016	3.06	33100000
Nariai et al.						
5300	700000	189019	0.1	0.006	3.92	16100000
6700	1080000	135012	0.1	0.006	0	16000000
6200	1470000	156262	0.1	0.006	0	17200000
6300	590000	142931	0.1	0.006	0	16300000

6000	590000	151294	0.1	0.006	9.44	15500000
6100	590000	147113	0.1	0.006	2.71	19700000
6300	590000	188923	0.1	0.006	2.64	19100000
6400	290000	138479	0.1	0.006	0	12800000
6100	290000	159390	0.1	0.006	9.44	14200000
6400	290000	155208	0.1	0.006	2.71	14900000
6100	290000	159390	0.1	0.006	2.64	15400000
6200	290000	151026	0.1	0.006	2.61	13700000
6300	200000	138397	0.1	0.006	0	12100000
6200	200000	142580	0.1	0.006	9.44	13100000
6200	200000	142580	0.1	0.006	3.91	12900000
6200	200000	155127	0.1	0.006	2.71	13400000
6200	200000	146763	0.1	0.006	2.71	13300000
6200	290000	151026	0.1	0.006	2.61	13700000
7400	100000	167585	0.1	0.006	0	9300000
7400	100000	167585	0.1	0.006	8.66	10100000
7400	100000	167585	0.1	0.006	4.27	12000000
7400	100000	163403	0.1	0.006	2.67	13100000
7400	100000	163403	0.1	0.006	0	9400000
7400	100000	167585	0.1	0.006	8.66	11000000
7400	100000	163403	0.1	0.006	4.27	11400000
7400	100000	167585	0.1	0.006	2.67	14200000
Hata et al						
9687	800000	371965	0.0595	0.006	3.39	15182100
9726	800000	347310	0.0595	0.006	3.39	15877500
9820	800000	281197	0.0595	0.006	3.39	20049700
9825	800000	277194	0.0595	0.006	3.39	19238400
9822	800000	279914	0.0595	0.006	3.39	18195400
9832	800000	271519	0.0595	0.006	3.39	19933800
9916	800000	200537	0.0595	0.006	3.39	22135800
9918	800000	198037	0.0595	0.006	3.39	21672200

9925	800000	191265	0.0595	0.006	3.39	21556300
10002	800000	96934	0.0595	0.006	3.39	27119200
10005	800000	90380	0.0595	0.006	3.39	28046400
10020	800000	57135	0.0595	0.006	3.39	26539700
10019	800000	57560	0.0595	0.006	3.39	24221900
10023	800000	45007	0.0595	0.006	3.39	24453600
13082	800000	355811	0.0595	0.006	3.39	20976800
13245	800000	270466	0.0595	0.006	3.39	23294700
13357	800000	199463	0.0595	0.006	3.39	25264900
13361	800000	196225	0.0595	0.006	3.39	25380800
13489	800000	69298	0.0595	0.006	3.39	34072800
13495	800000	57926	0.0595	0.006	3.39	30016600
13498	800000	49337	0.0595	0.006	3.39	32450300
9651	800000	381831	0.0595	0.006	2.39	20397400
9651	800000	382084	0.0595	0.006	2.39	19238400
9665	800000	373037	0.0595	0.006	2.39	20397400
9677	800000	365350	0.0595	0.006	2.39	18658900
9771	800000	301938	0.0595	0.006	2.39	22831100
9777	800000	297700	0.0595	0.006	2.39	21324500
9783	800000	293024	0.0595	0.006	2.39	22135800
9774	800000	299460	0.0595	0.006	2.39	20513200
9774	800000	299840	0.0595	0.006	2.39	20049700
9892	800000	202865	0.0595	0.006	2.39	22831100
9889	800000	205607	0.0595	0.006	2.39	20281500
9992	800000	73688	0.0595	0.006	2.39	28278100
9995	800000	66791	0.0595	0.006	2.39	29668900
9989	800000	79929	0.0595	0.006	2.39	26307900
13016	800000	375230	0.0595	0.006	2.39	23874200
13013	800000	376517	0.0595	0.006	2.39	22947000
13021	800000	372550	0.0595	0.006	2.39	23294700
13019	800000	373748	0.0595	0.006	2.39	21904000
13176	800000	294793	0.0595	0.006	2.39	25844400

13184	800000	290413	0.0595	0.006	2.39	25844400
13195	800000	284375	0.0595	0.006	2.39	24917200
13312	800000	212641	0.0595	0.006	2.39	28509900
13319	800000	208165	0.0595	0.006	2.39	28046400
13317	800000	209175	0.0595	0.006	2.39	27698700
13329	800000	201205	0.0595	0.006	2.39	29437100
13449	800000	90921	0.0595	0.006	2.39	28741700
13461	800000	72209	0.0595	0.006	2.39	32682100
13464	800000	66903	0.0595	0.006	2.39	31986800
9560	800000	376871	0.0595	0.006	4.45	16572800
9578	800000	365047	0.0595	0.006	4.45	15877500
9690	800000	287453	0.0595	0.006	4.45	17268200
9710	800000	272036	0.0595	0.006	4.45	18890700
9716	800000	267522	0.0595	0.006	4.45	17847700
9784	800000	208590	0.0595	0.006	4.45	21556300
9784	800000	208962	0.0595	0.006	4.45	20745000
9883	800000	86560	0.0595	0.006	4.45	28625800
9882	800000	88834	0.0595	0.006	4.45	27698700
9884	800000	85319	0.0595	0.006	4.45	27119200
9881	800000	89932	0.0595	0.006	4.45	25612600
12909	800000	364760	0.0595	0.006	4.45	18079500
13049	800000	293246	0.0595	0.006	4.45	22251700
13066	800000	283604	0.0595	0.006	4.45	21092700
13196	800000	201730	0.0595	0.006	4.45	24453600
13208	800000	193659	0.0595	0.006	4.45	24221900
13319	800000	87552	0.0595	0.006	4.45	33725200
13320	800000	86709	0.0595	0.006	4.45	33029800
13320	800000	86353	0.0595	0.006	4.45	30711900
13322	800000	82450	0.0595	0.006	4.45	31523200
13325	800000	78055	0.0595	0.006	4.45	31523200

Feinstein et al.

15476	344737	173731	0.102	0.00635	2	31590000
19595	344737	182842	0.102	0.00635	2	37220000
38030	344737	224933	0.102	0.00635	2	47330000
51181	344737	221304	0.102	0.00635	2	66580000
51271	344737	223839	0.102	0.00635	2	64680000
64241	344737	217367	0.102	0.00635	2	87510000
19692	344737	89804	0.102	0.00635	2	30320000
39426	344737	100772	0.102	0.00635	2	53980000
66414	344737	111930	0.102	0.00635	2	79390000
67058	344737	104696	0.102	0.00635	2	87710000
15699	344737	225109	0.102	0.00635	4	19490000
30808	344737	235477	0.102	0.00635	4	33280000
30956	344737	254592	0.102	0.00635	4	24230000
39096	344737	253555	0.102	0.00635	4	31240000
67242	344737	248202	0.102	0.00635	4	59330000
19874	344737	126697	0.102	0.00635	4	19190000
20188	344737	114798	0.102	0.00635	4	23230000
39762	344737	124797	0.102	0.00635	4	39570000
68094	344737	131406	0.102	0.00635	4	60760000
16264	344737	243868	0.102	0.00635	6	15440000
37888	344737	257898	0.102	0.00635	6	27710000
53041	344737	242784	0.102	0.00635	6	51270000
66999	344737	261878	0.102	0.00635	6	44850000
20135	344737	120639	0.102	0.00635	6	21340000
39107	344737	127187	0.102	0.00635	6	37460000
67793	344737	128624	0.102	0.00635	6	63420000
67999	344737	143657	0.102	0.00635	6	47710000

Table A.7: Other SLTT CHF Data

Mass Flux [kg/m^2-s]	**Pressure [Pa]**	**Inlet Enthalpy [J/kg]**	**Heated Length [m]**	**Diameter [m]**	**Twist Ratio**	**Exp. CHF [W/m^2]**
Matzner et al.						
2835	6895000	1617000	1.219	0.01016	5	1688000
2848	6895000	1656000	1.219	0.01016	5	1606000
4272	6895000	1613000	1.219	0.01016	5	2000000
4231	6895000	1547000	1.219	0.01016	5	2211000
4245	6895000	1527000	1.219	0.01016	5	2401000
4259	6895000	1375000	1.219	0.01016	5	2584000
2902	6895000	1471000	1.219	0.01016	5	2095000
2862	6895000	1543000	1.219	0.01016	5	1899000
1465	6895000	1855000	1.219	0.01016	5	1205000
1410	6895000	1783000	1.219	0.01016	5	1325000
1424	6895000	1717000	1.219	0.01016	5	1429000
1424	6895000	1588000	1.219	0.01016	5	1555000
6903	6895000	1517000	1.219	0.01016	5	2571000
6903	6895000	1426000	1.219	0.01016	5	2748000
6822	6895000	1387000	1.219	0.01016	5	3312000
9670	6895000	1270000	1.219	0.01016	5	3817000
5547	6895000	1540000	1.219	0.01016	5	2461000
5561	6895000	1447000	1.219	0.01016	5	2653000
5438	6895000	1385000	1.219	0.01016	5	2956000
5547	6895000	1212000	1.219	0.01016	5	2776000
4150	6895000	1223000	1.219	0.01016	5	2662000
4082	6895000	1104000	1.219	0.01016	5	2868000
6740	6895000	1303000	1.219	0.01016	5	3319000
5371	6895000	1323000	1.219	0.01016	5	2962000
2821	6895000	1557000	2.438	0.01016	5	981100
2821	6895000	1467000	2.438	0.01016	5	1161000

2835	6895000	1388000	2.438	0.01016	5	1319000
2821	6895000	1285000	2.438	0.01016	5	1467000
2821	6895000	1228000	2.438	0.01016	5	1587000
4231	6895000	1494000	2.438	0.01016	5	1246000
2740	6895000	1460000	2.438	0.01016	5	1186000
4042	6895000	1407000	2.438	0.01016	5	1571000
4096	6895000	1338000	2.438	0.01016	5	1738000
4109	6895000	1267000	2.438	0.01016	5	1918000
3974	6895000	1474000	2.438	0.01016	5	1347000
4910	6895000	1430000	2.438	0.01016	5	1653000
5506	6895000	1345000	2.438	0.01016	5	2025000
5479	6895000	1241000	2.438	0.01016	5	2281000
2821	6895000	1194000	2.438	0.01016	5	1735000
2712	6895000	1118000	2.438	0.01016	5	1883000
4082	6895000	1171000	2.438	0.01016	5	2095000
5479	6895000	1100000	2.438	0.01016	5	2372000
4096	6895000	1070000	2.438	0.01016	5	2287000
5276	6895000	1007000	2.438	0.01016	5	2587000
1438	6895000	1667000	2.438	0.01016	5	798100
1424	6895000	1551000	2.438	0.01016	5	905400
1343	6895000	1486000	2.438	0.01016	5	959000
1397	6895000	1389000	2.438	0.01016	5	1104000
1370	6895000	1290000	2.438	0.01016	5	1224000
5398	6895000	1444000	2.438	0.01016	5	1549000
6646	6895000	1432000	2.438	0.01016	5	1738000
6632	6895000	1363000	2.438	0.01016	5	2079000
6686	6895000	1285000	2.438	0.01016	5	2366000
6835	6895000	1210000	2.438	0.01016	5	2508000
6903	6895000	1097000	2.438	0.01016	5	2445000
8761	6895000	1335000	2.438	0.01016	5	2502000
9494	6895000	1260000	2.438	0.01016	5	2994000

9792	6895000	1122000	2.438	0.01016	5	2909000
9548	6895000	1059000	2.438	0.01016	5	3054000
9575	6895000	1004000	2.438	0.01016	5	3451000
9561	6895000	944007	2.438	0.01016	5	3795000
Hassid et al.						
1100	5001000	1197000	1.51	0.0151	1.02	2198000
1100	5001000	1311000	1.51	0.0151	1.02	2059000
1100	5001000	1480000	1.51	0.0151	1.02	1848000
2200	5001000	1050000	1.51	0.0151	1.02	2727000
2200	5001000	1195000	1.51	0.0151	1.02	2597000
2200	5001000	1278000	1.51	0.0151	1.02	2597000
2200	5001000	1401000	1.51	0.0151	1.02	2442000
2200	5001000	1499000	1.51	0.0151	1.02	2125000
3800	5001000	999816	1.51	0.0151	1.02	3175000
3800	5001000	1128000	1.51	0.0151	1.02	3126000
3800	5001000	1247000	1.51	0.0151	1.02	3427000
3800	5001000	1344000	1.51	0.0151	1.02	3403000
3800	5001000	1506000	1.51	0.0151	1.02	2816000
1100	5001000	1230000	1.51	0.0151	0.907	2165000
1100	5001000	1297000	1.51	0.0151	0.907	2068000
1100	5001000	1492000	1.51	0.0151	0.907	1823000
2200	5001000	1076000	1.51	0.0151	0.907	2727000
2200	5001000	1214000	1.51	0.0151	0.907	2654000
2200	5001000	1304000	1.51	0.0151	0.907	2613000
2200	5001000	1389000	1.51	0.0151	0.907	2450000
2200	5001000	1506000	1.51	0.0151	0.907	2068000
3800	5001000	1016000	1.51	0.0151	0.907	3435000
3800	5001000	1085000	1.51	0.0151	0.907	3297000
3800	5001000	1157000	1.51	0.0151	0.907	3280000
3800	5001000	1237000	1.51	0.0151	0.907	3451000
3800	5001000	1328000	1.51	0.0151	0.907	3321000

3800	5001000	1480000	1.51	0.0151	0.907	2841000
1100	5001000	1195000	1.51	0.0151	0.572	2190000
1100	5001000	1332000	1.51	0.0151	0.572	2059000
1100	5001000	1473000	1.51	0.0151	0.572	1799000
2200	5001000	1045000	1.51	0.0151	0.572	2890000
2200	5001000	1204000	1.51	0.0151	0.572	2727000
2200	5001000	1290000	1.51	0.0151	0.572	2621000
2200	5001000	1420000	1.51	0.0151	0.572	2320000
2200	5001000	1499000	1.51	0.0151	0.572	1946000
3800	5001000	1030000	1.51	0.0151	0.572	3679000
3800	5001000	1145000	1.51	0.0151	0.572	3468000
3800	5001000	1245000	1.51	0.0151	0.572	3549000
3800	5001000	1313000	1.51	0.0151	0.572	3468000
3800	5001000	1466000	1.51	0.0151	0.572	2906000
1100	5001000	1221000	1.51	0.0151	0.907	2175000
1100	5001000	1291000	1.51	0.0151	0.907	2062000
1100	5001000	1481000	1.51	0.0151	0.907	1851000
2200	5001000	1077000	1.51	0.0151	0.907	2735000
2200	5001000	1212000	1.51	0.0151	0.907	2646000
2200	5001000	1289000	1.51	0.0151	0.907	2597000
2200	5001000	1385000	1.51	0.0151	0.907	2459000
2200	5001000	1502000	1.51	0.0151	0.907	2086000
3800	5001000	1015000	1.51	0.0151	0.907	3433000
3800	5001000	1085000	1.51	0.0151	0.907	3303000
3800	5001000	1159000	1.51	0.0151	0.907	3279000
3800	5001000	1238000	1.51	0.0151	0.907	3458000
3800	5001000	1325000	1.51	0.0151	0.907	3303000
3800	5001000	1481000	1.51	0.0151	0.907	2841000
1100	5001000	1188000	1.51	0.0151	0.907	2191000
1100	5001000	1325000	1.51	0.0151	0.907	2029000
1100	5001000	1490000	1.51	0.0151	0.907	1826000
2200	5001000	1058000	1.51	0.0151	0.907	2751000

2200	5001000	1221000	1.51	0.0151	0.907	2711000
2200	5001000	1262000	1.51	0.0151	0.907	2662000
2200	5001000	1394000	1.51	0.0151	0.907	2208000
2200	5001000	1495000	1.51	0.0151	0.907	1964000
3800	5001000	995910	1.51	0.0151	0.907	3506000
3800	5001000	1140000	1.51	0.0151	0.907	3352000
3800	5001000	1231000	1.51	0.0151	0.907	3539000
3800	5001000	1344000	1.51	0.0151	0.907	3450000
3800	5001000	1473000	1.51	0.0151	0.907	3011000
1100	5001000	1198000	1.51	0.0151	1.02	2234000
1100	5001000	1356000	1.51	0.0151	1.02	2003000
2200	5001000	1063000	1.51	0.0151	1.02	2714000
2200	5001000	1126000	1.51	0.0151	1.02	2648000
2200	5001000	1140000	1.51	0.0151	1.02	2607000
2200	5001000	1219000	1.51	0.0151	1.02	2637000
2200	5001000	1306000	1.51	0.0151	1.02	2569000
2200	5001000	1354000	1.51	0.0151	1.02	2511000
2200	5001000	1431000	1.51	0.0151	1.02	2258000
2200	5001000	1520000	1.51	0.0151	1.02	2054000
3800	5001000	990628	1.51	0.0151	1.02	3354000
3800	5001000	1063000	1.51	0.0151	1.02	3231000
3800	5001000	1243000	1.51	0.0151	1.02	3362000
3800	5001000	1343000	1.51	0.0151	1.02	3302000
3800	5001000	1495000	1.51	0.0151	1.02	2789000
1100	5001000	1229000	1.51	0.0151	1.02	2168000
1100	5001000	1311000	1.51	0.0151	1.02	2053000
1100	5001000	1477000	1.51	0.0151	1.02	1821000
2200	5001000	1049000	1.51	0.0151	1.02	2739000
2200	5001000	1193000	1.51	0.0151	1.02	2605000
2200	5001000	1282000	1.51	0.0151	1.02	2586000
2200	5001000	1402000	1.51	0.0151	1.02	2429000

2200	5001000	1496000	1.51	0.0151	1.02	2119000
3800	5001000	1002000	1.51	0.0151	1.02	3168000
3800	5001000	1128000	1.51	0.0151	1.02	3100000
3800	5001000	1238000	1.51	0.0151	1.02	3451000
3800	5001000	1341000	1.51	0.0151	1.02	3375000
3800	5001000	1512000	1.51	0.0151	1.02	2780000
1100	5001000	1231000	1.566	0.0151	0.907	2065000
1100	5001000	1373000	1.566	0.0151	0.907	1911000
1100	5001000	1486000	1.566	0.0151	0.907	1682000
1100	5001000	1523000	1.566	0.0151	0.907	1822000
1100	5001000	1695000	1.566	0.0151	0.907	1465000
1100	5001000	1817000	1.566	0.0151	0.907	1282000
1100	5001000	1894000	1.566	0.0151	0.907	1182000
2200	5001000	1084000	1.566	0.0151	0.907	2672000
2200	5001000	1251000	1.566	0.0151	0.907	2556000
2200	5001000	1304000	1.566	0.0151	0.907	2464000
2200	5001000	1381000	1.566	0.0151	0.907	2300000
2200	5001000	1483000	1.566	0.0151	0.907	2154000
2200	5001000	1522000	1.566	0.0151	0.907	2090000
2200	5001000	1607000	1.566	0.0151	0.907	1990000
2200	5001000	1641000	1.566	0.0151	0.907	1806000
2200	5001000	1695000	1.566	0.0151	0.907	1752000
2200	5001000	1772000	1.566	0.0151	0.907	1503000
3800	5001000	1032000	1.566	0.0151	0.907	3291000
3800	5001000	1193000	1.566	0.0151	0.907	3193000
3800	5001000	1199000	1.566	0.0151	0.907	3193000
3800	5001000	1256000	1.566	0.0151	0.907	3176000
3800	5001000	1326000	1.566	0.0151	0.907	3011000
3800	5001000	1343000	1.566	0.0151	0.907	2891000
3800	5001000	1479000	1.566	0.0151	0.907	2616000
3800	5001000	1491000	1.566	0.0151	0.907	2663000
3800	5001000	1533000	1.566	0.0151	0.907	2590000

3800	5001000	1579000	1.566	0.0151	0.907	2285000
3800	5001000	1669000	1.566	0.0151	0.907	2149000
1100	6963000	1185000	1.566	0.0151	0.907	1956000
1100	6963000	1257000	1.566	0.0151	0.907	1890000
1100	6963000	1309000	1.566	0.0151	0.907	1770000
1100	6963000	1335000	1.566	0.0151	0.907	1843000
1100	6963000	1415000	1.566	0.0151	0.907	1703000
1100	6963000	1431000	1.566	0.0151	0.907	1666000
1100	6963000	1475000	1.566	0.0151	0.907	1620000
1100	6963000	1563000	1.566	0.0151	0.907	1535000
1100	6963000	1586000	1.566	0.0151	0.907	1489000
1100	6963000	1638000	1.566	0.0151	0.907	1442000
1100	6963000	1720000	1.566	0.0151	0.907	1376000
1100	6963000	1739000	1.566	0.0151	0.907	1320000
1100	6963000	1816000	1.566	0.0151	0.907	1199000
1100	6963000	1889000	1.566	0.0151	0.907	1106000
2200	6963000	1182000	1.566	0.0151	0.907	2242000
2200	6963000	1211000	1.566	0.0151	0.907	2324000
2200	6963000	1260000	1.566	0.0151	0.907	2277000
2200	6963000	1319000	1.566	0.0151	0.907	2166000
2200	6963000	1345000	1.566	0.0151	0.907	2212000
2200	6963000	1407000	1.566	0.0151	0.907	2091000
2200	6963000	1418000	1.566	0.0151	0.907	2146000
2200	6963000	1485000	1.566	0.0151	0.907	2025000
2200	6963000	1516000	1.566	0.0151	0.907	1960000
2200	6963000	1537000	1.566	0.0151	0.907	1923000
2200	6963000	1560000	1.566	0.0151	0.907	1895000
2200	6963000	1589000	1.566	0.0151	0.907	1839000
2200	6963000	1640000	1.566	0.0151	0.907	1755000
2200	6963000	1697000	1.566	0.0151	0.907	1662000
2200	6963000	1764000	1.566	0.0151	0.907	1514000

3800	6963000	1198000	1.566	0.0151	0.907	2712000
3800	6963000	1257000	1.566	0.0151	0.907	2738000
3800	6963000	1350000	1.566	0.0151	0.907	3014000
3800	6963000	1405000	1.566	0.0151	0.907	2856000
3800	6963000	1418000	1.566	0.0151	0.907	2902000
3800	6963000	1441000	1.566	0.0151	0.907	2699000
3800	6963000	1469000	1.566	0.0151	0.907	2652000
3800	6963000	1482000	1.566	0.0151	0.907	2800000
3800	6963000	1511000	1.566	0.0151	0.907	2596000
3800	6963000	1555000	1.566	0.0151	0.907	2531000
3800	6963000	1612000	1.566	0.0151	0.907	2327000
3800	6963000	1676000	1.566	0.0151	0.907	2170000
1100	6963000	1220000	2.366	0.0151	0.907	1445000
1100	6963000	1329000	2.366	0.0151	0.907	1319000
1100	6963000	1486000	2.366	0.0151	0.907	1125000
1100	6963000	1639000	2.366	0.0151	0.907	931285
1100	6963000	1767000	2.366	0.0151	0.907	791217
2200	6963000	1204000	2.366	0.0151	0.907	1802000
2200	6963000	1329000	2.366	0.0151	0.907	1635000
2200	6963000	1407000	2.366	0.0151	0.907	1507000
2200	6963000	1500000	2.366	0.0151	0.907	1347000
2200	6963000	1567000	2.366	0.0151	0.907	1247000
2200	6963000	1631000	2.366	0.0151	0.907	1106000
2200	6963000	1692000	2.366	0.0151	0.907	998998
3800	6963000	1240000	2.366	0.0151	0.907	2273000
3800	6963000	1332000	2.366	0.0151	0.907	2193000
3800	6963000	1424000	2.366	0.0151	0.907	1999000
3800	6963000	1505000	2.366	0.0151	0.907	1710000
3800	6963000	1597000	2.366	0.0151	0.907	1536000
3800	6963000	1606000	2.366	0.0151	0.907	1429000
1100	6963000	1172000	0.766	0.0151	0.907	2897000
1100	6963000	1220000	0.766	0.0151	0.907	2855000

1100	6963000	1302000	0.766	0.0151	0.907	2690000
1100	6963000	1376000	0.766	0.0151	0.907	2773000
1100	6963000	1461000	0.766	0.0151	0.907	2690000
1100	6963000	1529000	0.766	0.0151	0.907	2628000
1100	6963000	1616000	0.766	0.0151	0.907	2545000
1100	6963000	1710000	0.766	0.0151	0.907	2152000
1100	6963000	1795000	0.766	0.0151	0.907	1945000
1100	6963000	1886000	0.766	0.0151	0.907	1697000
2200	6963000	1177000	0.766	0.0151	0.907	3766000
2200	6963000	1242000	0.766	0.0151	0.907	3580000
2200	6963000	1350000	0.766	0.0151	0.907	3787000
2200	6963000	1418000	0.766	0.0151	0.907	4035000
2200	6963000	1486000	0.766	0.0151	0.907	4138000
2200	6963000	1571000	0.766	0.0151	0.907	4097000
2200	6963000	1648000	0.766	0.0151	0.907	3993000
2200	6963000	1741000	0.766	0.0151	0.907	3766000
2200	6963000	1784000	0.766	0.0151	0.907	3580000
2200	6963000	1852000	0.766	0.0151	0.907	3331000
2200	6963000	1939000	0.766	0.0151	0.907	2483000
3800	6963000	1271000	0.766	0.0151	0.907	4925000
3800	6963000	1350000	0.766	0.0151	0.907	6045000
3800	6963000	1429000	0.766	0.0151	0.907	5923000
3800	6963000	1508000	0.766	0.0151	0.907	6050000
3800	6963000	1582000	0.766	0.0151	0.907	5991000
3800	6963000	1625000	0.766	0.0151	0.907	6013000
3800	6963000	1681000	0.766	0.0151	0.907	6263000
1100	6963000	1200000	0.5	0.0151	0.907	3856000
1100	6963000	1316000	0.5	0.0151	0.907	3693000
1100	6963000	1363000	0.5	0.0151	0.907	3817000
1100	6963000	1434000	0.5	0.0151	0.907	3877000
1100	6963000	1515000	0.5	0.0151	0.907	4000000

1100	6963000	1614000	0.5	0.0151	0.907	4028000
1100	6963000	1676000	0.5	0.0151	0.907	3962000
1100	6963000	1746000	0.5	0.0151	0.907	3833000
1100	6963000	1797000	0.5	0.0151	0.907	3483000
1100	6963000	1889000	0.5	0.0151	0.907	2848000
1100	6963000	2030000	0.5	0.0151	0.907	1452000
1100	6963000	2052000	0.5	0.0151	0.907	1293000
2200	6963000	1243000	0.5	0.0151	0.907	4580000
2200	6963000	1321000	0.5	0.0151	0.907	5114000
2200	6963000	1403000	0.5	0.0151	0.907	5268000
2200	6963000	1465000	0.5	0.0151	0.907	5045000
2200	6963000	1541000	0.5	0.0151	0.907	5515000
2200	6963000	1603000	0.5	0.0151	0.907	5418000
2200	6963000	1684000	0.5	0.0151	0.907	4909000
2200	6963000	1760000	0.5	0.0151	0.907	4274000
2200	6963000	1858000	0.5	0.0151	0.907	3386000
2200	6963000	1934000	0.5	0.0151	0.907	3004000
3800	6963000	1484000	0.5	0.0151	0.907	8233000
3800	6963000	1619000	0.5	0.0151	0.907	8291000
3800	6963000	1754000	0.5	0.0151	0.907	7243000
1100	6963000	1645000	0.29	0.0151	0.907	5239000
1100	6963000	1786000	0.29	0.0151	0.907	4570000
1100	6963000	1971000	0.29	0.0151	0.907	2966000
1100	6963000	2126000	0.29	0.0151	0.907	1857000
1100	6963000	2257000	0.29	0.0151	0.907	970166
1100	6963000	2305000	0.29	0.0151	0.907	802077
2200	6963000	1662000	0.29	0.0151	0.907	5512000
2200	6963000	1820000	0.29	0.0151	0.907	5116000
2200	6963000	1976000	0.29	0.0151	0.907	3953000
2200	6963000	2121000	0.29	0.0151	0.907	2845000
2200	6963000	2262000	0.29	0.0151	0.907	1793000

Peterlongo et al.

1120	5001392	1566000	2.492	0.0151	2.8	1079000
1120	4991585	1508000	2.492	0.0151	2.8	1101000
1120	4991585	1505000	2.492	0.0151	2.8	1096000
1120	5001392	1447000	2.492	0.0151	2.8	1153000
1110	5011198	1386000	2.492	0.0151	2.8	1213000
1110	4991585	1390000	2.492	0.0151	2.8	1219000
1120	4991585	1327000	2.492	0.0151	2.8	1297000
1140	4991585	1331000	2.492	0.0151	2.8	1300000
1130	5011198	1226000	2.492	0.0151	2.8	1388000
1150	5011198	1218000	2.492	0.0151	2.8	1403000
2180	5001392	1445000	2.492	0.0151	2.8	1293000
2200	5001392	1445000	2.492	0.0151	2.8	1314000
2200	4991585	1406000	2.492	0.0151	2.8	1399000
2200	4991585	1404000	2.492	0.0151	2.8	1406000
2200	5011198	1342000	2.492	0.0151	2.8	1524000
2200	5011198	1335000	2.492	0.0151	2.8	1524000
2190	5001392	1280000	2.492	0.0151	2.8	1621000
2190	4991585	1279000	2.492	0.0151	2.8	1624000
2190	4991585	1208000	2.492	0.0151	2.8	1731000
2190	4991585	1204000	2.492	0.0151	2.8	1731000
2200	4991585	1101000	2.492	0.0151	2.8	1898000
3820	4991585	1373000	2.492	0.0151	2.8	1742000
3820	4991585	1374000	2.492	0.0151	2.8	1745000
3800	4991585	1304000	2.492	0.0151	2.8	1968000
3810	5001392	1239000	2.492	0.0151	2.8	2114000
3960	4991585	1228000	2.492	0.0151	2.8	2133000
3880	5011198	1156000	2.492	0.0151	2.8	2197000
3920	5011198	1152000	2.492	0.0151	2.8	2208000
3870	5001392	1013000	2.492	0.0151	2.8	2288000
1120	6462582	1574000	2.492	0.0151	2.8	968000
1110	6462582	1584000	2.492	0.0151	2.8	971000

1160	6482196	1483000	2.492	0.0151	2.8	1052000
1140	6472389	1471000	2.492	0.0151	2.8	1037000
1120	6452776	1437000	2.492	0.0151	2.8	1074000
1120	6452776	1440000	2.492	0.0151	2.8	1077000
1100	6462582	1369000	2.492	0.0151	2.8	1101000
1120	6492002	1324000	2.492	0.0151	2.8	1150000
1120	6462582	1326000	2.492	0.0151	2.8	1150000
2220	6462582	1435000	2.492	0.0151	2.8	1333000
2190	6462582	1437000	2.492	0.0151	2.8	1330000
2200	6452776	1405000	2.492	0.0151	2.8	1375000
2240	6462582	1384000	2.492	0.0151	2.8	1399000
2200	6462582	1328000	2.492	0.0151	2.8	1421000
2220	6452776	1242000	2.492	0.0151	2.8	1488000
2230	6462582	1186000	2.492	0.0151	2.8	1510000
2230	6442969	1188000	2.492	0.0151	2.8	1532000
1150	5001392	1683000	1.662	0.0151	2.8	1356000
1120	5001392	1627000	1.662	0.0151	2.8	1405000
1070	4981778	1588000	1.662	0.0151	2.8	1448000
1100	4981778	1579000	1.662	0.0151	2.8	1465000
1160	5001392	1502000	1.662	0.0151	2.8	1577000
1100	4991585	1511000	1.662	0.0151	2.8	1541000
1110	4991585	1442000	1.662	0.0151	2.8	1614000
1110	4991585	1440000	1.662	0.0151	2.8	1607000
1130	5011198	1380000	1.662	0.0151	2.8	1682000
1130	5011198	1383000	1.662	0.0151	2.8	1682000
2330	5001392	1522000	1.662	0.0151	2.8	1812000
2210	5001392	1531000	1.662	0.0151	2.8	1765000
2290	5001392	1487000	1.662	0.0151	2.8	1913000
2190	5001392	1489000	1.662	0.0151	2.8	1873000
2180	4991585	1433000	1.662	0.0151	2.8	1995000
2140	4971972	1435000	1.662	0.0151	2.8	1962000
2280	5001392	1360000	1.662	0.0151	2.8	2129000

2230	4991585	1364000	1.662	0.0151	2.8	2124000
2180	4981778	1288000	1.662	0.0151	2.8	2208000
2180	4981778	1287000	1.662	0.0151	2.8	2190000
2180	4981778	1198000	1.662	0.0151	2.8	2233000
2190	4981778	1197000	1.662	0.0151	2.8	2246000
3680	4991585	1379000	1.662	0.0151	2.8	2601000
3810	5001392	1375000	1.662	0.0151	2.8	2644000
3760	4991585	1302000	1.662	0.0151	2.8	2799000
3770	4981778	1301000	1.662	0.0151	2.8	2808000
3800	5011198	1223000	1.662	0.0151	2.8	2789000
3800	5011198	1223000	1.662	0.0151	2.8	2789000
4050	5011198	1027000	1.662	0.0151	2.8	2457000
3820	5011198	1044000	1.662	0.0151	2.8	2476000
3810	5050425	1045000	1.662	0.0151	2.8	2430000
1090	4991585	1811000	0.832	0.0151	2.8	1576000
1090	4991585	1754000	0.832	0.0151	2.8	1709000
1080	4981778	1711000	0.832	0.0151	2.8	1771000
1050	4981778	1715000	0.832	0.0151	2.8	1771000
1060	4981778	1697000	0.832	0.0151	2.8	2001000
1050	4991585	1699000	0.832	0.0151	2.8	1981000
1120	5021005	1622000	0.832	0.0151	2.8	2417000
1100	4991585	1652000	0.832	0.0151	2.8	2334000
3860	4991585	1313000	0.832	0.0151	2.8	3729000
1110	6472389	1705000	0.832	0.0151	2.8	1793000
2220	6462582	1463000	0.832	0.0151	2.8	2532000
2220	6462582	1455000	0.832	0.0151	2.8	2656000
2230	6472389	1429000	0.832	0.0151	2.8	2912000
2230	6462582	1430000	0.832	0.0151	2.8	2908000

A.3 Two-phase Pressure Drop Data

The following table presents the diabatic two-phase pressure drop data of Matzner et al. [64] that was used to validate the modified Kanizawa et al. [47] pressure drop correlation for both FLTT and SLTT data.

Table A.9: FLTT Pressure Drop Data

Mass Flux [kg/m^2-s]	**System Pressure [Pa]**	**Inlet Temp [C]**	**Inlet Pressure Fluctuations [Pa]**	**Heated Length [m]**	**Diameter [m]**	**Twist Ratio**	**Heat Flux [W/m^2]**	**Exit Quality**	**Experimental Pressure Drop [Pa]**	**Predicted Pressure Drop [Pa]**
2889	6895000	272.22	6894.76	4.877	0.01016	15	1347000	0.605	744634.1	907387.5
2780	6895000	246.67	6894.76	4.877	0.01016	15	1486000	0.612	655002.2	793628.8
2848	6895000	223.89	27579.04	4.877	0.01016	15	1659000	0.599	641212.7	753948.9
2862	6895000	195.56	241316.6	4.877	0.01016	15	1861000	0.597	620528.4	704717.3
1451	6895000	272.22	6894.76	4.877	0.01016	15	981100	0.883	365422.3	392856.8
1465	6895000	245.56	6894.76	4.877	0.01016	15	1076000	0.877	317159.0	375326
1533	6895000	221.11	34473.8	4.877	0.01016	15	1148000	0.815	303369.4	358155.9
1424	6895000	197.22	255106.1	4.877	0.01016	15	1139000	0.807	275790.4	299853.2
1397	6895000	178.33	344738	4.877	0.01016	15	1167000	0.793	262000.9	275772.7
1261	6895000	169.44	275790.4	4.877	0.01016	15	1120000	0.844	234421.8	246095.7
1410	6895000	125.56	34473.8	4.877	0.01016	15	1366000	0.808	227527.1	264282.3
2875	6895000	189.44	324053.7	4.877	0.01016	15	1893000	0.581	606738.9	677858.4
2726	6895000	129.44	82737.12	4.877	0.01016	15	2161000	0.551	455054.2	516858.6
2102	6895000	272.22	6894.76	4.877	0.01016	15	1284000	0.787	551580.8	661887.7
2129	6895000	242.78	6894.76	4.877	0.01016	15	1420000	0.766	530896.5	612913.9
2156	6895000	217.78	68947.6	4.877	0.01016	15	1552000	0.75	489528.0	575179.3
2089	6895000	190.00	344738	4.877	0.01016	15	1609000	0.727	461948.9	497879.0
2129	6895000	176.11	344738	4.877	0.01016	15	1681000	0.708	441264.6	486557.1
2034	6895000	129.44	68947.6	4.877	0.01016	15	1801000	0.679	344738	397024.7

4272	6895000	271.11	20684.28	4.877	0.01016	15	1454000	0.431	1082477	1318134
4286	6895000	247.22	41368.56	4.877	0.01016	15	1852000	0.481	1075583	1333839
4245	6895000	226.11	41368.56	4.877	0.01016	15	2215000	0.532	1103162	1343791
4218	6895000	207.78	34473.8	4.877	0.01016	15	2303000	0.509	979055.9	1209762
4299	6895000	180.56	172369	4.877	0.01016	15	2423000	0.441	854950.2	1005041
4326	6895000	159.44	344738	4.877	0.01016	15	2555000	0.393	744634.1	853406.7
4516	6895000	113.33	255106.1	4.877	0.01016	15	3069000	0.332	655002.2	708920.6
4598	6895000	203.33	103421.4	4.877	0.01016	15	2662000	0.528	1151425	1423845

Table A.11: MSLTT Pressure Drop Data

Mass Flux [kg/m^2-s]	System Pressure [Pa]	Inlet Temp [C]	Inlet Pressure Fluctuations [Pa]	Heated Length [m]	Diameter [m]	Initial Twist Ratio	Heat Flux [W/m^2]	Exit Quality	Experimental Pressure Drop [Pa]	Predicted Pressure Drop [Pa]
2835	6895000	249.44	6894.76	1.219	0.01016	5	1688000	0.424	255106.1	276673.9
2848	6895000	262.78	6894.76	1.219	0.01016	5	1606000	0.44	275790.4	296751.9
4272	6895000	271.67	6894.76	1.219	0.01016	5	2000000	0.381	489528.0	550650.7
4231	6895000	248.89	13789.52	1.219	0.01016	5	2211000	0.355	420580.4	476840.9
4245	6895000	229.44	34473.8	1.219	0.01016	5	2401000	0.355	386106.6	434934.5
4259	6895000	194.44	255106.1	1.219	0.01016	5	2584000	0.268	317159.0	342607.9
2902	6895000	192.78	344738	1.219	0.01016	5	2095000	0.368	220632.3	231356.0
2862	6895000	220.56	55158.08	1.219	0.01016	5	1899000	0.397	227527.1	251050.1
1465	6895000	257.22	6894.76	1.219	0.01016	5	1205000	0.654	133758.3	134200.9
1410	6895000	219.44	13789.52	1.219	0.01016	5	1325000	0.643	110316.2	118174.1
1424	6895000	191.11	186158.5	1.219	0.01016	5	1429000	0.62	108937.2	112854.5
1424	6895000	142.78	310264.2	1.219	0.01016	5	1555000	0.563	102042.4	100471.3
6903	6895000	269.44	0	1.219	0.01016	5	2571000	0.287	186158.5	1008505
6903	6895000	246.67	34473.8	1.219	0.01016	5	2748000	0.235	710160.3	796482.5
6822	6895000	221.11	48263.32	1.219	0.01016	5	3312000	0.237	634317.9	737722.7
9670	6895000	213.89	13789.52	1.219	0.01016	5	3817000	0.131	758423.6	892804.0
5547	6895000	261.67	6894.76	1.219	0.01016	5	2461000	0.325	655002.2	739245.1
5561	6895000	236.11	13789.52	1.219	0.01016	5	2653000	0.274	537791.3	599384.1
5438	6895000	209.44	96526.64	1.219	0.01016	5	2956000	0.254	448159.4	514148.3
5547	6895000	179.44	68947.6	1.219	0.01016	5	2776000	0.126	262000.9	321868.7
6835	6895000	175.00	20684.28	1.219	0.01016	5	3133000	0.075	289579.9	364384.4
4150	6895000	152.22	172369	1.219	0.01016	5	2662000	0.178	189605.9	236153.7

5411	6895000	148.89	34473.8	1.219	0.01016	5	2940000	0.078	199948.0	250727.1
6727	6895000	150.00	13789.52	1.219	0.01016	5	3464000	0.054	262000.9	326006.4
4082	6895000	111.67	41368.56	1.219	0.01016	5	2868000	0.119	151684.7	185703.8
5398	6895000	113.89	13789.52	1.219	0.01016	5	3407000	0.059	184779.6	234386.9
6754	6895000	187.78	27579.04	1.219	0.01016	5	2883000	0.083	303369.4	371938.0
6740	6895000	201.67	124105.7	1.219	0.01016	5	3319000	0.184	496422.7	580461.3
5371	6895000	194.44	213737.6	1.219	0.01016	5	2962000	0.216	379211.8	435684.2
2821	6895000	277.22	13789.52	2.438	0.01016	5	981100	0.416	310264.2	330518.0
2821	6895000	247.78	6894.76	2.438	0.01016	5	1161000	0.397	275790.4	287918.5
2835	6895000	220.00	68947.6	2.438	0.01016	5	1319000	0.379	241316.6	259573.2
2821	6895000	185.00	413685.6	2.438	0.01016	5	1467000	0.346	220632.3	221485.6
2821	6895000	162.78	344738	2.438	0.01016	5	1587000	0.335	206842.8	208550.3
4231	6895000	275.00	6894.76	2.438	0.01016	5	1246000	0.341	510212.2	564911.6
2740	6895000	246.67	6894.76	2.438	0.01016	5	1186000	0.406	248211.4	286973.2
4042	6895000	243.89	13789.52	2.438	0.01016	5	1571000	0.343	413685.6	480748.8
4096	6895000	222.22	124105.7	2.438	0.01016	5	1738000	0.32	358527.5	437230.0
4109	6895000	198.33	275790.4	2.438	0.01016	5	1918000	0.3	330948.5	395896.4
3974	6895000	266.67	6894.76	2.438	0.01016	5	1347000	0.356	468843.7	520186.3
4910	6895000	258.33	13789.52	2.438	0.01016	5	1653000	0.325	586054.6	677461.4
5506	6895000	235.00	20684.28	2.438	0.01016	5	2025000	0.289	579159.8	694950.3
5479	6895000	202.78	227527.1	2.438	0.01016	5	2281000	0.251	448159.4	566044.4
2821	6895000	151.11	275790.4	2.438	0.01016	5	1735000	0.346	186158.5	221757.3
2712	6895000	116.11	275790.4	2.438	0.01016	5	1883000	0.346	172369	200376.0
4082	6895000	166.67	193053.3	2.438	0.01016	5	2095000	0.266	268895.6	336002.3
5479	6895000	166.67	62052.84	2.438	0.01016	5	2372000	0.168	324053.7	400971.6
4096	6895000	133.89	110316.2	2.438	0.01016	5	2287000	0.228	234421.8	292416.1
5276	6895000	133.33	20684.28	2.438	0.01016	5	2587000	0.143	262000.9	338747.4
1438	6895000	265.56	6894.76	2.438	0.01016	5	798100	0.621	137895.2	145318.4
1424	6895000	227.78	27579.04	2.438	0.01016	5	905400	0.595	124105.7	130410.5
1343	6895000	196.11	172369	2.438	0.01016	5	959000	0.602	117210.9	114907.8
1397	6895000	159.44	137895.2	2.438	0.01016	5	1104000	0.586	117210.9	116143.5
1370	6895000	115.56	275790.4	2.438	0.01016	5	1224000	0.586	96526.64	109906.0

5398	6895000	270.00	6894.76	2.438	0.01016	5	1549000	0.303	648107.4	791831.3
6646	6895000	272.22	6894.76	2.438	0.01016	5	1738000	0.279	889424.0	1083024
6632	6895000	248.89	6894.76	2.438	0.01016	5	2079000	0.266	758423.6	940283.7
6686	6895000	224.44	41368.56	2.438	0.01016	5	2366000	0.24	648107.4	811549.9
6835	6895000	205.56	137895.2	2.438	0.01016	5	2508000	0.199	565370.3	696809.8
6903	6895000	182.78	103421.4	2.438	0.01016	5	2445000	0.116	420580.4	496430.5
8761	6895000	248.33	34473.8	2.438	0.01016	5	2502000	0.23	1096267	1365239
9494	6895000	226.67	55158.08	2.438	0.01016	5	2994000	0.199	1054898	1310687
9792	6895000	200.00	68947.6	2.438	0.01016	5	2909000	0.096	723949.8	843359.1
9548	6895000	181.11	55158.08	2.438	0.01016	5	3054000	0.069	627423.2	704681.8
9575	6895000	160.00	34473.8	2.438	0.01016	5	3451000	0.059	586054.6	672876.7
6781	6895000	158.33	68947.6	2.438	0.01016	5	2625000	0.086	365422.3	421746.8
6781	6895000	137.78	68947.6	2.438	0.01016	5	2852000	0.07	344738	393971.9
9561	6895000	138.33	20684.28	2.438	0.01016	5	3795000	0.042	544686.0	626867.7
6808	6895000	113.89	34473.8	2.438	0.01016	5	3186000	0.061	324053.7	384007.9

A.4 Single-phase Swirl Decay Data

The following table presents all of the single-phase swirl decay data that was used to validate the Wu et al. [99] swirl decay model.

Table A.13: Single-phase Swirl Decay Data

Reynolds	**Length to Diameter Ratio**	**V_tan/V_ax**	**Experimental Swirl Fraction**	**Predicted Swirl Fraction**
Wu et al.				
50000	0.00	0.5100	1.0000	1.0000
50000	1.36	0.4811	0.9433	0.8810
50000	2.08	0.4502	0.8828	0.8321
50000	3.02	0.4211	0.8257	0.7782
50000	10.03	0.2153	0.4221	0.5421
50000	29.89	0.1338	0.2624	0.2535
50000	34.98	0.1370	0.2686	0.2101
50000	40.35	0.1076	0.2110	0.1724
50000	50.16	0.0712	0.1396	0.1202
50000	55.28	0.0572	0.1122	0.0996
50000	60.19	0.0330	0.0647	0.0832
Najafi et al.				
60000	0.00	0.2880	1.0000	1.0000
60000	0.82	0.2801	0.9726	0.9322
60000	1.76	0.2663	0.9246	0.8684
60000	3.32	0.2525	0.8766	0.7846
60000	6.61	0.2248	0.7805	0.6620
60000	9.89	0.2040	0.7085	0.5757
60000	16.62	0.1625	0.5644	0.4471
60000	20.85	0.1418	0.4923	0.3844
60000	25.07	0.1210	0.4203	0.3310
60000	29.14	0.1037	0.3602	0.2868

60000	33.21	0.0865	0.3002	0.2486
60000	41.66	0.0657	0.2281	0.1848
60000	49.96	0.0484	0.1681	0.1382
60000	58.26	0.0346	0.1201	0.1033
60000	66.56	0.0242	0.0841	0.0773
60000	74.86	0.0173	0.0600	0.0578
60000	0.00	0.5660	1.0000	1.0000
60000	0.85	0.5429	0.9593	0.9223
60000	1.63	0.5222	0.9226	0.8644
60000	3.35	0.4911	0.8676	0.7661
60000	6.63	0.4357	0.7698	0.6406
60000	10.07	0.3908	0.6904	0.5504
60000	16.48	0.3216	0.5682	0.4299
60000	20.86	0.2836	0.5010	0.3665
60000	24.93	0.2455	0.4338	0.3168
60000	29.16	0.2179	0.3849	0.2726
60000	33.38	0.1902	0.3360	0.2347
60000	41.67	0.1383	0.2444	0.1752
60000	49.97	0.1037	0.1833	0.1309
60000	58.11	0.0761	0.1344	0.0984
60000	66.41	0.0519	0.0916	0.0736
60000	74.86	0.0380	0.0672	0.0547
60000	0.00	0.9800	1.0000	1.0000
60000	0.73	0.7781	0.7940	0.9154
60000	1.66	0.7470	0.7622	0.8318
60000	3.38	0.6951	0.7093	0.7225
60000	6.66	0.6156	0.6281	0.5914
60000	9.94	0.5533	0.5646	0.5053
60000	16.66	0.4496	0.4587	0.3844
60000	20.88	0.3977	0.4058	0.3279
60000	24.94	0.3493	0.3564	0.2824

60000	29.17	0.3078	0.3141	0.2423
60000	33.23	0.2697	0.2752	0.2094
60000	41.68	0.2040	0.2082	0.1550
60000	49.98	0.1556	0.1588	0.1157
60000	58.27	0.1141	0.1165	0.0864
60000	66.57	0.0865	0.0882	0.0646
60000	74.86	0.0622	0.0635	0.0483
60000	0.00	1.0280	1.0000	1.0000
60000	0.91	0.9718	0.9453	0.8943
60000	1.84	0.9303	0.9049	0.8135
60000	3.24	0.8576	0.8343	0.7239
60000	6.68	0.7539	0.7334	0.5843
60000	9.95	0.6709	0.6526	0.4987
60000	16.67	0.5464	0.5315	0.3788
60000	20.89	0.4842	0.4710	0.3229
60000	24.95	0.4254	0.4138	0.2780
60000	29.02	0.3769	0.3667	0.2398
60000	33.40	0.3320	0.3229	0.2049
60000	41.69	0.2559	0.2489	0.1525
60000	49.98	0.1937	0.1884	0.1138
60000	58.27	0.1487	0.1447	0.0850
60000	66.57	0.1107	0.1076	0.0635
60000	74.87	0.0830	0.0807	0.0475
60000	0.00	1.1880	1.0000	1.0000
60000	0.77	1.1135	0.9373	0.8985
60000	1.70	1.0617	0.8937	0.8083
60000	3.42	0.9787	0.8238	0.6940
60000	6.69	0.8542	0.7190	0.5617
60000	9.97	0.7608	0.6404	0.4770
60000	16.68	0.6190	0.5211	0.3604
60000	20.74	0.5464	0.4599	0.3084
60000	24.96	0.4807	0.4046	0.2635

60000	29.18	0.4323	0.3639	0.2258
60000	33.25	0.3804	0.3202	0.1950
60000	41.54	0.2939	0.2474	0.1450
60000	49.98	0.2282	0.1921	0.1075
60000	58.28	0.1764	0.1485	0.0803
60000	66.73	0.1314	0.1106	0.0597
60000	74.87	0.0968	0.0815	0.0448
30000	0.00	0.2880	1.0000	1.0000
30000	0.80	0.2751	0.9554	0.9219
30000	1.75	0.2630	0.9132	0.8458
30000	3.35	0.2448	0.8500	0.7483
30000	6.70	0.2145	0.7446	0.6099
30000	10.05	0.1861	0.6463	0.5155
30000	16.74	0.1416	0.4917	0.3827
30000	20.89	0.1173	0.4074	0.3210
30000	25.03	0.0971	0.3372	0.2697
30000	29.18	0.0809	0.2810	0.2268
30000	33.49	0.0647	0.2248	0.1895
30000	41.78	0.0425	0.1475	0.1341
30000	49.91	0.0283	0.0983	0.0956
30000	58.36	0.0182	0.0632	0.0672
30000	66.65	0.0121	0.0421	0.0476
30000	74.94	0.0101	0.0351	0.0337
30000	0.00	0.9800	1.0000	1.0000
30000	0.96	0.7809	0.7969	0.8746
30000	1.75	0.7405	0.7556	0.7972
30000	3.35	0.6777	0.6916	0.6849
30000	6.54	0.5806	0.5925	0.5454
30000	10.05	0.5078	0.5182	0.4485
30000	16.74	0.3965	0.4046	0.3268
30000	20.89	0.3399	0.3468	0.2723

30000	25.03	0.2913	0.2973	0.2277
30000	29.02	0.2509	0.2560	0.1921
30000	33.33	0.2124	0.2168	0.1602
30000	41.62	0.1497	0.1528	0.1131
30000	50.07	0.1052	0.1073	0.0794
30000	58.36	0.0708	0.0723	0.0562
30000	66.65	0.0486	0.0495	0.0398
30000	74.94	0.0324	0.0330	0.0281
15000	0.00	0.2880	1.0000	1.0000
15000	0.80	0.2731	0.9483	0.9078
15000	1.59	0.2610	0.9062	0.8329
15000	3.35	0.2367	0.8219	0.7087
15000	6.70	0.1962	0.6814	0.5560
15000	10.05	0.1639	0.5690	0.4555
15000	16.74	0.1153	0.4004	0.3199
15000	20.73	0.0890	0.3091	0.2617
15000	25.03	0.0688	0.2388	0.2111
15000	29.18	0.0546	0.1897	0.1718
15000	33.33	0.0425	0.1475	0.1399
15000	41.78	0.0243	0.0843	0.0920
15000	50.07	0.0142	0.0492	0.0610
15000	58.36	0.0081	0.0281	0.0405
15000	66.65	0.0040	0.0140	0.0268
15000	74.94	0.0061	0.0211	0.0178
15000	0.00	0.9800	1.0000	1.0000
15000	0.80	0.7769	0.7927	0.8744
15000	1.75	0.7283	0.7432	0.7660
15000	3.35	0.6494	0.6627	0.6419
15000	6.70	0.5766	0.5884	0.4873
15000	10.05	0.4471	0.4562	0.3926
15000	16.74	0.3298	0.3365	0.2713
15000	20.89	0.2711	0.2766	0.2190

15000	25.03	0.2225	0.2271	0.1775
15000	29.18	0.1801	0.1837	0.1441
15000	33.49	0.1457	0.1486	0.1162
15000	41.62	0.0931	0.0950	0.0776
15000	50.07	0.0647	0.0661	0.0510
15000	58.36	0.0425	0.0434	0.0338
15000	66.65	0.0283	0.0289	0.0224
15000	75.10	0.0162	0.0165	0.0148
Kreith et al.				
122000	1.95	0.6012	0.9764	0.8612
122000	2.00	0.5994	0.9263	0.8586
122000	12.03	0.3891	0.7178	0.5574
122000	12.03	0.3891	0.7338	0.5573
122000	22.01	0.2848	0.4812	0.4080
122000	22.01	0.2848	0.5193	0.4080
122000	34.93	0.1941	0.3449	0.2781
122000	35.03	0.1936	0.3890	0.2772
122000	49.94	0.1253	0.2105	0.1795
122000	49.94	0.1253	0.2246	0.1795
122000	1.95	0.3669	0.9664	0.8760
122000	2.00	0.3659	0.9363	0.8735
122000	12.03	0.2445	0.7519	0.5838
122000	12.07	0.2442	0.6276	0.5830
122000	22.01	0.1808	0.5033	0.4317
122000	22.11	0.1803	0.4471	0.4305
122000	34.98	0.1239	0.3308	0.2957
122000	35.02	0.1237	0.2987	0.2953
122000	49.93	0.0803	0.1825	0.1918
122000	49.94	0.0803	0.2366	0.1918
36000	12.16	0.3187	0.6443	0.4565
36000	12.21	0.3180	0.6303	0.4555

36000	22.13	0.2108	0.4320	0.3019
36000	35.08	0.1260	0.2564	0.1805
36000	35.08	0.1260	0.2564	0.1805
36000	49.88	0.0705	0.1515	0.1010
36000	49.98	0.0702	0.1655	0.1006
36000	12.11	0.2022	0.6243	0.4827
36000	12.16	0.2018	0.6463	0.4817
36000	22.08	0.1348	0.4059	0.3218
36000	22.13	0.1345	0.3658	0.3212
36000	35.08	0.0808	0.2705	0.1928
36000	49.98	0.0451	0.1375	0.1076
36000	50.03	0.0450	0.1475	0.1074

Appendix B

Pressure Drop Sensitivity Analysis

This appendix examines the effect of removing the two-phase multiplier and the viscosity correction terms from the proposed friction pressure drop calculations using the data from Matzner et al. [64] in an attempt to simplify the proposed methodology. The sensitivity analysis will be performed in the following order:

- Two-Phase Multiplier Removed from Form Loss Coefficient: Section B.1
- Viscosity Correction Term Removed from Friction Factor: Section B.2
- Both Terms Removed: Section B.3

B.1 Removal of the Two-Phase Multiplier

This section examines the need for the two-phase multiplier, presented in Equation 5.21, that was intended to be applied to the form loss coefficient of Gambill et al. [27], presented in Equation 5.17. Only the MSLTT data from Matzner et al. [64] was examined for this sensitivity analysis since this data set is the only one where two-phase flow exists at the entrance of a SLTT. First, the ratios of the predicted results were compared with each other as a function of quality at the second twisted-tape because the first SLTT was always in single-phase flow. As shown in Figure B-1, the ratio of the predicted total pressure drop decreases with increasing flow quality at the second SLTT. The important thing to take away from this figure is that the relative difference is actually quite small, never exceeding 5%.

Furthermore, when the results of the mean and standard deviation of the pressure drop predictions for the MSLTT experiments are compared as shown in Table B.2, the results are statistically similar. This result indicates that the two-phase multiplier can be removed from the form loss coefficient calculation without introducing large errors.

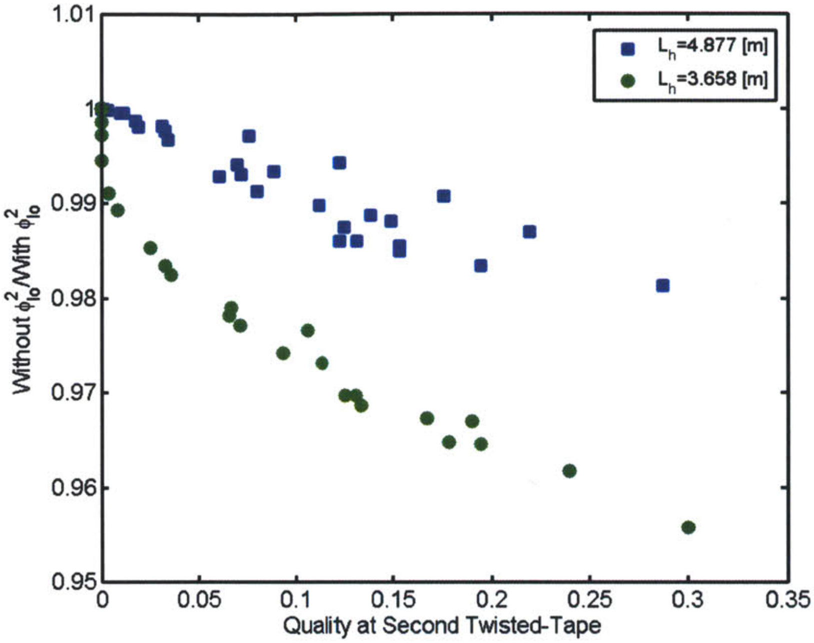

Figure B-1: Ratio of Total Pressure Drop Without and With ϕ^2_{lo}

Table B.1: Relative Error of Removing ϕ^2_{lo} from the Swirl Form Loss Coefficient

ϕ^2_{lo} Included?	$\mu(R)$	$\sigma(R)$
Yes	1.000	0.059
No	0.999	0.067

Excludes the one outlier of the data set

B.2 Removal of the Viscosity Correction Term

Since the wall viscosity correction factor, given in Equation 5.13, is applicable to all swirl intensities, all of the Matzner et al. [64] data was examined to determine if the removal of this term has a large effect. The results of this comparison are presented as a ratio of the total pressure drop with the correction divided by the total pressure drop without the correction. Since the wall viscosity correction term is applied only in the single-phase heat transfer region, the ratio of total pressure drop is presented as a function of single-phase heat transfer length as shown in Figure B-2. The effect of removing this viscosity correction term is not large, i.e. less than 7%.

The statistical comparison of removing the wall viscosity correction term is shown in Table B.2. Since the results do not differ significantly, the viscosity correction term can be removed without introducing large errors. This simplifies the calculation of pressure drop significantly since the wall temperature is no longer needed.

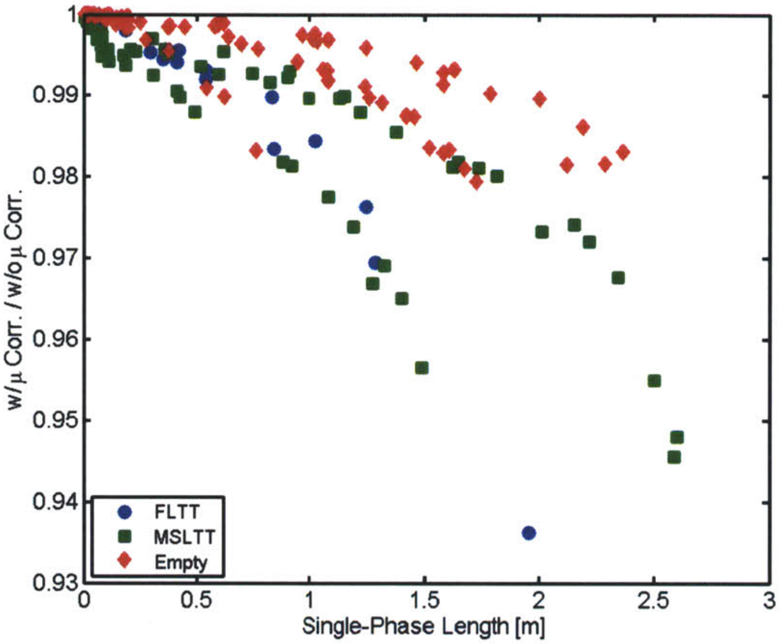

Figure B-2: Removal of the Wall Viscosity Correction Term Comparison

Table B.2: Relative Error of Removing the Viscosity Correction Factor

Data Description	With/Without	$\mu(R)$	$\sigma(R)$
Empty Tube	w/	0.841	0.130
	w/o	0.845	0.132
FLTT	w/	1.068	0.063
	w/	1.076	0.056
MSLTT$_1$	w/	1.000	0.059
	w/o	0.989	0.062

1. Excludes the one outlier in the data set

B.3 Removal of Both Terms

For the same reason given in Section B.1, only the MSLTT data was used to examine the effect of removing both the two-phase multiplier and the viscosity correction term. The results of the analysis with both these terms removed is shown in Figure B-3. Clearly there is no large effect by removing the wall viscosity correction and two-phase multiplier term from the pressure drop calculation. By removing these terms, the calculation of the channel pressure drop is made significantly simpler due to the removal of the wall temperature calculation as well as the complicated formulation of the two-phase multiplier calculation.

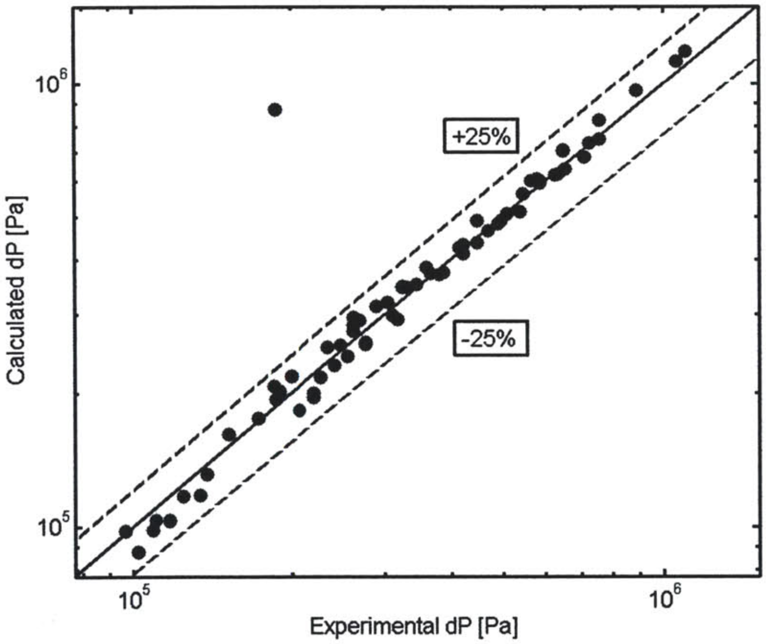

Figure B-3: Comparison with MSLTT Data from Matzner et al. [64] with Both the Wall Viscosity Correction and Two-Phase Multiplier Removed

Appendix C

Existing Twisted-Tape Correlations

This appendix is an attempt to compile all of the correlations encountered during the literature review for this study. Each section consists of a brief description of the correlation, then the formulation of the correlation is presented. The appendix is organized as follows:

- Overview of Existing Twisted-Tape Correlations: Appendix C.1
- Gambill et al.: Appendix C.2
- Drizius et al.: Appendix C.3
- Whalley: Appendix C.4
- Jensen: Appendix C.5
- Nariai et al.: Appendix C.6
- Tong et al.: Appendix C.7
- Ferroni et al.: Appendix C.8
- Krug et al.: Appendix C.9
- Hata et al. Appendix C.10

C.1 Twisted-Tape Correlations

The operating range for each correlation is shown in Table C.1. While some non-uniform circumferential heating CHF correlations exist for twisted-tape equipped tubes, they are not presented here because they are considered to be outside the scope of this study as discussed in Section 3.1. With the exception of the entries in this table that are otherwise noted, all variables in this appendix are expressed in SI units, i.e. q''_{cr} has units of $\frac{W}{m^2}$.

Table C.1: Twisted-Tape Correlations

Author	Ref	P (MPa)	G ($\frac{kg}{m^2 s}$)	x_{cr}	L_h (cm)	D(mm)	y
Gambill et al.	[27]	0.101 - 3.758	4476 - 47555	(-0.383) - 0.113	3.454-44.12	3.45-10.21	2.08 - 12.03
Drizius et al.	[21]	0.393 - 1.335	4500 - 24800	(-0.157) - (-0.046)	3.7-14.1	1.6	1.25 - 10.25
Whalley	[97]	6.90	2712	not published	366.0	12.62	4.04
Jensen	[44]	0.101 - 13.8	120 - 5840	0.01 - 0.99	28.0-487.7	7.0-20.0	2.5 - 34.5
Nariai et al.	[71]	0.101 - 1.47	5300 - 7400	(-0.256) - (-0.054)	10.0	6	2.61 - ∞
Weisman et al.	[95]	0.777 - 20.75	$0.3G_c$ - 40000	$x_1 > -0.3$; $\langle\alpha\rangle < 0.64$	3.5-365.0	1.15-37.5	2.3 - 12
Tong et al.	[87]	0.392 - 1.398	5049 - 18290	(-0.306) - (-0.129)	0.664-15.7	2.44-6.54	1.9 - 7.1
Krug et al.	[57]	0.100 - 20.1	200 - 39000	(-0.45) - 0.95 (x_{in})	0.95-480 L/D		1 - 34.5
Modified Jensen	[23]	0.101 - 13.8	120 - 5840	0.01 - 0.99	28.0-487.7	7.0-20.0	y < y_{crit} *
Hata et al.	[34]	0.775 - 0.889	4016 - 13950	(-0.28) - (-0.11)	5.95	6.0	2.39 - 4.45

***y_{crit} refers to an upper bound on twist-ratio due to a non-physical trend of the correlation. A full description can be found in Ferroni's thesis [23].**

C.2 Gambill, W.R., Bundy, R.D., and Wansbrough, R.W. [27]

This correlation is based primarily on the resultant velocity at the pipe wall due to the rotation induced by the twisted-tape. Pressure, quality, and mass flux are indirectly included in this expression through the resultant velocity. The full expression for the Gambill correlation is shown in Equation (C.1).

$$\frac{q''_{cr}}{10^6} = 4.17\frac{V_r}{(\frac{L_h}{D})^{1/3}} \tag{C.1}$$

where,

$V_r = resultant\ velocity = V_{ax}\frac{\sqrt{4y^2+\pi}}{2y}$

$V_{ax} = \frac{G}{\rho_m}$

$\rho_m = \frac{x}{\rho_g} + \frac{1-x}{\rho_l}$

y = twist ratio

The term multiplying the axial velocity accounts for the helicoidal path the fluid takes in the case of swirling flow. This term indicates that the near-wall velocity for a swirling flow is higher than that of an empty tube at the axial velocity.

C.3 Drizius, M.R.M., Skema, and Slanciauskas, A.A. [21]

The Drizius correlation was developed for a very narrow range of data that covered low pressures and high mass fluxes. The correlation does not take into account pressure and is left in a form that is only meaningful if the user is interested in design conditions near the range used in this study. The Drizius correlation is shown in Equation (C.2).

$$\frac{q''_{cr}}{y^{-0.1}G} = \frac{a_1}{l_q} + \frac{a_2 l_q}{a_3^{0.01 l_q}} \tag{C.2}$$

where,

$a_1 = 1.7 \times 10^5$

$a_2 = 17.3$

$a_3 = 4.0$

$l_q = \frac{L_h}{D}$

C.4 Whalley, P.B. [97]

This correlation is unique because it attempts to formulate a mechanistic model of Dryout for a tube containing a SLTT. The correlation is applicable for pipes in the annular flow regime and is based on a mechanistic model developed in Whalley et al. [98]. The model predicts Dryout when the thickness of the liquid film on the tube wall is equal to zero. This model was developed by altering the model for empty pipe CHF by making two major assumptions. First, upon exiting a SLTT, all of the liquid droplets entrained in the central flow were re-deposited on the pipe wall. Second, the swirling flow prevents entrainment from occurring for a length of approximately fifty pipe diameters from the exit of the twisted-tape. Whalley arrived at the value of fifty diameters by using a simplified version of the swirl decay model developed in Section 4.2.2.

The main limitation with this model is that it is only for Dryout conditions and is not applicable to low quality flows. It also treats swirl decay as a step function, i.e. the effect of swirl persists at the same intensity for approximately fifty diameters from the twisted-tape exit, then the effects stop abruptly.

The basic formulation of the model is shown in Equation (C.3).

$$\frac{dG_{LF}}{dz} = \frac{4}{d}\left(D - E - \frac{q''}{h_{fg}}\right) \tag{C.3}$$

where,

G_{LF} = liquid film mass flux $\left[\frac{kg}{m^2 s}\right]$

d = tube diameter [m]

D = deposition rate $\left[\frac{kg}{m^2 s}\right]$

E = entrainment rate $\left[\frac{kg}{m^2 s}\right]$
q'' = operating heat flux $\left[\frac{W}{m^2}\right]$
h_{fg} = heat of vaporization $\left[\frac{J}{kg}\right]$

The models for the entrainment and deposition rates have since been improved by Hewitt and Govan [36]. There is potential that this model could be altered using a swirl based local concentration as discussed in Section 8.2.

C.5 Jensen, M.K. [44]

The Jensen correlation was developed using saturated boiling FLTT data and covers a large range of operating conditions as shown in Table C.1. The correlation is based on a ratio of the CHF of a tube containing a FLTT to that of an empty tube, as shown in Equation (C.4). The basic form of the correlation is given by Equation (C.5). The axial velocity is calculated using the homogeneous flow model as was done for the Gambill et al. correlation [27] in Appendix C.2.

$$A = \frac{q''_{cr_{FLTT}}}{q''_{cr_{empty}}} \tag{C.4}$$

$$A = \left(4.597 + 0.09254y + 0.004154y^2\right)\left(\frac{\rho_g}{\rho_f}\right)^{0.7012} + 0.09012ln\left(\frac{a}{g_c}\right) \tag{C.5}$$

where,
$g_c = 9.81\ \frac{m}{s^2}$
$\left(\frac{a}{g_c}\right) = \frac{2}{g_c D}\left(\frac{V_{ax}\pi}{2y}\right)^2$

The empty tube CHF value is calculated using the Katto correlation [48], which is not presented in this section due to its complexity. There are several issues with using this correlation for DNB calculations. It was developed using only saturated boiling CHF data, leaving the majority of the operating quality of a PWR outside the range of this correlation. Also, since the Katto correlation is based on a series of non-dimensional regions of CHF that have distinct governing equations, it undergoes drastic discontinuities when transitioning from one region to the next as shown in Figure C-1. This problem can cause complications when using this correlation for design since these discontinuities sometimes occur near the location of MDNBR, resulting in uncertainty in the accuracy of the design margin.

C.6 Nariai, H., Inasaka, F., Fujisaki, W., and Ishiguro, H. [71]

The approach the authors of this study took was similar to that of the development of the Jensen correlation in that this correlation incorporates a twisted-tape CHF ratio. The expression is shown in Equation (C.6), where P_{ex} is the pressure at the exit of the pipe in MPa.

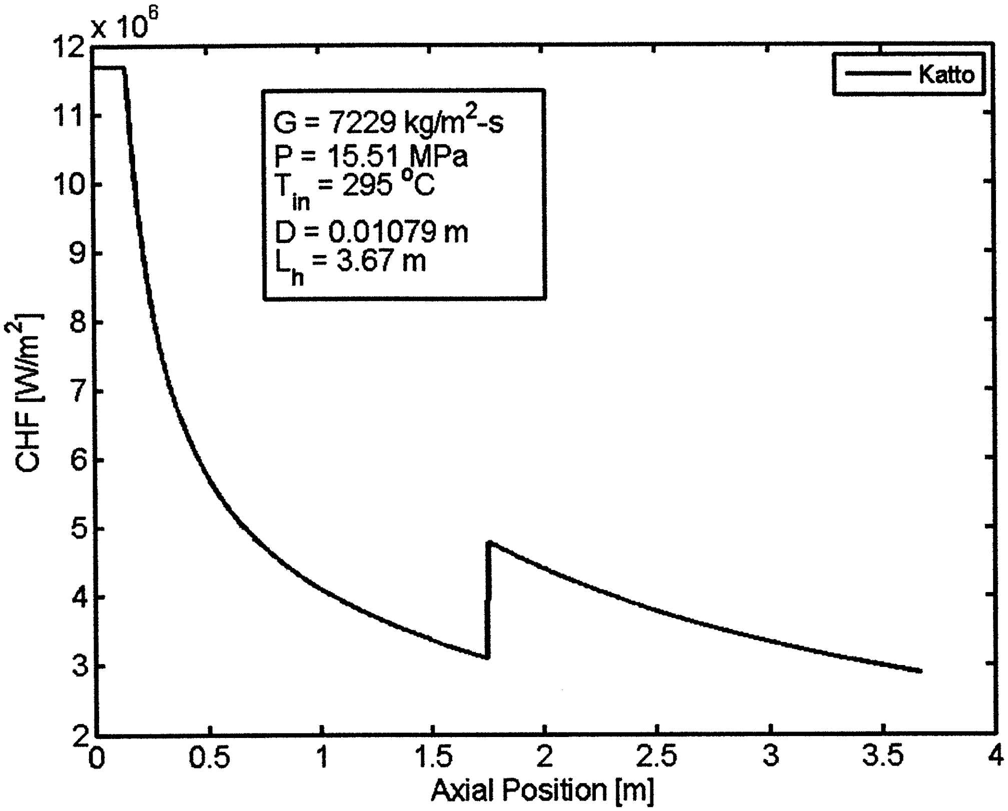

Figure C-1: Katto Non-physical Jump

$$\gamma = \left\{1 + 0.01\theta exp\left[-\left(P_{ex} \times 10^{-6}\right)^2\right]\right\}^{1/6} \tag{C.6}$$

where,

$\theta = \frac{\pi^2 V_{gx}^2}{2 g_c y^2 D}$

γ is the same as the "A" term in Equation (C.4) in Section C.5. The term γ is consistent with the one used by Nariai et al. [71]

The empty pipe CHF value for this ratio is calculated using the modified Tong correlation as presented in Inasaka and Nariai's paper [42]. The original presentation of the correlation is a bit convoluted, therefore some of the parameters have been renamed in order to clear up the implementation. Equations (C.7)-(C.9) should be applied in the order that they appear.

$$C_1 = 1.76 - 7.433x_{eq} + 12.222x_{eq}^2 \tag{C.7}$$

$$\frac{C_2}{C_1} = 1 - \frac{52.3 + 80x_{eq} - 50x_{eq}^2}{60.5 + \left(P_{ex} \times 10^{-5}\right)1.4} \tag{C.8}$$

$$\frac{q''_{cr_{empty}}}{h_{fg}} = C_2 \frac{G^{0.4}\mu_f^{0.6}}{D^{0.6}} \tag{C.9}$$

C.7 Tong, W., Bergles, A.E., and Jensen, M.K. [87]

While this correlation is presented in two forms in Ref. [87], only the second form is being presented here. This correlation attempted to capture all of the physical parameters that may have an effect on DNB at low pressure, subcooled flow in relatively small diameter pipes. The basic form of the correlation is shown in Equation (C.10), and the final form of the correlation is presented in Equation (C.11).

$$q''_{cr} = A_o \left(\frac{y}{y_o}\right)^a \left(\frac{G}{G_o}\right)^b \left(\frac{D}{D_o}\right)^c \left(\frac{P_e}{P_{e,o}}\right)^d \left(\frac{T_{sat,i} - T_i}{T_{sat,i} - T_{i,o}}\right)^e \left[\frac{L_h/D}{(L_h/D)_o}\right]^f \tag{C.10}$$

$$\frac{q''_{cr}}{10^6} = 31.7109 \frac{\left(\frac{G}{G_o}\right)^{0.6799} \left(\frac{P_e}{P_{e,o}}\right)^{0.2840} \left(\frac{T_{sat,i}-T_i}{T_{sat,i}-T_{i,o}}\right)^{1.1892}}{\left(\frac{y}{y_o}\right)^{0.2589} \left(\frac{D}{D_o}\right)^{0.0834} \left[\frac{L_h/D}{(L_h/D)_o}\right]^{0.4764}} \tag{C.11}$$

where,
subscript "i" indicates inlet conditions
subscript "e" indicates exit conditions
$G_o = 10,000\ \frac{kg}{m^2 s}$
$P_{e,o} = 10\ bar$
$T_{i,o} = 296.15\ K$
$y_o = 1.93$
$D_o = 2.44\ mm$
$(\frac{L_h}{D})_o = 24$

C.8 Ferroni, P. [23]

The Ferroni correlation was originally developed for use with MSLTTs and is based on the Jensen correlation [44] and is modified to account for decaying swirl downstream from the exit of a twisted-tape using the swirl decay model of Algifri et al. [4]. According to Ferroni [25], the Jensen correlation needed to be modified due to a non-physical phenomena found at high twist ratios. This limitation is shown in Equation (C.12) as it was presented in Ferroni's thesis [23]. At twist ratios larger than this critical twist ratio, the Jensen correlation predicts a non-physical solution in that the CHF increases in tubes with increasing twist ratios.

$$y_{crit} = \begin{cases} 23.023p^{-0.4114} & for\ 0.1 \leq p \leq 3\ MPa \\ -5.6794ln(p) + 20.134 & for\ 3 < p \leq 21\ MPa \end{cases} \tag{C.12}$$

Ferroni theorized that the TTCHFR for a SLTT would be directly related to the CHF obtained by using a FLTT multiplied by swirl fraction. This is true provided that the SLTT went through at least 1-1.5 turns according to the findings of Hassid et al. [33]. The swirl fraction is simply the ratio of the swirl intensity at location z to the swirl intensity at the exit of the twisted-tape. The formulation of this TTCHFR is shown in Equation (C.13).

$$TTCHFR \equiv \left(\frac{q''_{cr_{SLTT}}}{q''_{cr_{empty}}}\right) = 1 + \left(\frac{q''_{cr_{FLTT}}}{q''_{cr_{empty}}} - 1\right) S_f \tag{C.13}$$

The governing equations for the swirl fraction are presented in Equations (C.14) and (C.15).

$$S_f\left(z_T\right) = \sqrt{\frac{\int_0^{R_{ci}} \left[W\left(r, z_T\right)\right]^2 rdr}{\int_0^{R_{ci}} \left[W\left(r, 0\right)\right]^2 rdr}} \tag{C.14}$$

where,

R_{ci} =inner pipe radius

z_T =axial distance from the exit of the twisted-tape

W = dimensionless ratio of the axial and tangential velocity components of the flow

There were two formulations of the expression for $W\left(r, z_T\right)$; however, only the presentation by Algifri et al. [4] is presented here.

$$\begin{aligned} W\left(r, z_T\right) \quad = \quad & \tfrac{7.73}{4y} J_1\left(7.664\tfrac{r}{D}\right) exp\left[-\tfrac{29.368(1+\varepsilon_d)}{N_R}\tfrac{z_T}{D}\right] - \tfrac{5.26}{4y} J_1\left(14.032\tfrac{r}{D}\right) exp\left[-\tfrac{98.448(1+\varepsilon_d)}{N_R}\tfrac{z_T}{D}\right] \\ + \quad & \tfrac{4.04}{4y} J_1\left(20.346\tfrac{r}{D}\right) exp\left[-\tfrac{206.98(1+\varepsilon_d)}{N_R}\tfrac{z_T}{D}\right] - \tfrac{3.38}{4y} J_1\left(26.648\tfrac{r}{D}\right) exp\left[-\tfrac{355.06(1+\varepsilon_d)}{N_R}\tfrac{z_T}{D}\right] \\ + \quad & \tfrac{3.00}{4y} J_1\left(32.928\tfrac{r}{D}\right) exp\left[-\tfrac{542.12(1+\varepsilon_d)}{N_R}\tfrac{z_T}{D}\right] - \tfrac{3.06}{4y} J_1\left(39.232\tfrac{r}{D}\right) exp\left[-\tfrac{769.58(1+\varepsilon_d)}{N_R}\tfrac{z_T}{D}\right] \\ + \quad & \tfrac{3.33}{4y} J_1\left(45.520\tfrac{r}{D}\right) exp\left[-\tfrac{1036.04(1+\varepsilon_d)}{N_R}\tfrac{z_T}{D}\right] - \tfrac{5.43}{4y} J_1\left(50.612\tfrac{r}{D}\right) exp\left[-\tfrac{1280.8(1+\varepsilon_d)}{N_R}\tfrac{z_T}{D}\right] \end{aligned} \tag{C.15}$$

where,

$N_R = \frac{Re_{empty}}{2}$

$\varepsilon_d = \ dimensionless\ eddy\ diffusivity\ = 4.15 \times 10^{-3} N_R^{0.86}$

J_1=Bessel function of the order 1

C.9 Krug, A.F., Kuzma-Kichta, Y.A., and Komendantov, A.S. [57]

The Krug correlation is by far the most comprehensive correlation in literature. It was derived using nearly all existing twisted-tape CHF data; however, because the correlation covers such a broad range, its accuracy is poor. The database from which this correlation was developed included a large amount of non-uniform circumferential heating; however, no correction factor for this mechanism was implemented even though it has been shown that this phenomena is significant by Kinoshita et al. [52, 51].

A new formulation of this correlation is being developed by Bergles et al. [8]; however, since it is still in development the published version by Krug et al. [57] is presented here. This correlation consists of a base equation with a series of correction factors for mass flux, quality, heated length, twist ratio, and pressure. Unless otherwise noted, these correction factors are valid for subcooled and saturated boiling conditions.

$$\frac{q''_{cr}}{10^6} = 0.4G^n k_x k_l k_y k_p \tag{C.16}$$

where,

$$n = \sqrt{0.035\left(1-x\right)^{1/8} log(G)}$$

$$k_x = \left[0.66 + 0.25\left(1-x\right)^3\right]^3$$

$$k_l = \begin{cases} 1 + \frac{1.3}{\sqrt[8]{L_h/D}}\left(1 + \frac{25000}{Re_{lq}L_h/D}\right)\left(Pr_{lq}\right)^{-1/3} exp\left(-0.031\left(L_h/D\right)^2\right) & if\ L_h/D < 10 \\ 1 & if\ L_h/D \geq 10 \end{cases}$$

$$k_y = \left(1 + \frac{14}{G^{0.37}y^{3/2}}\right)^2$$

$$k_p = \begin{cases} 1 & if\ x_{eq} \leq 0 \\ \left(1 + 0.035P - 0.00622P^2 + 0.000185P^3\right)\left(1-x\right)^{1/8}\left[1 + \left(\frac{1}{log(G)}\right)^2\right] & if\ x_{eq} > 0 \end{cases}$$

G = mass flux $\left[\frac{kg}{m^2-s}\right]$

P = system pressure [MPa]

Re_{lq} =Reynolds number calculated using liquid properties at the exit

Pr_{lq} =Prandtl number calculated using liquid properties at the exit

C.10 Hata, K. and Masuzaki, S. [34]

The Hata correlation was developed using non-dimensional numbers, making it very user friendly. The experiments that this correlation is based on were all for very short tubes, therefore it is difficult to utilize this correlation for practical design cases in nuclear engineering. Two correlations were developed in their study. One was derived for cases where the inlet conditions are known as shown in Equation (C.17), and the second for known outlet conditions as shown in Equation (C.18). The definition of the non-dimensional numbers follow these two equations.

$$Bo_{sw} = C_1 D^{*-0.1} We_{sw}^{-0.3} \left(\frac{L_h}{D}\right)^{-0.1} exp\left(-\frac{\left(\frac{L_h}{D}\right)}{C_2 Re^{0.4}}\right) Sc^{*C_3} \tag{C.17}$$

$$Bo_{sw} = 0.082 D^{*-0.1} We_{sw}^{-0.3} \left(\frac{L_h}{D}\right)^{-0.1} Sc^{0.7} \tag{C.18}$$

where,

$Bo_{sw} = \frac{q''_{cr}}{Gh_{fg}} \frac{\left(\pi D^2 - 4w\delta_T\right)}{\pi D^2} \frac{2y}{\sqrt{4y^2+2\pi^2}}$

$C_1 = \begin{cases} 0.082 & if \quad \frac{L_h}{D} \lesssim 40 \\ 0.092 & if \quad \frac{L_h}{D} \gtrsim 40 \end{cases}$

$C_2 = \begin{cases} 0.53 & if \quad \frac{L_h}{D} \lesssim 40 \\ 0.85 & if \quad \frac{L_h}{D} \gtrsim 40 \end{cases}$

$C_3 = \begin{cases} 0.7 & if \quad \frac{L_h}{D} \lesssim 40 \\ 0.9 & if \quad \frac{L_h}{D} \gtrsim 40 \end{cases}$

$D^* = \frac{D}{\sqrt{\frac{\sigma}{g(\rho_l - \rho_g)}}}$

$We_{sw} = \frac{GD^2}{\rho_l \sigma} \left(\frac{\pi D^2}{\pi D^2 - 4w\delta_T}\right)^2 \left[\frac{\sqrt{4y^2+2\pi^2}}{2y}\right]^2$

L_h =heated length

D = diameter

$Re = \frac{GD}{\mu_l}$

$Sc^* = \frac{c_{pl}\Delta T_{sub,in}}{h_{fg}}$

$Sc = \frac{c_{pl}\Delta T_{sub,out}}{h_{fg}}$

$\Delta T_{sub,in/out} = T_{sat} - T_{in/out}$

Appendix D

Subchannel Analysis Code

This appendix presents the subchannel analysis code that was developed during this study for the implementation of the new DNB correlation and pressure drop methodology, in the following order:

- Thermal-Hydraulic Subchannel Analysis Code: Section D.1
- Example Case: Section D.2

D.1 Computer Code

This section is divided into seven subsections. The first subsection presents the main driver code and the subsequent sections present the sub-functions required to run the analysis. The section is organized as follows:

- Driver Code: Section D.1.1
- Flow Properties: Section D.1.2
- Swirl Decay: Section D.1.3
- Wall Temperature: Section D.1.4
- Pressure Drop: Section D.1.5
- CHF: Section D.1.6
- Core Sizing: Section D.1.7

This is an incomplete listing of programs. Particularly the code for the Groeneveld LUT [30] has been left out for copyright purposes. The core sizing code was also left out since the methodology was already presented in Ferroni's thesis [23]. Finally, the file XSteam.m [40] was left out due to its length. This file acts as a thermodynamic property lookup table for water from 0-1000 bar and from $0 - 2000^oC$.

D.1.1 Driver Code

```
%This file creates a pressure drop, CHF, and wall temperature trace
%for a pipe containing multiple short length twisted tapes.
clear all
close all
clc
%*************************************************************************
%************************   INPUTS   *************************************
%*************************************************************************
%Computational
comp.N_nodes=1000;          %number of computational nodes
comp.it_limit=20;           %iteration limit
comp.epsilon=1e-4;          %convergence criteria for iterative processes
%Geometry
geom.L_h=3.67;                              %heated length [m]
geom.z=linspace(0,geom.L_h,comp.N_nodes);   %z-position vector [m]
geom.D_rod=0.0133;                          %pipe diameter [m]
geom.D_h=geom.D_rod;                        %tube diameter [m]
geom.squiggle=1.5e-6;                       %pipe roughness [m]
geom.rough_flag=0;                          %DO NOT USE
                                            %uses rough friction factor = 1
                                            %, Blasius = 0 for swirl decay
%Operations
power_inc=1.15; %multiplies channel power to find max power for the channel
oper.Q_pin=power_inc*249.1e3;               %total channel power [W]
oper.Press=15.51e6;                         %operating pressure [Pa]
oper.T_in=295;                              %Inlet temperature [C]
%Inlet enthalpy [J/kg]
oper.h_in=XSteam('h_pT',oper.Press/1e5,oper.T_in)*1000;
oper.delta_h=195.2e3;                       %core enthalpy rise [J/kg]
%power to flow ratio (only valid for constant channel diameter)
oper.Power_Flow=3.384e-6;
oper.m_dot=oper.Power_Flow*oper.Q_pin;      %mass flow rate [kg/s]
oper.G=oper.m_dot/(pi/4*geom.D_rod^2);      %mass flux [kg/m^2-s]
oper.P_bar=oper.Press*1e-5;                 %system pressure [bar]
oper.flux_shape=1;
%neutron flux shape, 0 = bottom peaked, 1 = chopped cosine
oper.axialpeak=1.515;         %axial peaking factor for chopped cosine shape
oper.radialpeak=1.515;      %radial peaking factor used only for total power
%Saturated properties
sat.rho_f=XSteam('rhoL_p',oper.P_bar);         %sat liquid density [kg/m^3]
sat.rho_g=XSteam('rhoV_p',oper.P_bar);         %sat vapor density [kg/m^3]
sat.h_f=XSteam('hL_p',oper.P_bar)*1000;        %sat liquid enthalpy [J/kg]
```

```
sat.h_g=XSteam('hV_p',oper.P_bar)*1000;         %sat vapor enthalpy [J/kg]
sat.h_fg=sat.h_g-sat.h_f;                       %heat of vaporization [J/kg]
sat.T_sat=XSteam('Tsat_p',oper.P_bar);          %saturation temperature [C]
sat.mu_f=XSteam('my_ph',oper.P_bar,sat.h_f/1000*0.99);
%sat liquid viscosity [N-s/m^2]
sat.mu_g=XSteam('my_ph',oper.P_bar,sat.h_g/1000*1.01);
%sat vapor viscosity [N-s/m^2]
sat.k_f=XSteam('tcL_p',oper.P_bar);%sat liquid thermal conductivity [W/m-K]
sat.cp_f=XSteam('CpL_p',oper.P_bar)*1000;%sat liquid specific heat [J/kg-K]
sat.Pr_f=sat.cp_f*sat.mu_f/sat.k_f;       %sat liquid prandtl number
%Twisted tape info
tape_info.y_TTs=[2.5 2.5];                  %twist ratio of each SLTT
tape_info.N_TTs=length(tape_info.y_TTs);    %number of twisted tapes
tape_info.z_TTs=[1.3 2.5];                  %z-location of each SLTT
tape_info.N_turns=[1.5 1.5];      %number of 360-deg rotations for each SLTT
tape_info.FLTT=0;                           %0 = MSLTT; 1 = FLTT; 2 = empty
tape_info.t_TT=5e-4;                        %twisted tape thickness [m]


%***************************************************************************
%**********************    START COMPUTATIONS    ***************************
%***************************************************************************


%initialize
oper.incip_index=comp.N_nodes;  %node of boiling incipience
oper.dep_index=comp.N_nodes;    %node of bubble departure
oper.sat_index=comp.N_nodes;    %first node where x_eq>0

%%%%%%%%%%%%%%%%%%%%%%%%%%%%%%%%%%%%%%%%%%%%%%%%%%%%%%%%%%%%%%%%%%%%%%%%%%%
%Flow properties
[oper]=flow_props(comp,geom,oper,sat);
%Effective Twist Ratio and form pressure drop due to twisted tapes
[oper]=Decay(oper,geom,comp,tape_info);
%Wall temperature if the entire pipe was in axial flow
[oper]=T_wall(comp,geom,oper,sat,tape_info);
%Pressure drop
[oper]=P_drop(comp,geom,oper,sat);
dP_tot=oper.Press-oper.Pz(comp.N_nodes)
%Critical Heat Flux correlation
[CHF CHF_st]=Arment_TTCHF(comp,geom,oper,sat);
DNBR=CHF./oper.q_dp_z;
MDNBR=min(DNBR)
%Core Sizing and Total Power
N_chan=Ferroni_chan(geom);
Power=N_chan*oper.Q_pin/oper.radialpeak
%%%%%%%%%%%%%%%%%%%%%%%%%%%%%%%%%%%%%%%%%%%%%%%%%%%%%%%%%%%%%%%%%%%%%%%%%%%%
```

```
%Figures
%CHF and operating heat flux
figure(1)
plot(oper.x_eq,CHF,'r—',oper.x_eq,CHF_st,'b',oper.x_eq,oper.q_dp_z,'k—')
xlabel('Equilibrium Quality')
ylabel('Heat Flux')
%DNBR
figure(2)
plot(oper.x_eq,DNBR)
xlabel('Equilibrium Quality')
ylabel('DNBR')
axis([-0.33 0.01 0 5])
```

D.1.2 Flow Properties

```
function [oper]=flow_props(comp,geom,oper,sat)
%This function performs a detailed thermal hydraulic subchannel analysis
%and ouputs the following parameters:
% Heat flux                       [W/m^2]
% Flow quality
% Equilibrium Quality
% Bulk coolant temperature        [C]
% Average density                 [kg/m^3]
% Boiling length                  [m]
% Surface tension                 [N/m]
% Liquid viscosity                [N-s/m^2]
% Void fraction
% Average coolant enthalpy        [J/kg]
% Linear heat generation rate     [W/m]
% Node of bubble departure        [-]
% Node of saturated boiling       [-]
% Dynamic density                 [kg/m^3]
% Liquid thermal conductivity     [W/m-K]
% Liquid phase density            [kg/m^3]
%
%Read in variables
%Computational
N_nodes=comp.N_nodes;
%Geometry
z=geom.z;
L_h=geom.L_h;
D_rod=geom.D_rod;
D_h=geom.D_h;
```

```
%Operations
Q_pin=oper.Q_pin;
G=oper.G;
P_Pa=oper.Press;
h_in=oper.h_in;
m_dot=oper.m_dot;
P_bar=P_Pa*1e-5;
peaking=oper.axialpeak;
%Saturated properties
rho_f=sat.rho_f;
rho_g=sat.rho_g;
h_f=sat.h_f;
h_fg=sat.h_fg;
T_sat=sat.T_sat;
mu_f=sat.mu_f;
k_f=sat.k_f;
cp_f=sat.cp_f;
%**************************************************************************
%Start Calculations
q_prime=Q_pin/L_h;                 %average linear heat generation rate [W/m]
if oper.flux_shape==0
    %bottom peaked flux
    alpha=1.96;                  %coefficient for the heat flux shape assumed
    %This expression normalizes the flux shape to the total pin power
    q_prime_ref=(q_prime*(alpha^2+pi^2)*exp(alpha))/((exp(alpha)+1)*pi);
    %linear heat generation rate as a function of z [W/m]
    q_prime_z=q_prime_ref.*exp(-alpha.*z./L_h).*sin(pi.*z./L_h);
elseif oper.flux_shape==1
    %cosine shaped flux
    Le_f=@(Le) (L_h+2*Le)*(cos(pi*Le/(L_h+2*Le))-cos(pi*(L_h+Le)/...
        (L_h+2*Le)))-L_h*pi/peaking;          %extrapolated length function
    L_e=fzero(Le_f,0.07);%extrapolated length for chopped cosine flux shape
    q_prime_z=q_prime.*peaking.*sin(pi*(z+L_e)./(L_h+2*L_e));
elseif oper.flux_shape==2
    q_prime_z=q_prime.*ones(1,N_nodes);
end
q_dp_z=q_prime_z./(pi*D_rod);          %heat flux as a function of z [W/m^2]
%Enthalpy, bulk temperature, surface tension,
%and liquid viscosity distribution
h_avg_z(1)=h_in;
T_bulk(1)=XSteam('T_ph',P_bar,h_avg_z(1)/1000);
sigma(1)=XSteam('st_T',T_bulk(1));
if T_bulk(1)==T_sat
    mu_l(1)=mu_f;
    rho_l(1)=rho_f;
```

```
else
    mu_l(1)=XSteam('my_pT',P_bar,T_bulk(1));
    rho_l(1)=XSteam('rho_pT',P_bar,T_bulk(1));
end
for i=2:length(z)
    h_avg_z(i)=h_in+trapz(z(1:i),q_prime_z(1:i))/m_dot;
    T_bulk(i)=XSteam('T_ph',P_bar,h_avg_z(i)/1000);
    sigma(i)=XSteam('st_T',P_bar,T_bulk(i));
    if T_bulk(i)<T_sat*.999
        mu_l(i)=XSteam('my_pT',P_bar,T_bulk(i));
        rho_l(i)=XSteam('rho_pT',P_bar,T_bulk(i));
        k(i)=XSteam('tc_pT',P_bar,T_bulk(i));
    else
        mu_l(i)=mu_f;
        rho_l(i)=rho_f;
        k(i)=k_f;
    end
end
%Equilibrium Quality
x_eq=(h_avg_z-h_f)./h_fg;
%Flow Quality Profile
T_avg=(T_bulk(1)+T_sat)/2;%approximate temp to eval. cp and k at for Pe
if T_avg==T_sat
    cp_l=XSteam('CpL_p',P_bar)*1000;
    k_l=XSteam('tcL_p',P_bar);
else
    cp_l=XSteam('Cp_pT',P_bar,T_avg)*1000; %specific heat capacity [J/kg-K]
    k_l=XSteam('tc_pT',P_bar,T_avg);       %thermal conductivity [W/m-K]
end
Pe=G*D_h*cp_l/k_l;                         %Peclet number
ST_dep=0.0065;  %bubble departure stanton number for Pe>70000
Nu_dep=455;     %bubble departure Nusselt number for Pe<70000
%Bubble departure using the Saha-Zuber correlation
if Pe<7e4
    Nu=0;
    j=1;
    while Nu<Nu_dep && j<N_nodes
        if T_bulk(j)<0.99*T_sat
            kl=XSteam('tc_pT',P_bar,T_bulk(j));
        else
            kl=k_f;
        end
        Nu=(q_dp_z(j)*D_h)/(kl*(T_sat-T_bulk(j)));
        j=j+1;
        if j==N_nodes
```

```
            break
        end
    end
    dep_index=j;
elseif Pe>=7e4
    ST=0;
    j=1;
    while ST<ST_dep && j<N_nodes
        if T_bulk(j)<0.99*T_sat
            cpl=XSteam('Cp_pT',P_bar,T_bulk(j))*1000;
        else
            cpl=cp_f;
        end
        ST=q_dp_z(j)/(G*cpl*(T_sat-T_bulk(j))); %Stanton
        j=j+1;
        if j==N_nodes
            break
        end
    end
    dep_index=j;
end
if j==N_nodes
    L_b=0;
else
    L_b=z(N_nodes)-z(dep_index); %boiling length [m]
end
%flow quality using the Levy profile-fit method
if h_avg_z(1)>=h_f
    x_flow=x_eq;
else
    for j=1:length(z)
        if j<=dep_index || dep_index==N_nodes
          x_flow(j)=0;
        else
          x_flow(j)=x_eq(j)-x_eq(dep_index)*exp(x_eq(j)/x_eq(dep_index)-1);
        end
        if x_flow(j)>1
          x_flow(j)=1;
        end
    end
end
%Void fraction and density
for i=1:length(T_bulk)
    if x_flow(i)<=0
        rho(i)=rho_l(i);
```

```
        rhomp(i)=rho(i);
        alpha(i)=0;
    else
        beta_flow=1./(1+(1-x_flow(i))./x_flow(i).*rho_g./rho_l(i));
        b=(rho_g/rho_f)^0.1;
        C_o=beta_flow.*(1+(1./beta_flow-1).^b);
        %void fraction according to Dix, T&K 1st ed. p. 479-480
        alpha(i)=beta_flow./C_o;
        rho(i)=alpha(i).*rho_g+(1-alpha(i)).*rho_l(i);
        rhomp(i)=(x_flow(i)^2/(rho_g*alpha(i))+(1-x_flow(i))^2/...
            (rho_l(i)*(1-alpha(i))))^(-1); %dynamic density
    end
end
%finds where saturated boiling starts
sat_index=1;
while h_avg_z(sat_index)<h_f
    sat_index=sat_index+1;
    if sat_index>N_nodes
        sat_index=N_nodes;
        break
    end
end
%read out new structured variables
oper.q_dp_z=q_dp_z;
oper.x_flow=x_flow;
oper.x_eq=x_eq;
oper.T_bulk=T_bulk;
oper.rho=rho;
oper.L_b=L_b;
oper.sigma=sigma;
oper.mu_l=mu_l;
oper.alpha=alpha;
oper.h_z=h_avg_z;
oper.q_prime_z=q_prime_z;
oper.dep_index=dep_index;
oper.sat_index=sat_index;
oper.rhomp=rhomp;
oper.k=k;
oper.rho_l=rho_l;
end
```

D.1.3 Swirl Decay

```
function[oper]=Decay(oper,geom,comp,tape_info)
%This function solves for the angular velocity of the fluid at a given
%position from a twisted tape.
%
%G = mass flux [kg/m^2-s]
%P_Pa = pressure [Pa]
%D = diameter [m]
%x_eq = equilibrium quality array
%z = distance from exit of the twisted tape [m]
%y_TTs = twist ratio vector for all twisted tapes (can be different for
%each tape
%N_TTs = number of twisted tapes
%N_turns = vector of number of 360 deg turns for each tape
%N_nodes = number of total nodes for the pipe
%z_TTs=vector of the locations of the upstream end of the twisted tapes [m]
%h = enthalpy vector [J/kg]
%decay_flag = whether a twisted tape is present or not; 0 = twisted tape
%present, 1 = no twisted tape. before the first TT it doesn't matter
%because the code recognizes that y_eff=0 means that there is no TT
%
%Read in variables
%Computations
N_nodes=comp.N_nodes;
%Operation
G=oper.G;
rhomp=oper.rhomp;
rhom=oper.rho;
mu=oper.mu_l;
%geometry
D=geom.D_h;
z=geom.z;
squiggle=geom.squiggle;
rough_flag=geom.rough_flag;
%Define variables
y_TTs=tape_info.y_TTs;
N_TTs=tape_info.N_TTs;
z_TTs=tape_info.z_TTs;
N_turns=tape_info.N_turns;
FLTT_flag=tape_info.FLTT;
t_TT=tape_info.t_TT;
%***********************************************************************
%Start Computation
V_ax=G./rhom;        %axial velocity [m/s]
%Geometry
dz=z(2)-z(1);        %step size [m]
```

```
%find the index of the inlet, steady-state swirl, and outlet of each SLTT
for i=1:N_TTs
    inlet(i)=floor(z_TTs(i)/dz);
    if i==1 && inlet(i)==0
        inlet(i)=1;
    end
    ss(i)=floor(1.5*y_TTs(i)*D/dz)+inlet(i);
    exit(i)=floor(N_turns(i)*y_TTs(i)*D/dz)+inlet(i);
    inlet(N_TTs+1)=N_nodes;
end
%total decay length after each SLTT
for i=1:N_TTs-1
    Ld_tot(i)=z(inlet(i+1))-z(exit(i));
end
%Calculate y_eff arrays for the regions of the pipe
j=1;
omega_o(j)=0;
%empty tube
if FLTT_flag==2
    y_eff=zeros(1,N_nodes);
    decay_flag=ones(1,N_nodes);
    form_dp=zeros(1,N_nodes);
%FLTT
elseif FLTT_flag==1
    y_eff=y_TTs.*ones(1,N_nodes);
    decay_flag=zeros(1,N_nodes);
    K=1/8*(pi/y_TTs)^2*(0.25*pi*D^2/(0.25*pi*D^2-t_TT*D))^2;
    form_dp(1)=K*G^2/(2*rhomp(1));
    form_dp(2:N_nodes)=0;
%SLTTs
elseif FLTT_flag==0
    for i=1:N_nodes
            %before the entrance to the first TT
        if i<inlet(j) && j==1
            y_eff(i)=0;
            decay_flag(i)=1;
            form_dp(i)=0;
            %developing swirl (entrance to a TT)
        elseif i>=inlet(j) && i<=ss(j)
            if i==inlet(j)
                K=1/8*(pi/y_TTs(j))^2*(0.25*pi*D^2/(0.25*pi*D^2-t_TT*D))^2;
                form_dp(i)=K*G^2/(2*rhomp(i));
            else
                form_dp(i)=0;
            end
```

```
        %usues a quickly decaying exponential for swirl build up
        %this has not been validated with any data
        omega_ss(j)=(V_ax(ss(j))*pi)/(y_TTs(j)*D);
        omega=omega_ss(j)*(1-exp(-5.*(z(i)-z(inlet(j)))/D))+...
            omega_o(j)*exp(-5.*(z(i)-z(inlet(j)))/D);
        w(i)=omega;
        y_eff(i)=V_ax(i)*pi/(omega*D);
        decay_flag(i)=0;
        if y_eff(i)>1e6
            y_eff(i)=0;
        end
        %fully developed swirl still inside a TT
    elseif i>ss(j) && i<=exit(j)
        y_eff(i)=y_TTs(j);
        decay_flag(i)=0;
        form_dp(i)=0;
        %decaying swirl
    elseif i>exit(j) && i<inlet(j+1) || i>exit(N_TTs)
        %initial swirl constant and z value
        aa=2*3^0.5;
        z_o=pi/(2*y_TTs(j));
        Co_num=6+2*z_o^2+aa*(z_o^4+3*z_o^2+3)^0.5;
        Co_den=aa+aa*z_o^2-2*(z_o^4+3*z_o^2+3)^0.5;
        C_o=log(Co_num/Co_den);
        Re=G*D/mu(i);
        %axial flow friction factor
        if rough_flag==0
            f_st=0.3164/Re^0.25;
        else
            %don't use this, it doesn't work
            f_st=0.0096+(squiggle/D)^0.5+(2.88/Re)^0.5;
        end
        LD=(z(i)-z(exit(j)))/D; %length-to-diameter ratio
        %swirl intensity
        Sw_func=@(z) aa*f_st*(LD-6*exp(-0.25*LD)+6)+...
            C_o-log((6+2*z^2+aa*(z^4+3*z^2+3)^0.5)...
            /(aa+aa*z^2-2*(z^4+3*z^2+3)^0.5));
        if i==exit(j)+1
            z_loc(i)=fzero(Sw_func,z_o);
        else
            z_loc(i)=fzero(Sw_func,z_loc(i-1));
        end
        y_eff(i)=pi/(2*z_loc(i));
        form_dp(i)=0;
        decay_flag(i)=1;
```

```
            omega_f=(V_ax(i)*pi)/(D*y_eff(i));
        end
        if i==inlet(j+1)-1
            j=j+1;
            if j==N_TTs+1
                j=N_TTs;
            end
            omega_o(j)=omega_f;
        end
    end
end
%outputs
oper.y_eff=y_eff;
oper.form_dp=form_dp;
oper.decay_flag=decay_flag;
end
```

D.1.4 Wall Temperature

```
function [oper]=T_wall(comp,geom,oper,sat,tape_info)
%Heat Transfer Coefficient
%Calculates the heat transfer coefficient using the Chen correlation for
%the saturated region, the Collier equation, and the Gnielinski
%equation for subcooled. Refer to T&K pp. 443, 538-540
%
%Read in parameters
%computational terms
it_limit=comp.it_limit;     %iteration limit for wall temperature
epsilon=0.1;                %convergence criteria
N_nodes=comp.N_nodes;
%Geometry
D_h=geom.D_h;
z=geom.z;
%Operations
x_flow=oper.x_flow;
x_eq=oper.x_eq;
P_Pa=oper.Press;
P_bar=P_Pa*1e-5;                  %Pressure [bar]
P_psia=P_bar*14.5;                %Pressure [psia]
G=oper.G;
incip_index=oper.incip_index;%only for nonheated channels is this important
q_dp=oper.q_dp_z;
q_dp_e=q_dp.*0.3172;              %heat flux [Btu/hr-ft^2]
```

```
T_bulk=oper.T_bulk;
sigma=oper.sigma;
mu_l=oper.mu_l;
y_eff=oper.y_eff;       %effective twist ratio, special case: 0 = no swirl
decay_flag=oper.decay_flag;           %inside a twisted tape (0) or not (1)
%Saturated Properties
h_f=sat.h_f;
h_fg=sat.h_fg;
Pr_f=sat.Pr_f;
mu_f=sat.mu_f;
mu_g=sat.mu_g;
T_sat=sat.T_sat;
T_sat_e=(T_sat*9/5)+32;                 %saturation temp [F]
k_f=sat.k_f;
cp_f=sat.cp_f;
rho_f=sat.rho_f;
rho_g=sat.rho_g;
%tape info
t_TT=tape_info.t_TT;
%gravity
g=9.81;
%**************************************************************************
%Start Calculations
super_flag=0;              %flag that marks the point of boiling incipience
for i=1:N_nodes
    it=0;
    clear error Tg
    if x_flow(i)<=0
        mu_b=mu_l(i);
        k=XSteam('tc_pT',P_bar,T_bulk(i));
        %specific heat capacity [J/kg-K]
        cp=XSteam('Cp_pT',P_bar,T_bulk(i))*1000;
        Pr=cp*mu_b/k;
        Re=G*D_h/mu_b;
    else
        k=k_f;
        mu_b=mu_f;
        Pr=Pr_f;
        Re=G*D_h/mu_f;
    end
    %Wall Temperature Calculation
    %single phase flow Gnielinski correlation, swirl Manglik and
    %Bergles, decaying swirl, Jensen and Bensler
    if x_flow(i)<=0 && super_flag==0
        if i==1
```

```
    delta_T_guess=0.01;
elseif i>1 && T_w(i-1)>T_sat
    delta_T_guess=T_w(i-1)-T_sat;
else
    delta_T_guess=T_w(i-1)-T_bulk(i-1);
end
delta_T_flag=0;
while delta_T_flag==0
    T_w_guess=T_bulk(i)+delta_T_guess;
    if T_w_guess>=T_sat*0.99
        mu_w(i)=mu_f;
    else
        mu_w(i)=XSteam('my_pT',P_bar,T_w_guess);
    end
    %no swirl
    if y_eff(i)==0
        Pr_w=cp*mu_w(i)/k;
        f=1/(1.82*log10(Re)-1.64)^2;
        Nu_guess=((f/8)*(Re-1000)*Pr)/(1+12.7*sqrt(f/8)*...
            (Pr^(2/3)-1))*(1+D_h/z(i))^(2/3)*(Pr/Pr_w)^0.11;
    %swirl
    elseif y_eff(i)>0 && decay_flag(i)==0
        Nu_guess=0.023*Re^0.8*Pr^0.4*(1+0.769/y_eff(i))*...
            (pi/(pi-4*t_TT/D_h))^0.8*((pi+2-2*t_TT/D_h)/...
            (pi-4*t_TT/D_h))^0.2*(mu_b/mu_w(i))^0.18;
        %correct for entrance region effects
        if z(i)>0 && z(i)/D_h<60
            Nu_guess=Nu_guess*(1+D_h/z(i))^0.7;
        elseif z(i)==0 && z(i)/D_h<60
            T_w(i)=T_bulk(i);
            delta_T_flag=1;
        end
    elseif y_eff(i)>0 && decay_flag(i)==1
        alpha_t=1/(2*y_eff(i))*sqrt(4*y_eff(i)^2+pi^2);
        Nu_guess=0.020*(alpha_t*Re)^0.8*Pr^0.4;
        %correct for entrance region effects
        if z(i)>0 && z(i)/D_h<60
            Nu_guess=Nu_guess*(1+D_h/z(i))^0.7;
        elseif z(i)==0 && z(i)/D_h<60
            T_w(i)=T_bulk(i);
            delta_T_flag=1;
        end
    end
    htc=Nu_guess*k/D_h;
    T_ww=q_dp(i)/htc+T_bulk(i);
```

```
        %check convergence
        error=abs(T_ww-T_w_guess);
        if abs(error)<epsilon
            T_w(i)=T_w_guess;
            delta_T_flag=1;
            htc=q_dp(i)/(T_w(i)-T_bulk(i));
            Nus(i)=htc*D_h/k;
        else
            delta_T_guess=T_ww-T_bulk(i);
            it=it+1;
            if it>it_limit+50
                disp('Wall Temp did not conv beyond ent 1-phase')
                break
            end
        end
    end
%subcooled boiling modified Chen and modified Jensen Bensler (1986)
elseif x_flow(i)>0 && x_eq(i)<0  || super_flag==1
    delta_T_flag=0;
    if T_w(i-1)>T_sat
        delta_T_guess=T_w(i-1)-T_sat;
    else
        delta_T_guess=5;
    end
    while delta_T_flag==0
        T_w_guess=T_sat+delta_T_guess;
        if T_w_guess>=T_sat
            mu_w(i)=mu_f;
        else
            mu_w(i)=XSteam('my_pT',P_bar,T_w_guess);
        end
        %convective heat transfer coefficient
        %no swirl
        if y_eff(i)==0
           h_c=0.023*((G*(1-x_flow(i))*D_h)/mu_f)^0.8*Pr_f^0.4*k_f/D_h;
           %suppression factor
           S=(1+2.53e-6*Re^1.17)^(-1);
        %with swirl (I just used the same methodology as the extension
        %of Chen to subcooled boiling
        elseif y_eff(i)>0
            D_e=D_h*pi/(pi+2);
            alpha_t=1/(2*y_eff(i))*sqrt(4*y_eff(i)^2+pi^2);
            h_c=0.020*(alpha_t*G*D_e/mu_f)^0.8*Pr_f^0.4*k_f/D_e;
            X_o=0.041*sqrt(sigma(i)/(g*(rho_f-rho_g)));
            S=k_f/(h_f*X_o)*(1-exp(-h_f*X_o/k_f));
```

```
        end
        delta_p=(T_w_guess-T_sat)*h_fg*rho_g/T_sat;
        h_nb=S*0.00122*((k_f^0.79*cp_f^0.45*rho_f^0.49)/...
            (sigma(i)^0.5*mu_f^0.29*h_fg^0.24*rho_g^0.24))*...
            delta_T_guess^0.24*delta_p^0.75;
        T_ww=(q_dp(i)+h_c*T_bulk(i)+h_nb*T_sat)/(h_nb+h_c);
        %check convergence
        error=abs(T_ww-T_w_guess);
        it=it+1;
        Tg(it)=T_ww;
        if abs(error)<epsilon
            T_w(i)=T_w_guess;
            delta_T_flag=1;
            h_2p=q_dp(i)/(T_w(i)-T_bulk(i));
            Nus(i)=h_2p*D_h/k;
        elseif it<4
            delta_T_guess=T_ww-T_bulk(i);
            if delta_T_guess<0
                delta_T_guess=0.001;
            end
            if it>it_limit
                disp('Wall Temperature did not converge sub')
                break
            end
        elseif it>=4 && Tg(it)==Tg(it-1)
            T_w(i)=T_ww;
            delta_T_flag=1;
            h_2p=q_dp(i)/(T_w(i)-T_bulk(i));
            Nus(i)=h_2p*D_h/k;
        end
    end
%saturated boiling  Chen
elseif x_eq(i)>=0 || super_flag==1
    X_tt=((x_flow(i)/(1-x_flow(i)))^0.9*(rho_f/rho_g)...
        ^0.5*(mu_g/mu_f)^0.1)^(-1);
    if 1/X_tt<=0.1
        F=1;
    else
        F=2.35*(0.213+1/X_tt)^0.736;
    end
    %no swirl
    if y_eff(i)==0
        %convective heat transfer coefficient
        h_c=0.023*((G*(1-x_flow(i))*D_h)/mu_f)^0.8*Pr_f^0.4*k_f/D_h*F;
        Re_nb=Re*(1-x_flow(i))*F^1.25;
```

```
    S=(1+2.53e-6*Re_nb^1.17)^(-1);
%swirl
elseif y_eff(i)>0
    D_e=D_h*pi/(pi+2);
    alpha_t=1/(2*y_eff(i))*sqrt(4*y_eff(i)^2+pi^2);
    X_o=0.041*sqrt(sigma(i)/(g*(rho_f-rho_g)));
    h_c=0.020*(alpha_t*G*(1-x_flow(i))*D_e/mu_f)^0.8*...
        Pr_f^0.4*k_f/D_e;
    S=k_f/(h_f*F*X_o)*(1-exp(-h_f*F*X_o/k_f));
end
delta_T_flag=0;
if i==1
    delta_T_guess=5;
elseif i>1 && T_w(i-1)>T_sat
    delta_T_guess=T_w(i-1)-T_sat;
else
    delta_T_guess=5;
end
while delta_T_flag==0
    T_w_guess=T_sat+delta_T_guess;
    delta_p=(T_w_guess-T_sat)*h_fg*rho_g/T_sat;
    h_nb=S*0.00122*((k_f^0.79*cp_f^0.45*rho_f^0.49)/...
        (sigma(i)^0.5*mu_f^0.29*h_fg^0.24*rho_g^0.24))*...
        delta_T_guess^0.24*delta_p^0.75;
    T_ww=T_sat+q_dp(i)/(h_nb+h_c);
    %check convergence
    error=abs(T_ww-T_w_guess);
    if abs(error)<epsilon
        T_w(i)=T_w_guess;
        if T_w(i)>=T_sat
            mu_w(i)=mu_f;
        else
            mu_w(i)=XSteam('my_pT',P_bar,T_w(i));
        end
        h_2p=q_dp(i)/(T_w(i)-T_sat);
        Nus(i)=h_2p*D_h/k;
        delta_T_flag=1;
    else
        delta_T_guess=T_ww-T_sat;
        it=it+1;
        if it>it_limit
            disp('Wall Temperature did not converge sat')
            break
        end
    end
```

```
        end
        %Saturated boiling for L/D<60
        if z(i)/D_h<60
            Nu_inf=h_2p*D_h/k;
            Nu=Nu_inf*(1+D_h/z(i)^0.7);
            h_2p=Nu*k/D_h;
            T_w(i)=q_dp(i)/h_2p+T_sat;
        end

    end
    %find wall superheat where bubble nucleation occurs
    T_wse=T_sat_e+(q_dp_e(i)/(15.6*P_psia^1.156))^(P_psia^0.0234/2.3);
    T_wsm=(T_wse-32)*5/9;
    if T_wsm<=T_w(i) && super_flag==0
        incip_index=i;
        super_flag=1;
    end
end
mu_w(1)=mu_w(2);
Nus(1)=Nus(2);
%output
oper.T_wall=T_w;
oper.Nus=Nus;
oper.incip_index=incip_index;
oper.mu_w=mu_w;
end
```

D.1.5 Pressure Drop

There are two files required to calculate the channel pressure drop. The first code, P_drop.m, calculates the components of pressure drop, i.e. acceleration, friction, form, and gravity losses. Within the P_drop.m file the Kanizawa.m file is called to calculate the friction pressure drop.

```
function [oper]=P_drop(comp,geom,oper,sat)
%Total Pressure drop across the heated length. This code outputs the
%following pressure drops:
%Entrance and Exit losses
%Form Losses due to grid spacers
%Friction Pressure Drop
%Gravity
%Acceleration
%
%Read in variables
```

```
%Computation
N_nodes=comp.N_nodes;
%Geometry
z=geom.z;
dz=z(2)-z(1);
%Operations
rhomp=oper.rhomp;
Press=oper.Press;
G=oper.G;
%gravity
g=9.81;                     %gravity [m/s^2]
%**************************************************************************
%Start calculations
%Entrance and Exit Losses
oper.dp_ent=G^2/(2*rhomp(1))/2;
oper.dp_exit=G^2/(2*rhomp(N_nodes));
%Friction Pressure drop
[oper]=Kanizawa(geom,oper,sat,comp);
dp_fric=oper.dP_Kan;
for i=1:N_nodes
    %Acceleration Pressure Drop
    if i==1
        dp_acc(i)=G^2/(2*rhomp(1));
    elseif i>1 && i<N_nodes
        dp_acc(i)=G^2.*(1./rhomp(i)-1./rhomp(i-1));
    elseif i==N_nodes
        dp_acc(i)=-G^2/(2*rhomp(N_nodes));
    end
    %Gravity Pressure Drop
    dp_grav(i)=rhomp(i)*dz*g;
    %total pressure drop
    dp(i)=dp_acc(i)+dp_fric(i)+dp_grav(i)+oper.form_dp(i);
    if i==1
        P(i)=Press-oper.dp_ent;
    elseif i<=N_nodes-1 && i>1
        P(i)=P(i-1)-dp(i);
    else
        P(i)=P(i-1)-dp(i)-oper.dp_exit;
    end
end
%Total Pressure Drop
oper.Pz=P;
oper.acc=dp_acc;
oper.g=dp_grav;
oper.fric=dp_fric;
```

```
end
```

```
function [oper]=Kanizawa(geom,oper,sat,comp)
%This function calculates the two-phase pressure drop according to the
%Kanizawa et al. (2011) friction factor correlation for FLTTs.
%
%Read in variables
%Geometry
D=geom.D_rod;
z=geom.z;
dz=z(2)-z(1);
%operations
G=oper.G;
x_flow=oper.x_flow;
rho_l=oper.rho_l;
rhomp=oper.rhomp;
mu_l=oper.mu_l;
mu_w=oper.mu_w;
decay_flag=oper.decay_flag;
y=oper.y_eff;
incip_index=oper.incip_index;
%sat properties
rho_g=sat.rho_g;
rho_f=sat.rho_f;
mu_g=sat.mu_g;
%computations
N_nodes=comp.N_nodes;
%constants
C_ms=3;
g=9.81;
% Fr_sat=G^2/(g*D*pi/(pi+2)*rho_f^2);
%************************************************************************
%start calculations
for i=1:N_nodes
    if decay_flag(i)==0
        d_h=D*pi/(pi+2);
        n=0.35;
    else
        d_h=D;
        n=0.28;
    end
    Re_l=G*d_h/mu_l(i);
    Re_v=G*d_h/mu_g;
    %Single phase liquid, low Reynolds number
```

```
if x_flow(i)<=0 && Re_l<=1187
    if i<=incip_index
        f_p(i)=64/Re_l*(mu_w(i)/mu_l(i))^n*(d_h/D);
    else
        f_p(i)=64/Re_l;
    end
%Single phase liquid, high Reynolds number
elseif x_flow(i)<=0 && Re_l>1187
    if i<=incip_index
        f_p(i)=0.3164/Re_l^0.25*(mu_w(i)/mu_l(i))^n*(d_h/D);
    else
        f_p(i)=0.3164/Re_l^0.25;
    end

%Two-phase flow, low Reynolds number
elseif x_flow(i)>0 && Re_l<=1187
    f_l=64/Re_l;
    if Re_v<=1187
        f_v=64/Re_v;
    else
        f_v=0.3164/Re_v^0.25;
    end
    A=G^2*f_l/(2*rho_l(i)*d_h);
    B=G^2*f_v/(2*rho_g*d_h);
    beta=A+2*(B-A)*x_flow(i);
    dp_tp=(beta*(1-x_flow(i))^(1/C_ms)+B*x_flow(i)^C_ms)*dz;
    f_p(i)=dp_tp*rhomp(i)*d_h*2/(G^2*dz);

%Two-phase flow, high Reynolds number
elseif x_flow(i)>0 && Re_l>1187
     f_l=0.316/Re_l^0.25;
    if Re_v<=1187
        f_v=64/Re_v;
    else
        f_v=0.316/Re_v^0.25;
    end
    A=G^2*f_l/(2*rho_l(i)*d_h);
    B=G^2*f_v/(2*rho_g*d_h);
    beta=A+2*(B-A)*x_flow(i);
    dp_tp=(beta*(1-x_flow(i))^(1/C_ms)+B*x_flow(i)^C_ms)*dz;
    f_p(i)=dp_tp*rhomp(i)*d_h*2/(G^2*dz);
end
Fr=G^2/(g*d_h*rhomp(i)^2);
if y(i)==0
    f_ratio=1;
```

```
    else
        f_ratio=(1+2*y(i)^(-0.4)*Fr^(-0.1))^1.5;
    end
    f_sw(i)=f_p(i)*f_ratio;
    dP(i)=dz*f_sw(i)*G^2/(2*rhomp(i)*d_h);
    if x_flow(i)<=0
        TPM(i)=1;
    elseif x_flow(i)>0 && y(i)>0
        A_sat=G^2*f_l/(2*rho_f*d_h);
        Fr_sat=G^2/(g*d_h*rho_f^2);
        TPM(i)=(beta*(1-x_flow(i))^(1/3)+B*x_flow(i)^3)/A_sat*...
            (1+2*y(i)^(-0.4)*Fr^(-0.1))^1.5/(1+2*y(i)^(-0.4)...
            *Fr_sat^(-0.1))^1.5;
    elseif x_flow(i)>0 && y(i)==0
        A_sat=G^2*f_l/(2*rho_f*d_h);
        TPM(i)=(beta*(1-x_flow(i))^(1/3)+B*x_flow(i)^3)/A_sat;
    end
end
oper.dP_Kan=dP;
oper.f_sw=f_sw;
oper.TPM=TPM;
end
```

D.1.6 Critical Heat Flux

The code for the Groeneveld LUT [30] is not supplied in this section. The code linearly interpolates between entries of mass flux, pressure, and equilibrium quality presented in the Groeneveld paper. The code also applies correction factors for non-uniform heating, channel diameter, and boiling length.

```
function [CHF CHF_st]=Arment_TTCHF(comp,geom,oper,sat)
%Read in variables
%Computational
N_nodes=comp.N_nodes;
%Geometry
z=geom.z;
L_h=geom.L_h;
D=geom.D_h;
%Operations
G=oper.G;
P_Pa=oper.Press;
x_eq=oper.x_eq;
rho_m=oper.rho;
q_dp_z=oper.q_dp_z;
```

```
alpha=oper.alpha;
sat_index=oper.sat_index;
x_flow=oper.x_flow;
y=oper.y_eff;
%Saturated properties
rho_f=sat.rho_f;
rho_g=sat.rho_g;
g=9.81;
%*************************************************************************
%Start Computations
%Groeneveld Empty tube CHF
[CHF_st] = Groeneveld(z,N_nodes,x_eq,G,P_Pa,D,q_dp_z,alpha,...
    L_h,sat_index,0,x_flow);
for i=1:N_nodes
    V_ax=G/rho_m(i);
    theta=pi^2*V_ax^2/(2*g*y(i)^2*D);
    ratio=(1+0.7*theta*exp(-(rho_f/rho_g)*0.09))^0.14;
    if ratio<1
        ratio=1;
    end
    if y(i)==0
        CHF(i)=CHF_st(i);
    else
        CHF(i)=CHF_st(i)*ratio;
    end
end
end
```

D.1.7 Core Sizing

Since this code was developed in a previous study, and the presentation of this code would occupy significant space it is not presented here. The methodology for finding the number of coolant channels in the IPWR can be found in Ferroni's thesis [23].

D.2 Example Case

The hot subchannel of the modified case presented in Section 7.4 was analyzed using the preceding Matlab code. Two SLTTs with y=2.5 were placed 1.3 and 2.5 meters from the bottom of the core. This placement was selected based on observing the plot of DNBR vs. axial height as shown in Figure D-1. This SLTT placement was selected so that the channel was not MDNBR limited. Once the twisted-tape placement and twist ratio were adjusted, the channel power was increased by increasing the power_inc variable until the pressure drop limit was reached. This was done with the oper.Power_Flow ratio variable. The value of this

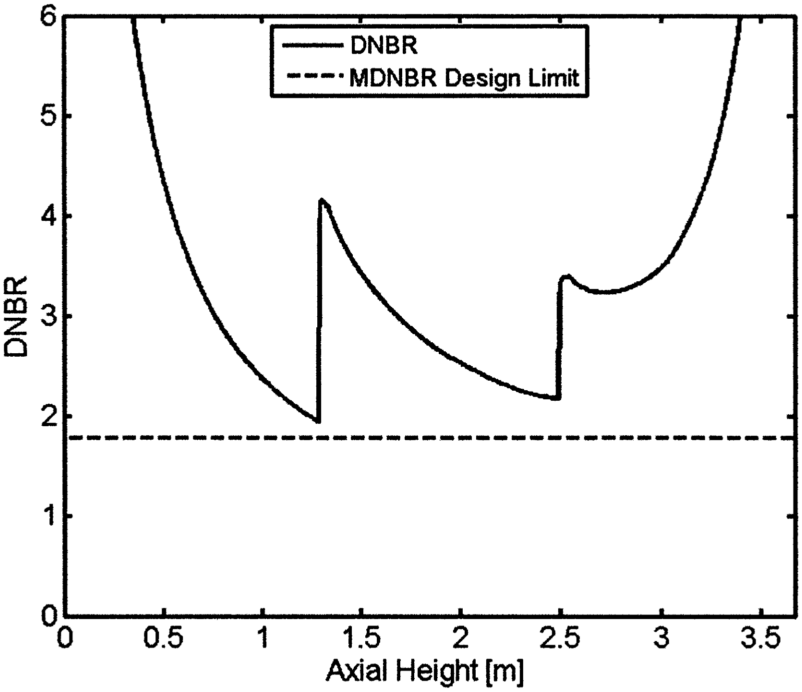

Figure D-1: DNBR vs. Axial Height for Modified MSLTT Design Case

variable is only valid if the channel diameter and number of channels are kept constant. If either of the values change, this value must be recalculated such that the average channel maintains a constant enthalpy rise of 195.2 kJ/kg.

This example case is only a rough optimization. If more time was spent optimizing the channel an increase of at least 5% relative to the maximum power E-IPWR is expected.